# Transition metal point defects in diamond

Watkins, Matthew Benjamin

# Transition metal point defects in diamond.

A thesis submitted for the degree of Doctor of Philosophy in the University of London.

Matthew Benjamin Watkins

Dept. of Physics
King's College
University of London

August 2003

To My Parents

*"When... in the course of all these thousands of years has man ever acted in accordance with his own interests?"*

*Notes from the Underground, Fyodor Dostoevsky.*

# Published Papers.

G Davies, B Campbell, A Mainwood, M E Newton, M Watkins, H Kanda, T R Anthony, " Interstitials, vacancies and impurities in diamond", Phys. Stat. Solid. A, **186**(2): 187 (2001)

A Smith, A Mainwood, M Watkins, " The kinetics of the capture of nitrogen by nickel defects in diamond", Diam. Relat. Mater., **11**, 312 (2002)

M Watkins, A Mainwood, G Davies, " The effects of spin-orbit coupling on uniaxial stress measurements", Diam. Relat. Mater., **12**, 503 (2003)

M Watkins, A Mainwood, G Davies, " *Ab initio* calculations of transition metal defects indiamond", J. Phys. C (in press)

M Watkins, A Mainwood, D Fisher, "The effect of Transition Metals on nitrogen aggregation in diamond"" Diam. Relat. Mater., (submitted)

# Abstract

In this thesis the structure and properties of transition metal point defects in diamond are studied. Transition metals are extensively used in the growth of synthetic diamond using high pressure, high temperature processes as solvent catalysts. They are consequently found in the diamond crystal as both large inclusions and as point defects, and have been observed by both optical spectroscopic techniques and electron paramagnetic resonance. The transition metal point defects are of interest for characterising synthetic stones (of interest to the gem trade), having possible application as photochromic centres and being potential shallow acceptors, they also exhibit interesting physics in their own right.

The structure of the defects has been investigated by *ab initio* calculations using the Hartree-Fock methodology, examing the main types of transition metal environment in diamond: interstitial, substitutional and semi-vacancy. The calculations allowed systematic study of changes in behaviour across the transition series, such as charge states, optical transition energies, binding energies and spin states.

A common method for the investigation of point defects in diamond is that of uniaxial stress in conjunction with optical absorption/luminescence, however, many transition metal defects have proved hard to characterise by this method. A possible cause for this is the neglect of spin-orbit coupling. The problem of uniaxial stress at tetrahedral centres with the inclusion of spin-obit coupling has been investigated.

Transition metals have been found to modify the macroscopic properties of diamonds they are included in by altering the aggregation of nitrogen; Nitrogen aggregation has been observed to be catalysed by the presence of transition metals. Experimental data has been fitted to a mechanistic scheme where the transition metal accelerates nitrogen aggregation by the release of carbon interstitials.

# Acknowledgements

I'd like to start by thanking Alison Mainwood, for her assistance throughout the last few years, and Gordon Davies for attempting to get me into a laboratory again; the enthusiasm slowly rubbed off.

Mum and Dad, thanks for putting up with this trial – and me. There's no way this thesis would have been presented without you. Many people have said that words are no substitute for actions, so I hope I can make things up to you in the future.

Everybody else, in the unlikely event that you read this, thank you. The undergrounders – Brendon, Alex, Lorenzo, Ruth, Jin, Fred etc. for some entertaining times / help and assistance. The Webb, Max and many others, purely for entertaining times. Also, not least, H and Marky. And in the even more unlikely event that anyone form the 'stone' reads this, thanks for the last year: particularly you Malmas.

To reiterate thanks Mum and Dad....

# Contents

# Chapter 4

## Spin-orbit coupling in Uniaxial stress experiments



# Chapter 5

## Review of known transition metal defects in diamond

# Chapter 6

## Transition Metals in Diamond: a Cluster Study using the Hartree-Fock method

# Chapter 7

## The effect of transition metals on nitrogen aggregation in diamond



# Chapter 8

# Chapter 1.

# Introduction

## 1.1 Synopsis

Diamond is best known as a highly attractive gemstone. However, diamonds also possess many remarkable properties of scientific/industrial interest. Indeed the market for gem diamonds is now exceeded by that for drill-bits, abrasives etc. As these uses suggest diamond is extremely hard, optically transparent in the visible region of the electromagnetic spectrum and a remarkable conductor of heat; it is, however, essentially an insulator. Diamond has a brilliant future assured as a component of high performance optical windows, detectors in extreme radiation environments, as heat sinks and other practical applications. The possibility of diamond electronic devices should not be discounted either, where its use would expand enormously.

This thesis is almost exclusively concerned with synthetic diamonds, which have been around since the 1950s and make up a large proportion of industrial diamond use. It is clearly of great interest both to perfect the growth process – to be able to produce synthetic gems, or stones with required thermal or electronic properties – and to understand it well enough to be able to detect synthetic stones reliably. This is where transition metals, the main topic of this thesis, are important, having a direct, but not well understood, role in the growth of many synthetic diamonds.

This first chapter presents general background material, that is drawn on in later chapters: it reviews some of the history of diamonds, their study and synthesis. It also details the developments in the study of transition metals in general, which places the following chapters into context. Chapters 2 and 3 go into the methods for modelling transition metal defects in some detail and Chapter 5 describes the transition metal centres currently identified in diamond. Chapters 4,6 and 7 outline the original work I

have carried out, applying the theory of chapters 2 and 3. Chapter 8 is a brief round up of all the significant results and suggests directions for further research.

## 1.2 A Brief History of Diamond

For a long time diamonds have been known to, and valued by, mankind. It is hard to trace their history in classical literature as they were little understood, or differentiated from, other gemstones; *Adamas* and *adamant,* deriving from the Greek *adamao* – I tame or I subdue - were applied quite indiscriminately to any hard mineral. Many ancient references, such as God's words to the prophet Ezekiel in the Bible 'As an adamant harder than flint have I made your forehead.' (Ezekiel, chapter 2, verse 9), may refer to diamond, but equally quartz or corundum would have been referred to by the same noun. Iron ore (lodestone) also fell within this group of hard materials and led to confusion with the Latin *adamare*, 'to attract', thus 'As iron to adamant' (Troilus and Cressida, William Shakespeare). Another etymological route travels from the Old French *diamant* to the Latin *adamans* (Oxford New Dictionary of English) with the modern spelling being adopted in the mid-sixteenth century.

The Koh-i-Noor (mountain of light) has the longest continuous history of any known diamond, with records of its existence dating back to 1304 and of its facetting predating 1530[1]. About this time diamonds begin to appear in Western Europe as signs of royal status, gems set into crowns of this period support the argument that cutting techniques had reached Europe by 1380 [2]. Trade in diamonds, however, predates these events by more than one and a half millennia, with diamonds leaving India for Babylon, Mesopotamia, Egypt and other Arabian countries from at least the fourth century BCE. Some diamonds made their way into the hands of the Roman Empire and then even on into China. It is interesting that in these times, before the cutting process was perfected, diamonds were prized for their mechanical and technological properties. After the cutting process was developed the gem market soared, offering economic benefits as described recently

# Introduction

'Diamonds represent perhaps the most concentrated form of wealth known to mankind...are easy to move...and are subject to fewer trading restrictions than many commodities...'[3]

which make diamonds a highly attractive trade item, both in the past and now, and the subject of fear, mysticism and conflict. Recently diamonds have again been valued for technological reasons, with the market for industrial diamonds exceeding the gem trade in value. One of the reasons for this inversion in market values is addressed in the next section; it has recently become practical to synthesise large quantities of industrial grade diamond.

Diamonds' extreme hardness has long been known. Pliny the Elder stated in a volume of his *Historia Naturalis*

'...they resist the blows to such an extent that an iron hammer may be split in two and even the anvil itself may be displaced...'

but then goes on to reveal the superstitious awe that was a feature of early reports on diamond

'...this invincible force which defies Nature's two most violent forces, iron and fire, can be broken by Ram's blood...and, even so, many blows are needed...'

Possibly some of these myths of diamonds' properties were encouraged by early traders, such as the belief that diamonds were poisonous to reduce the risk of theft by swallowing the stone and recovering it later[1], or the legend of the Valley of Diamonds in India to cover the real source of the stones in riverbeds[4]. It was the location of diamond deposits and the subsequent geological understanding that they had been produced deep in the Earth's crust that gave some of the clues necessary for the successful synthesis of diamonds.

Isaac Newton had used diamonds in optical experiments on refractive indices, but the experiments to determine the chemical makeup of diamond were not conducted for another hundred years. At the end of the 18th century Lavoisier, interested in the general theory of combustion, discovered that the by-product of burning diamond was carbon dioxide. After Lavoisier's death in the French revolution the English scientist Smithson Tennant conducted further experiments; by careful analysis of the products of diamond combustion he concluded that diamond was composed of a form of carbon[5]. Even then, the discovery of diamond's actual crystal structure, with its tetrahedrally linked carbon atoms, had to wait until 1913 when the technique of X-ray crystallography became available [6].

## 1.3 Synthesis of Diamond

That diamonds were formed deep within the earth was proved beyond doubt in the diamond fields of South Africa. There the most concentrated sources of diamond were found in a volcanic rock called Kimberlite (later carbon isotope experiments gave further conclusive evidence). The knowledge that diamonds were formed from carbon within the Earth at high temperatures and high pressures led to the conclusion that diamonds could be formed by exposing graphite (the other common allotrope of carbon) to similar pressures and temperatures.

The conditions necessary for the conversion of graphite to diamond were revealed in 1938 with the publication of the phase diagram for carbon[7], and they were extreme! Graphite was found to be the thermodynamically stable form of carbon in all normal conditions: diamond became stable at high temperatures and at pressures of tens of thousands of atmospheres. The technology to produce these sorts of pressures was not trivial, but by the mid 1950s graphite had been subject to pressures of over 100,000 atmospheres, and diamond still did not form. Clearly something had not been considered and this is where the main topic of this thesis, transition metals (TMs), become involved.

For any reaction to occur it must not just be thermodynamically favourable, it must also occur at an appreciable rate - diamonds are unstable at room temperature and pressure, but they are, apparently, "forever". The reaction needed a solvent to dissolve the graphite and catalyse the reaction: metals, particularly transition metals, were found to be most efficacious. The first reported *, reproducible synthesis of diamond occurred in 1954 when Tracy Hall, working for General Electric, compressed a mixture of iron sulphide with excess iron and graphite to a pressure of approximately 70,000 atmospheres and heated it to temperatures of around 1600°C for 38 minutes; several small diamonds were found embedded in the sample cell [8].

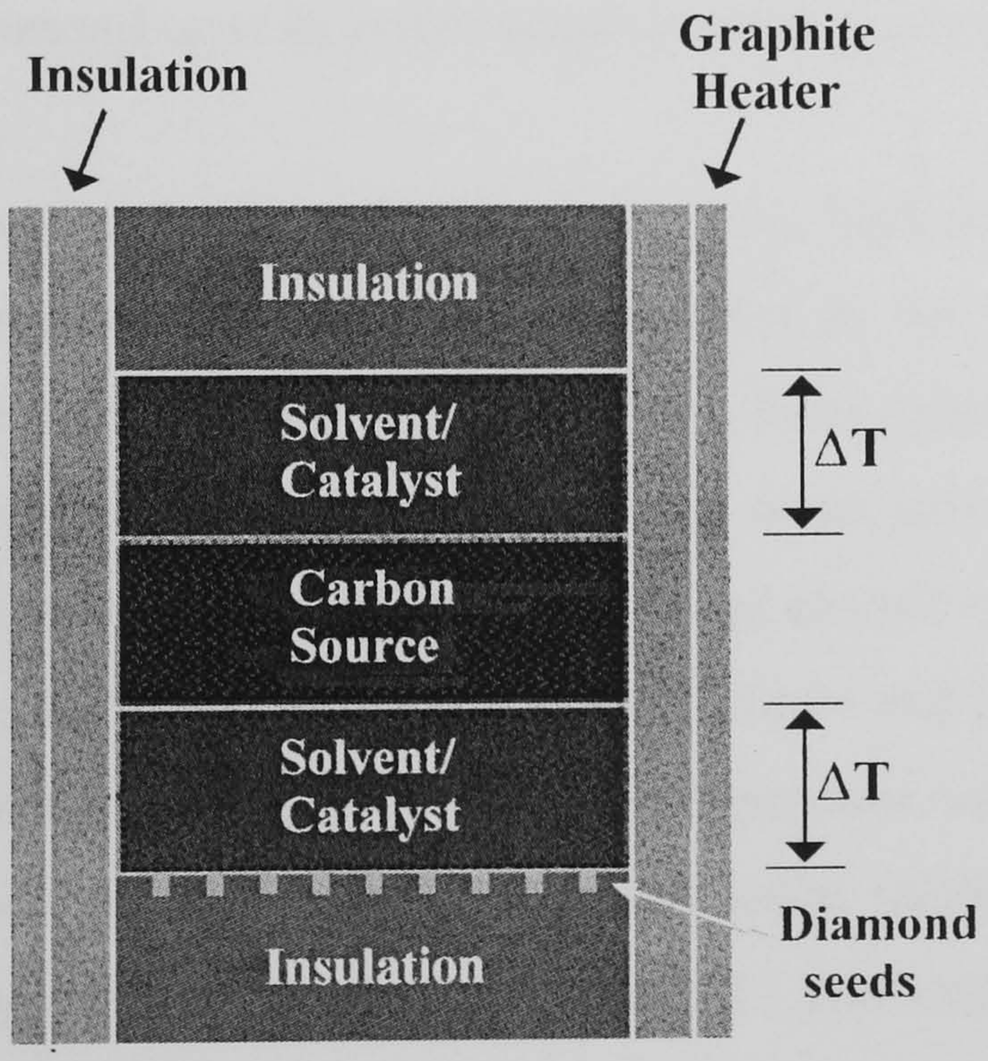


**Figure 1.1.** Schematic diagram of a capsule suitable for growing large diamonds by the temperature gradient method. The temperature differences are normally about 30°C.

---

* It is accepted that a group led by Baltazar von Platen, at the Allmanna Svenska Elektriska Aktiebolaget (ASEA) Laboratory in Stockholm, Sweden, succeeded in producing synthetic diamonds in 1953, but this initial success was not publicised or published.

The exact role of the metal solvent/catalyst is still not well established. A recent survey[9] compared all the metals commonly used as catalysts. The most important properties of the metal were thought to be: the ability to breakdown the graphite carbon source, the ability to dissolve large quantities of carbon and, for ease of operation, a low melting point. The survey concluded that Co was, overall, the most efficient metal followed by Fe, Mn, Ni and Cr. The presence of an unfilled d-shell assisted in dissolving carbon, whilst the earlier transition metals have a tendency to form carbides rather than metal/carbon solution. Given that the transition metals are present at the growth of synthetic diamonds it is, perhaps, not surprising that they are to be found in the resultant crystals. The importance of these defects in synthetic diamond crystals is discussed in the next section.

Two basic types of high temperature, high pressure processes are in common use for synthesising diamonds, which differ in the size and quality of the diamonds to be produced and the time required to form them. Small diamonds for industrial use are produced by placing graphite and metal solvent in an electrically insulating capsule. Pressure is then applied and a large electric current heats the sample rapidly, melting the metal, dissolving the carbon source and finally forming small diamonds. Termed 'direct heating' this method will produce small diamonds in tens of minutes [10]. To form larger diamonds the temperature gradient method is used, a schematic of the apparatus is shown in Figure 1.1. The carbon source dissolves on application of indirect heat, and the temperature gradient provides a driving force for the dissolved carbon to precipitate out of solution at the diamond seeds, forming larger diamonds around these nucleation sites. Several days are required to form diamonds with dimensions in millimetres. This type of method was used to make the diamonds used in chapter 7 of this thesis.

The importance of synthetic diamonds to industry is enormous; about eighty percent of mined diamonds are used for industrial purposes yet more than four times that production is grown synthetically, about 100 tonnes a year! The rate that diamond use has accelerated can be appreciated as in 1978 it was estimated that about 200 tons of diamond had been mined since their initial discovery thousands of years ago [1].

There are other methods of growing synthetic diamonds, however, they do not require the metal solvent/catalyst and, as such, are of no direct interest to this thesis. The most important of them is the Chemical Vapour Deposition (CVD) method, in which diamond films are grown by atomic deposition of gas phase carbon atoms onto surfaces seeded with nucleation sites.

As well as using synthetic diamonds for industrial purposes there is an obvious motive for being able to manufacture gem quality diamonds. The title of a popular book by R M Hazen, *The New Alchemists* (1993)[11], illustrates the idea nicely. As yet the processes have not been refined sufficiently to make growing gem diamonds commercially viable, but the gem trade is very sensitive to their existence and research is directed to ensuring that synthetic diamonds can always be identified as such [12].

## 1.4 Defects in diamond

Pure diamond has many remarkable properties, such as its extreme hardness and transparency in the visible and near infrared region of the electromagnetic spectrum. However, defects within a diamond crystal can produce dramatic changes in its macroscopic properties. Indeed, as discussed in the next section, diamonds are categorised principally by the presence or absence of nitrogen impurities. Aside from using diamonds simply for their extreme hardness, as abrasives or drill bits for example, many uses depend strongly on the properties of the defects present in the crystal.

The title of this thesis specifies the study of transition metal point defects, this makes two points. The first is that the interest lies with isolated TM atoms in the diamond, not lumps of solid metal that are termed inclusions. The second is that diamond, with its extremely wide band-gap (≈5eV), behaves very differently from other semiconductors. As has been pointed out [13] diamond generally behaves essentially as an insulator and defects within the crystal tend to have limited interaction with the

band structure. This means that the term point defect is indeed appropriate, the defects are localised in space and do not have appreciable electron density spread throughout the crystal.

### *1.4.1 Intrinsic defects: Self-interstitials and Vacancies.*

These are termed intrinsic defects as no elements other than carbon are involved. They have been extensively studied as they are the primary products of radiation damage[14] and diamond is the ideal radiation-hard material for detectors in extreme environments[15]. The self-interstitial is well understood [16.17], despite only having been positively identified recently[18]. It is highly mobile in diamond at relatively low temperatures[19], and in chapter 7 evidence is presented that it acts as an intermediate in the TM assisted aggregation of nitrogen.

The vacancy is formed simply by the absence of a carbon atom form the lattice. Again it is well characterised. Here a very brief description of its electronic structure is given because, as will be seen later (chapters 3,5 and 6), it bears a strong resemblance to certain TM defects. When a carbon atom is removed from the crystal lattice there are four tetrahedrally arranged carbon atoms neighbouring the vacant site. Each of these atoms now has a $sp^3$ hybridised orbital pointing towards the vacant site that previously participated in bonding to the missing atom. The electrons in these so called 'dangling bonds' then rearrange themselves to form the electronic states of the vacancy. Specifically the four dangling bonds form an $a_1$ orbital and a set of $t_2$ orbitals at higher energy (see Figure 1.2).

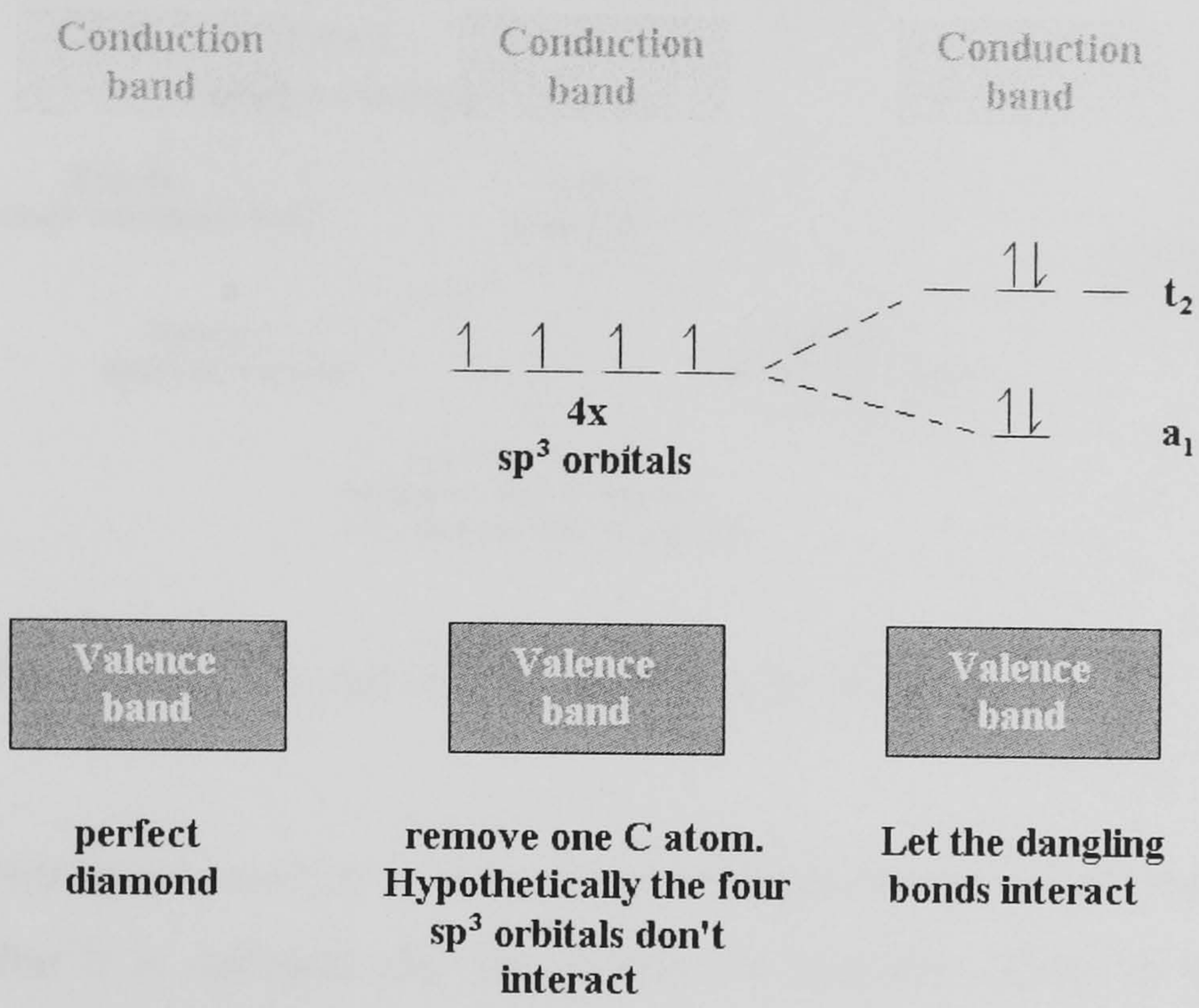


**Figure 1.2.** On the left are the energy levels of a perfect diamond. There are no energy levels in the band-gap. If one carbon atom is removed, then four 'dangling bonds are formed (see text), these will overlap less than the bonds between neighbouring atoms and consequently will be in the band gap. The middle diagram shows the hypothetical situation where the dangling bonds do not overlap at all. If the bonds overlap then the situation becomes that shown in the right-hand diagram, labels are the symmetry species in the $T_d$ point group.

### *1.4.2 Nitrogen and Boron in diamond.*

These two elements are similar in size to carbon atoms and consequently are readily incorporated into the crystal lattice. Nitrogen is, in fact, an almost ubiquitous impurity in diamonds, both natural and synthetic, and its concentration and state largely determine many properties of the crystal. Boron is generally present at a much lower concentration than nitrogen, but is still a very common defect.

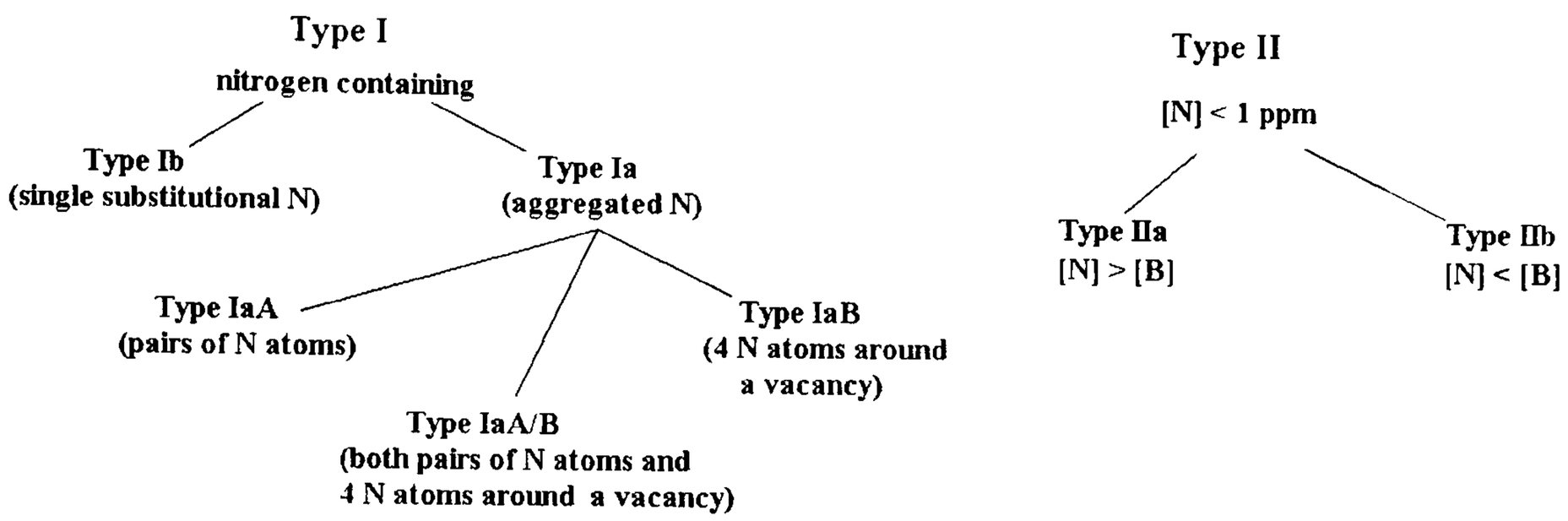


**Figure 1.3.** The classification scheme for diamonds.

Nitrogen is mobile in diamond given high enough temperatures and it has been shown that it is energetically favourable for nitrogen atoms to aggregate together[20]. It is thought that initially nitrogen is found as individual atoms that aggregate into pairs (A centres) then further into groups of four nitrogen atoms and a vacancy (B centres). Chapter 7 is concerned with how transition metals effect this aggregation process and more detail can be found there. The state of aggregation affects the macroscopic properties of diamond, especially coloration, which greatly influences the value of gem diamonds [21].

### *1.4.3 Transition metal impurities.*

As has been described, transition metals are vital as solvent/catalysts in the growth of synthetic diamonds. The huge market value for synthetic stones makes an in-depth understanding of the growth process an important topic for research. The role of the transition metal is not fully understood, especially whether it acts as a catalyst or merely as a solvent for carbon. In the formation of carbon nanotubes transition metal play a similar catalytic role where they are believed to function by preventing closure of the growing nanotube [22]. It is desirable to have a similar picture of the role of TMs in diamond synthesis. To this end knowing the distribution of TMs in the diamond and where in the growing crystal they become trapped is of interest.

Another question is whether the presence of TM centres could be used as diagnostic test for synthetic diamonds. As described in chapter 5, several Co and Ni centres have been detected and their presence would be unusual in a natural stone. Furthermore, transition metals influence the state of nitrogen aggregation, which will tend to alter the relative concentrations of various nitrogen centres. Understanding how the TMs affect nitrogen aggregation could provide another test for synthetic stones. The TMs are also known to occupy several environments within the diamond crystal (see chapters 3 and 5), annealing at high temperatures changes the favoured environment. Understanding the structural changes TM impurities undergo would allow information to be obtained about the thermal history of a diamond, which would be of interest given some of the heat treatments now available to improve the colour of gemstones [23].

As well as helping to understand the growth process and identify synthetic stones, TMs in diamond are of some scientific interest just in themselves. Being constrained to the dimensions of the crystal, the bondlengths between TM and carbon atoms are far shorter than found in, for instance, organometallic compounds, leading to the possibility of interesting behaviour, such as the observation of unusual spin-states. Whether any TM defect could act as shallow acceptor, or especially donor, also needs to be addressed.

Experimental evidence suggests that transition metals in diamond occur in three fundamental forms:

i) Substitutional, notated throughout this thesis as $TM_s^x$ where x is the formal charge on the defect – the transition metal simply replaces a carbon atom in the diamond lattice. As the TM is much larger than the atoms of the host crystal the lattice is considerably distorted around the TM and the defect is presumably highly strained. The $TM_s$ defect has $T_d$ symmetry.

ii) Interstitial, $TM_i$ – the TM occupies a tetrahedral site in the diamond lattice. Again, the defect will strain the crystal considerably. This site has $T_d$ symmetry.

iii) Semivacancy, $TM_{sv}$ – this environment can be thought of as deriving from the substitutional defect. One of the nearest neighbour carbons is removed and the TM moves to a site half way between its original location and that of the displaced carbon atom. The site symmetry is lowered to $D_{3d}$.

## 1.5 Methods of Study

### *1.5.1 Interaction of electromagnetic radiation and matter.*

The principle probe used to gain information about matter is its interaction with electromagnetic radiation.

Taking an initial system that has a set of states with wavefunctions, $\Psi$, that are eigenvalues of the Hamiltonian for the system, $\mathbf{H}^0$, we have

$$\Psi_n(q,t) = \Psi_n(q)\exp(-iE_n t/\hbar) = |n\rangle\exp(-iE_n t/\hbar) \qquad (1.1)$$

where $E_n$ is the energy of the system, $q$ are the nuclear and electronic coordinates, the system evolves in time by parameter $t$ and $n$ labels the state referred to. To find the effect of a perturbing field $\mathbf{H}^{(1)}(q,t)$ the time-dependent Schrodinger equation for the system must be solved to find the perturbed state of the system, $\Phi(q,t)$

$$\left(\mathbf{H}^0 + \mathbf{H}^1\right)\Phi(q,t) = i\hbar\frac{\partial\Phi(q,t)}{\partial t} \qquad (1.2)$$

The perturbed state of the system can be expanded in the initial states of the system

$$\Phi(q,t) = \sum_n a_n(t)\Psi_n(q,t) \tag{1.3}$$

If the initial system was in a state $\Psi_0$ before the perturbation was applied at $t$=0, then the probability of it having changed to a state $\Psi_j$ at time $t$ is given by $|a_j(t)|^2$. With a perturbing field oscillating at angular frequency $\omega$ of the form

$$\mathbf{H}^{(1)}(t) = 2\mathbf{H}^{(1)}\cos\omega t \equiv \mathbf{H}^{(1)}\left(\exp(i\omega t) + \exp(-i\omega t)\right) \tag{1.4}$$

time-dependent perturbation theory shows that

$$a_j(t) = \frac{H_{jo}^{(1)}}{i\hbar}\left\{\frac{\exp\left[i\left(\omega_{jo}+\omega\right)t\right]-1}{i\left(\omega_{jo}+\omega\right)} + \frac{\exp\left[i\left(\omega_{jo}-\omega\right)t\right]-1}{i\left(\omega_{jo}-\omega\right)}\right\} \tag{1.5}$$

where $H_{j0} = \langle n|\mathbf{H}^{(1)}|0\rangle$ and $\hbar\omega_{no} = E_n - E_0$. The probability of the system being in state $\Psi_n$ does not increase with time unless either $\omega_{no}$-$\omega \approx 0$ or $\omega_{no}$+$\omega \approx 0$. The first term corresponds to the absorption of a photon of frequency $2\pi\omega_{n0}$ and the second to the emission of a similar photon.

Hence we can see how electromagnetic radiation acts as a probe for the system; peaks in experimental absorption or emission spectra correspond to the energies between stationary states of the unperturbed system.

It can be shown that the total probability of a transition from $\Psi_0$ to $\Psi_n$ per unit time is given by

$$p_{no} = \frac{2\pi}{\hbar}\rho(E_{n0})\left|\langle n|\mathbf{H}^{(1)}|0\rangle\right|^2 \tag{1.6}$$

where $\rho(E_{n0})$ is the energy density of the final states. $p_{n0}$ is related to the Einstein coefficient for absorption, $B_{n0}$, by $B_{n0} = \frac{p_{no}}{\Xi(\omega_{n0})}$ where $\Xi(\omega) = \frac{1}{8\pi}\left(\overline{|\mathbf{E}|^2 + |\mathbf{H}|^2}\right)$, the energy density of the electromagnetic wave. As $\mathbf{H}^{(1)}$ is Hermitian the Einstein coefficient for stimulated emission, $B_{0n}$, has the same value.

From the correspondence principle with classical mechanics, the interaction of electromagnetic radiation with matter, to first order in the vector potential, A, is given by

$$\mathbf{H}^{(1)} = \sum_{part} \frac{i\hbar Q_{part}}{M_{part} c} \mathbf{A}_{part} \cdot \nabla_{part} \qquad (1.7)$$

where the summation runs over all the particles (*part* = electrons and nuclei) in the system, $Q$ and $M$ are the charge and mass of a particle and -ih$\nabla/2\pi$ is the momentum of a particle.

Inserting Equation 1.7 into Equation 1.6 it is found that

$$B_{no} = \frac{\pi}{6\varepsilon_0 \hbar^2}\left|\langle n|\sum_j e\mathbf{r}_j|0\rangle\right|^2 + \frac{\pi}{6\varepsilon_0 \hbar^2}\left|\langle n|\sum_j \mu_B \mathbf{l}_j|0\rangle\right|^2 + \frac{\pi\omega_{n0}^{\ 2}}{40\varepsilon_0 \hbar^2 c^2}\left|\langle n|\sum_j eq_j|0\rangle\right|^2 \qquad (1.8)$$

where the sum is now over the electrons in the system, $\mu_B$=($eh/4\pi mc$) is the Bohr magneton, $\mathbf{l}$ an angular momentum operator and $q$ quadratic operators (transforming like an angular momentum with $l$=2). The three terms from left to right in Equation 1.8 are operators for absorption processes due to electric dipole, magnetic dipole and electric quadrupole mechanisms respectively. The three transition mechanisms are of the order of magnitude

$$\left|\langle n|e\mathbf{r}|0\rangle\right|^2 \approx e^2 a_0^2 = 7.2\times10^{-59}\,C^2m^2$$

$$\left|\langle n|\mu_B\mathbf{l}|0\rangle\right|^2 \approx \mu_B^2 = 9.6\times10^{-64}\,C^2m^2 \qquad \text{with } \omega_{n0}=0.25 \text{ eV } (\approx 2000 \text{ cm}^{-1})$$

$$\frac{3\pi\omega_{n0}^2}{20c^2}\left|\langle n|eq_j|0\rangle\right|^2 \approx \frac{3\pi\omega_{n0}^2 e^2 a_a^4}{20c^2} = 4.4\times10^{-65}\,C^2m^2$$

(1.9)

It can be seen that an electric dipole will be the dominant mechanism if it is present in the system. However, electron paramagnetic resonance (EPR) is a powerful experimental technique that utilises the magnetic dipole mechanism.

### *1.5.2 Selection Rules.*

As shown in section 1.5.1 the intensity of transitions depend upon integrals of the form <*final state* | operator | *initial state*>. Group theory is of great benefit in evaluating integrals of this form. Both wavefunctions and the operator are representations of the point group of the defect, and from general principles it can be shown that the integral will be non-zero only if it is totally symmetric.

If the initial state transforms like the irreducible representation $\Gamma_i$ of the point group, the operator as $\Gamma_o$ and the final state as $\Gamma_f$ then the integral will be non-zero only if the direct product $\Gamma_i \otimes \Gamma_f$ contains $\Gamma_o$.

Later in this thesis, an electric dipole transition from an $A_2$ initial state to a $T_2$ final state at a tetrahedral impurity ($T_d$ point group) is described in detail. The direct product $A_2 \otimes T_2 = T_1$ but the electric dipole operator transforms as $T_2$ , hence $\langle T_2 | T_2 | A_2 \rangle = 0$. It can immediately be seen that there will be no intensity generated by this mechanism, the transition is forbidden.

When the initial or final states are degenerate it is possible to find the relative intensities of transitions between the various sublevels or with different polarisations of the perturbing light by application of the Wigner-Eckart theorem. Labelling the

irreducible representation of a state or operator with a capital letter and the sublevel with lower case the Wigner-Eckart theorem is

$$\langle Ff\,|Oo|\,Ii\rangle = (F)^{-1/2}\,(FIfi|FIOo)\langle F\,\|O\|\,I\rangle \qquad (1.10)$$

where (F) is the dimension of F. What this has done is reduce the matrix element into two parts:

(i) A coupling coefficient $(FIfi|FIOo)$. These are geometric terms depending only upon the symmetry species present. They are well known and tabulated, see for instance Ref. 24.

(ii) A 'reduced matrix element' $\langle F\,\|O\|\,I\rangle$. This does not depend on the sublevels (i, f and o) and so is a very general parameter.

This theorem is used extensively in the theory of uniaxial stress measurements (see chapter 4) to relate the absorption of impurities with different orientations in a diamond crystal.

### *1.5.3 Optical spectroscopy.*

The basic ideas are very simple, shine light at a sample and light will be absorbed at energies that correspond to the separation of energy states in the sample or excite the sample by some suitable means and analyse the emission spectrum. Generally, the absorption/emission by the sample occurs through electric dipoles that interact with the light far more strongly than magnetic dipoles or quadrupole moments. Within these confines there are a broad array of techniques that vary in the frequency of the radiation applied. Infrared (IR) radiation is used to probe transitions of up to around $2000cm^{-1}$ (0.25 eV), which generally correspond to the vibrational energy levels of the sample, and visible or ultra-violet light is used to probe higher energy electronic states.

Absorption methods have the advantage that the total absorption is proportional to the concentration of absorbing centres. This means that the concentration of defects can easily be found if the strength of the absorption can be calibrated against a quantitative method (often EPR see next section). The calibrations for nitrogen related centres are well known [25-29], and were used to obtain the data for chapter 7 of this thesis. Other calibrations are well established [30], of particular note to this thesis is that the concentration of Nickel atoms is believed to correlate with the concentration of positively charged nitrogen in the sample.

Emission methods, such as photoluminescence (sample is excited with laser light) or cathodo-luminescence (sample excited by electrons), can be more sensitive than absorption (potentially even studying luminescence from a single defect) and by varying the source of excitation additional information about the excited state structure of a defect can sometimes be obtained. Unfortunately for these techniques, because the emitting states are formed indirectly by thermal (non-radiative) decay, from initially formed high-energy states, the strength of emission does not necessarily correlate with defect concentration.

Optical methods are easily conducted and, especially with Fourier transform (FT) methods, much data can quickly be obtained. However, in many cases the information obtained from experiments is limited, perhaps just a single line associated with a centre of interest. Uniaxial stress (see chapter 4) is a technique that combines optical measurement with the application of a stress perturbation, which splits transition lines and provides more information about a centre. It is also desirable to correlate optical observation of centres with other techniques (such as EPR) to broaden the picture of the defect obtained.

### *1.5.4 EPR*

EPR is the other main technique used to study defects in diamond. When it can be used it is extremely powerful, revealing a wealth of information about the defect studied. However, it does have one main disadvantage, as its name suggests the

technique is only applicable to paramagnetic species, fortunately many defects of interest in diamond fall into this category. Being a well-established technique many reviews of the method are available, Ref. 31 and 32 are probably the most complete and applicable to this work.

The method works by first applying a static magnetic field. This gives rise to a Zeeman effect at the (paramagnetic) centres of interest. In orbitally non-degenerate states the energy shift of a level is proportional to the value of $M_S$, the projection of the spin along the magnetic field direction. The steady magnetic field causes splittings in the microwave region of the electromagnetic spectrum.

A high frequency magnetic field is then applied perpendicular to the steady field. This induces magnetic dipole transitions between the levels split by the steady field. In contrast to optical spectroscopy, all measurements are on members of one unperturbed state, which is normally the ground state of the system but occasionally a low energy metastable excited state e.g. the self-interstitial (R2) centre, where EPR is observed from an excited (≈50 meV) triplet state [33].

When the paramagnetic state is energetically remote from other states and orbitally non-degenerate the response to the static magnetic field is $\Delta E = g\mu_B HM_s$ where $g$=2.0023 is the splitting factor for a free electron, $\mu_B$ is the Bohr magneton, $H$ is the magnetic field strength and $M_s$ is the component of the spin in the magnetic field direction.

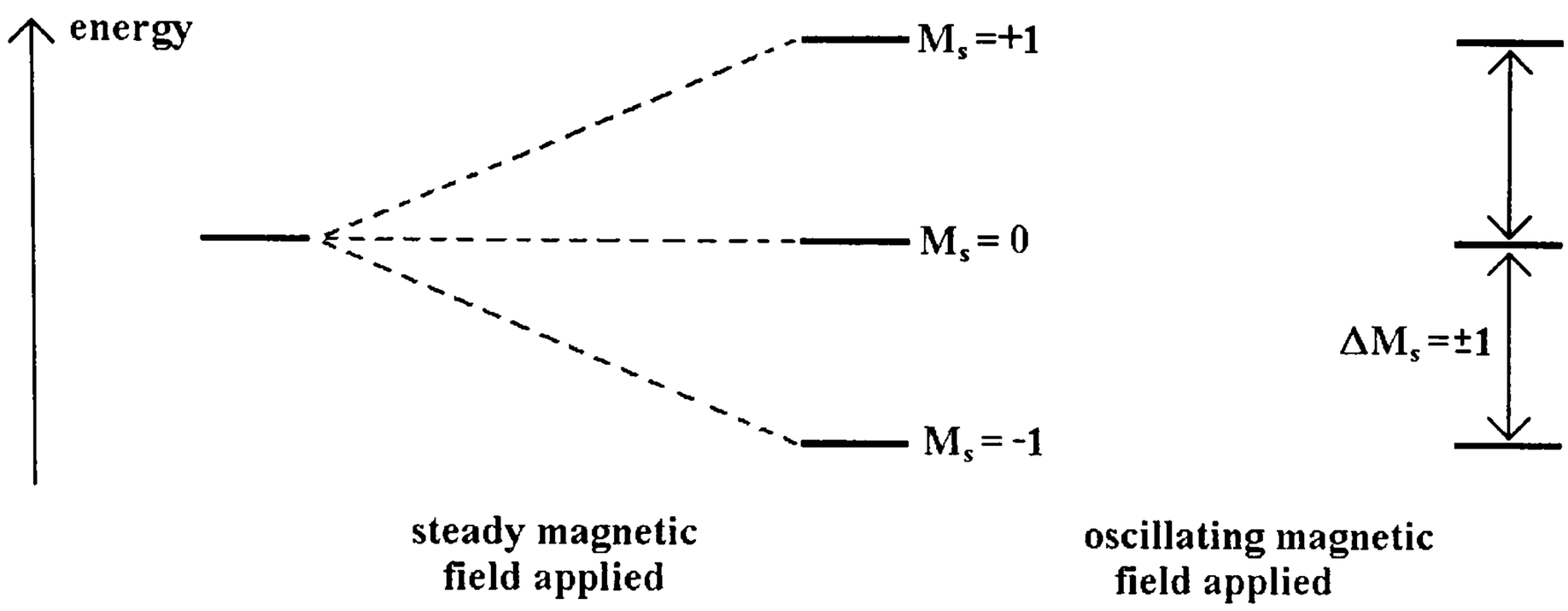


**Figure 1.4.** Schematic diagram illustrating the basic idea behind an EPR experiment. On the left is an orbitally non-degenerate triplet state. A static magnetic field is applied which lifts the degeneracy of the three levels; the energy change for each level is proportional to $M_s$ the projection of the spin in the direction of the magnetic field.

Paramagnetic states in crystals are subject to many interactions: particularly the interaction between orbital motion and spin (spin-orbit coupling, see chapter 4), with the applied field, with nearby nuclear magnetic moments and finally the crystalline environment can have an effect. To describe all these effects a 'Spin Hamiltonian' is used, which is a phenomenological effective Hamiltonian for the system. It is constructed as a polynomial in S, the spin operator, and has the following form

$$H_{spin} = \mu_B \mathbf{H} \cdot \mathbf{g} \cdot \mathbf{S} + \mathbf{S} \cdot \mathbf{D} \cdot \mathbf{S} + \mathbf{S} \cdot \mathbf{A} \cdot \mathbf{I} \qquad (1.11)$$

The three terms describe the interaction with the static magnetic field, the crystalline environment and the 'hyperfine' interaction with atomic nuclei respectively. As all properties are tensors it is readily concluded that the splittings will change with the direction of the applied field. Detailed analysis of the pattern of transitions at different field directions yields the symmetry of the defect. The interaction with neighbouring nuclei also aids identifying the molecular environment of the defect e.g. the W8 centre was known to occupy a substitutional site in the diamond lattice because $^{13}C$ hyperfine structure of four nearest neighbours and twelve next nearest neighbours was observed.

The deviation of **g** from the free electron value reveals substantial information about the system, especially for transition metal defects where the change in value can be large. For transition metal ions crystal field theory (see chapter 3) allows deviation in the **g** value to be related to the ratio of two important parameters: $\Delta$, the energy gap between two states of interest, and $\lambda$, the size of the spin-orbit coupling at the defect.

## 1.6 History of modelling TM defects.

It has long been known that chemical compounds exist that are composed of collections of atoms that have a well-defined composition and steric arrangement. By the turn of the 19$^{th}$ century, empirical laws were well established governing the formation of molecules and ions from their constituents. Soon after the discovery of the electron in 1897, suggestions were made that molecules where held together by electrostatic forces generated by the transfer of an electron from one atom to another. In 1916 Lewis [34] postulated that it was possible for an electron to be shared between two atoms, giving stability to both. The Lewis structures, and the octet rule used to draw stable structures, were remarkably successful. In some cases, however, they broke down irretrievably and the lack of underlying understanding could not be resolved until the advent of quantum mechanics proper, in circa 1926.

Transition metal complexes were completely baffling to these early methods, as realised by Werner in the late 19th century. Various *ad hoc* methods, including the introduction of primary and secondary valence (roughly corresponding to formal charge and co-ordination number) were tried, but the bonding in transition metal complexes is of essentially quantum mechanical origin.

After the publication of Schrodinger's paper in 1926 the theory of chemical bonding was largely resolved within a few years, to the point that in 1929 Dirac stated

"the underlying physical laws for the mathematical theory of a large part of physics and the whole of chemistry are thus completely known."

It was also in 1929 that Bethe [35] published a paper detailing the use of point group symmetry in the handling of the electronic structures of polyatomic molecules. With this the ingredients for explaining the properties of transition metal complexes were in place.

In 1931-2 Pauling [36.37] showed how to formulate the bonding in transition metal complexes in quantum mechanical terms. His paper was supplemented by Van Vleck, [38] who explained group theoretically the orbital hybrids used by Pauling and showed how the metal orbitals interacted with ligand orbitals of the same symmetry. Unfortunately the computational power to check these theories did not exist at the time, and the attack on the problem from first principles had to be left for some time.

In the following years what is now termed crystal field theory was developed. Based on the work of Bethe the ligands were treated as point charges and by perturbing an atomic metal atom with their electrostatic field much progress was made, Van Vleck and co-worker's [39. 40] work on magnetic susceptibilities was particularly influential. Work also showed that the influence of the ligands depended on their arrangement around the transition metal; Gorter showed that the crystal field splitting would be of opposite sign for tetrahedral and octahedral environments [41]. The Jahn-Teller theorem [42] was shown to have important consequences for the spectra of transition metal ions, by removing remaining orbital degeneracy [43. 44].

Crystal field theory also allowed excited states to be studied; the first system examined was $[Cr(H_20)_6]^{3+}$ (Refs. 45 and 46) in 1940. The question of the intensity source in these d-d transitions was also addressed [46]. The transitions assigned were spin forbidden, the broad featureless bands of the allowed transitions escaped notice for another 10 years (spectrophotometers capable of dealing with broad unstructured lines were developed in the late forties). It was not appreciated that the width of the observed transitions depended upon the change in bonding when an electron changes orbital until Orgel published his complete solutions to the crystal field perturbation problem in 1955 [47]. At this point very little work was done on the crystal-field model

that had been developed ; only three groups were actively researching the field - Van Vleck in Harvard, Kramers in Leiden, Holland and Penney in Imperial College, London. At this point the natural progression of research was broken by the onset of the Second World War.

While crystal field theory was still being developed Van Vleck published a paper showing that it could be generalised into what is now called ligand field theory [48]. This provided the unification of crystal field theory and molecular orbital methods (section 3.3.2).

The first spin-allowed transition was reported in 1951 [49, 50] in $[Ti(H_20)_6]^{3+}$ (actually contained in Ilse's thesis of 1946, but he died shortly afterwards and the results weren't published for 5 years). Orgel independently identified the broad lines with spin-allowed transitions and published a complete correlation diagram for a $d^2$ electronic configuration (diagram showing the position of all the many-electron states as a function of the crystal field splitting)[51]. Soon after Tanabe and Sugano published complete matrices for the ($d^{1-9}$) configurations as well as the correlation diagrams [52].

Further papers by Orgel gave more correlation diagrams [53], discussed the spin-state of the ground-state [54] and showed how the band widths of optical lines could be predicted from correlation diagrams [47].

In parallel with this optical work, EPR was being explored as a technique for probing transition metals electronic structure. In 1950 the perturbation procedure to obtain Zeeman energy splittings was published [55]. EPR also showed the need to consider delocalised covalent bonding and empirical parameters were introduced to correct crystal field theory [56]. All of the features needed to characterise transition metal complexes were considered by Owen [57].

At this point the theory was well understood; it soon received wider notice. The sandwich structure of ferrocene (bis-cyclo-pentodienyl iron(II)) proposed in 1952 was the perfect highly symmetric molecule to apply the methods of crystal and ligand field

theory to. Several qualitative molecular orbital schemes were put forward [58-61] and showed the broad applicability of the methods.

An article by Moffitt and Ballhausen in 1956 gave a review and bibliography of the quantum theory of transition metals [62]. The methods for treating complexes of all the transition metals, actinides and lanthanides were in place and huge numbers of papers dealing with these topics were produced by inorganic chemists.

About this time computational power started to increase dramatically and less empirical methods became more practical. In 1952 Wolfberg and Helmholtz applied a semi-empirical method (extended Huckel theory) to $[MnO_4]^-$ and $[CrO_4]^-$ [63]. From then on computers made more and more sophisticated calculations practical, till the current time when *ab initio* calculations can be, more or less, routinely run on a desktop PC; details of the *ab initio* methods are discussed in the next chapter.

---

[1] E Bruton, *Diamonds, 2nd Ed.*, N.A.G. Press, 1978.

[2] G E Harlow, *Following the History of diamonds: The Nature of diamonds*, George Harlow (Ed.) CUP, Cambridge

[3] A W Eastham, Special Negotiator for Conflict Diamonds, Bureau of Economic and Business Affairs (US): Testimony before the Senate Committee on Government Affairs, Subcommittee on Oversight of Government Management, 2002

[4] S Tolansky, *The History and Use of Diamond*, Methuen, London, 1962.

[5] S Tennant, Phil. Trans. Royal Soc., **87**, 97, 123 (1797)

[6] W H Bragg and W L Bragg, Proc. Roy. Soc. (London), **A89**, 277 (1913)

[7] F D Rossini and R S Jessop, J. Res. Nat. Bur. Stand., **21**, 491 (1938)

[8] F P Bundy, T H Hall, H M Strong and R H Wentorf, Nature, **176**, 51 (1955)

[9] C M Sung and M F Tai, Int. J. Refract. Metals Hard Mater., **15**, 237 (1997)

[10] A T Collins, H Kanda, J Isoya, C J Ammerlaan and J A van wyk, Diam. Relat. Mater., **7**, 333 (1998)

[11] Hazen, Robert M. (1993). *The New Alchemists*. Times Books, Random House, New York.

[12] A T Collins and T Jeffries, *Differentiating gem quality natural and synthetic diamonds*. Presented at the Diamond Conference, St. Catherines College, Oxford, 1999 (Unpublished).

[13] A T Collins, J. Phys. Condens. Matter, **14**, 3743 (2002)

[14] B Campbell, W Choudhury, A Mainwood, M Newton and G Davies, Nuclear Instruments and Methods A, **476**, 680-685 (2002)

[15] A Mainwood, Semiconductor Science and Technology, **15**, R55-63 (2000)

[16] G Davies, H Smith and H Kanda, Phys. Rev. B , **62** 1528 (2000).

[17] A Mainwood, in "*Properties of diamond*", edited by MH Nazare and A Neves, Emis DataReview series (IEE, Inspec, London, 2000) p 188-192.

[18] D C Hunt, D J Twitchen, M E Newton, J M Baker, T R Anthony and W F Banholzer, Phys. Rev. B, **61** (2000)

[19] G Davies, B Campbell, A Mainwood, M Newton, M Watkins, H Kanda and T R Anthony, invited talk at Haselt workshop, Phys Stat Solidi (a), **186**, 187 (2001)

[20] A Mainwood, Phys. Rev. B, **49**, 7934 (1994)

[21] E Frietch, in "*The Nature of Diamonds*", George Harlow (Ed.), CUP, Cambridge, (1998)

[22] YH Lee, S G Kim, D Tomanek, Phys. Rev. Let., **78,** 2393 (1997)

[23] A T Collins, J. Gemmology **27**, 341-359 (2001)

[24] J S Griffith, *The Theory of Transition Metal Ions*, CUP, Cambridge, 1964

[25] I Kiflawi, A E Mayer, P M Spear, J A van Wyk, G S Woods, Philos. Mag. B, **69**, 1141 (1994)

[26] G A Woods, J A van wyk, A T Collins, Philos. Mag. B, **62**, 589 (1990)

[27] S C Lawson, D Fisher, D C Hunt, M E Newton, J. Phys. Condens. Matter, **10** , 6171 (1998)

[28] S R Boyd, I Kiflawi, G S Woods, Philis. Mag. B, **69**, 1149 (1994)

[29] G S Woods, G C Purser, A S S Mtimkulu, A T Collins, J. Phys. Chem. Solids, **51**, 1191 (1990)

[30] G Davies, Physica B, **273-274**, 15 (1999)

[31] A Abragam and B Bleaney, *Electron Paramagnetic Resonance of Transition metal Ions*, OUP, Oxford, 1970

[32] D J Twitchen, D.Phil. Thesis, University of Oxford, 1997

[33] D C Hunt, D J Twitchen, M E Newton, J M Baker, T R Anthony, W F Banzoler, S S Vagarali, Phys. Rev. B, **61**, 3863 (2000)

[34] G N Lewis, J. Amer. Chem. Soc., **38**, 762 (1916)

[35] H Bethe , H., Ann. Physick., **133** (1929)

[36] L Pauling, J. Amer. Chem. Soc., **53**, 1367 (1931)

[37] L Pauling, J. Amer. Chem. Soc., **54**, 988 (1932)

[38] J H Van Vleck, J. Chem. Phys., **3**, 803 (1935)

[39] J H Van Vleck, Phys. rev., **31**, 587 (1928)

[40] R Schlapp and W G Penney, Phys. Rev., **42**, 666 (1932)

[41] C J Gorter, Phys. Rev., **42**, 427 (1932)

[42] H A Jahn and E Teller, Proc. Roy. Soc.(London), **A161**, 220 (1937)

[43] J H Van Vleck, J. Chem. Phys., **7**, 61 (1939)

[44] J H Van Vleck, J. chem. Phys., **7**, 72 (1939)

[45] R Finkelstein and J H Van Vleck, J. Chem. Phys., **8**, 790 (1940)

[46] J H Van Vleck, J. Chem. Phys., **8**, 787 (1940)

[47] L J Orgel, J. Chem. Phys., **23**, 1824 (1955)

[48] J H Van Vleck, J. Chem. Phys., **3**, 807 (1935)

[49] F E Ilse and h Hartmann, Zeit. fur Phys. Chem., **197**, 239 (1951)

[50] F E Ilse and h Hartmann, Z. Naturforsch., **6a**, 751 (1951)

[51] L E Orgel, J. Chem. Soc., 4756 (1952)

[52] Y Tanabe and S Sugano, J. Phys. Soc. (Japan), **9**, 753 and 766 (1954)

[53] L E Orgel, J. Chem. Phys., **23**, 1004 (1955)

[54] L E Orgel, J. Chem. Phys., **23**, 1819 (1955)

[55] M H L Pryce, Proc. Roy. Soc. (London), **163**, 25 (1950)

[56] K W H Stevens, Proc. Roy. Soc., **A219**, 542 (1953)

[57] J Owen, Proc. Roy. Soc., **A227**, 183 (1955)

[58] E Ruch and E O Fischer, Z. Naturforsch., **7b**, 676 (1952)

[59] H H Jaffe, J. Chem. Phys., **21**, 156 (1953)

[60] J D Dunitz and L E Orgel, Nature, **171**, 121 (1953)

[61] W Moffit, J. Chem. Phys., **25**, 1189 (1956).

---

[62] W Moffitt and C J Ballhausen, Ann. Rev. Phys. Chem., **7**, 107 (1956)

[63] M Wolfberg and L Helmholtz, J. Chem. Phys., **20**, 837 (1952)

# Chapter 2.

# First principles calculations of transition metal defects.

A first principles study of a large molecule involves solving the Schrodinger equation for the full system of the nuclei and electrons it is constructed from. A variety of theoretical approaches to this many-body problem have been developed and in this section the approximations and theory of the most prevalent – Hartree-Fock theory, its extensions and density functional theory – are outlined in some detail.

The aim of this section is to explain the techniques and approximations used in the *ab initio* quantum chemistry package GAMESS (General Atomic and Molecular Electronic Structure System)[1] and the ways it can be used to model atomic clusters. GAMESS is based on the Hartree-Fock methodology; the advantages (and disadvantages) of this theoretical formulation compared to density functional theory, its main competitor, are explored. Later (Chapter 6), GAMESS is used to investigate the incorporation of the first row transition metals into a diamond crystal.

## 2.1 *Ab Initio* calculations.

The solution to the (time independent) Schrodinger equation for an atom or molecule leads to a knowledge of the wavefunction(s) of the system, and with it, in principle, a complete description of the system's physical properties. The wavefunction is a function of all the electronic, nuclear and spin coordinates of the material considered: in all but the simplest cases, approximations must be introduced to make the problem tractable – the approximations define the computational model used.

Throughout this thesis, capital Greek or Roman characters represent many-electron wave functions, lower case characters refer to one-electron or basis functions. The whole of this chapter uses atomic units.

### *2.1.1 The Electronic Problem.*

The full time-independent, non-relativistic Hamiltonian for a system of $n$ electrons and $M$ nuclei in atomic units is

$$H = -\sum_{i=1}^{n}\frac{1}{2}\nabla_i^2 - \sum_{A=1}^{M}\frac{1}{2M_A}\nabla_A^2 - \sum_{i=1}^{n}\sum_{A=1}^{M}\frac{Z_A}{r_{iA}} + \sum_{i=1}^{n}\sum_{j>i}^{n}\frac{1}{r_{ij}} + \sum_{A=1}^{M}\sum_{B>A}^{M}\frac{Z_A Z_B}{R_{AB}} \qquad (2.1)$$

where $M_X$ and $Z_X$ are the mass and atomic number of nuclei $X$, $R_{XY}$ is the distance between nuclei $X$ and $Y$, $r_{iX}$ is the distance between electron $i$ nuclei $X$, $r_{ij}$ is the distance between electrons $i$ and $j$.

The first two terms are the operators for the kinetic energy of the electrons and the nuclei, the third term is the Coulomb attraction between the nuclei and electrons, the fourth term the Coulomb repulsion between the electrons and the final term the repulsion between the nuclei.

The first step in attempting to find a solution to the full Schrodinger equation is to separate the motion of the nuclei and electrons.

#### The Born-Oppenheimer Approximation.

The Born-Oppenheimer approximation [2] is central to electronic structure calculations; almost all calculations will make use of it. The conditions under which it breaks down and the problem of deriving corrections to it are well understood [3].

Qualitatively, it is assumed that the nuclei, with their much greater mass, move far more slowly than the electrons in the system. Hence the electrons may be considered to be moving in the Coulomb field of the fixed nuclei. Within this approximation the

kinetic energy of the nuclei may be ignored, and the repulsion between the nuclei considered constant. The electronic Hamiltonian is then,

$$H_{elec} = -\sum_{i=1}^{n} \frac{1}{2} \nabla_i^2 - \sum_{i=1}^{n} \sum_{A=1}^{M} \frac{Z_A}{r_{iA}} + \sum_{i=1}^{n} \sum_{j>i}^{n} \frac{1}{r_{ij}} \qquad (2.2)$$

The solution of the electronic Schrodinger equation,

$$H_{elec} \Phi_{elec} = E_{elec} \Phi_{elec} \qquad (2.3)$$

is the electronic wavefunction, $\Phi_{elec}$, where

$$\Phi_{elec} = \Phi_{elec}(\{r_i\};\{R_A\}) \qquad (2.4)$$

which only depends parametrically upon the nuclear coordinates, as does the electronic energy. The total energy of the system, $E_{tot}$, considering the nuclei to be stationary is found by adding the constant nuclear repulsion.

$$E_{total}(\{R_A\}) = E_{elec}(\{R_A\}) + \sum_{A=1}^{M} \sum_{B>A}^{M} \frac{Z_A Z_B}{R_{AB}} \qquad (2.5)$$

The equilibrium geometry, in this approximation, is the set of nuclear coordinates that minimise the total energy.

When the electronic problem has been solved it is then possible to solve for the motion of the nuclei using the same assumptions as used to formulate the electronic problem. The nuclei move on the potential energy surface, $E_{tot}(R)$, obtained by solving the electronic problem. This would allow the determination of properties like vibrational frequencies, but will not be considered further. Car and Parinello devised a method to solve both the electronic problem and the nuclear motion simultaneously, which allowed a much more efficient way to model the dynamics of a system [4].

### *2.1.2 Approximations to the Wavefunction.*

The solution of the electronic Schrodinger equation is an $n$-electron wavefunction, $\Phi(\boldsymbol{x}_1, \boldsymbol{x}_2, \ldots, \boldsymbol{x}_n)$. To aid computation this many-body function is expanded in terms of

products of $n$ one-electron functions, or orbitals; each orbital is a function of the spatial and spin coordinates, **x**, of one electron, a spin-orbital, $\psi_i(\boldsymbol{x}_i)$.

$$\Phi_{elec}(\{x_1, x_2, \ldots x_n\};\{R_A\}) = \sum_K C_K \Phi_K(x_1, x_2, \ldots x_n) \qquad (2.6)$$

In order to ensure that the Pauli exclusion principle is obeyed the product of one-electron functions is taken as a Slater determinant.

$$\Psi_{1,2,\ldots n} = \frac{1}{\sqrt{n!}}\left|\psi_1(\mathbf{x}_1)\psi_2(\mathbf{x}_2)\ldots\psi_n(\mathbf{x}_n)\right| \qquad (2.7)$$

If the one-electron functions $\psi_i$ form a complete set, then the determinants form a complete set, spanning the active space of the $n$-electron many body problem. Hence any arbitrary $n$-electron wave function, $\Phi$, may be written as a linear combination of determinants

$$\Phi = \sum C_{k_1,k_2..k_n}\Psi_{k_1,k_2..k_n} \qquad (2.8)$$

The variational principle implies that an approximate solution to the Schrodinger equation can be found by minimising the expectation value of the energy with respect to the coefficients, $C$, determining the wavefunction. Functional variation of the expectation value leads to a matrix eigenvalue equation **HC=SCE,** where $H_{IJ} = \langle \Psi_I | H | \Psi_J \rangle$ is the matrix representation of the Hamiltonian in the $n$-electron basis, **S** is a similar overlap matrix, **E** a matrix of eigenvalues and **C** the corresponding matrix of eigenvalues. The matrix elements of the Hamiltonian can be found with the use of Slater's rules.[5.6]

At this stage the calculation is still exact, and the matrices are formally infinite and computationally intractable. The size of the $n$-electron basis is reduced by expanding the orbitals in a limited set of basis functions, $\chi$. As a finite number of basis functions are used, they no longer form a complete set, and the size of the $n$-electron basis is limited. The expansion in Slater determinants then becomes only an approximation to the true $n$-electron wavefunction. Often the basis functions are taken to be of

Gaussian type for finite systems, or plain waves for extended/infinite systems. This approximation imposes no theoretical limitation upon the model, it is merely made for computational ease; the smaller the set of basis functions chosen, the faster, and less accurate, the calculation.

The introduction of basis functions is still not sufficient to allow ready solution of the Schrodinger equation in matrix form. The number of *n*-electron determinants that can be constructed from *m* spin-orbitals is *n!/[m!(n-m)!]* and quickly becomes unmanageable, even for small systems. Further approximations attempt to truncate the expansion of the wavefunction, whilst still giving accurate results.

### *2.1.3 The Hartree-Fock approximation.*

The Hartree-Fock theory approximates the wavefunction by the best single determinant (except in certain spin-adapted linear combinations used for restricted open-shell calculations). The 'best' determinant is found by minimising its energy with respect to the spin-orbitals forming it. Functional variation of the expectation value of the energy of a single determinant, with the constraint that the wavefunction remains normalised, leads to a system of coupled integro-differential equations for the spin-orbitals [7].

$$F(1)\psi_i(1) = \sum_j^N \psi_j(1)\varepsilon_{ji} \qquad (2.9)$$

Where the Fock-operator *F(1)*, an effective one-electron operator, is

$$F(1) = h(1) + \sum_i^N J_i(1) - K_i(1) \qquad (.2.10)$$

The first term, *h(1),* is a one electron operator, for the kinetic energy of electron one and its Coulombic attraction to the nuclei,

$$h(1) = -\frac{1}{2}\nabla_1^2 - \sum_{A=1}^{M}\frac{Z_A}{r_{1A}} \tag{2.11}$$

The second term in Equation 2.10 is an effective one-electron operator called the Hartree-Fock potential, $v^{HF}$. $v^{HF}$ is made up of the sum of two operators

$$J_i(1)\psi_j(1) = \left[\int d\mathbf{r}_2 \left|\psi_i^*(2)\right|^2 r_{12}^{-1}\right]\psi_j(1) \tag{2.12}$$

and

$$K_i(1)\psi_j(1) = \left[\int d\mathbf{r}_2 \psi_i^*(2) r_{12}^{-1}\psi_j(2)\right]\psi_i(1) \tag{2.13}$$

$J_i$ (1) is the coulomb potential experienced by an electron in the spin-orbital $\psi_i$ and $K_i$(1) is a non-local operator, whose existence is necessitated by the Pauli principle, termed the exchange potential.

A unitary transformation of the spin-orbitals can be made to transform the integro-differential Equation 2.9 into a pseudo linear eigenvalue problem,

$$F(1)\psi_i(1) = \varepsilon_i\psi_i(1) \tag{2.14}$$

Equation 2.14 is a pseudo linear eigenvalue problem as the Fock operator has a functional dependence, through the coulomb and exchange operators, on the actual solutions to the eigenvalue equation. The Hartree–Fock equations are really non-linear, and must be solved iteratively: they are often described as a self-consistent field (SCF) method for this reason.

### *2.1.4 Solving the HF equations in practice.*

Removing the spin coordinates.

Two different types of electronic configurations are met with when examining molecular systems. Closed shell systems, when the spin-orbitals with alpha and beta spin functions are equally occupied, and open shell systems, where there are an excess of electrons with one spin function, conventionally alpha. Closed shell systems are easily treated, as the spatial functions of electrons with either spin function will be identical. In open shell systems this in no longer necessarily the case and two different ways of dealing with the problem are used: unrestricted Hartree-Fock

(UHF), and restricted open shell Hartree-Fock (ROHF). They differ in whether the spatial functions of alpha and beta spin electrons are forced to be the same.

Restricted closed shell problems

The equations 2.6-2.14 above refer to general spin-orbitals, the only restriction being that the spin-orbitals are products of a spatial and spin function. It is then possible to convert the pseudo-eigenvalue equation to an eigenvalue equation involving only the spatial functions, which can be solved by conventional linear algebraic methods; this is achieved by integrating out the spin functions. The equations are left in a similar form, but the sums are now over various combinations of spatial functions instead of over spin-orbitals. For a closed shell configuration the Fock operator becomes

$$f = h_{ii} + \sum_{j}^{N/2} 2J_{ij} - K_{ij} \qquad (2.15)$$

which shows explicitly the fact that the exchange operator only acts upon spin-orbitals having parallel spin functions. The coulomb operator acts between all spin-orbitals, hence the factor of 2. There is no mention of spin as the spatial parts of the spin-orbitals are the same (restricted), so the interactions between electrons of differing spins can be collected together.

Open shell problems.

In the UHF method the spatial part of the spin-orbitals is no longer identical for electrons with different spins. This results in there being two different Fock operators, one for electrons with alpha spin, and a second for those with beta spin. The spin-orbitals can then be written as

$$\psi_i(\mathbf{x}) = \begin{cases} \varphi_i^{\alpha}(\mathbf{r})\alpha \\ \varphi_i^{\beta}(\mathbf{r})\beta \end{cases} \qquad (2.16)$$

Inserting these definitions into Equation 2.14 leads to the two Fock operators

$$f^{\alpha}(1)\varphi_i^{\alpha}(\mathbf{r})\alpha = \varepsilon_i^{\alpha}\varphi_i^{\alpha}(\mathbf{r})\alpha \qquad (2.17)$$

$$f^{\beta}(1)\varphi_i^{\beta}(\mathbf{r})\alpha = \varepsilon_i^{\beta}\varphi_i^{\beta}(\mathbf{r})\beta \qquad (2.18)$$

and the corresponding definitions of the Fock operators

$$f^{\alpha}(1) = h(1) + \sum_{a}^{N_{\alpha}} \left[ J_a^{\alpha}(1) - K_a^{\alpha}(1) \right] + \sum_{a}^{N_{\beta}} J_a^{\beta}(1) \tag{2.19}$$

$$f^{\beta}(1) = h(1) + \sum_{a}^{N_{\beta}} \left[ J_a^{\beta}(1) - K_a^{\beta}(1) \right] + \sum_{a}^{N_{\alpha}} J_a^{\alpha}(1) \tag{2.20}$$

It can be seen that when the spatial orbitals are identical and $N_\alpha = N_\beta = N/2$ these equations reduce to Equation 2.15. In the general case the electrons of different spin have different energies, an effect called spin polarisation. The electrons with alpha spins have additional exchange interactions compared to those with a beta spin and are consequently at a lower energy.

In the ROHF method all electrons except for the excess electrons required to occupy open shells are placed in restricted closed-shell orbitals. The focus is then not on the difference between alpha and beta electrons, but between closed shell electrons, and those occupying open shells. Again two Fock operators are formed, one for closed shell electrons, and one for those in an open shell. The process of solving the ROHF equations is somewhat complicated by the fact that the ROHF equations are not invariant under a unitary transformation of all spin-orbitals, due to coupling between the closed and open shell orbitals. Ways around this problem are well known, but produce far more complicated equations than for RHF or UHF. A detailed account of the methods can be found in Ref. 8.

The pros and cons of the two methods are discussed in section 2.2, and the methods used in this thesis are explained.

### Introduction of a Basis.

The last step in formulating the Hartree-Fock equations, in a form amenable to numerical analysis, is the introduction of a basis. After the removal of the spin coordinates from the problem, a set of coupled spatial integro-differential equations remain, which can be solved numerically only for atoms and linear molecules [9,10]. Roothaan showed for closed shell configurations, that the introduction of spatial basis functions allowed the differential equations to be converted into algebraic equations

and solved by conventional matrix techniques[11]. Extensions to restricted open-shell systems are also due to Roothaan[12], more detail can be found in references 13 and 14.

The molecular orbitals are expanded in a set of known basis functions, $\{\chi_i(r), i=1,2,\ldots,L\}$, giving

$$\psi_i = \sum_{j=1}^{L} c_{ji}\chi_j \qquad (2.21)$$

The problem then reduces to calculating the expansion coefficients, $c_{ji}$. This step is exact if the basis set is complete, however, for computational purposes a finite set must be used – a compromise is needed between a small basis set for computational ease, and a large set to give accurate results. The basis sets used in this thesis are described in section 6.2.2.

The introduction of the basis into Equation 2.15 leads to the Roothaan equations

$$\mathbf{Fc} = \mathbf{Sc}\varepsilon \qquad (2.22)$$

Similarly inserting Equation 2.21 into Equation 2.17 and Equation 2.18 gives rise to the Pople-Nesbet equations[15]

$$\mathbf{F}^{\alpha}\mathbf{c}^{\alpha} = \mathbf{Sc}^{\alpha}\varepsilon^{\alpha} \qquad (2.23)$$

$$\mathbf{F}^{\beta}\mathbf{c}^{\beta} = \mathbf{Sc}^{\beta}\varepsilon^{\beta} \qquad (2.24)$$

which are generalisations of Equation 2.22. The equations for the two spins are coupled and must be solved simultaneously, as $\mathbf{F}^{\alpha}$ and $\mathbf{F}^{\beta}$ depend on both $\mathbf{c}^{\alpha}$ and $\mathbf{c}^{\beta}$.

The SCF Procedure.

A rough algorithm for the solution of the pseudo eigenvalue problem is:

1. Specify the system examined by a set of nuclear coordinates $\{R\}$, atomic numbers $\{Z\}$, number of electrons, $n$, and define a basis set.
2. Make an initial guess at the electronic states to define the Fock operator.
3. Solve the equations to obtain a new electronic configuration, defined by the orbital energies, $\varepsilon$, and the expansion coefficients, $c$.

4. See if the procedure has converged; the solution is converged when the electron density obtained is the same as the previous iteration within a defined accuracy. If not return to step 3.

5. If converged, calculate properties of interest from the solution.

Within the Born-Oppenheimer approximation this determines a wavefunction and energy for a collection of electrons moving in the field of the nuclei. To this the energy of the nuclear-nuclear repulsion can be added, to give a total energy. Mapping the total energy as a function of the nuclear coordinates, the potential surface for nuclear motion is obtained. The set $\{R\}$ that minimises this potential is the equilibrium geometry of the system.

## Interpretation of the solutions of the Hartree-Fock equations

The Hartree-Fock equations have the great advantage that their solutions can be given a physical significance. As an approximation to the true $n$-electron problem, the energy of a single determinant is minimised. This leads to a pseudo-eigenvalue equation for the $n$ occupied spin-orbitals. When the occupied spin-orbitals are known, the Fock operator becomes a well defined Hermitian operator, which will have a finite number of eigenvalues equal to the number, $X$, of basis functions used

$$f|\psi_i\rangle = \varepsilon_i|\psi_i\rangle \quad i=1,2,....X \tag{2.25}$$

Each of the eigenvectors, $\psi_i$, has a spin-orbital energy, $\varepsilon_i$, which Koopmans' theorem[16] allows to be interpreted.

The energy of an occupied spin-orbital, $\varepsilon_O$, is the negative of the energy required to ionise that electron, if all the other spin-orbitals remain unchanged, and provides an approximation to the ionisation energy of the system. Similarly, the energy of an unoccupied spin-orbital, $\varepsilon_U$, is an approximation to the negative of the system's electron affinity.

The 'frozen orbital' approximation assumes that the ($n\pm1$) electron systems have identical spin-orbitals to the $n$-electron system studied. This is of course a gross

approximation, ignoring the relaxation of the spin-orbitals in the ($n\pm1$)-electron system. Optimising the energy of the ($n\pm1$)-electron system will lower their energy, and thus their relaxation leads to ionisation energies being too positive and electron affinities being too negative. The other factor neglected by the single determinant approximation is the correlation energy (see 2.1.5 below). Correlation effects tend to be largest for systems with the highest number of electrons: this effect tends to compensate for the relaxation error in ionisation energies, but increase the error in electron affinities – in general Koopmans' electron affinities are unreliable. Transition energies of localised defects cannot be obtained from this relation, as the relaxation of orbitals is very significant. The success of this approximation in predicting ionisation energies depends on the cancellation of orbital relaxation and correlation energy terms[17].

This physical interpretation and the fact that a wavefunction is obtained, allowing the calculation of many of a system's properties, makes the Hartree-Fock method a valuable tool for studying systems theoretically.

### The role of symmetry.

One of the main computational barriers to implementing HF theory is the number of two-electron integrals that must be calculated and stored. The number of two electron integrals to be evaluated grows as the number of basis functions to the fourth power.

The use of symmetry can greatly reduce the number of these integrals. In HF theory, the Fock operators transform as the totally symmetric representation of the appropriate point group. This means that integrals of the Fock operator can only be non-zero if both the basis functions involved belong to the same irreducible representation of the point group; consequently many integrals can be set to zero without evaluation. In $T_d$ symmetry the time/memory saving can be spectacular; efficient use of symmetry, including the use of reduced matrix elements for different sub-species of irreducible representations, can lead to a reduction in the number of integrals by over 80%[18].

This use of abelian symmetry requires that the problem can be stated in terms of only the irreducible representations of the basis sets, and not their subspecies. For a closed-shell system with Fock matrix $\mathbf{F}^{\Gamma\gamma}$ for symmetry sub-species $\gamma$ of the degenerate representation $\Gamma$

$$F_{rs}^{\Gamma\gamma} = h_{rs}^{\Gamma\gamma} + \sum_{\mathrm{K}} \sum_{\kappa\in\mathrm{K}} \sum_{tu} P_{rs,tu}^{\Gamma\gamma,\mathrm{K}\kappa} D_{tu}^{\mathrm{K}\kappa} \tag{2.26}$$

Where $\boldsymbol{h}$ is the matrix of one electron interactions, $\boldsymbol{D}$ the density matrix formed from the coefficients of the basis functions and $\boldsymbol{P}$ is the matrix of the two electron operators $J$ and $K$.

$$P_{rs,tu}^{\Gamma\gamma,\mathrm{K}\kappa} = J_{rs,tu}^{\Gamma\gamma,\mathrm{K}\kappa} - \frac{1}{2} K_{rs,tu}^{\Gamma\gamma,\mathrm{K}\kappa} \tag{2.27}$$

From symmetry considerations it is known that the matrix elements are independent of $\gamma$. Introducing the reduced matrix elements

$$F_{tu}^{\Gamma} = \frac{1}{N_{\Gamma}} \sum_{\gamma\in\Gamma} F_{tu}^{\Gamma\gamma} \tag{2.28}$$

$$h_{tu}^{\Gamma} = \frac{1}{N_{\Gamma}} \sum_{\gamma\in\Gamma} h_{tu}^{\Gamma\gamma} \tag{2.29}$$

$$D_{tu}^{\Gamma} = \frac{1}{N_{\Gamma}} \sum_{\gamma\in\Gamma} D_{tu}^{\Gamma\gamma} \tag{2.30}$$

and

$$P_{rs,tu}^{\Gamma,\mathrm{K}} = \frac{1}{N_{\Gamma} N_{\mathrm{K}}} \sum_{\gamma\in\Gamma} \sum_{\kappa\in\mathrm{K}} P_{rs,tu}^{\Gamma\gamma,\mathrm{K}\kappa} \tag{2.31}$$

Then inserting Equation 2.26 into Equation 2.28 and using Equation 2.29, Equation 2.30 and Equation 2.31 it is found that

$$F_{rs}^{\Gamma} = h_{rs}^{\Gamma} + \sum_{\mathrm{K}} \sum_{tu} P_{rs,tu}^{\Gamma,\mathrm{K}} D_{tu}^{\mathrm{K}} \tag{2.32}$$

which is of the same form as Equation 2.26, but without the summation over the sub-species. This form can be used in the SCF scheme and only the reduced matrix elements need to be stored.

The derivation for the closed shell reduced matrix elements can be shown to hold with minor changes for ROHF and UHF cases with maximum spin, and for state averaged calculations (see 2.2.1) - the full non-abelian symmetry can be used in these cases.

Most other calculations, such as MCSCF (Multi-Configuration Self Consistent Field) and perturbation theory (see 2.1.5), cannot implement this, and the calculations can only be conducted in the highest order abelian sub-group. This makes these calculations far more computationally intensive.

Semi-Empirical SCF methods.

Approximations to the HF method are made by parameterising some of the terms that appear in the HF equations, particularly the two electron integrals, which take up most of the computational effort.

### *2.1.5 Correlation energy and improvements to the HF method.*

The correlation energy of a system is normally defined as, the difference in energy between the exact solution of the non-relativistic many-electron Schrodinger equation within the Born-Oppenheimer approximation and the Hartree-Fock limit (i.e. the solution to the HF equations with a complete basis set) for the system[19]. It is so called, for the same reason that the Hartree-Fock method is often termed uncorrelated; electrons of opposite spin remain uncorrelated and are not forced to remain apart in space, unlike electrons with parallel spins.

The correlation energy can conveniently be divided into two contributions, based on partitioning the orbitals into internal and external sets[20]. The internal orbitals are essentially the valance orbitals of the system, which includes the orbitals of the active space in a MCSCF calculation. Excitations of electrons within the active region have only relatively small promotion energies, and hence these excitations' contribution to the correlation energy is termed near-degenerate. Excitation from both the active orbitals and other inert orbitals contributes to the rest of the correlation energy, termed dynamic.

We can see how this partitioning is useful conceptually by considering the binding energy and transition energies of the clusters studied. The binding energy of the cluster has a large contribution to it from the change in correlation energy between the free transition metal ion/atom and the transition metal bonded into the cluster. It is likely, especially when the ground-state of the cluster is well described by a single reference wavefunction, that the body of the correlation energy will be dynamic from the many excitations from the metal into the conduction band of the cluster. On the other-hand, when considering the transition energies of the clusters, we are subtracting the correlation energies of two clusters. The vast majority of the dynamic correlation energy will cancel. The body of the correlation energy contribution to the transition energy will be near degenerate from configurations in, or energetically near, the active space. Different methods are needed to deal with these situations.

## MCSCF and CI.

Many molecular properties can be understood in the context of Hartree-Fock theory. However, as noted, the method is essentially based upon an independent particle approximation, and no Coulomb correlation is included in the wavefunction. Another failing of the restricted Hartree-Fock method is that it is incapable of describing the formation, or breaking, of bonds in molecules.

The simplest conceptually, though not necessarily computationally, way of improving upon the Hartree-Fock method is to include additional determinants in the expansion of the many-electron wavefunction. This leads to MCSCF (Multi Configuration SCF) or CI (Configuration Interaction) wavefunctions.

MCSCF employs a limited set of configurations to form the total wavefunction

$$\Phi = \sum_{k=1}^{active} C_k \Psi_k \qquad (2.33)$$

In a similar manner to the Hartree-Fock method the spin-orbitals are optimised, but in a MCSCF calculation the expansion coefficients of the configurations, $C_k$, are also optimised. The expectation value of the energy of this type of wavefunction is

$$E = \sum_{ij} D_{ij} h_{ij} + \sum_{ijkl} D_{ijkl} \left\langle \Psi_i(1)\Psi_k(2) \middle| g_{12} \middle| \Psi_j(1)\Psi_l(2) \right\rangle \qquad (2.34)$$

$D_{ij}$ and $D_{ijkl}$ are the first and second order density matrices constructed from the expansion coefficients, $C_k$. Variation with respect to the expansion coefficients leads to secular equation for the expansion coefficients, whilst variation with respect to the spin-orbitals leads to an orbital equation similar to the Hartree-Fock equation. In general, however, there is no transformation to convert the orbital equation into a pseudo-eigenvalue equation[21].

Each MCSCF iteration consists of the following steps:

1) Transformation of AO integrals into the current MO basis,

2) Generation of the Hamiltonian matrix and optimisation of the CI coefficients.

3) Generation of the first and second order density matrix,

4) Improvement of the molecular orbitals.

5) Check for convergence

This is just a more complex version of the SCF cycle in section 2.1.4; here the CI coefficients must be optimised as well as the orbitals.

A special case of the MCSCF method is the CASSCF (Complete Active Space SCF) method, where all CSFs (Configuration State Functions)* arising from the distribution of a limited number of electrons over a specified set of active orbitals are included in

---

* CSFs are an antisymmetrised product of a symmetry adapted spatial orbital product and a spin adapted linear combination of simple alpha and beta spin functions. They are an alternative way of creating the many-electron space, and have the advantage over determinants that they are genuine eigenfunctions of the total spin operator.

the expansion [22,24]. The advantage of CASSCF, is that the wavefunction is invariant to rotations amongst the active orbitals, and, thus, the first order density matrix can be diagonalised. CASSCF wavefunctions can describe bond formation and dissociation, but the number of determinants grows extremely rapidly with the size of the active space. As MCSCF involves truncating the CI expansion severely, choosing the best determinants is very important, a good account of how to choose the best active space is given in Ref 25. A well-chosen MCSCF wavefunction, should recover much of the near degenerate correlation energy, but little of the dynamic.

Configuration Interaction methods do not involve the optimisation of the orbital set. Instead a fixed orbital set is imported from a previous calculation, e.g. HF theory, and used to generate the determinants for the CI calculation. The determinants in the CI expansion can be described by their variation from the reference wavefunction, $\Psi_0$, derived from some other SCF technique. So $\Psi_i^a$ is obtained by replacing orbital $i$ that is occupied in $\Psi_0$, with orbital $a$ that is unoccupied in the reference CSF. The CI wavefunction may be written

$$\Phi = \Psi_0 + \sum_{i,a} C_i^a \Psi_i^a + \sum_{i<j} \sum_{a<b} C_{ij}^{ab} \Psi_{ij}^{ab} + \cdots \qquad (2.35)$$

The expansion coefficients in the series are then varied to minimise the energy, leading to secular equations in a similar manner to the Hartree-Fock method; if there are $N$ determinants in the expansion, there will be $N$ solutions to the secular equations. The lowest energy solution(s) represent the ground state(s) of the system, and the other solutions the excited states. Configuration Interaction recovers some of the correlation energy. Full CI based on a SCF calculation with a complete basis set gives the exact solution to the non-relativistic time-independent Schrodinger equation. The expansion, however, rapidly becomes huge and computationally infeasible, and is always truncated at some point. Wave functions derived only from single and double replacements (SD-CI) are often encountered. The correlation energy recovered depends on the configurations included into the expansion of the wavefunction; unfortunately, the size of the CI matrix makes this method impractical for all but the smallest molecules.

## Perturbation theory.

An alternative to the MCSCF and CI methods, which try and improve on the wavefunction by expanding it using more determinants, is to use a perturbation theory approach. The idea, as ever, is to use known solutions to an approximate model, in this case the HF or MCSCF wavefunctions, and perturb them by a term that is considered relatively small: for HF the difference between the HF potential and the real two-electron interaction term, $r_{ij}^{-1}$. Unlike the CI approach, the calculation of second order perturbation energy corrections is only about as computationally expensive as the basic SCF or MCSCF calculation [26](but abelian symmetry cannot be used, see section 2.1.4).

For closed-shell RHF the Hamiltonian is partitioned as

$$H = H_0 + V \tag{2.36}$$

Where $H_{0\,is}$ the Hartree-Fock Hamiltonian,

$$H_0 = \sum_i f(i) = \sum_i \left[h(i) + v^{HF}(i)\right] \tag{2.37}$$

and

$$V = \sum_{i<j} r_{ij}^{-1} - V^{HF} = \sum_{i<j} r_{ij}^{-1} - \sum_{i<j} v^{HF}(i) \tag{2.38}$$

This partitioning of the Hamiltonian is often called Mosser-Plesset perturbation theory and referred to as MPx, where x is the order that the perturbation expansion is carried to. Partitioned like this, the zeroth-order perturbation energy is the sum of the occupied orbital energies, and the first order energy correction yields the Hartree-Fock total energy. Generally the perturbation expansion is taken to second order (MP2) and the correlation correction energy can be written for a closed shell system as,

$$E^2 = 2\sum_{abrs}^{N/2} \frac{\langle ab|rs\rangle\langle rs|ab\rangle}{\varepsilon_a + \varepsilon_b - \varepsilon_r - \varepsilon_s} - \sum_{abrs}^{N/2} \frac{\langle ab|rs\rangle\langle rs|ba\rangle}{\varepsilon_a + \varepsilon_b - \varepsilon_r - \varepsilon_s} \qquad (2.39)$$

where $\langle ab|rs\rangle = \int d\mathbf{x}_1 d\mathbf{x}_2 \chi_a^*(\mathbf{x}_1)\chi_b^*(\mathbf{x}_2) r_{12}^{-1} \chi_r(\mathbf{x}_1)\chi_s(\mathbf{x}_2)$ are two electron integrals over the spatial orbitals. Similar, but more complex, expressions hold for open shell systems and MCSCF wavefunctions.

Perturbation theory should recover much of the cluster's dynamic correlation energy relatively cheaply. The amount of correlation energy recovered by a given method is commonly referenced to a full CI calculation on methylene [27], where second order perturbation methods typically recover around 80% of the correlation energy.

### *2.1.6 Density Functional Theory.*

Density functional theory is an alternative method for *ab initio* calculations of electronic structure. The Hohenberg-Kohn theorem[28], proved using an argument *reductio ad absurdum,* states that the ground state (of a given symmetry) of a many electron system is a unique functional of the electron density, $\rho(\boldsymbol{r})$. The energy of the ground state can be expressed in terms of the density of the ground state as,

$$E_{ground} = T[\rho] + \int d\mathbf{r}\rho(\mathbf{r})V(\mathbf{r}) + \frac{1}{2}\int d\mathbf{r}_1 \int d\mathbf{r}_2 \frac{\rho(\mathbf{r}_1)\rho(\mathbf{r}_2)}{|\mathbf{r}_1 - \mathbf{r}_2|} + E_{XC}[\rho] \qquad (2.40)$$

in which $T[\rho]$ is the kinetic expression for a system of non-interacting particles and $E_{XC}$ is the exchange and coulomb correlation contribution to the total energy. The great benefit of this formulation is that the ground state energy can then be determined by direct variation of the density. This should be contrasted with the usual variational approach, where the ground state energy is minimised with respect to the spin-orbitals constructing the ground state wavefunction. The density $\rho[r]$ is a real, positive function of a single vector variable, whereas, the wave function is a complex function of $N$ vector variables. Kohn and Sham [29] expand the electron density in one-electron basis functions,

$$\rho(\mathbf{r}) = \sum_{i}^{N} \left|\psi_i(\mathbf{r})\right|^2 \tag{2.41}$$

and derive the Kohn-Sham equations by substitution into the energy expression and functional variation with respect to the density

$$\left[T + V(\mathbf{r}) + V_C(\mathbf{r}) + V_{XC}(\mathbf{r})\right]\psi_i(\mathbf{r}) = \varepsilon_i \psi_i \tag{2.42}$$

$$V_{XC}(\mathbf{r}) = \frac{\partial E_{XC}[\rho]}{\partial \rho(\mathbf{r})} \tag{2.43}$$

and

$$V_C(\mathbf{r}) = \int d\mathbf{r}' \frac{\rho(\mathbf{r}')}{|\mathbf{r}' - \mathbf{r}|} \tag{2.44}$$

Again this is an effective one-electron equation, but now includes an expression for the exchange correlation potential.

In general, the exchange-correlation potential is unknown, so in most cases approximations based upon a free-electron gas are introduced.

The Kohn-Sham equations are normally solved using numerical techniques. However, the ease of solution in varying the density rather than the coordinates of $N$ electrons does bring disadvantages: the one-electron energies - excepting the highest occupied eigenvalue, which corresponds to the chemical potential - cannot be interpreted as frozen orbital ionisation energies or electron affinities, as in the Hartree Fock method (excitation and ionisation energies are normally calculated using Slater's transition state concept [30]) and, as is implicit in the derivation, the results apply only to the ground state of the system – excited states within the DFT approach require additional approximations and assumptions. A further disadvantage is that only the total electron density is obtained, therefore properties that depend upon the character of the wavefunction cannot be calculated.

## 2.2 Specifics of the GAMESS implementation.

In this section, details of the methods by which GAMESS implements the theory of section 2.1 are given. Calculations were performed using the PC GAMESS version [31] of the GAMESS (US) QC package

The calculations were carried out upon finite atomic clusters using Gaussian basis sets. Super cell calculations require much larger clusters to prevent interaction between the repeating units and methods based upon plane-wave expansions of the wavefunction are inappropriate for such localised defects as the transition metals.

### *2.2.1 SCF Calculations.*

The SCF calculations in this thesis have been carried out within the RHF or ROHF framework. The use of the ROHF formulation is to counteract a common problem with defects of high symmetry, often referred to as 'charge sloshing'. When degenerate, or near degenerate, orbitals are present in the system, discontinuities in the energy can occur in the SCF cycle (section 2.1.4). In the case of degenerate orbitals, such as TM d-orbitals in a tetrahedral environment, the problem occurs as occupied orbitals of the degenerate set will experience a different potential from the unoccupied

members, changing their respective energies. However, in the next cycle of the calculation the orbitals occupied may be different members of the set. The result of this is that the electron shifts from one degenerate orbital to the next and the energy oscillates rather than converging. GAMESS overcomes this problem for ROHF calculations by partially occupying the degenerate orbitals equally. For instance, a pair of e orbitals, occupied by one electron, will have half an electron in each of the e orbitals. This leads to the wavefunction being an average of all states of appropriate spin that can be derived from the electronic configuration - a sort of state averaged SCF. In theory, this procedure can be used to force convergence to excited states by specifying the occupancy of various orbitals, however, convergence would be very poor in cases where there is more than one open shell.

This method of calculation makes the initial guess for the electronic density crucially important. The state averaged SCF specifies the occupied open shell orbitals, and they remain occupied even if some of the 'virtual orbitals' become lower in energy. This makes a good choice of initial guess essential, and close examination of the converged solution necessary, e.g. a calculation on a $Co_s^-$ defect converged readily to a solution that appeared too high in energy, a subsequent MCSCF calculation showed that two sets of $t_2$ orbitals had been filled in the wrong order: the state averaged SCF calculation converged an excited $(t_2)^2(t_2)^4$ configuration rather than the ground state $(t_2)^4(t_2)^2$ as these two sets of orbitals were reversed in energy for the initial guess.

The method of obtaining reliable initial guess wavefunctions has been to use the results from a similar cluster that can be treated with RHF or ROHF with no orbital degeneracy, e.g. a $(t_2)^3$ configuration, which converge readily, and use results of these runs to start the required calculation. As indicated in section 2.1.4 the full symmetry of the cluster can be used in these calculations.

An alternative to this procedure is to use finite temperatures. This is the method utilised in the LDA (Local density approximation) DFT calculations previously conducted on TM defects in diamond. The electrons are distributed over near degenerate energy levels using Fermi statistics. This method again ensures that degenerate orbitals are treated equally, and retain the same radial distributions. In some cases it can obscure the physics of a situation, such as removing the driving force for a Jahn-Teller distortion.

No provision is made for such state-averaged calculations using UHF theory and, therefore, these calculations have rarely been utilised in this thesis. The main advantage of UHF calculations is that they describe the unpaired electron density much better than ROHF. The restriction on ROHF calculations, that the alpha and beta spin-orbitals have the same spatial functions, means that unpaired spin density can only be found at a nucleus if open-shell orbitals contain s-orbitals of that atom. In tetrahedral clusters the metal's s-orbitals cannot mix into functions of e or $t_2$ symmetry. As these are the symmetries found (chapter 3) for the open shell orbitals

of the interstitial and substitutional TM clusters, no spin density is found at the metal. This is clearly incorrect – $Ni_s^-$ was identified by $^{61}Ni$ hyper-fine structure[32]. As this restriction is lifted in UHF theory, the occupation of the TM s-orbitals can be different in the alpha and beta orbital sets, giving a net spin density at the TM nucleus. UHF calculations also give solutions of lower energy, as there is more variational freedom in choosing the wave function.

### *2.2.2 MCSCF calculations.*

The GUGA (Graphical Unitary Group Approach) CI package was used which is based around CSFs rather than determinants [33,34]. This implementation was used as CSFs are properly spin-adapted, which ensures that the many-electron wavefunctions obtained have well defined total spin, i.e. they are genuine singlets, doublets etc., allowing proper high-spin and low-spin configurations to be examined to determine the ground state of the clusters (see Chapters 3 and 6). All calculations were of the complete active space type.

## 2.3 Summary.

In this chapter, the two main theoretical methods used in *ab initio* calculations have been detailed. In the next chapter, it is explained how Crystal-field theory and Ligand field theory can be interpreted as particular parameterisations of the Hartree-Fock theory. Throughout this thesis, defects are described in the language of crystal field theory and the connection between Hartree-Fock theory and crystal-field theory underpins this (in chapter 4 the crystal field model of the well characterised TM defects is given). In Chapter 6, the results of *ab initio* calculations on TM defects in diamond are presented and details of the methods and the interpretation of calculations draws heavily on this chapter.

As well as presenting the methods of Hartree-Fock and density functional theory the differences between the two have been emphasised. Density functional theory is uniquely suitable for determining many ground state properties of defects, however, the very feature of the theory that makes it so effective also limits it. By concentrating

on the ground state and only dealing with the charge distribution in the defect, excited states are hard to treat with DFT; no wavefunction is obtained and the nature of the one-electron orbitals found is ill-defined. Conversely, Hartree-Fock theory obtains a genuine wavefunction, by using multi-reference wavefunctions real many-electron states can be found, and Koopmans' theorem and the connection to crystal field theory allow HF calculations to be interpreted in a framework familiar to physicists and chemists. But in gaining this information, a much harder problem must be solved (to obtain the wavefunction as a function of all the electron coordinates), which restricts the HF method to smaller systems, and correlation energy is treated in a much less systematic manner, if at all.

It is not a case of one method being better than the other, instead they should be seen as complementary, the HF method being more interpretable and flexible but DFT much more efficient and accurate when used on suitable systems.

## References.


[1] M W Schmidt, K K Baldridge, J A Boatz, S T Elbert, M S Gordon, J J Jensen, S Koseki, N Matsunaga, K A Nguyen, S Su, T L Windus, M Dupuis, J A Montgomery, J. Comput. Chem., **14**, 1347-1363 (1993)

[2] M Born and J R Oppenheimer, Ann Physik, **84**, 457 (1927)

[3] B T Sutcliffe, in *Computational Techniques in Quantum Chemistry,* G H F Diercksen, B T Suttcliffe and A Veillard (Eds), Reidel, Boston, 1975

[4] R Car and CM Parrinello, Phys. Rev. Lett. **55,** 2471 (1985)

[5] R McWeeny and B T Suttcliffe, *Methods of Molecular Quantum Mechanics*, (London: Academic Press, 1969)

[6] A Szabo and N S Ostaland, *Modern Quantum Chemistry*, (New York, London: Macmillan, 1982)

[7] V Fock, Z. Phys., **61**, 126 (1930)

[8] S Krebs, Comp. Phys. Com., **116,** 137-277 (1999)

[9] D R Hartree, *The calculation of Atomic structures,* (New York: Wiley Interscience, 1957)

[10] P A Cristiasen and E A McCullough Jr., J. Chem. Phys., **67**, 1877 (1977)

[11] C C Roothaan, Rev. Mod. Phys, **23**, 69 (1951)

[12] C C Roothaan, Rev. Mod. Phys, **23**, 179 (1960)

[13] R, McWeeny and B T Sutcliffe, *Method of Molecular Quantum Mechanics,* (London: Academic Press, 1969)

[14] A C Hurley, *Introduction to the Electronic theory of small molecules,* (London: Acedemic Press, 1976)

[15] J A Pople and R K Nesbet, J. Chem. Phys., **22**, 571 (1954)

[16] T Koopmans, Physica , **1**, 104 (1933)

[17] Fowler, *Phys. Rev.,* **151**, 657 (1966)

[18] G Van De Rector, PhD Thesis, University of Groningen, 1988

[19] P O Lowdin, Phys. Rev., **97**, 1509 (1955)

[20] H J Silverstone and O Sinanoglu, J. Chem. Phys., **44**, 1899 (1966)

[21] A C Wahl and G Das, *The Multiconfigurational self-consistant field method,* in *Methods of Electronic Structure Theory,* H F Schaefer III (Ed.), (Plenum, New York, 1977, p51)

[22] B Roos, P Taylor and P Siegbahn, Chem. Phys., **48**, 157 (1980)

[23] P Siegbahn, A Heiberg , B Roos and B Levy, Phys. Scr., **21**, 323 (1980)

[24] P Siegbahn, J Almlof, A Heiberg , B Roos, J. Chem. Phys., **74**, 2384 (1980)

[25] M W Schmidt and M S Gordon, Annu. Rev. Phys. Chem., **49**, 233 (1998)

[26] K Anderson, B O Roos, Int. J. Quantum Chem., **45**, 591-607 (1993)

[27] C W Bauchlicher and P R Taylor, J. Phys. Chem., **85**, 6510 (1986)

[28] P Hohenberg and W Kohn, Phys. Rev. B, **3,** 864 (1964)

[29] W Kohn and L J Sham, Phys. Rev. B, **4,** 1133 (1965)

[30] J C Slater, Phys. Rev., **81,** 385 (1951)

[31] Alex A. Granovsky, www http://classic.chem.msu.su/gran/gamess/index.html

[32] M I Samoilovich *et al.*, JETP Lett., **14 ,** 379 (1971)

[33] B Brooks and H F Schaefer, J. Chem. Phys., **70**, 5092 (1979)

---

[34] B Brooks, W Laidig, P Saxe, N Handy and H F Schaefer, Physica Scripta, **21**, 312 (1980 )

# Chapter 3.

# Crystal and Ligand field theory of Transition Metal impurities.

## 3.1 Introduction.

The transition metals of interest in this thesis are those of the first transition series, the iron group, which have partially filled 3d shells. It is these incompletely filled shells that give rise to the characteristic properties of transition metal impurities, magnetism and optical absorption , which lead to bulk samples being coloured and their ability to be incorporated, in varying charge states, at a variety of sites.

It is possible to describe the properties of transition metals by *ab initio* calculations, taking all electrons into account, but the above statement, that many of their properties can be explained by examining the incompletely filled 3d orbitals, means many theories focus their attention upon just these orbitals.

Two essential assumptions are made to concentrate attention on the area of interest:

i) The ion in its crystal environment is supposed to maintain a strong resemblance to the free ion. This means that the inner, filled shells have little interaction with the diamond host and that the one-electron wavefunctions of the unfilled shell have the same symmetry properties as those of the free ion (but with the descent in symmetry to that of the impurity site taken into account). The 3d-electrons of a first row transition metal will transform like d-functions in the point symmetry of the defect site.

ii) The properties of the transition metal are determined only by a small part of the crystal. This portion of the whole is termed the complex, and often only includes nearest neighbours – termed the ligands. Sometimes more of the crystal must be included, e.g. the interstitial site in diamond must include the six next nearest neighbours to achieve results consistent with experimental evidence.

The first assumption cannot be justified formally, but intuitively appears plausible and is justified by comparison with much experimental evidence (see section 1.6). The connection with the free ion has the very important corollary that reasonable initial guess wavefunctions are available from the theory of atomic spectra, without the need for detailed computation. The second assumption is more soundly based, overlap with other more distant neighbours is often very small, because the 3d electrons are quite localised on the metal ion and do not extend far into the crystal.

Various levels of theory have been built upon these assumptions. The ones of interest here are crystal field theory, essentially an electrostatic description of the effect of the ligands, and ligand field theory, an empirical molecular orbital treatment of the valence orbitals of the complex. They are tied together because both theories use extensive symmetry arguments, and many of the results of the simpler crystal field theory can be directly imported into the more physically correct ligand field model.

## 3.2 Crystal Field Theory.

The Hamiltonian for the complex can be written using the first assumption above

$$H = H_{FREE\ ION} + V_{CRYSTAL} \qquad (3.1)$$

The various ways of developing crystal field theory depend upon which terms are considered to be dominant – the electron-electron repulsions present in the free ion term or the potential from the host crystal. When the electron-electron interactions are strongest the weak field coupling scheme is used; the terms in the Hamiltonian dealing with electron-electron repulsions are diagonalised first, and then the crystal field is incorporated. This means eigenstates are very like free ion terms, but split by

the lower symmetry crystal potential. This scheme is appropriate for iron group elements in many situations. The ground state obtained is often called a high spin configuration, as the initial guess state to be perturbed will by Hund's rules have maximum spin multiplicity. Conversely, when the crystal field is deemed to be dominant, termed the strong field coupling case, the one-electron states in the host crystal are found first and filled to give many electron terms, in a sort of *aufbau* process, then the electron-electron interactions are taken into account. This gives the low spin state for the impurity. It will be shown that this scheme (chapters 5 and 6) is often relevant for TM defects in diamond.

The basic idea of crystal field theory is that the metal ion in a co-ordinated environment is subjected to an electric field originating from its neighbours[1].

The Hamiltonian written out in detail is

$$H = -\frac{\hbar^2}{2m}\sum_i \nabla_i^2 - \sum_i \frac{Ze^2}{r_i} + \frac{1}{2}\sum_{i<j}\frac{e^2}{r_{ij}} + V_{CRYSTAL} \qquad (3.2)$$

This is the Hamiltonian for the free ion, with the addition of a potential originating from the host crystal. The solutions to the free ion terms are known[2]. As the free ion terms are solutions to a problem with full spherical symmetry, the potential due to the host crystal can conveniently be expanded in a series of spherical harmonics the first sum being over the i-electrons of the transition metal ion.

$$V_{CRYSTAL} = \sum_i \sum_l \sum_m Y_l^m(\Theta_i, \varphi_i) R_{nl}(r_i) \qquad (3.3)$$

The term with $l$=0 is by far the most important energetically, however, it often has little effect on the electronic properties of the complex; if the radial function of the d-orbitals in different terms are the same, it will only cause a uniform shift in all levels with the same number of electrons, and for many purposes can be neglected. It should be emphasised though, that it is this term that is responsible for the majority of the binding energy of the ion.

Symmetry arguments can then be utilised to show that the rest of $V_{CRYSTAL}$ has the form in Cartesian co-ordinates.

$$V_{CRYSTAL} = x^4 + y^4 + z^4 - \tfrac{3}{5} r^4 \qquad (3.4)$$

The great beauty of this method is that most of the work can be taken straight from the well-understood theory of atomic spectra. Also, excited states are treated entirely equally to the ground state, so the method is uniquely suited to analysis of optical spectra.

### *3.2.1 One electron*

The effect of the crystal potential on a d-electron in cubic symmetry is to split the original five fold degenerate d-orbitals into a triply degenerate, $t_2$ set,

$$t_2^0 = \frac{1}{\sqrt{2}}(d_2 - d_{-2}) \qquad t_2^{\pm 1} = d_{\pm 1} \qquad (3.5)$$

and a doubly degenerate, e set,

$$e^a = d_0 \qquad e^b = \frac{1}{\sqrt{2}}(d_2 + d_{-2}) \qquad (3.6)$$

expressed in terms of linear combinations of atomic d-functions.

For a single electron the energies of these orbitals may be written, relative to an energy $E_0$ shifted form the atomic value by the action of the $l$=0 part of the crystal field

$$E(e) = E_0 + \int \phi^*(e^a) V_{CRTSTAL} \phi(e^a) = E_0 + x \qquad (3.7)$$

$$E(t_2) = E_0 + \int \phi^*(t_2{}^a) V_{CRYSTAL}\, \phi(t_2{}^a) = E_0 + y$$

The energy difference $x$-$y$ is defined as $10Dq$, or $\Delta$ (see Ref 3). The values of $x$ and $y$ can be found by considering the energy when the orbitals are completely filled – this gives rise to a completely symmetric term, which $V_{CRYSTAL}$ does not influence. Then $0=4x + 6y$. Combining these equations gives

$$\int \phi^*(e^a) V_{CRYSTAL} \phi(e^a) = 6Dq$$
$$\int \phi^*(t_2{}^0) V_{CRYSTAL}\, \phi(t_2{}^0) = -4Dq \qquad (3.8)$$

The reason for these splittings can readily be seen. The $t_2$ orbitals are directed mainly along a threefold symmetry axis, whereas the e orbitals have greatest amplitude along the cube directions. In $O_h$ symmetry, the ligand sigma orbitals are directed mainly along the cube directions and will interact most strongly with the e orbitals. The ligands are generally anions, or have the negative ends of dipoles pointing towards the metal, and so the $t_2$ orbitals will be energetically more stable for an electron.

In tetrahedral symmetry the situation is reversed and *Dq* changes sign; the ligand orbitals point along a three-fold axis and will influence the $t_2$ orbitals most effectively, hence the e orbitals will lie lower in energy.

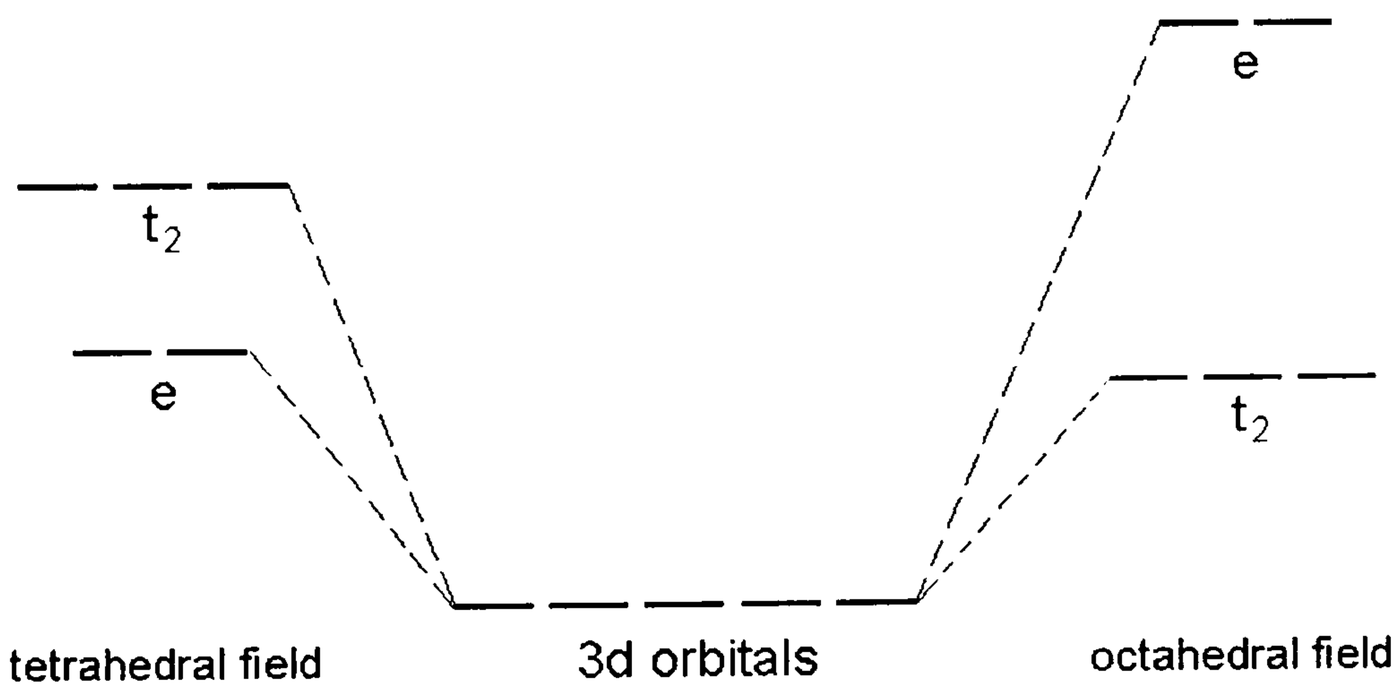


**Figure 3.1**. The splitting (not to scale) of the five degenerate d-orbitals (centre) when placed in a cubic crystal field of tetrahedral (left), or octahedral (right) symmetry. Note the effect of the $l$=0 (see equation 3.3) is to raise the energy of the orbital in the complex.

The form of the potential stays the same in any theory, as it is based solely on symmetry arguments, but in crystal field theory it arises from the electrostatic potential of the nearest neighbours. Explicit calculation gives

$$\Delta_{OCT} = \frac{Ze^2}{R}\frac{\langle r^4 \rangle}{R^4}\frac{3}{5} \text{ and } \Delta_{TET} = -\frac{Ze^2}{R}\frac{\langle r^4 \rangle}{R^4}\frac{4}{15} \qquad (3.9)$$

for octahedral and tetrahedral co-ordination respectively [4]. $\langle r^4 \rangle$ is the radial distribution of charge which becomes negligible for $r>R$. The order of magnitude for the results is reasonable [5-7], but this is known to be fortuitous [8]. The physical origin of the splitting arises from covalency in the complex; for this reason the calculation of $Dq$ in the crystal field theory approximation is of little interest and, as such, $10Dq$ is taken as an empirical parameter. When dealing with interstitial transition metal ions in diamond, the results above, that tetrahedral and octahedral crystal fields cause opposite splittings of the d-orbitals and that the octahedral field splitting is almost twice as strong as that exerted by a tetrahedral arrangement of ligands, will be needed to explain the observed orbital ordering.

In crystal field theory, the energy difference between the metal $t_2$ and e one-electron orbitals is termed delta, or $10Dq$, and is one of the main parameters in the theory. When the level of theory advances to ligand field, or to a full *ab initio* treatment, it is hard to reclaim this conceptually simple idea. Indeed, it has been shown [9] that rather than being a good parameter defining a complex, $10Dq$ changes significantly in different many-electron states, and an average over all configurations would be necessary to extract a splitting parameter[10].

### *3.2.2 Many-electron states.*

When dealing with a many-electron situation, the problem can be approached from one of two extremes, depending on whether it is thought that electron-electron repulsion or the crystal field potential is dominant energetically. The problem is then set up using states that are diagonal in the dominant part of the Hamiltonian and the rest of the Hamiltonian is treated as a perturbation.

### 3.2.2.1 Weak Crystal Fields.

The weak crystal field limit occurs when $V_{CRYSTAL} << e/r_{12}$, and electron repulsion terms are dominant. The basis states are taken to be those of the free atom, particularly the quantum numbers L and S retain their validity. Because the atomic terms are assumed to be well separated compared to the size of the crystal field, it is only necessary to see how an atomic term is split by the cubic field.

From section 3.2.1 the effect of the crystal field on the d-orbital basis can be found

$$\begin{aligned} \langle \pm 2|V_{CRYSTAL}|\pm 2\rangle &= Dq \qquad & \langle \pm 2|V_{CRYSTAL}|\mp 2\rangle &= 5Dq \\ \langle \pm 1|V_{CRYSTAL}|\pm 1\rangle &= -4Dq \qquad & \langle 0|V_{CRYSTAL}|0\rangle &= 6Dq \end{aligned} \tag{3.10}$$

where Dirac notation is used, the number labelling the magnetic quantum number $M_L$ of the original set of d-orbitals. Knowing these relations, and the make up of the atomic terms, all that is needed to find the energies in the crystal field is to find how the atomic term splits in the lower symmetry.

Taking a $(d)^2$ system in octahedral symmetry, the ground atomic term is $^3F$, and utilising descent in symmetry, it splits into $^3A_2$, $^3T_2$ and $^3T_1$ states in an octahedral field. Taking a basis labelled by L, $M_L$ the make-up of the octahedral states can be found by applying the symmetry operations of O to the basis states. Representative spatial orbitals of the different states are,

$$T_1 = |3,0\rangle \qquad T_2 = \frac{1}{\sqrt{2}}\left(|3,+2\rangle + |3,-2\rangle\right) \quad \text{and} \quad A_2 = \frac{1}{\sqrt{2}}\left(|3,+2\rangle - |3,-2\rangle\right)$$

where the quantum numbers are (L, $M_L$). From the theory of atomic spectra the (L, $M_L$, S, $M_S$,) states are known in terms of the d-orbitals, e.g. $|3,2,1,1>=|3,+2>=|2^+,0^+|$. The last expression is a determinant formed from the metal d-orbital basis $|2^+,0^+|=d_2(\mathbf{r}_1)\alpha(\omega_1)\ d_0(\mathbf{r}_2)\alpha(\omega_2) - d_2(\mathbf{r}_2)\alpha(\omega_2)\ d_0(\mathbf{r}_1)\alpha(\omega_1)$. The energy of the $^3A_2$ state can then be evaluated,

$$E(^3A_2) = \frac{1}{\sqrt{2}}\left(\langle 3,+2| - \langle 3,-2|\right) V_{CRYSTAL} \frac{1}{\sqrt{2}}\left(|3,+2\rangle - |3,-2\rangle\right) \qquad (3.11)$$

substituting d-orbital determinants for the ($L,M_L$) expressions and expanding the determinants gives

$$E(^3A_2) = \langle d_2 | V_{CRYDTAL} | d_2 \rangle + \langle d_0 | V_{CRYDTAL} | d_0 \rangle + \langle d_2 | V_{CRYSTAL} | d_{-2} \rangle \qquad (3.12)$$

and evaluating the integrals using Equation 3.10 it is found that

$$E(^3A_2) = Dq + 6Dq + 5Dq = 12Dq \qquad (3.13)$$

Similarly, it is found that the energies of the other triplet states are

$E(^3T_2) = 2\,Dq$ and $E(^3T_1) = -6\,Dq$

If $Dq$ is positive, as for octahedral complexes, then $^3T_1$ is the ground state and transitions to $^3T_2$ and $^3A_2$ are expected at energies of 8 $Dq$ and 18 $Dq$ respectively.

### 3.2.2.2 Strong Crystal fields.

When the crystal field is much stronger than the correlative interactions of the electrons, a different scheme is used. The crystal field causes a Paschen-Back effect, destroying the (L,S) coupling of the electrons, and L and S are no longer good quantum numbers. Instead, the occupation numbers of the $t_2$ and e orbitals are used to label states. As the crystal field is assumed large, the lower energy orbitals ($t_2$ in octahedral symmetry) are filled first, when these are filled the higher energy orbitals become occupied. Generally, several states can be constructed from a given $(t_2)^n(e)^m$ configuration, these states are then split by the Coulomb repulsions of the electrons.

Energies of states are evaluated by finding the crystal field stabilisation energy – just –4 $Dq$ for each electron in a $t_2$ orbital, and +6 $Dq$ for each electron occupying an e orbital. To this energy is added the electron repulsion terms, calculated in the same manner as for atomic terms. This is possible because in crystal field theory the e and $t_2$ orbitals are purely derived from the metal d-orbitals, so the repulsion terms can be expressed in terms of atomic Coulomb ($J$) and exchange ($K$) integrals.

Looking again at the $(d)^2$ octahedral case, but from the strong-field point of view, the two electrons will be placed into the $t_2$ orbitals. The states formed from the $(t_2)^2$ configuration can be found from group theory: $t_2 \times t_2 = A_1 + E + [T_1] + T_2$. The $T_1$ state is the anti-symmetric product, and can thus be paired with a triplet spin state to form a $^3T_1$ state in accordance with the Pauli exclusion principle – the other states are singlets. This gives the $^3T_1$ wavefunctions in determinants formed from atomic d-orbitals as $\varphi_1=|(xy)(yz)|$ , $\varphi_2=|(yz)(zx)|$ and $\varphi_3=|(zx)(xy)|$, where, for instance, the spin-orbital $xy=[d_1(\boldsymbol{r}_1)-d_{-1}(\boldsymbol{r}_1)]\alpha(\omega_1)$. The energy of the $^3T_1$ state is then,

$$E(^3T_1) = J(xy, yz) - K(xy, yz) - 8Dq = F_0 - 5F_2 - 24F_4 - 8Dq \qquad (3.14)$$

and the energy of the first $^3T_2$ excited state is (representative orbital $\varphi_1=|(xy)(z^2)|$),

$$E(^3T_2) = J(xy, z^2) - K(xy, z^2) + 2Dq = F_0 - 8F_2 - 9F_4 + 2Dq \qquad (3.15)$$

and a transition energy of

$$\Delta E = 10Dq - 3F_2 + 15F_4 \qquad (3.16)$$

The $Dq$ terms are the crystal field stabilisation and are the same for all states arising from the same $(t_2)^n(e)^m$ state. The remaining terms are the electron repulsion energies, which split the states arising from the same $(t_2)^n(e)^m$ configuration, and are expressed in terms of the atomic Condon-Shortley-Slater parameters $F_2$ and $F_4$ [2, 11] (or Racah's $B$ and $C$, which are linear combinations of $F_2$ and $F_4$ ). No energy difference depends on the parameter $F_0$, this was mentioned in section 3.2 where it was pointed out that the $l$=0 term in the expansion of the crystal field shifted all states equally, in the approximation that the orbitals considered are pure d-orbitals. The singlet terms are found to be at a higher energy, as they have greater electron-electron repulsion energy. Values for $F_2$ and $F_4$ can be obtained from the spectra of free ions [12, 13].

### 3.2.2.3 Intermediate Fields.

Often the real situation does not correspond to one of the extremes above, but is somewhere in-between. In this case, the method used is similar, couched in the language of one of the methods above, but additional states must be considered that were previously neglected. For instance, in the weak field calculation of a $d^2$ electronic configuration, the states derived from the $^3P$ atomic state were ignored because the atomic term splittings were taken to be very large. Including this state,

the energy of the ground $^3T_1$ state moves smoothly from the weak field limit to the strong field limit, as size of *Dq* increases relative to the energy splitting $^3F - {}^3P$. The same result can be found starting from the strong-field limit, and including states coming from other $(t_2)^n(e)^m$ configurations; this approach includes configuration interaction with states previously ignored, because their energies were considered to be much higher than the states being examined.

### 3.2.2.4 Low-spin versus High-Spin complexes.

It is found that the weak and strong field paradigms predict the same ground states, except for $d^4$, $d^5$, $d^6$ and $d^7$ (for an octahedral crystal field - $d^3$, $d^4$, $d^5$ and $d^6$ in a tetrahedral environment). When the two approaches predict different ground states, there is an energetic competition between minimising the electronic repulsion (which favours states with high spin multiplicity) or maximising the crystal field stabilisation energy (where the maximum number of electrons are placed in the orbitals of lowest energy).

The conditions for favouring either high or low spin can be seen in Table 3.1. For the low spin case to be found, the gain in crystal field stabilisation energy must be much larger than the increase in electron-repulsion energy. For instance, for a $d^6$ configuration, the low spin case will be found when $20\ Dq >> 5F_2 + 255F_4$.

| Atomic configuration | Strong field ground state | Gain in crystal field stabilisation energy | Weak field ground state | Reduction in electron repulsion energy |
|---|---|---|---|---|
| $d^4$ | $^3T_1$ | 10 Dq | $^5E$ | $6F_2+145F_4$ |
| $d^5$ | $^2T_2$ | 20 Dq | $^6A_1$ | $15F_2+275F_4$ |
| $d^6$ | $^1A_1$ | 20 Dq | $^5T_2$ | $5F_2+255F_4$ |
| $d^7$ | $^2E$ | 12 Dq | $^4T_1$ | $7F_2+105F_4$ |

**Table 3.1.** The values of the competing energies, and the predicted ground states for a transition metal ion in an octahedral crystal field.

When neither energy term dominates, the more complex intermediate field problem must be used to calculate the ground and excited states of the complex.

## 3.3 Ligand field theory.

Crystal field theory has been extremely successful in explaining the magnetic and optical properties of transition metal complexes. However, its physical model of the ligands affecting the transition metal ion by the electrostatic field they create is, in general, far from the truth. It is found that many of the predictions of crystal field theory still hold in a more realistic physical model, because they are based on symmetry arguments, which remain valid no matter the exact model used for the interaction of the ligands with the transition metal ion. However, the physical interpretation of the crystal field parameters needs reinterpretation.

The most direct proof that the crystal field theory is incorrect is the measurement of ligand hyperfine structure in EPR measurements of transition metal complexes (c.f. the identification of $Ni_s^-$ ). Crystal field theory does not consider the overlap of the transition metal d-orbitals with orbitals of the ligands, and hence the unpaired electron density is predicted to lie entirely on the metal. The EPR measurements necessitate rephrasing the content of crystal field theory in terms of molecular orbitals extending over at least the nearest neighbours to the metal (Van Vleck was considering this from a valence bond point of view as early as 1935![14]).

Ligand field theory is really a semi-empirical SCF method. However, it evolves naturally from the crystal field picture, and the crystal field method can be shown to be a limiting form of ligand field theory.

For a complex with closed shell(s) of valence orbitals, the energy of the *N*-valence orbitals, in atomic units, are found as solutions of

$$H_{VAL}\Psi(1,.....N) = E_{VAL}\Psi(1,.....N) \tag{3.17}$$

$$\text{where } H_{VAL} = \sum_{j=1}^{N} h_{core}(j) + \sum_{i<j}^{N} e^2 \Big/ r_{ij} \tag{3.18}$$

$$\text{and } h_{core}(1) = -\frac{1}{2}\nabla_1^2 - \sum_{M}\frac{Z_M}{r_{M1}} + \sum_{core}(2J_k - K_k) \tag{3.19}$$

*orbitals*

The terms in $h_{core}$ are the kinetic energy of the electron, the electrostatic energy of interaction with the nuclei and the repulsion caused by the core electrons.

The self-consistent field operator for the closed shells of valence orbitals is then,

$$F = h_{core}(1) + \sum_{j=1}^{N}\left(2J_j - K_j\right) \tag{3.20}$$

and

$$F\psi_j = \varepsilon_j\psi_j \tag{3.21}$$

Assuming that only overlap with the $L$ nearest neighbours is of importance, the wavefunctions for the bonding, $\psi_b$ (pure ligand orbitals in crystal field theory), and anti-bonding, $\psi_a$, (pure metal d-orbital in crystal field theory), can be taken to be

$$\psi_b = \chi_{L\gamma} \tag{3.22}$$

and

$$\psi_a = \frac{1}{\sqrt{1-G_\gamma^2}}\left(\chi_{M\gamma} - G_\gamma\chi_{L\gamma}\right) \tag{3.23}$$

where $\chi_{M\gamma}$ is the coefficient of the pure metal d-orbital, $\chi_{L\gamma} = \sum_{j=1}^{L} c_{j\gamma}\chi_j$ is a linear combination of the ligand orbitals transforming as the irreducible representation $\gamma$, and $G_\gamma = \langle\chi_{M\gamma}|\chi_{L\gamma}\rangle$ is termed the group-overlap integral. The group-overlap integral effectively defines the amount of covalency found in the complex: if $G_\gamma = 0$, then the anti-bonding orbital becomes pure metal d-orbital and the CFT limit is reached.

### *3.3.1 Origin of the 'crystal field splitting' in the ligand field model.*

It is assumed that $\psi_b$ and $\psi_a$ are good approximations to the Hartree-Fock orbitals of the metal complex. Then,

$$F\psi_a = w_a\psi_a \tag{3.24}$$

$$F\psi_b = w_b\psi_b \tag{3.25}$$

**Equation 3.25**

Substituting for $\psi_a$ in Equation 3.24 above and using equation 3.25 it is found that

$$F\chi_{M\gamma} + (w_{a\gamma} - w_{b\gamma})G_\gamma\chi_{L\gamma} = w_{a\gamma}\chi_{M\gamma} \tag{3.26}$$

Pre-multiplying by $\chi_{M\gamma}$, integrating, and then expanding in powers of $G_\gamma$ gives, correct to terms in $G_\gamma^2$,

$$w_{a\gamma} \approx (1 + G_\gamma^2)\langle\chi_{M\gamma}|F|\chi_{M\gamma}\rangle - w_{b\gamma}G_\gamma^2 \tag{3.27}$$

Taking the energy difference between the one-electron e and $t_2$ orbitals as $\Delta$, which for a one-electron system is

$$\Delta = w_a(e) - w_a(t_2) \approx (1 + G_e^2)\langle\chi_{Me}|F|\chi_{Me}\rangle - w_{be}G_e^2 - (1 + G_{t_2}^2)\langle\chi_{Mt_2}|F|\chi_{Mt_2}\rangle + w_{bt_2}G_{t_2}^2 \tag{3.28}$$

Assuming the energy of the ligand bonding orbitals to be little changed, $w_{be} \approx w_{bt_2} = w_b$, and expanding the integrals

$$\Delta \approx (G_e^2 - G_{t_2}^2)T_{KINETIC}(d) - (G_e^2 - G_{t_2}^2)w_b \tag{3.29}$$

where $T_{KINETIC}(d)$ is the kinetic energy of an electron in a metal d-orbital. In an octahedral complex $G_e$ is likely to be larger than $G_t$, as the metal and ligand e-orbitals have much better overlap than those of $t_2$ symmetry (see section 3.2.1). For an octahedral complex $\Delta$ is expected to be positive and from Equation 3.29 it can be seen it is the change in kinetic energy between the 'metal orbitals' that principally causes the energy shift. Furthermore, it is the Pauli-repulsion of the closed shell ligand orbitals that forces the metal orbitals orthogonal to the ligand orbitals, and governs the value of $\Delta$.

Put less mathematically, the form of the orthogonalised metal orbitals $\chi_M - G\chi_L$ creates a nodal plane between the metal and the ligands. The larger the overlap integral, the larger the gradient of the wavefunction at the nodal surface, and consequently the larger the kinetic energy of the electron. Hence, the better the overlap between the metal and ligands, the higher the energy of the anti-bonding orbital because of its increased kinetic energy.

### *3.3.2 Returning to the CF point of view.*

When $G_e=G_t=0$, from (3.23) the anti-bonding orbitals revert to being pure metal d-orbitals. Then for a single electron (3.27) gives

$$w_e - w_{t_2} = \langle \chi_{Me} | h_{core} | \chi_{Me} \rangle - \langle \chi_{Mt_2} | h_{core} | \chi_{Mt_2} \rangle = 10Dq \qquad (3.30)$$

And, following the derivation of section 3.2.2.1, it is also found that,

$$4\langle \chi_{Me} | h_{core} | \chi_{Me} \rangle + 6\langle \chi_{Mt_2} | h_{core} | \chi_{Mt_2} \rangle = 0 \qquad (3.31)$$

Then, if an effective one-electron Fock operator, $F$, gives $F\chi_M=E\chi_M$, the crystal field theory is re-established. This definition in terms of a Fock operator being entirely equivalent to the strong field limit described in section 3.2.2.2

Returning to the $d^2$ configuration used for the strong field example,

$$E_{T_2} - E_{T_1} = \left[h_{core}(e) + h_{core}(t_2) + J_{xy,z^2} - K_{xy,z^2}\right] - \left[2h_{core}(t_2) + J_{xy,yz} - K_{xy,yz}\right] \qquad (3.32)$$
$$= \Delta - 3F_2 + 15F_4$$

as found from the crystal field method.

Note that this means that the one-electron energies used in crystal field theory are not the same as those found from SCF methods; conventional crystal field diagrams use the one electron orbital energies given by $h_{core}$ whilst SCF calculations give one electron energies that include average electron-repulsion terms. The two quantities are linked by (3.18), in which many electron-repulsion terms appear. This means that the crystal-field energy level ordering does not necessarily coincide with the SCF orbitals.

### *3.3.3 Comparison of ligand field and crystal field theory.*

In crystal field theory many of the optical transition energies can be directly associated with a parameter in the theory. For instance, a $d^3$ atom has a $^4A_2$ ($\left|\psi_{xy}^{\alpha}\psi_{yz}^{\alpha}\psi_{zx}^{\alpha}\right|$) ground state, with a $^4T_2$ excited state $\left|\psi_{yz}^{\alpha}\psi_{zx}^{\alpha}\psi_{x^2-y^2}^{\alpha}\right|$ at an energy,

$$W_{T_2} - w_{A_2} = \Delta + 2J_{xz-x^2-y^2} - 2K_{xz-x^2-y^2} - 2J_{yz,zx} + 2K_{yz,zx} = \Delta \qquad (3.33)$$

In the crystal field approximation the sum of atomic electron repulsion integrals is zero, and the energy transition can be directly related to Δ. The major weakness of ligand field theory is that in general it introduces too many parameters. The electron repulsion integrals cannot be evaluated as easily when the wavefunctions are not pure metal orbitals and the electron-repulsion terms in Equation 3.33 do not cancel. When the complex's wavefunctions have the form of Equation 3.22 and 3.23, then the two electron integrals can be expanded. For example, correct to second order in *G*,

$$K_{xz,yz} = (1 - G_{t_2}^2)K_{xz,yz}^{ATOMIC} \qquad (3.34)$$

Similar equations hold for the other electron-repulsion integrals. The dependence on *G* increases the number of parameters: in $O_h$ there are 10 independent two-electron integrals. The main problem is that transition energies become dependent on $F_0$ through terms like $(G_{t_2}^2 - G_e^2)F_0$. As the parameters in the first transition series are of the order $F_0 \approx 25$ eV, $F_2 \approx 250$ meV, and $F_4 \approx 25$ meV, the term involving $F_0$ dominates and the crystal field definition of Δ does not apply.

A further point that affects the interpretation of HF calculations is that the one electron energies of the ligand orbitals change from one many-electron state to another. The general form of the bonding and anti-bonding orbitals is,

$$\psi_a = N_a(\chi_M - \lambda_a\chi_L) \qquad (3.35)$$

and

$$\psi_b = N_b(\chi_L - \lambda_b\chi_M) \qquad (3.36)$$

The requirement of orthogonality then provides a link between the parameters in the wavefunctions

$$G - \lambda_a + \lambda_b - \lambda_a \lambda_b G = 0 \tag{3.37}$$

This connection between the coefficients of the ligand and 'metal' molecular orbitals means that the core orbitals change in the different many-electron states of the valence orbitals, this makes interpretation of HF calculations more complicated.

The main problem with ligand-field theory is that it introduces too many parameters, almost invariably more than can be deduced unambiguously from experiment. Ligand-field theory reduces to Crystal-field theory in the limit that overlap between the ligand and metal orbitals is zero, this allows much of the theory of atomic spectra to be applied directly to the problem and reduces the number of parameters required to three; for these reasons crystal-field theory is still commonly used. It is known that the physical approximations used are not reasonable, but the results of crystal field calculations can be interpreted using ligand field theory to explain the values of parameters e.g. the electron repulsion terms $F_n$ are all reduced from atomic values because of covalent bonding. In summary, crystal field theory is used because of its simplicity and ability to treat excited states, but the empirical crystal field parameters found by fitting to experimental data must be interpreted with care, using a more rigorous physical model.

## 3.4 Crystal field picture of TM defects in diamond.

In this thesis transition metals will be examined in three fundamental crystalline environments: as substitutional atoms, where the transition metal replaces a carbon atom in the diamond structure, as interstitial atoms, where the transition metal occupies a tetrahedral-site in the diamond crystal and in semivacancy sites, where the TM is situated midway between the sites previously occupied by two carbon atoms that have been removed from the crystal. In the first two environments the TM has tetrahedral symmetry, whilst the semivacancy site belongs to the $D_{3d}$ point group. In this section a brief description of the crystal field model of these complexes is given. The next chapter gives a full review of the experimental systems observed, along with their interpretation.

### *3.4.1 Interstitial transition metals.*

Interstitial transition metal defects, $TM_i$, occupy tetrahedral sites in the diamond lattice. The transition metal has four carbon nearest neighbours arranged in a tetrahedron and six next nearest neighbours that form an octahedron. From section 3.2.1, it is to be expected that the nearest and next-nearest neighbours will produce crystal fields of opposite signs at the transition metal.

From ligand field theory, it is known that the extent of the crystal splitting depends on the difference in overlap between the different metal d-orbitals and the ligand molecular orbitals. This means that the sign of the overall crystal field depends strongly on the relative distances of the nearest and next-nearest neighbours – this can also be seen from Equation 3.9. Equation 3.9 also shows that the octahedral field is almost twice as strong as a crystal field, if the ligands are at the same distance from the metal. Therefore, it is expected that the interstitial transition metal defects will behave as if experiencing a net octahedral crystal field, as long as the nearest and next-nearest neighbours are at a similar distance from the transition metal. This has been confirmed experimentally for $Ni_i^+$, whose optical transitions are fitted assuming a slightly distorted octahedral field is generated by the ligands [15]. Previous calculations [16,17] suggest that when the diamond relaxes to its equilibrium geometry, the distance from the TM to the two sets of ligands differ by around 10% (1.84 and 2.00 Angstroms [16]). Calculations in this thesis found values of 1.73 and 1.96 Angstroms.

An octahedral crystal field splits the metal's d-electrons into two sets of orbitals, of $t_2$ and e symmetry, as shown in figure 1 above. These orbitals are then filled with the electrons which occupy 4s and 3d orbitals in the atomic metal e.g. for $Ni_i^0$ the atomic metal has the electronic configuration $(4s)^2(3d)^8$ and ten electrons are placed in the cluster's $t_2$ and e orbitals, completely filling them in this case. The many-electron states are then found using crystal or ligand field theory as detailed in sections 3.2 and 3.3.

### *3.4.2 Substitutional transition metal defects.*

Substitutional transition metals, $TM_s$, replace a single carbon atom in the lattice, and are hence strongly bonded into the crystal. The four nearest neighbour carbons are arranged in a tetrahedron and, therefore, cause a tetrahedral crystal field at the transition metal. The effect of a tetrahedral field is shown in Figure 3.1 above. There is a complication in this case, however, the nearest neighbour carbons can be viewed as having a single $sp^3$ hybridised orbital pointing toward the transition metal, which are formed when the TM disrupts the bonding in the crystal. These dangling bonds are at high energies, within the band gap of diamond, and similar in energy to the transition metal's d-orbitals. Two different descriptions of the bonding at substitutional sites have emerged.

*Ludwig-Woodbury model* [18]. This model is consistent with the ideas of crystal field theory discussed above, the dangling bond orbitals form low energy bonding molecular orbitals of $a_1$ and $t_2$ symmetry, similar to the bonding in methane. As each dangling bond contributes one electron, the metal contributes a further four to fill these levels. The metal d-orbitals are at a higher energy, and the remaining valence electrons occupy these levels. The metal orbitals are spilt as expected by the tetrahedral field from the ligands, and crystal field theory can be used to determine the many-electron states found.

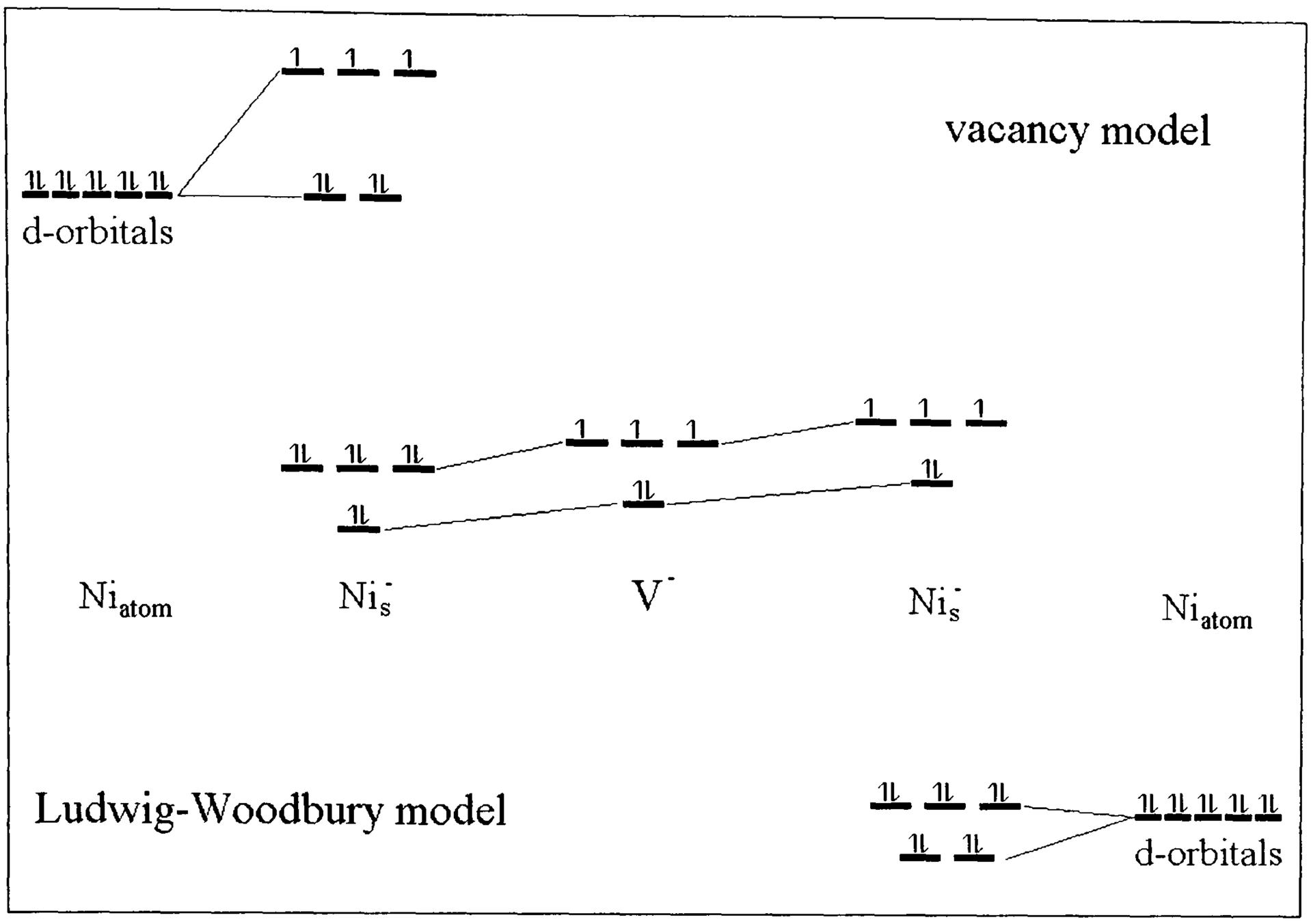


**Figure 3.2.** A schematic MO diagram showing the MOs of $Ni_s^-$. The left-hand side of the diagram shows the LW model, with the metal 3d orbitals higher in energy than those derived from the vacancy. The right hand side of the diagram shows the electronic configuration if the vacancy model applied to this centre.

*The vacancy model*[19]. This model assumes the opposite orbital ordering to that of Ludwig and Woodbury. The metal orbitals are assumed to be of low energy, and fully occupied, the remaining electrons go into the dangling bond orbitals. For example, the vacancy model of $Ni_s^-$ has ten valence electrons from the metal, four from the dangling bonds and one from the charge state; ten electrons fill the metal d-orbitals, the remaining five fill the vacancy orbitals.

This model predicts that the valence orbitals will be predominantly centred on the carbon nearest-neighbours and, clearly, applying straight crystal field theory will be a very poor approximation here.

### *3.4.3 Semivacancy transition metal defects.*

In a semivacancy environment, the transition metal is surrounded by a nearly octahedral array of carbon atoms. Each of the six nearest neighbour atoms contributes a dangling bond and an electron, in a similar way to the substitutional defects.

The situation is very similar to the substitutional TM defects: either the TM d-orbitals are high in energy and all the dangling bonds are filled by the transfer of six electrons from the TM, or the dangling bonds lie higher in energy. If the dangling bonds are highest in energy the TM d-orbitals will be filled, then remaining electrons will fill the dangling bonds. In this case the dangling bonds will not resemble the vacancy but the divacancy. Figure 3.3 shows schematic MO diagrams of these bonding schemes, comparison with Figure 3.2 shows the similarity to the bonding in $TM_s$ defects.

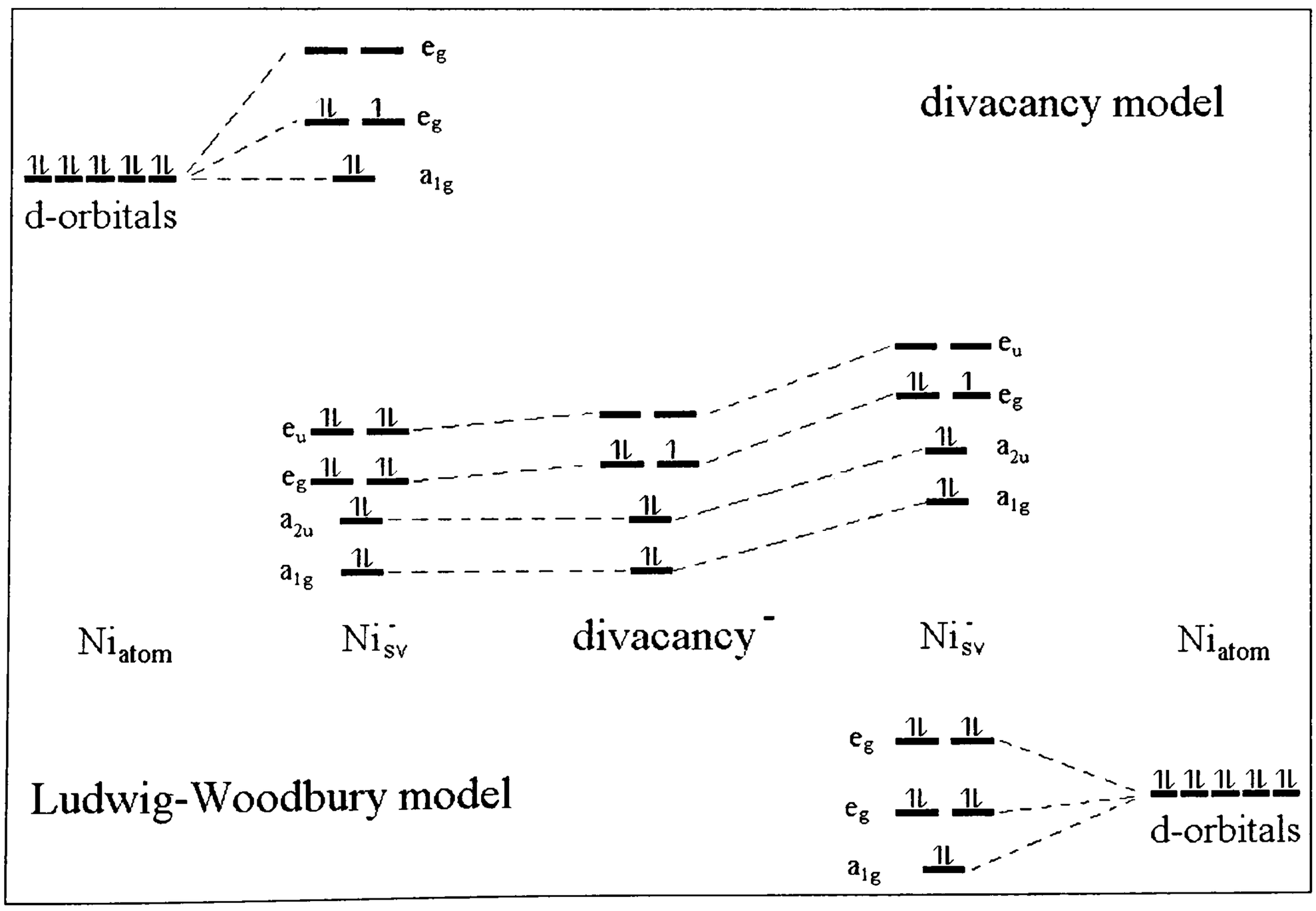


**Figure 3.3.** Schematic MO diagram showing the MOs of $Ni_{sv}^-$. The left-hand side of the diagram shows the LW model, with the metal 3d orbitals higher in energy than

those derived from the divacancy. The right hand side of the diagram shows the electronic configuration if the divacancy model applied to this centre.

## 3.5 Summary

In this chapter, the crystal and ligand field methods have been detailed. These methods produce a simple molecular orbital model that can be used for the interpretation of transition metal defects. Almost all of the later work in this thesis is described in the language of this chapter.

A very important point is that ligand field theory can be viewed as a particular parameterisation of the Hartree-Fock method and, furthermore, that crystal field theory is a limiting case of ligand field theory. This provides a link between the common interpretations of experimental data (chapter 5) and the results of the *ab initio* calculations conducted later (chapter 6). This connection is spelt out in section 3.3.2, and Equation 3.18 gives a semi-quantitative measure of how the one-electron orbitals of strong-field crystal field theory differ from those derived from HF calculations.

The crystal field models for the main TM defects are also described. The Ludwig-Woodbury and (di)vacancy models of $TM_s$ and $TM_{sv}$ centres will be encountered frequently later.

## References


1 J Becquerel, Z Phyzik, **58**, 205 (1929)

2 E U Condon and G H Shortley, *Theory of atomic spectra*, (Cambridge University Press, Cambridge and New York, 1935)

3 R Schlapp and W G Penny, Phys. Rev, **42**, 666 (1932)

4 A M Stoneham, *Theory of Defects in Solids*, OUP, 1975

5 J H Van Vleck, J. Chem. Phys., **7**, 72 (1939).

6 H Bethe , H., Ann. Physick., **133** (1929.)

[7] D Polder, Physica, **9**, 709 (1942).

[8] Y Tanabe and S Sugano, J. Proc. Soc. (Japan), **11**, 864 (1956).

[9] H S Jarrett, J. Chem. Phys., **31**, 1579 (1959)

[10] R E Watson and H J Freeman, Phys. Rev., **134**, A1526, (1964)

[11] C J Ballhausen, *Introduction to Ligand Field Theory*, McGraw-Hill, 1962.

[12] L E Orgel, J. Chem. Phys, **23**, 1819 (1955)

[13] D A Brown, J. Chem. Phys, **28**, 67 (1958)

[14] J H Van Vleck, J. Chem. Phys., **3**, 803 (1935).

[15] P W Mason, F S Ham, G D Watkins, Phys. Rev. B, **60** 8 (1999) 5417

[16] J P Goss, PhD thesis: Exeter University, 1997

[17] K A A Johnston and A Mainwood, Physica B, **273-274**, 647 (2000)

[18] G W Ludwig and H H Woodbury, Solid State Physics **13**,223 (1962)

[19] G D Watkins, Physica B + C, **117B-118B,** 9 (1983)

# Chapter 4.

# Spin-Orbit Coupling in Uniaxial stress experiments.

## 4.1 Introduction.

The application of an external perturbation to gain additional information about a system is completely general, and has been extensively used in many areas of scientific study. The most commonly applied perturbations are magnetic fields (Zeeman effect) and electric fields (Stark effect). Another possible perturbation is applied pressure or stress, which can be applied to liquid or solid samples. Like the better known Zeeman and Stark effects it lowers the symmetry at the sample and causes changes to electronic spectra. In molecular solids such as transition metal complexes the applied stress can cause a host of effects, acting intramolecularly (in a manner similar to that explained in detail later) perturbing the molecules that are bound together to form the crystal and intermolecularly – changing the way the molecules are packed together to form the crystal, possibly introducing conformational changes in the molecules (piezochromism) [1]. In extended ionic or covalent crystals the magnitude of the applied pressure is, generally, less extreme and, as the crystals tend to be less compressible, the perturbation at a given centre tends to be smaller. When looking at isolated defects in such a substrate (uniaxial stress) the similarity to Zeeman or Stark effects is more pronounced, the main effect of the stress being to lower the symmetry of the defect centre, causing optical lines to split and possibly inducing previously forbidden transitions by interaction between energy levels.

Uniaxial stress is a powerful, well established technique, which gives information on the symmetry of energy levels involved in optical transitions[2-6], helping to provide information on a wide range of defects. Applied stress lifts the equivalence of different axes in the crystal, causing previously degenerate energy levels to split in energy. Two types of degeneracy can be removed: that arising from different orientations of centres in the crystal [2] and electronic degeneracy [3-6].

## Spin-Orbit Coupling in Uniaxial stress experiments.

The magnitude of the splittings caused by the applied stress are observed to be of the order 5 meV / GPa in diamond, with pressures of up to approximately 3 GPa being applied. This is sufficiently large to allow the splittings to be clearly resolved in favourable cases. Relatively small pressures are used to simplify later analysis, as in this regime the energy shifts of electronic states tend to be linear with the applied stress (With some diamond anvil cells (DACs) it would be relatively routine to reach pressures of around 25 GPa [1]). The number of lines induced by the stress, and the relative intensities of the different components give enough information to determine the point group of the defect and determine the symmetry species of the energy levels involved in the transition. This greatly aids building a molecular model of the defect examined.

Knowing the point group of a defect is, of course, insufficient to characterise it fully. Additional information, such as the growth conditions of the diamond, is used to augment any information gleaned from uniaxial stress measurements. Several transitions that are suspected of occurring at a TM centre in diamond have proved very hard to characterise with uniaxial stress, with numbers of lines and intensities not fitting any of the expected patterns. Attempts to explain these experiments have been made, with varying degrees of success (such as assuming defects are not homogeneously orientated in the crystal [7]). Here we investigate whether spin-orbital coupling could provide an explanation for the inexplicable uniaxial stress results, give a general treatment of spin-orbital coupling in uniaxial stress measurements at a tetrahedral defect and examine the regimes in which the model will be valid.

Recent studies have observed the effect of spin-orbit coupling upon two transition metal centres in diamond, both nickel related: $Ni_i^+$ at 1.4 eV [8, 9] and $Ni_s^-$ at 2.51 eV[10]. Spin-orbit coupling adds extra structure to their spectra, and the effect of spin-orbit coupling was needed to explain the uniaxial stress data in references 8 and 10. The energy differences due to spin-orbit coupling are observed to be of the same order as the stress perturbation [8-10] - spin–orbit coupling may cause a perturbation of similar magnitude to the stress terms, and in general should be considered[11].

We will specifically be examining transition metal centres in diamond that exhibit very high symmetry, though the theory applies generally to uniaxial stress applied to high symmetry defects. Transition metal centres are expected to exhibit sizeable spin-orbit splittings due to their large mass - spin-orbit coupling increases approximately as the atomic number to the fourth power.

## 4.2 Spin-Orbit coupling in optical Spectroscopy.

The spin-orbit interaction is a relativistic effect, which couples the orbital magnetic moment of an electron to the magnetic moment arising from its intrinsic spin. In a many electron atom/ion this generalises to coupling the total orbital angular momentum, **L**, to the total spin, **S**. The energy of the state produced depends upon the total angular momentum, **J**, produced by the spin-orbit coupling. The size of the energy splittings produced depends upon $\lambda$, the spin orbit coupling constant. This increases approximately as the atomic number to the fourth power.

When an atom/ion is placed into a crystal lattice, its symmetry is reduced and its orbital angular momentum tends to be removed (quenched): at least threefold degeneracy is needed to carry angular momentum. However, states of three-fold degeneracy are observed to still carry **L**=1. Thus, spin-orbit coupling is expected to be observed at tetrahedral TM centres when either the ground or excited state is triply degenerate.

### *4.2.1 Derivation of the spin-orbit coupling Hamiltonian*

Spin-Orbit coupling is a relativistic phenomenon [12], however, its approximate form, within a non-relativistic quantum mechanical framework, can be seen in this derivation.

A particle of charge –e, velocity **v**, in an electric field **E**, experiences a magnetic field

## Spin-Orbit Coupling in Uniaxial stress experiments.

$$\mathbf{B} = \frac{\mathbf{E} \times \mathbf{v}}{c^2} \tag{4.1}$$

The first major assumption is that around an atom, even if part of a crystal, there is an electric potential $\phi(\mathbf{r})$. That is that the atom's electrons are spherically distributed. The electric field near the nuclei is given by, $\mathbf{E} = -\frac{\mathbf{r}}{r}\frac{d\phi}{dr}$ and it then follows that

$$\mathbf{B} = -\frac{1}{rc^2}\frac{d\phi}{dr}\mathbf{r} \times \mathbf{v} \tag{4.2}$$

This can be rewritten using the definition of an orbital momentum, $\mathbf{l} = \mathbf{r} \times \mathbf{p} = m_e \mathbf{r} \times \mathbf{v}$

$$\mathbf{B} = -\frac{1}{m_e rc^2}\frac{d\phi}{dr}\mathbf{l} \tag{4.3}$$

The Hamiltonian for the interaction is the scalar product of the magnetic moment of the electron, **m**, and the magnetic field, **B**,

$$\mathbf{H}_{SO} = -\mathbf{m}.\mathbf{B} = \frac{1}{m_e rc^2}\frac{d\phi}{dr}\mathbf{m}.\mathbf{l} = -\frac{e}{2m_e rc^2}\frac{d\phi}{dr}\mathbf{s}.\mathbf{l} \tag{4.4}$$

The factor of a half is due to a relativistic phenomenon called the Thomas precession – in hand waving terms the electron 'spins round its own axis' thus affecting the magnetic field produced [13].

The general form of the atomic spin-orbit Hamiltonian is then

$$\mathbf{H}_{SO} = \xi(r)\mathbf{l}.\mathbf{s} \tag{4.5}$$

or equivalently in terms of the raising and lowering angular momentum operators

$$\mathbf{H}_{SO} = \xi(r)[l_z s_z + \tfrac{1}{2}(l_+ s_- + l_- s_=)] \tag{4.6}$$

In a molecule with $N$ nuclei and $n$ electrons, the spin-orbit coupling can be written as the sum of $N$ spherical potentials centred at the nuclei

$$\mathbf{H}_{SO} = \sum_i^N \sum_j^n \xi_i(r)\mathbf{l}_{ij}.\mathbf{s}_j = \lambda(r)\mathbf{L}.\mathbf{S} = \lambda(r)\left[L_z S_z + 1/2(L_+ S_- + L_- S_=)\right] \tag{4.7}$$

Equation 4.7 shows that for a many electron state the sums over the different nuclei can be collected into a single parameter, $\lambda(r)$, which contains all the information about the radial dependence of the spin-orbit coupling. The method of connecting the molecular state spin-orbit parameter and the atomic coupling terms is outlined in section 4.2.5.

### *4.2.2 Size of the atomic Spin-Orbit interaction.*

In general, as the derivation is so rough, only expected to be accurate within an order of magnitude, $\xi(r)$ is taken as an experimental parameter. Its approximate behaviour can be seen in the case of a hydrogen-like atom. Taking a Coulombic potential, $\phi = \frac{Ze}{4\pi\varepsilon_0 r}$

$$\xi = \frac{Ze^2}{8\pi\varepsilon_0 m_e^2 c^2 \langle r^3 \rangle} \tag{4.8}$$

For a hydrogenic orbital, with quantum numbers $n$, $l$, $m_l$, $\langle r^3 \rangle = \frac{Z^3}{n^3 a_0^3 l(l+\frac{1}{2})(l+1)}$.

Then using the fine structure constant $\alpha = \frac{e^2}{4\pi\varepsilon_0 \hbar c}$ and Rydberg's constant $R$

$$\xi_{nl} = \frac{\alpha^2 R Z^4}{n^3 l(l+\frac{1}{2})(l+1)} \tag{4.9}$$

This gives a value of $\approx$0.2cm$^{-1}$ for Hydrogen, and scaling by $Z^4$, 80 cm$^{-1}$ for Nickel, which is about 10 meV. This gives an indication of the size of the additional structure that spin-orbit coupling will produce in optical spectra. From atomic and ionic spectra $\xi$ is found to be of the order 50 meV for first row transition metals. However, there are two reasons why the observed size of $\lambda$ may be quite different:

i) Covalent bonding. The above value of $\lambda$ is for an electron centred upon the transition metal. Covalent bonding to carbon ligands transfers electron density to neighbouring carbon atoms, which have $\xi \approx 3.6$ meV. In fact some calculations suggest that the valence orbitals, which carry the orbital angular momentum, are very carbon-like (i.e. TM defects that approximate well to the vacancy model – see chapter 3) and $\lambda$ would be expected to be nearer to the carbon value than that of the TM.

ii) The Jahn-Teller 'effect' (JTE) [14]. Orbitally degenerate electronic states are subject to distortions that lower their symmetry, either permanently distorting (static JTE) or dynamically moving between several minima (dynamic JTE). This gives rise to the Ham effect [15], which can reduce the effect of spin-orbit coupling by up to two orders

of magnitude (this has been invoked to explain the small first order spin-orbit coupling in $Ni_s^-$ (Ref 10)).

The size of the above effects is hard to estimate in general and hence it is very difficult to assess the magnitude of $\lambda$ *a priori*.

### *4.2.3 Symmetry arguments.*

There are two ways of looking at the problem, either using the full symmetry classification of the double group, which classifies the whole wavefunction's symmetry – including the spin, or just the orbital part of the wave function in the point group of the complex can be examined, this is often sufficient.

In the double group we need to examine the symmetry of the spin-orbit operator. This is easily seen to be totally symmetric, **L** and **S** both having the same symmetry properties. We can then see that matrix elements will only be non-zero if the two states involved have the same symmetry within the double group.

Alternatively we can just look at the orbital part of the wavefunction, and the only part of the spin-orbit operator that effects this is **L.** Since the spin operators $S_x$, $S_y$, $S_z$, transform as $T_1$ in Td symmetry, to make the spin-orbit coupling operator totally symmetric **L** will transform as the same irreducible representation, $T_1$. Then first order spin-obit coupling will only produce non-zero coupling terms between states whose symmetric direct product contains $T_1$; first order spin-orbit coupling is only expected within T states. As a first approximation the effect of spin-orbit coupling can be ignored within states of single or double degeneracy – an exception to this is the $d^7$ case described by Nazare et al [10], where the spin-orbit coupling transfers intensity into a forbidden transition.

### *4.2.4 Cases considered*

From symmetry considerations (section 4.2.3), first order spin-orbit coupling is only expected within states of T symmetry. In this work it is assumed that coupling between different many-electron states can be neglected, as energy levels are far apart compared to the size of the spin-orbit coupling - energy differences between many-

electron states are of the order 1-10 eV, whilst the spin-orbit coupling parameter is around 10-100 meV. This means that corrections to the wavefunction will be only about 1%, and the corresponding intensities will change only by a similar amount. These effects can be significant where the transition is forbidden to a first approximation [10] and make noticeable differences to EPR spectra, but will not be significant to allowed optical transitions. Because configuration interaction between different multiplets can be ignored the approximation below (section 4.2.5) can be made.

### *4.2.5 Fictitious angular momentum.*

Solving the full spin-orbit problem is immensely complex; the number of states that must be considered for $d^3$-$d^7$ configurations makes the problem ridiculously cumbersome. Also, in the next section (4.2.6) the effects of an external applied stress will also be included and so approximations must be made. A symmetry based equivalence of atomic p-orbitals and molecular $t_i$ orbitals [16.17.18] will be utilised to make the calculations feasible [19 20 21].

The equivalence of atomic p-orbitals and molecular $t_i$ orbitals is based on their common behaviour under the application of the orbital angular momentum operators $\mathbf{l}_z$, $\mathbf{l}_+$, $\mathbf{l}_-$. To illustrate this behaviour two set of functions are examined, a set of p-orbitals diagonal with respect to $\mathbf{l}_z$, $|p,m_l\rangle$ and a set of functions transforming as $T_2$ in $O_h$ symmetry, $|t,+1\rangle$, $|t,0\rangle$ and $|t,-1\rangle$ *. Then the operation of the angular momenta operators on the two basis sets, providing the operation on the $t_2$ orbitals stays within the three t-basis-functions, can be seen to be isomorphic.

$$l_+\begin{pmatrix}|p,1\rangle\\|p,0\rangle\\|p,-1\rangle\end{pmatrix}=1\begin{pmatrix}0&0&0\\\sqrt{2}&0&0\\0&\sqrt{2}&0\end{pmatrix}\begin{pmatrix}|p,1\rangle\\|p,0\rangle\\|p,-1\rangle\end{pmatrix},\quad l_+\begin{pmatrix}|t,1\rangle\\|t,0\rangle\\|t,-1\rangle\end{pmatrix}=-1\begin{pmatrix}0&0&0\\\sqrt{2}&0&0\\0&\sqrt{2}&0\end{pmatrix}\begin{pmatrix}|t,1\rangle\\|t,0\rangle\\|t,-1\rangle\end{pmatrix}$$

---

* $\left(|t,\pm1\rangle=\mp\frac{1}{\sqrt{2}}\left(d_{yz}\pm id_{zx}\right),|t,0\rangle=d_{xy}\right)$

$$l_{-}\begin{pmatrix}|p,1\rangle\\|p,0\rangle\\|p,-1\rangle\end{pmatrix}=1\begin{pmatrix}0&\sqrt{2}&0\\0&0&\sqrt{2}\\0&0&0\end{pmatrix}\begin{pmatrix}|p,1\rangle\\|p,0\rangle\\|p,-1\rangle\end{pmatrix},\quad l_{-}\begin{pmatrix}|t,1\rangle\\|t,0\rangle\\|t,-1\rangle\end{pmatrix}=-1\begin{pmatrix}0&\sqrt{2}&0\\0&0&\sqrt{2}\\0&0&0\end{pmatrix}\begin{pmatrix}|t,1\rangle\\|t,0\rangle\\|t,-1\rangle\end{pmatrix}$$

$$l_{z}\begin{pmatrix}|p,1\rangle\\|p,0\rangle\\|p,-1\rangle\end{pmatrix}=1\begin{pmatrix}1&0&0\\0&0&0\\0&0&-1\end{pmatrix}\begin{pmatrix}|p,1\rangle\\|p,0\rangle\\|p,-1\rangle\end{pmatrix},\qquad l_{z}\begin{pmatrix}|t,1\rangle\\|t,0\rangle\\|t,-1\rangle\end{pmatrix}=-1\begin{pmatrix}1&0&0\\0&0&0\\0&0&-1\end{pmatrix}\begin{pmatrix}|t,1\rangle\\|t,0\rangle\\|t,-1\rangle\end{pmatrix}$$

(4.10)

The functions transform in exactly the same way, apart from a constant factor of –1. This same symmetry relation holds for any explicit form of the t orbitals, but the proportionality factor, $\alpha$, changes depending on the exact form of the basis states [22] - T states behave like atomic p-terms and can be characterised by a fictitious angular momentum operator $\mathbf{L}^{f}$=1, but with a constant of proportionality, $\alpha$, that depends on the exact state described (see below). Another advantage is that $J^{f}_{z} = L^{f}_{z} + S_{z}$ is a good quantum number.

In general this will leave accidental degeneracy within the T state, as configuration interaction with other states has been ignored. The validity of ignoring these other states was argued in section 4.2.4. In crystal field theory, where the valence orbitals are pure metal d-orbital the connection between the state spin-orbit parameters, $\alpha\lambda$, and the atomic coupling parameters, $\xi_i$, can easily be deduced. For instance, one sublevel of the $^4T_2$ excited state of $Ni_s^-$ has an electronic configuration, within the LW model, $\left|t_{+1}^{+}t_{0}^{+}t_{-1}^{+}t_{-1}^{-}e_{\theta}^{+}e_{\theta}^{-}e_{\varepsilon}^{+}\right|$ where the subscript for the t orbitals indicates the value of $l^{f}_{z}$ and the superscript indicates the spin-function (spin-up +, spin-down -). This state can also be written $\left|1,\tfrac{3}{2}\right\rangle$ labelled by $L^{f}_{z}$ and $S_z$ as indicated above.

Equation 4.7 can then be used to obtain a value of $\alpha\lambda$ in terms of the atomic spin-orbit coupling parameter for nickel, $\xi_{Ni}$ (the state $\left|1,\frac{3}{2}\right\rangle$ is used because having maximum $L^{f}_{z}$ and $S_z$ only the $\mathbf{L}^{f}_{z}\mathbf{S}_z$ term of the Hamiltonian is non zero).

$$\sum_{n=1}^{7}\xi_{Ni}l_{zn}s_{zn}\left|t_+^+t_0^+t_-^+t_-^-e_\theta^+e_\theta^-e_\varepsilon^+\right| = \alpha\lambda L_z^f S_z\left|1,\tfrac{3}{2}\right\rangle \qquad (4.11)$$

$$\tfrac{1}{2}\xi_{Ni} = \tfrac{3}{2}\alpha\lambda$$

and finally the spin-orbit coupling Hamiltonian for the crystal-field $^4T_2$ excited state can be written as

$$H_{SO} = \frac{1}{3}\xi_{Ni}\left(L_z^f S_z + L_+^f S_- + L_-^f S_+\right) \qquad (4.12)$$

As ever, the evaluation of the left-hand side of Equation 4.11 is much harder when ligand field theory is used and the wavefunction contains some vacancy-like character. Given the approximations in deriving the expression for the first-order spin-orbit coupling, $\alpha\lambda$ is best left as an experimental parameter if a detailed knowledge of the system examined is not possessed. It is only the evaluation in terms of the atomic spin-orbit coupling coefficient that depends on the exact form of the T state, the fictitious angular momentum formulation is completely general.

### *4.2.6 Matrix elements within a T state.*

A general angular momentum operator has matrix elements of the form

$$\left\langle J,m_J\left|J_Z\right|J',m_J'\right\rangle = m_J\delta_{JJ'}\delta_{m_Jm_J'}$$

$$\left\langle J,m_J\pm1\left|J_\pm\right|J,m_J\right\rangle = \sqrt{(J\pm m_J+1)(J\mp m_J)} \qquad (4.13)$$

These relations, combined with the fictitious angular momentum scheme of 4.2.5, allow the evaluation of the required matrix elements. As basis states the real form of the T orbitals will be used (see footnote above). This form is used to simplify the stress perturbation terms that will also be included.

The wave functions operated upon are then $\psi_i\sigma(S,m_S)$ where $\sigma$ is the appropriate spin function for the state and $\psi_i$ is one of the T sublevels.

$$\langle\psi_Y\sigma_1|\alpha\lambda\mathbf{L}^f.\mathbf{S}|\psi_X\sigma_2\rangle = i\alpha\lambda\langle\sigma_1|S_Z|\sigma_2\rangle$$

$$\langle\psi_Z\sigma_1|\alpha\lambda\mathbf{L}^f.\mathbf{S}|\psi_X\sigma_2\rangle = \frac{\alpha\lambda}{2}.\langle\sigma_1|S_+ - S_-|\sigma_2\rangle$$

$$\langle\psi_Z\sigma_1|\alpha\lambda\mathbf{L}^f.\mathbf{S}|\psi_Y\sigma_2\rangle = \frac{i\alpha\lambda}{2}.\langle\sigma_1|S_+ + S_-|\sigma_2\rangle \qquad (4.14)$$

## 4.3 Uniaxial Stress

Uniaxial stress is a method for probing the symmetries of electronic states involved at a defect centre in a crystal. Stress is applied along specific crystallographic directions, this lifts the cubic symmetry of the diamond, causing electronic energy levels to shift. It is possible, by studying the splittings caused, to assign the point group of the centre examined. The symmetry of the energy levels involved in the optical transition can also be determined.

The Hamiltonian for the applied stress in $T_d$ is,

$$H_{STRESS} = C_A(S_{XX}+S_{YY}+S_{ZZ}) + C_{E\varepsilon}(2S_{ZZ}-S_{XX}-S_{YY}) + \sqrt{3}C_{E\theta}(S_{XX}-S_{YY}) + C_{YZ}S_{YZ} + C_{ZX}S_{ZX} + C_{XY}S_{XY} \qquad (4.15)$$

where the linear combinations of the stress tensor components, $S_{ij}$, are taken so as to be representations of the $T_d$ point group. The electronic operators $C_{\Delta\delta}$ transform in the same way as the combination of stress tensors following them so that the Hamiltonian is totally symmetric. They do not operate upon the spin part of the wavefunction, so can only couple states of the same $M_S$. The Wignier-Eckart theorem can then be used to evaluate the matrix elements of this Hamiltonian on the basis set.

$$\langle\Gamma_f\tau_f|C_{\Delta\delta}|\Gamma_i\tau_i\rangle = \Delta^{-1}(\Gamma_f\Gamma_i\Delta|\tau_f\tau_i\delta)\langle\Gamma_f\|\Delta\|\Gamma_i\rangle$$

Coupling coefficient. A geometric term depending upon the symmetry of the states and sub levels.

Integral only dependent upon the irreducible representations of the states involved – i.e. the same for all sub levels

This allows the matrix elements to be written in terms of only a few parameters, as the coupling coefficients are known.

The stresses are commonly applied along the <001>, <111> and <110> directions. Light is then applied perpendicular to the stress direction, polarised into sigma and pi polarisations for <001>, <111> stress, and in three inequivalent directions with <110> stress.

## 4.4 Combined stress and spin-orbit perturbations.

The magnitude of energetic terms at the transition metal atom are

- Electron repulsions ≈ 1-3 eV
- Ligand field created by the diamond crystal ≈ 1-3 eV
- The applied stress ≈ 5 meV/GPa
- Spin orbit coupling ≈ 10 meV

It can be seen from the sizes of the terms that the gross features of the spectra will be determined by the first two effects, this is the problem addressed by crystal/ligand field theory (see Chapter 3). Subtle influences will then be exerted by the latter two terms. The solutions to the first two terms are known within the crystal field approximation and then first order perturbation theory can be applied to determine the combined effect of the spin-orbit coupling and applied stress.

The Hamiltonian for the TM metal defect has the following form:

$$H = H_0 + H_{STRESS} + H_{SO} \qquad (4.16)$$

$H_0$ describes the effect of the carbon ligands and electron-electron repulsions, giving rise to the electronic terms of the transition metal atom in the diamond lattice; These are the crystal field theory terms for ground and excited states of a TM with $n$ d-electrons, which are well known and tabulated. These electronic terms are then used as basis states to calculate the effect of the external applied stress, $H_{STRESS.}$ and spin-orbit interaction, $H_{SO}$, at the TM centre.

## Spin-Orbit Coupling in Uniaxial stress experiments.

The combined effect of the spin-orbit coupling and external stress upon the TMs electronic states is somewhat analogous to the Zeeman effect on an atom and can similarly be divided up into three regimes.

i) $H_{SO} >> H_{STRESS}$ . Here the spin-orbit interaction couples the orbital angular momentum, L, to the spin, S, producing states characterised by a total angular momentum J. The coupling to produce the angular momenta J removes some of the degeneracy in the electronic states producing additional structure in the TM's optical spectrum. J is a good quantum number in this regime.

ii) $H_{SO} \approx H_{STRESS}$ . In the intermediate case there is no simple expression for the energies of states, and the full Hamiltonian matrix must be diagonalized. The spin-orbit interaction mixes states of different $M_S$ and the applied stress mixes different orbital components together.

iii) $H_{SO} << H_{STRESS}$ . In this limit the spectra tend towards the normal uniaxial stress results. This is the analogue of the Paschen-Back effect in the Zeeman effect, where the orbital and spin angular momenta become decoupled.

Relative intensities of transitions between the ground and excited states can then be calculated (section 4.5.3) using standard selection rules. Performing these calculations for different values of the applied stress produces fan diagrams and spectra in a form directly comparable with experimental results.

First, all the previous results are combined to set up the Hamiltonian matrix that must be diagonalised to yield the eigenvalues and eigenvectors of the full system for the different cases encountered, coupling between the excited and ground states will be neglected.

### *4.4.1 $^{2S+1}T_i$ States*

The basis states are taken to be the direct product of a set of orbital states labelled $|X>$, $|Y>$, $|Z>$ transforming as $T_1$ or $T_2$ and spin states, labelled by the value of $M_S$ , $|S>$, $|S-1>$, …,$|-S+1>$ and $|-S>$ transforming as the appropriate irreducible representation(s) in the $T_d$ double group. As long as interaction with other states is ignored a fictitious

angular momentum $L^f$ =1 can be defined, which operates on the spatial functions as defined in section 4.2.5 and the matrix elements already developed for spin-orbit coupling (Equation 4.14) can be used. The effect of the applied stress can be expressed in three parameters

$$A=\langle T_i \| C(A_1) \| T_i \rangle,\ B=2/\sqrt{3}\langle T_i \| C(E) \| T_i \rangle,\ C=\langle T_i \| C(T_2) \| T_i \rangle$$

And using the coupling coefficients for the substates the matrix elements for the Hamiltonian $H=\alpha\lambda \mathbf{L}^f.\mathbf{S}+H_{STRESS}$ are:

$\langle i|\langle Sm_S|H|i\rangle|Sm_S\rangle = A(S_{ii}+S_{jj}+S_{kk})+B(S_{ii}-S_{jj}-S_{kk})$, where $i,j,k=x,y,z$ (and cyclic permutations of x,y,z)

$$\langle Y|\langle Sm_S|H|X\rangle|Sm_S\rangle = \frac{i\alpha\lambda}{2}m_S + CS_{XY}$$

$$\langle Z|\langle Sm_S|H|X\rangle|Sm_S\rangle = CS_{ZX}$$

$$\langle Z|\langle Sm_S|H|X\rangle|Sm_S \pm 1\rangle = \mp\frac{\alpha\lambda}{2}[S(S+1)-m_S(m_S \pm 1)]$$

$$\langle Z|\langle Sm_S|H|Y\rangle|Sm_S\rangle = CS_{ZY}$$

$$\langle Z|\langle Sm_S|H|Y\rangle|Sm_S \pm 1\rangle = -\frac{i\alpha\lambda}{2}[S(S+1)-m_S(m_S \pm 1)] \qquad (4.18)$$

### *4.4.2 $^{2S+1}E$ States*

Here, to first order, there is no spin-orbit coupling. Parameters are again introduced for the stress terms. The spin states are unaffected by the Hamiltonian

$$F=\langle E \| C(A_1) \| E \rangle,\ \ G=\sqrt{2}\langle E \| C(E) \| E \rangle \qquad (4.19)$$

and the matrix elements are:

$$\langle E\varepsilon|\langle Sm_S \| H_{STRESS} \| E\varepsilon\rangle|Sm_s\rangle = F(S_{XX}+S_{YY}+S_{ZZ})-G(2S_{ZZ}-S_{XX}-S_{YY})$$

$$\langle E\theta|\langle Sm_S \| H_{STRESS} \| E\theta\rangle|Sm_S\rangle = F(S_{XX}+S_{YY}+S_{ZZ})+G(2S_{ZZ}-S_{XX}-S_{YY})$$

$$\langle E\varepsilon|\langle Sm_S \| H_{STRESS} \| E\theta\rangle|Sm_S\rangle = F(S_{XX}+S_{YY}+S_{ZZ})+G(S_{XX}-S_{YY}) \qquad (4.20)$$

### *4.4.3 Calculating intensities.*

The matrix elements of the previous section allow the Hamiltonian matrix to be set up for any transition metal electronic states in $T_d$ symmetry, for any value of the spin-orbit coupling and stress. When the matrix is diagonalised the relevant eigenvalues and eigenvectors are found for the defect in the stressed state. These eigenvectors are linear combinations of the original basis states, so to calculate the intensities of transitions between the perturbed states, the (known) intensities between the original basis states are weighted according to their coefficients in the perturbed eigenstates. The selection rules for the original basis states can be found by applying the Wigner-Eckart to the electric dipole matrix elements between the states.

$$\langle T_2 x | \langle Sm_S | ez | E\theta \rangle | Sm_{S'} \rangle = \Delta_{T_2}^{-1/2} (T_2 Ex\theta | T_2 ET_1 z) \langle T_2 \| T_1 \| E \rangle \langle Sm_S | Sm_{S'} \rangle$$

$$= \frac{1}{\sqrt{3}} \cdot -\frac{1}{2} \langle T_2 \| T_1 \| E \rangle \delta_{m_S m_{S'}}$$

$\Delta_\Gamma$ is the degeneracy of the state

Coupling coefficient

Reduced matrix element

$\Delta m_S$=0 for an electric dipole

The actual intensities will depend on the squared modulus of these terms. So for a transition between perturbed levels we need to sum over all the ground basis states composing the perturbed ground state and all the basis states composing the excited state, then take the modulus squared of this term to get the intensity of a transition. The reduced matrix elements are parameters that depend upon the actual electron distribution in the complex examined, and are introduced empirically as group theory can say nothing about their magnitude.

The intensity, with light containing polarisation components $\gamma_{T_1}$, between two stressed states, g and e, is given by

$$I_{pol}(g \mapsto e) = \left( \frac{1}{\Delta_e \Delta_g} \right)^{\frac{1}{2}} \langle \Gamma_e \| \Gamma_{T_2} \| \Gamma_g \rangle^2 \left| \sum_{\gamma_{T2}}^{pol} \sum_{\gamma_e} \sum_{\gamma_g} \sum_{m_s} (\Gamma_e \Gamma_g \gamma_e \gamma_g | \Gamma_{T_2} \gamma_{T_2}) (c_{\gamma_e m_s})^* c_{\gamma_g m_s} \right|^2$$

**(4.22)**

Where $\Delta_i$ is the orbital degeneracy of state i, $\Gamma_i$ its irreducible representation and $\gamma_i$ its sub-states. The sum over the substates of the $T_1$ representation runs over those polarisation directions present in the light, pol. Within the squared modulus are the Clesch-Gorden coupling terms and the co-efficients of the basis states in the ground and excited eigenstates. The reduced matrix element is a common factor for all transitions arising form the original energy levels.

## 4.5 Results.

Here sample calculations using the formalism set up in the previous sections are presented that illustrate the various regimes described above (section 4.4). All transitions have been broadened with Lorentzians of 2 meV half width to resemble experimental data. Each calculation is presented as a set of spectra (i.e. relative intensity vs transition energy) at different applied stresses, and fan diagrams showing how the transition energies change with the magnitude of applied stress.

Figure 4.1 and 4.2 show simulated spectra for an $^3E \Leftrightarrow {}^3T_2$ transition. Figure 4.1 shows spectra with stress applied along a <100> direction and Figure 4.2 along <111>. Figure 4.3 shows a $^3T_1 \Leftrightarrow {}^3T_2$ transition with <001> applied stress.

The most immediate point to be drawn is the great increase in complexity due to the inclusion of spin-orbit coupling, compare Figure 4.1(a) and (c) (this can be seen even more clearly in Figure 4.3 (a) and (b)).

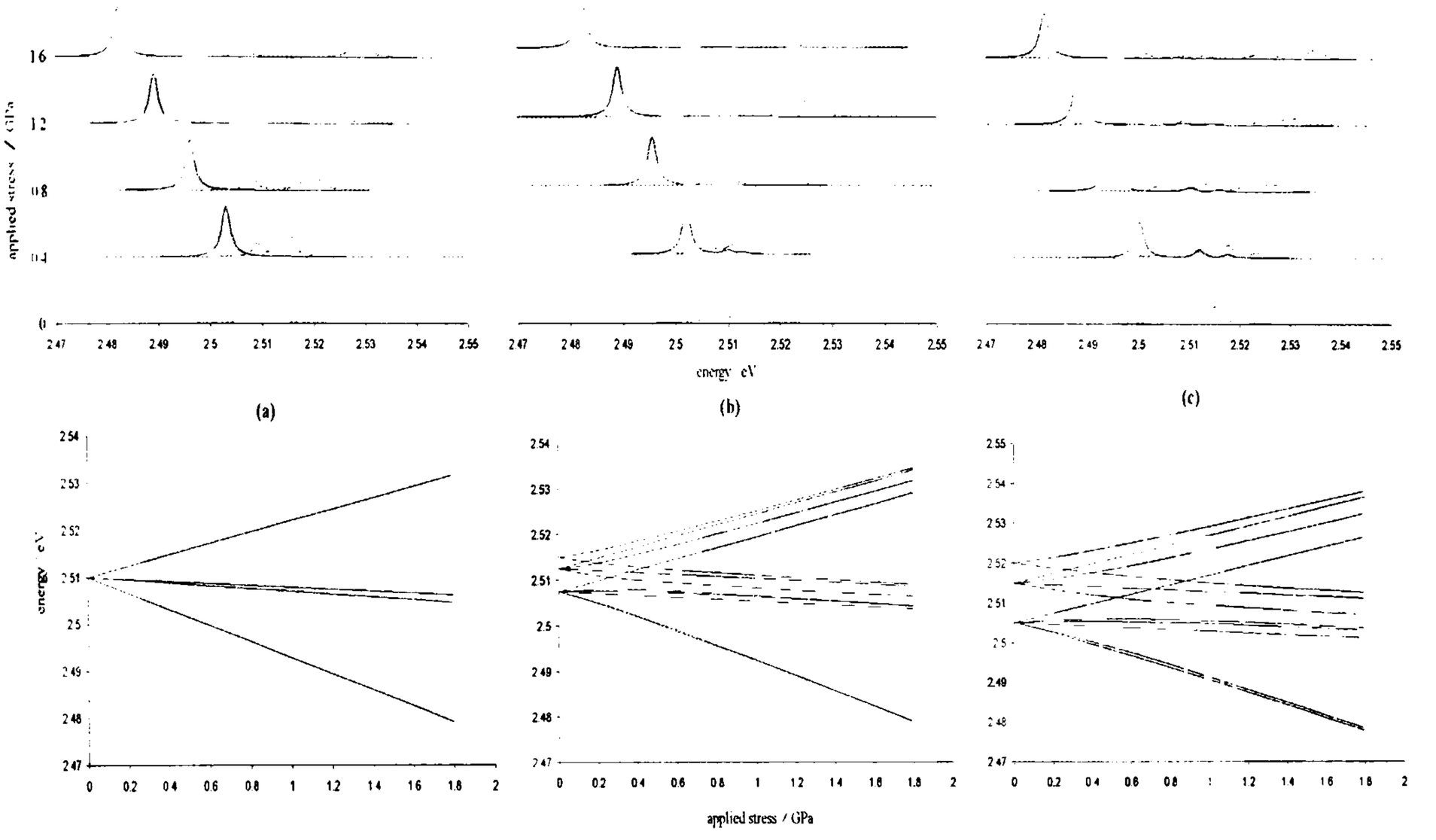


**Figure 4.1.** Simulated spectra and fan diagrams of a $^3E \Leftrightarrow {}^3T_2$ transition. Stress is applied along a <100> direction. All stress parameters were set to approximately 2.5 meV / GPa. In (a) $\alpha\lambda=0$ (b) $\alpha\lambda$=2.5 meV and (c) $\alpha\lambda$=5 meV. Lines were broadened with Lorentzians of half width 2 meV.

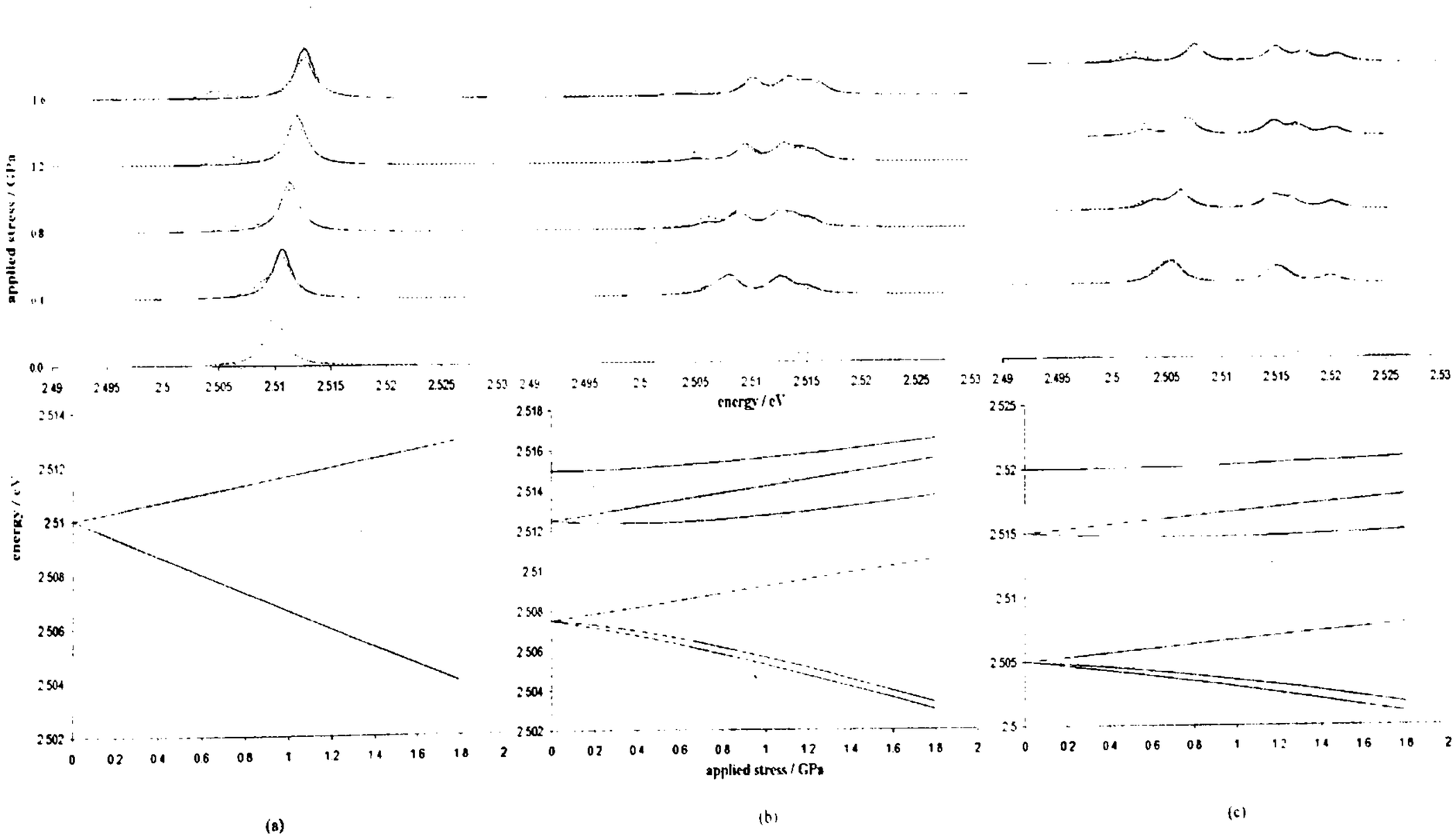


**Figure 4.2.** As Figure 4.1 but with stress applied along a <111> direction.

## Spin-Orbit Coupling in Uniaxial stress experiments.

A small portion of the parameter space has been sampled to produce results that are physically reasonable but illustrate the main features of the inclusion of spin-orbit coupling.

Looking at Figure 4.1 the size of the spin-orbit coupling increases from $\alpha\lambda$=0 meV to 5 meV (a conservative value given the approximate size of $\xi$ for the transition metals (section 4.2.2)). In Figure 4.1(b) with $\alpha\lambda$=2.5 meV the spectra at high stress clearly resemble the case with no spin-orbit coupling. Looking at the fan diagram for Figure 4.1(b) it appears that the spin and orbital angular momenta have nearly decoupled at high stress. This decoupling is more obvious in Figure 4.3(c) where the size of the stress parameters have been increased to 10 meV / GPa. A complete Paschen-Back effect has occurred; at high stresses the z orbital states are sufficiently far not to interact with x or y which remain orbitally degenerate. The three $|z,m_s\rangle$ orbitals are not split but the six $|x,m_s\rangle$ and $|y,m_s\rangle$ states split into two states at $E_{x,y}+\alpha\lambda/2$, two at $E_{x,y}$ and two at $E_{x,y}-\alpha\lambda/2$, independent of stress. This produces the pattern of three regularly spaced lines in the spectra at high stresses.

# Spin-Orbit Coupling in Uniaxial stress experiments.

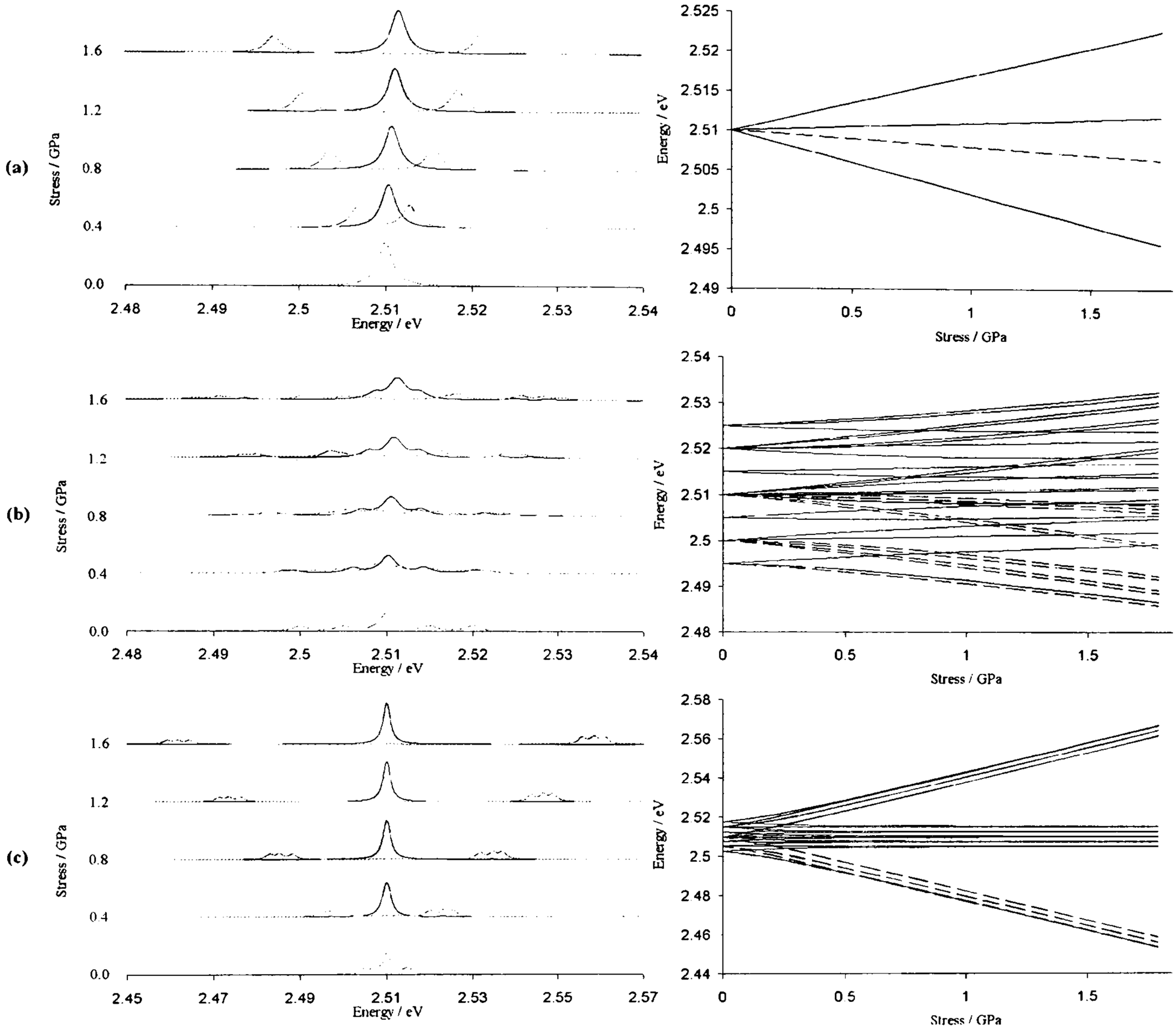


**Figure 4.3.** Simulated spectra of a $^3T_1 \Leftrightarrow {}^3T_2$ transition with <100> stress applied. In (a) and (b) stress parameters are as Figure 4.1 whilst in (c) they are increased to 10 meV / GPa. The size of the spin orbit coupling is (a)$\alpha\lambda$=0 meV, (b) $\alpha\lambda$=5 meV and (c) $\alpha\lambda$=2.5 meV . Lines were broadened with Lorentzians of half width 2 meV.

The behaviour when both stress and spin-orbit coupling are of similar magnitude can clearly be seen in Figure 4.2. In this regime there is no obvious connection between results with and without spin-orbit coupling. In the fan diagrams this regime is characterised by the regions with non-linear energy shifts with stress and the crossing of states (so in Figure 4.3(c) the stress dominates above approximately 0.5 GPa).

The case where the spin-orbit coupling is dominant has not been shown, but can be pictured from the low stress parts of Figure 4.1(c) and Figure 4.3(b). If the spin-orbit

coupling is very large, then the spin-orbit split levels will interact negligibly under the stress, and the previously tabulated results for the full double group would be appropriate [3].

The effect of spin-orbit coupling can be seen clearly in all figures at low stresses. Each T state is split into a distinctive pattern of three levels (if S>1/2) see Figure 4.1 and 4.2. Further splittings would be produced by interaction between electronic states. The main point here is that, even in Figure 4.3(c) where the spin-orbit coupling has very little effect on the spectra above about 0.5 GPa applied stress, the spin-orbit coupling produces recognisable features in the unstressed spectra and it should be obvious that a conventional uniaxial stress analysis will not be appropriate for the system.

## 4.6 Conclusions.

It appears that spin-orbit coupling will not offer an explanation of the troublesome uniaxial stress results found at some centres believed contain transition metals. Where the spin-orbit coupling is very large the transitions occur between single representations of the $T_d$ double group and the results are well known. As the spin-orbit coupling is reduced to a similar magnitude to that of the applied stress, the spin-orbit sublevels in the groundstate will become thermally populated and should be observed in conventional optical absorption/luminescence experiments; when it is recognised that spin-orbit coupling is important at a centre the method for tackling it in uniaxial stress experiments has been laid out here and elsewhere [8.10.11], and should provide a deal of information about the defect [8.10]. I cannot think of a situation where spin-orbit coupling would appreciably affect the results of a uniaxial stress measurement in an invidious manner, without its presence being clear from optical measurements without applied stress.

This chapter has concentrated exclusively on defects with $T_d$ symmetry, however, the theory can easily be adapted to centres with small distortions. For instance, a $C_{3v}$ defect with a small trigonal distortion can be tackled with the methods above, but including an additional constant <111> stress term. The slight complication is that

orientation degeneracy would have to be included, with each inherent <1 1 1> direction modelled separately, then the results averaged.

## References


[1] J K Grey and I S Butler, Coord. Chem. Rev., **219-221,** 713-759, (2001)

[2] A A Kaplyanskii, Opt. Spectrosc., **16,** 329 (1964)

[3] A A Kaplyanskii, Opt. Spectrosc., 557 (1964)

[4] A E Hughes and W A Runcimann, Proc. Phys. Soc., **90**, 827 (1967)

[5] K Mohammed, PhD Thesis, King's College London, University of London, (1982)

[6] G Davies and M H Nazare, J. Phys. C, **22**, 4127 (1980)

[7] G Davies, J. Phys. C, **8,** 2448 (1975)

[8] M H Nazare, A J Neves and G Davies, Phys. Rev. B, **43**, 14196 (1991)

[9] P W Mason, F S Ham, G D Watkins, Phys. Rev. B, **60**, 5417 (1999)

[10] M H Nazare, J C Lopes, A J Neves, Physica B, **308-310**, 616 (2001)

[11] I K Ludlow, J. Phys. C, **1**, 1194-1204 (1968)

[12] J Avery, *Creation and Annihilation Operators*, McGraw-Hill, 1976

[13] P W Atkins and R S Friedman, *Molecular Quantum Mechanics*, OUP, 1997

[14] H A Jahn and E Teller, Proc. Roy. Soc. (London), **A161**, 220 (1937)

[15] F S Ham, Phys. Rev., **138**, A1727 (1965)

[16] W Low, Phys. Rev., **109**, 256 (1958)

[17] R Newman and R M Chrenko, Phys. Rev., **115**, 1147, (1959)

[18] B Bleany, Proc. Roy. Soc. (London), **A63**, 405, (1950)

[19] J S Griffith, Trans. Faraday Soc, **56**, 193, (1960)

[20] A Abragam and M H L Pryce, Proc. Roy. Soc. (London), **A205**, 135, (1951)

[21] A Abragam and M H L Pryce, Proc. Roy. Soc. (London), **A206**, 173, (1951)

[22] J S Griffith, Trans. Faraday Soc., **54**, 1109 (1958)

# Chapter 5.

# Review of known transition metal defects in diamond.

In this chapter a brief review of the information available on TMs in diamond is given, along with a more detailed discussion of the two well-characterised defect centres, which are attributed to $Ni_i^+$ and $Ni_s^-$.

Synthetic diamonds grown using one of the high pressure, high temperature (HPHT) processes frequently contain some traces of the solvent-catalyst that was used to grow them [1,5]. Where nickel or cobalt are included in the solvent mixture, these metals form point defects in the diamond, usually concentrated in {111} growth sectors, which can be detected by optical [1,2,3] or electron paramagnetic resonance (EPR)[4,5] spectroscopy.

In addition, most of these synthetic diamonds contain appreciable concentrations of nitrogen, unless nitrogen is explicitly excluded by using nitrogen getters. HPHT diamonds grown at relatively low temperatures (1400-1500° C, for example) contain nitrogen in the form of single substitutional atoms, termed $N_s$ or C centres. The single nitrogen atom species are known to mobile at annealing temperatures of 1400°C and above, and there is evidence transition metals can act as a trap for these species, forming transition metal nitrogen complexes.

Synthetic type IIb, boron containing, diamonds can also be grown. There is no evidence that boron atoms are mobile in the diamond lattice, but some defect centres have been interpreted in terms of transition metal-boron centres formed during crystal growth.

## 5.1 Experimental evidence for TM defects in diamond.

Listed are the observed transition metal species, and the method by which they have been observed.

| molecular model | method of detection | notes |
|---|---|---|
| $Ni_i^+$(-X) | optical [6 7 8 9], EPR [10] (NIRIM-2) | <111> trigonal distortion, uncertain correlation of EPR and optical methods. |
| $Ni_i^+$ ? | EPR [10] (NIRIM-1) | |
| $Ni_i^{2+}$-$B_s^-$ | EPR [11] (NOL1) | |
| $Ni_i^-$ | EPR [12] (W31) | questionable assignment. |
| $Fe_i^+$ | optical [13] | questionable, circumstantial evidence. |

**Table 1.** Experimentally observed centres attributed to TMs in an interstitial environment.

| molecular model | method of detection | notes |
|---|---|---|
| $Ni_s^-$ | optical [7 14] EPR[15] (W8) | optical and EPR well correlated. |
| $Ni_s^+$ ? | EPR[10](NIRIM-1) | |
| $(Ni_s\text{-}N_s)^-$ | EPR[16] (AB5) | |
| $Co_s$-$N_s$ | optical [17 18 19 20] | |

**Table 2.** Experimentally observed centres derived from the TM in a substitutional site.

## Review of known transition metal defects in diamond.

| molecular model | method of detection | notes |
|---|---|---|
| $(C_3Ni_{sv}C_3)^-$ | EPR [21] (NE4) | |
| $(C_3Ni_{sv}NC_2)^{2-}$ | EPR [21 22] (NE7) | uncertain assignment |
| $(C_3Co_{sv}NC_2)^-$ | optical [23 20] EPR [24] (O4) | correlation uncertain |
| $(C_2NNi_{sv}NC_2)^-$ | optical [25] EPR[21](NE1) | |
| $(C_3Ni_{sv}N_2C)^-$ | EPR [21 22] (NE5) | |
| $(C_3Co_{sv}N_2C)^-$ | EPR [26] (NOL1) | |
| $(C_2NNi_{sv}N_2C)^0$ | optical [25 27] EPR[21] (NE2) | |
| $(C_2NNi_{sv}N_2C)^0$ | optical [25] EPR[21](NE3) | |
| $(C_3Ni_{sv}N_3)^0$ | EPR [28] (NE9) | |
| $(CN_2Ni_{sv}N_2C)^+$ | EPR [21 22] (NE8) | |

**Table 3.** Experimentally observed centres derived from TMs in a semivacancy site.

The above tables only contain the centres for which the experimental evidence is complete enough for a model of the defect to be suggested. There is a vast array of zero-phonon lines and uncategorised EPR signals. Further details and references on the transition metal centres can be found in Ref 29-31.

It can be seen that whilst there is a vast array of data that is associated with TMs, very few centres have been positively identified, the majority by EPR. Often there is too little data for any interpretation to be put forward for optical data, just a single zero-phonon line. Only two defects are at all well understood, $Ni_i^+$ and $Ni_s^-$, which are discussed below, and there are still some problems with the theoretical explanations of these two centres.

Most of the known centres are based on nickel, with three Co defects also detected. There is unconfirmed EPR evidence for Mn [32]and Cu[33], and the assignment of $Fe_i^+$ [13] (see Table 1) is based on very circumstantial evidence. Ti [17 34], Cr [17] and Zn [17] have been observed, but they were produced by ion implantation, rather than as by-products of crystal growth, and are of less interest. It is a real puzzle why other TMs,

especially Fe and Cu, which are commonly used in the growth process have not been positively identified.

It is believed that the transition metals initially enter the diamond lattice at either interstitial or substitutional sites. These sites are strained as the TM is much larger than the carbon atoms forming the lattice, and when annealed at high temperatures neighbouring carbon atoms are ejected and the semivacancy defects form. Indeed, it is inferred that the EPR centres NE1-9 involve Ni because they appear as $Ni_s^-$ anneals out [22]. This change in environment releases $C_i$ which has important consequences (see chapter 7).

## 5.2 Properties of the well characterised TM centres

### *5.2.1 Interstitial nickel.*

$Ni_i^+$ is proposed to be responsible for the 1.40 eV zero-phonon line found in some (mainly type IIb) diamonds. The zero-phonon line consists of a doublet at 1.401 and 1.404 eV, each component is then found to have resolved fine structure. This fine structure allowed the definite identification of the centre as Nickel containing; the relative intensity of fine structure in the doublet components is found to be temperature independent in both absorption and luminescence, which is most readily explained by the fine structure occurring at different centres containing different isotopes. The ratio of intensities of the fine structure fits that of the two most common isotopes of nickel - $[^{58}Ni]:[^{60}Ni]=68:26$=ratio of intensity of fine structure components. This also implies that the centre only contains one nickel atom. It was shown at the same time, by fitting to uniaxial stress data, that transitions occurred between a spin-orbit split $^2E$ ground state and a $^2A$ excited state, and trigonally distorted $Ni_i^+$ was proposed as a model for this centre.

This model was confirmed in outline and refined by magnetic circular dichromism measurements, which gave g values for the excited state [9]. A full fit to the experimental data could be obtained assuming that there was a dominant octahedral

crystal field, Δ=1.4 eV, a small trigonal splitting, K=-18 meV, and a spin-orbit coupling co-efficient, λ–55 meV.

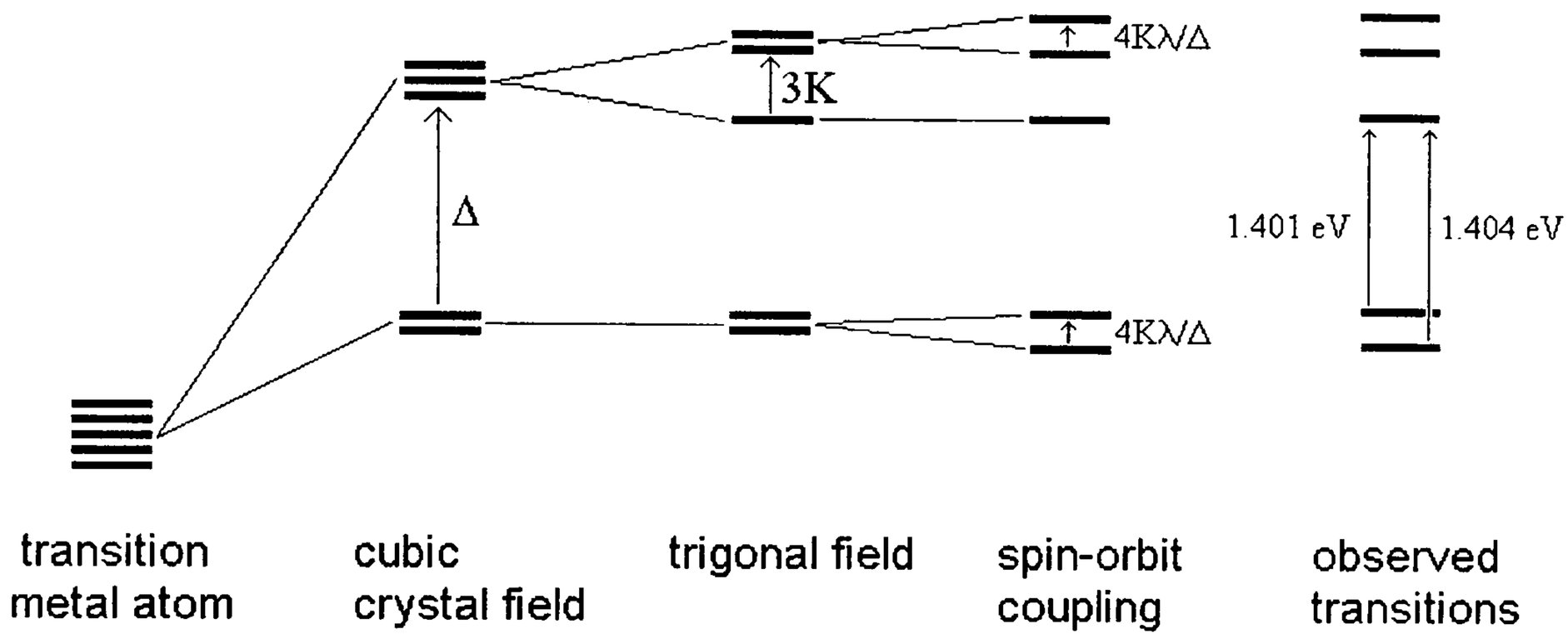


**Figure 1.** The crystal field description of the $Ni_i^+$ centre showing the many-electron states of the defect [35]. The large octahedral field splits the metal d-orbitals into $^2E$ and $^2T_2$ states separated by Δ=1.4 eV. A much smaller trigonal field splits the $^2T_2$ state into an $^2A_1$ state at Δ-2K and $^2E$ states at Δ+K. Spin-orbit coupling then further lifts the degeneracy of the $^2E$ states.

The cause of the trigonal splitting is unknown, some semi-empirical and *ab inito* calculations suggest it is intrinsic to the centre, but it has also been suggested that it is caused by a distant defect along a <111> direction, possibly a charge compensating boron atom. It has also been suggested recently that the NIRIM-2 EPR centre is the same defect as that responsible for the 1.4 eV optical transition [36].

### *5.2.2 Substitutional nickel.*

The W8 EPR centre has been convincingly interpreted as $T_d$ $Ni_s^-$; The W8 centre shows $^{13}C$ hyperfine structure characteristic of the substitutional position in the lattice – four carbon nearest neighbours, and twelve carbon next nearest neighbours – and is

indicative of a $3d^7$ ion with a $^4A$ ground state. The W8 centre has also been correlated with the 2.51 eV optical absorption line [1], which is thought to correspond to the transition $^4A_2 \Leftrightarrow {}^4T_2$ and is equal to the crystal field splitting parameter 10Dq or $\Delta$.

However, the interpretation of the data from the two experimental techniques is not entirely consistent. Specifically the strength of the spin-orbit coupling found from the two methods appears incompatible. In EPR the interaction with the magnetic field is measured in terms of the *g* value, when orbital angular momentum is entirely quenched it takes the spin-only value $g_e \approx 2$, deviations from this, $\Delta g = g - g_e$, indicate the size of the spin-orbit coupling, $\lambda$, to residual orbital angular momentum. In the case of a $3d^7$ ion $\Delta g = -8\lambda/\Delta$ and $\lambda = -9.3$ meV. However, spin-orbit coupling has been observed in fine structure of the 2.51 eV optical transition and uniaxial stress data (see chapter 4) has been fitted with $\lambda = -0.5$ meV.

The electronic configuration of the $Ni_s^-$ defect is shown in figure 3.2 for both the LW and vacancy models. Both models predict a $^4A_2$ ground state and the first excited state to be $^4T_2$ in the LW model, or $^4T_1$ in the vacancy model. The small size of the spin-orbit coupling parameter and the lack of resolved fine structure due to nickel isotopes suggest that the centre approximates the vacancy model, however, the optical data has been interpreted within the weak crystal field theory, where the valence orbitals are assumed to be pure transition metal d-orbital. The size of the spin-orbit coupling has been deduced using the weak crystal field model (LW), so it becomes a somewhat circular argument to use this parameter to conclude that the centre is vacancy-like.

## 5.3 Summary.

It can be seen from this chapter that whilst the transition metal defects in diamond are, in broad terms, well understood there is still a great deal of uncertainty about their exact nature; even the best understood centres have a few inconsistencies in their interpretation. The failure to observe TMs other than nickel and cobalt is puzzling and this indicates that the role of the TMs in the catalysis of synthetic HPHT diamonds is not fully understood. The largest hurdle to a full understanding and

characterisation of further TM defects is that optical spectroscopic techniques just do not provide enough information for molecular models to be constructed, in many cases just a zero-phonon line.

---

[1] A T Collins and P M Spear, J. Phys D., **15,** L183 (1982)

[2] S C Lawson, H Kanda, K Watanabe, I Kiflawi, Y Sato and A T Collins, J. Appl. Phys., **79,** 4348 (1996)

[3] S C Lawson and H Kanda, J. Appl. Phys., **73,** 6 (1993)

[4] J Isoya , H Kanda and Y Uchida, 1990 Phys. Rev. B., **42,** 9843 (1990)

[5] D C Hunt, D J Twitchen, M E Newton, J M Baker, J K Kirui, J A van Wyk, T R Anthony, W F Banholzer, Phys. Rev. B, **62,** 6587 (2000)

[6] T Pawlik *et al.*, J. Phys. Condens. Matter, **10,** 9833 (1998)

[7] A T Collins and P M Spear, J. Phys. C., **19,** 6845 (1983)

[8] M H Nazare, A J Neves, G Davies, Phys. Rev. B, **43,** 196 (1991)

[9] P W Mason, F S Ham, G D Watkins, Phys. Rev. B, **60,** 5417 (1999)

[10] J Isoya *et al.*, Phys. Rev. B, **42,** 3905 (1990)

[11] V A Nadolinny, private communication, 2001.

[12] J A van Wyk and J H N Loubser, Mater. Sci. Forum., **10-12,** 923 (1986)

[13] K Iakoubovskii and G J Adrianssens, J. Phys. Condens. Matter, **14,** L95 (2002).

[14] M H Nazare, J C Lopes, A J Neves, Physica B, **308-310,** 616 (2001)

[15] J Isoya et al., Phys. Rev. B, **41,** 3905 (1990)

[16] A J Neves *et al.*, Diam. Relat. Mater., **9,** 1057 (2000)

[17] A M Zeitzev, Phys. Rev. B, **61,** 12909 (2000)

[18] A T Collins, Diam. Relat. Mater., **9,** 417 (2000)

[19] S C Lawson *et al.*, J. Appl. Phys., **79,** 4348 (1996)

[20] I N Kupriyanov *et al.*, Diam. Relat. Mater., **10,** 59 (2001)

[21] V A Nadolinny *et al.*, Appl. Mag. Res., **12** (1997) 543

[22] V A Nadolinny *et al.*, J. Phys. Condens. Matter, **11** (1999) 7357.

[23] A P Yelisseyev *et al.*, private communication, (1998)

[24] D J Twitchen, J M Baker, M E Newton, K Johnston, Phys. Rev. B, **61,** 9 (2000)

[25] V A Nadolinny and A P Yelliseyev, Diam. Relat. Mater., **3,** 17 (1994)

[26] V A Nadolinny et al., proceedings of 53rd Diamond conference, 2002.

[27] S C Lawson and H Kanda, J. Appl. Phys., **75,** 3967 (1993)

[28] V A Nadolinny, private communication, 2001.

[29] The properties of natural and synthetic diamond, Ed. J E Field, Academic Press 1992, appendix H.

[30] A M Zaitsev, *Collection of optical data on superhard semiconductors*. Part 1, Diamond, ISTOK (1998)

[31] J M Baker, SPIE Procedings, 4766, (2002)

[32] K Iakoubovskii and A Stesmans, Phys. Stat. Sol. (a), **186,** 199 (2001)

[33] J M Baker, J. Phys. Condens. Matter, **13,** 2053 (2001)

[34] A A Gippius and A T Collins, Solid State Commun., **88,** 637 (1993)

[35] P W Mason, F S Ham, G D Watkins, Phys. Rev. B, **60,** 5417 (1999)

[36] M Baker, private communication 2003.

# Chapter 6.

# Transition Metals in Diamond: a Cluster Study using the Hartree-Fock Method.

## 6.1 Introduction

Transition metal impurities in diamond have been the subject of much experimental work, principally using the techniques of optical spectroscopy and electron paramagnetic resonance (EPR). However, systematic studies of transition metal impurities are much scarcer [1,3], and work has tended to concentrate on elucidating the structure of specific experimental data. A recent study [4] has carried out a survey of the properties of the first row transition metal impurities within the Local Density Approximation (LDA) formulation of density functional theory.

As described in chapter 3, experimental data is generally interpreted within a qualitative or semi-empirical molecular orbital picture. These interpretations give a clear explanation of the interaction of the TM with the lattice, allowing qualitative discussion of trends in the properties of the TM defects.

In this chapter the first row transition metals are studied using the Hartree-Fock formulation and some of its extensions. Specifically the transition metals at interstitial, substitutional and semivacancy sites in diamond have been modelled using the *ab initio* quantum chemical package GAMESS. The calculations facilitate the study of many properties of the TM defects, such as the binding energy of the TM in diamond, the accessibility of different charge states, the energies of optical transitions and equilibrium geometries: details of the calculations to obtain these quantities are described in section 6.2. Trends in the change of these properties across the first transition series are examined and compared to other available calculations and experimental data. The use of the

Hartree-Fock method, rather than density functional theory, produces real wavefunctions. The wavefunctions can readily be related to the models produced by analysing experimental data as long as care is taken, and examination of changes across the transition series allows us to get a feel for the effects shaping the electronic structure of the TM defects. Simple HF calculations provide a link between the qualitative picture commonly used, and more detailed calculations which are often hard to interpret. By going beyond the HF method to allow multi-reference wavefunctions, we can obtain genuine many-electron states (both ground and excited states are open to investigation).

Basis sets and clusters of varying size have been used in this thesis. It is shown that the results of these calculations are qualitatively consistent (It is noted in particular, that the ordering of the one-electron orbitals changes between the different cluster sizes and basis sets in only one case, $Co_s^-$); when computationally expedient, calculations can be conducted on the smaller clusters with a modest degree of confidence in the results produced.

It is also known that transition metals defects in diamond will form complexes with some other common defects, especially nitrogen (see chapter 3), and a DFT survey has recently made on some of these defects [5]. Calculations are also conducted upon the $TM_s$ defects with nitrogen or boron atom(s) replacing carbon atom(s) at nearest neighbour sites.

Overall, it is found that even very rough calculations can help elucidate the properties of TMs in diamond. More reliance can be placed on the calculations with larger clusters and/or better basis sets, but the qualitative results obtained from the simplest calculations still stand. It is also found that changing the transition metal makes little difference to the equilibrium geometry of the clusters.

To obtain reliable calculations of chemical accuracy would require far more computationally expensive calculations than have been performed here: but, by checking results are consistent across a range of clusters and basis sets, and that results are in

accord with chemical intuition, these calculations provide a useful tool for understanding the nature of TM defects in diamond.

## 6.2 Methodology.

In this section the specifics of the GAMESS calculations are described. The basis sets used are described, and the clusters used for the different TM environments are given. The binding energies of TM defects in diamond are defined and the various reference states and concepts used are outlined.

### *6.2.1 Theory*

For the reasons discussed in section 2.2.1 all SCF calculations are carried out within the ROHF framework (section 2.1.4) unless specifically stated otherwise.

MCSCF calculations were used to allow high spin states and genuine excited states to be considered. The active space used will be specified with the calculations. The calculations were run without symmetry, to ensure that all CSFs were generated, this restricted the MCSCF calculations to small clusters. No excited state would converge with the TZV basis sets so all MCSCF calculations are carried out with the MINI basis set.

### *6.2.2 Basis sets*

The majority of the following calculations were carried out using Huzingas' minimal basis set (MINI) [6]. Where explicitly stated, a much better basis set was utilised to carry out the same calculations on TM complexes. The basis sets used then were: 6-31G [7] on the carbon atoms, GAMESS' triple zeta valence (TZV) on the transition metal [8], which is a modified version of Wachters' original basis set [9], and a STO-3 basis set on the hydrogens [10 11]. When used this will be referred to as the TZV basis.

### 6.2.3 Clusters

A variety of clusters were used in these calculations. Calculations based around a substitutional site were for the very small $TM_sC_4H_{12}$ and the larger $TM_sC_{28}H_{36}$ clusters. When substitutional clusters were not relaxed the equilibrium geometry of $[Co_sC_4H_{12}]^+$ (taken from calculation in a MINI basis set) was used for the smaller cluster and the geometry from a calculation using a TZV basis set on $[Fe_sC_{28}H_{36}]^0$ for the larger cluster (Figure 6.1a). For the interstitial defects a $TM_iC_{10}H_{16}$ cluster was used, with a geometry optimised for $Co_i^+$ with a TZV basis set, or a $TM_iC_{26}H_{30}$ cluster (Figure 6.1b) with a geometry optimised for $Ni_i^0$ (MINI basis set). A $TM_{sv}C_{43}H_{42}$ cluster (Figure 6.1c) was used for calculations on TMs at semivacancy sites (geometry optimised for $Ni_{sv}^0$). These standard geometries were used in calculations unless specifically stated that relaxation has been allowed for a given calculation.

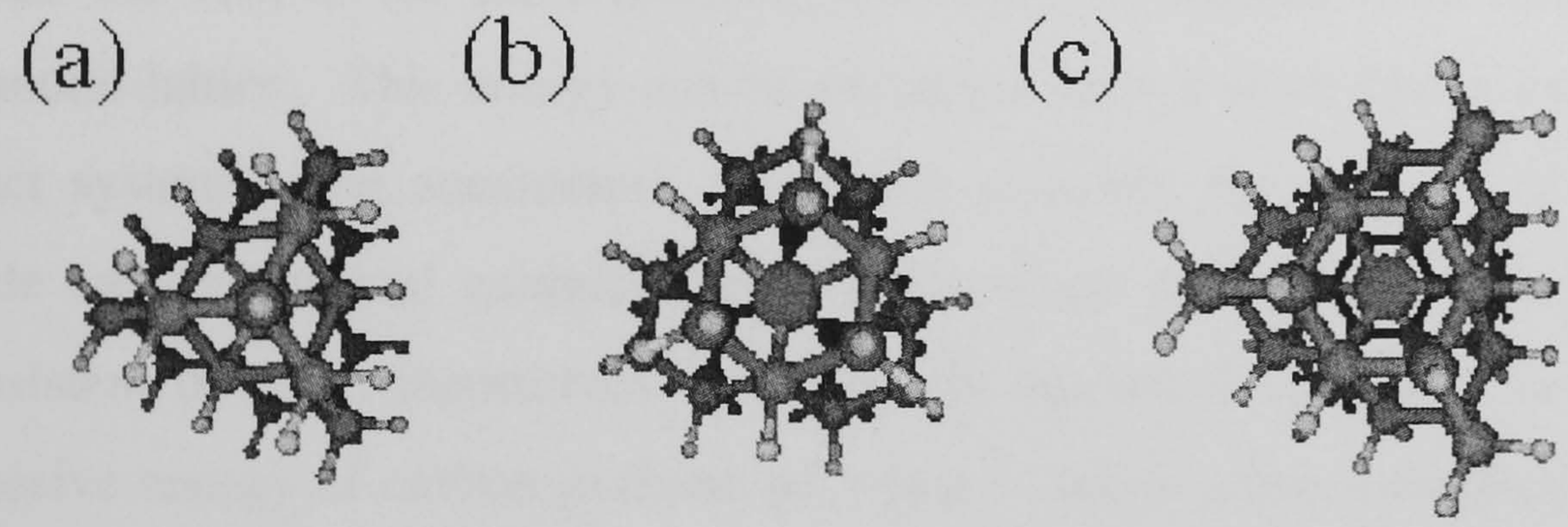


**Figure 6.1 (a-c).** TM clusters. Interstitial, substitutional, semivacancy from left to right. Viewed down a $C_3$ axis, with a $\sigma_d$ plane projecting out of the page, and along an $S_6$ axis respectively

When calculating the binding energies of charged defects, several centres of general interest in diamond were calculated: the substitutional nitrogen, C centre, in $N_sC_4H_{12}$ clusters with both basis sets, and in the larger $N_sC_{28}H_{36}$ clusters for the MINI basis set only. In a similar way, substitutional boron in $B_sC_4H_{12}$ and $B_sC_{28}H_{36}$ clusters were studied for the relevant charge states.

Often H atoms are held fixed and the geometry of the other atoms optimised. Fixing the position of the hydrogens prevents the smaller clusters from expanding outwards too far, which they will tend to do, as there are no outer shells of carbon atoms to restrict their relaxation. For reference clusters, such as the C centre, when TMs were not present the AM1 semi-empirical Hamiltonian was used to obtain approximate relaxed clusters, as it runs much faster than the full *ab initio* calculation.

### *6.2.4 Binding Energies.*

The binding energy of the TM is here defined as - the energy released from the system on placing the TM (in a specified reference state) into the diamond lattice at the appropriate site. This definition means that the more positive the binding energy the more strongly bound the TM, or the more thermodynamically favourable is its incorporation into the diamond lattice. This energy can be extracted from a Born-Haber cycle relevant to the exact system being considered. Wherever possible, the energies of all species in the cycle are the internal energies from Hartree-Fock calculations, which are likely to be consistent between themselves. Occasionally empirical data must be used, such as the cohesive energy of carbon in diamond when a carbon atom is displaced by the inclusion of the TM. The exact terms used are presented in the relevant sections.

Generally, a single TM atom/ion will needed to be included in the Born-Haber cycle. In principle its total energy can be easily calculated, however, it is unclear what state the TM atom should be in during the calculation. The energy of the TM depends on two factors; its environment and its electronic state (both of which make significant contributions to the value obtained for the binding energy).

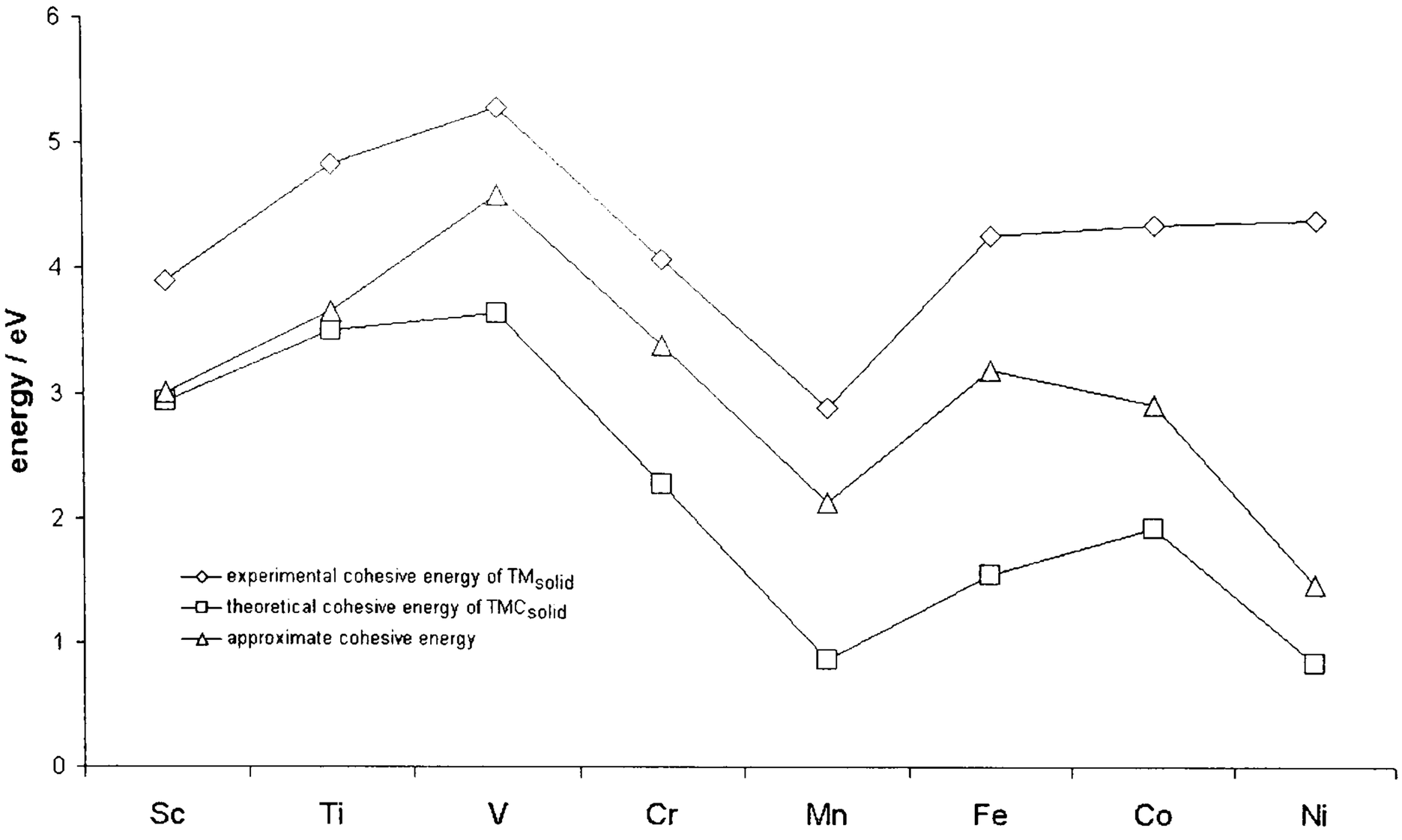


**Figure 6.2.** The cohesive energy of the first row transition metals in their solid state (experimental data) in TM mono-carbides (*ab initio* calculations [13]) and in carbides with the same carbon content as a saturated TM liquid at $1000^0$C (see text below).

The method by which HPHT synthetic diamonds are prepared suggests that rather than using an isolated TM ion as a reference, instead the metal in its liquid state should be used (or probably a saturated carbide of the metal at a high (but rather uncertain) temperature). Adequate data for the atomisation energy of the metal liquids is however unavailable, instead the isolated atom/ion is used as a reference to which is added the energy of atomisation of the solid metal [12]. To check the use of these experimental data, the cohesive energy of the TMs was estimated from independent sources. Data were taken from *ab initio* calculations on TMC (transition metal mono-carbide) compounds [13]; the bond energies (TM-TM, TM-C and C-C) from Ref. 13 were weighted by the solubility of carbon in the liquid TM at $1000^0$C [14] to obtain an approximate cohesive energy for the TM in a saturated TM/C mixture (Figure 6.2). It is observed that the experimental and corrected theoretical values are in good agreement, apart for Ni whose theoretical binding energy was badly underestimated [13]. Whilst not taking into account the changes in binding in the TM's liquid state, the general agreement of these data, from

such diverse sources, suggests that using the experimental cohesive energies of the solid TMs will introduce no gross errors into the calculations.

The electronic state of the transition metal must also be defined. When bound into the diamond lattice at an interstitial site, the ground state electronic configuration of the transition metals has been observed to be $d^N$. Isolated TMs, conversely, often have the 4s orbital wholly or partly filled, frequently $(4s)^2(3d)^{N-2}$.

The process of placing the transition metal into the diamond lattice can then be divided into two steps: the promotion of the 4s-electrons, changing the electronic configuration from $(4s)^2(3d)^{N-2}$ to $(3d)^N$, and then the excited ion being placed into its site in the diamond cluster. The promotion energy is always positive, but the second step can be of either sign. The promotion energies are hard to calculate within the HF framework, as the energies of atomic many electron states depend strongly upon correlation effects. The total Hartree-Fock energy of the ground state atom is always used in the thesis. The second contribution to the binding energy, is that of placing the excited TM into the diamond cluster. This energy depends upon the basis set used in the calculation and upon the size of the cluster used: the effects of both of these factors are examined later.

A further inconvenience is that the TM-Diamond cluster is described by a better basis set than either the pure diamond cluster, or the isolated transition metal, leading to an effect called basis set superposition error (BSSE). BSSE can be corrected for by calculating the energy of the TM atom and diamond cluster in the full basis of the TM-Diamond cluster. This method was used to estimate the BSSE of $Fe_iC_{26}H_{30}$; $E(Fe_{atom})$ and $E(C_{26}H_{30})$ were recalculated with the rest of the cluster present as 'ghost' atoms. The total BSSE was found to be 1.6 eV, fairly evenly distributed between the Fe atom (1.0 eV) and the carbon cluster (0.6 eV). For interstitial titanium in silicon, using a similar basis to the TZV used here and a $Ti_iC_{10}H_{16}$ cluster, the BSSE was found to be 0.96 eV [15]. Thus binding energies are expected to be overestimated by around to 1 eV for the TZV basis, and somewhat more for the smaller MINI basis set.

When considering different charge states, setting up a physically meaningful closed system is harder. 'Free' electrons or holes must be incorporated somewhere in the cycle, in an appropriate state. Doing this consistently is hampered by the fact that the position of the conduction and valance bands of the diamond shift, depending on the metal present, and its charge state. Two methods have been used to accommodate the charged species: either pinning the Fermi level to a certain energy below the conduction band (commonly that of the 1.7 eV nitrogen donor), or, as here, by incorporating another species in different charge states to model the process. We define the charging enthalpy for forming a charged cluster and charge compensating pair as

$$\Delta H_{CHARGE}=E[(TMcluster)^{+}] +E[(B_sC_{28}H_{36})^{-}]-E[(TMcluster)^{0}]-E[(B_sC_{28}H_{36})^{0}] \qquad (6.1)$$

$$\Delta H_{CHARGE}=E[(TMcluster)^{-}] +E[(N_sC_{28}H_{36})^{+}]-E[(TMcluster)^{0}]-E[(N_sC_{28}H_{36})^{0}] \qquad (6.2)$$

for the MINI basis set and similar cycles, but with $N_sC_4H_{12}$ and $B_sC_4H_{12}$, for the TZV basis. Using these cycles has the advantage that all the terms involved are total energies calculated by the Hartree-Fock method, and there is no need to resort to any empirical data. This does mean that the relative stabilities of the charge states depend crucially on how well the references are modelled by GAMESS, but it is anticipated that the simpler second row elements used have been described at least as well as the transition metals. It is also hoped that errors due to finite cluster size will to some extent be cancelled by this method.

Another consideration for the charged species is the finite size of the clusters used in this survey. Charge in a crystal is screened by the response of the crystal, the dielectric constant, ε, being the classical bulk expression of this. In a small cluster there is little chance to delocalise the charge, simply because of the cluster's size. This means that charged complexes should be stabilised by a term of the form, $E=-\frac{1}{2}(1-\frac{1}{\varepsilon}).\frac{q^2}{R}$, the self-energy of a charge in a finite space[16].

The radius, $R$, of the volume the charge is constrained within can be approximated by the Mott-Littleton radius, $R_{ML}$, of the cluster [17 18]. The corrections to the energies of charged clusters are given in Table 6.1.

| Cluster | $R_{ML}$ / nm | energy correction / eV |
|---|---|---|
| $C_5H_{12}$ | 0.22 | 2.69 |
| $C_{10}H_{16}$ | 0.27 | 2.23 |
| $C_{26}H_{30}$ | 0.36 | 1.66 |
| $C_{29}H_{36}$ | 0.37 | 1.58 |
| $C_{43}H_{42}$ | 0.42 | 1.42 |

**Table 6.1.** Corrections to charged TM defects due to the finite size of the clusters considered.

For instance, in this approximation the process of placing a single charge on a $C_{10}H_{16}$ interstitial TM cluster is stabilised by 2.23 eV and the formation of a $[TM_iC_{10}H_{16}]^-$ $[N_sC_{29}H_{26}]^+$ charge pair will be stabilised by 3.81 eV.

The stabilisation energy will be over-estimated by this model for two reasons: the model underestimates the size of the clusters as it is based on the size of a unit cell of pure diamond, rather than the expanded lattice around a TM. It double counts the effect of the near neighbours; they already provide some stabilisation in the HF model by delocalising the charge when forming MOs.

This simple model used to determine the charge stabilisation gives an upper bound to the stability of the charged species.

### *6.2.5 Ground states and Optical transition energies.*

As stated in section 2.4.4 ionisation energies derived using Koopmans' theorem from one-electron energy differences are only approximately correct due to a fortuitous cancellation of energy terms. One-electron orbital energy differences are often observed to be wildly inaccurate for localised defects. Hence they are only shown when they are in agreement with more rigorous calculations, and the approximate one-electron picture helps illustrate the process under examination.

Both CI and MCSCF calculations give genuine many-electron states, for both ground and excited states, and as such optical transition energies are simply the energy difference between given states. This ability of beyond Hartree-Fock theories to form real many-electron multiplets is one of its main advantages over DFT, which can only perform state-averaged calculations. In a similar way ground states are found from MCSCF calculations: both the low-spin and high-spin many-electron term of lowest energy are found, the ground state being identified with the lower energy.

### *6.2.6 Charge distributions*

The net charge on the metal in the cluster can be analysed using Mulliken's population analysis[19]. This is defined as the difference between the atomic charge and the number of electrons occupying atomic orbitals centred upon the metal nuclei.

This method has several drawbacks. The method of assigning the electrons to the nuclei is not unique, and the charge derived is strongly basis set dependent. However, as the same basis sets have been consistently used in this thesis, the trends in the charge on the TM are of some interest. Moreover, it is a useful tool to check the Hartree-Fock solutions are consistent across the series, and to examine the effect of changing cluster size.

### 6.2.7. Sources of error.

It is important to have an idea of the errors inherent in the various approximations utilised in carrying out *ab initio* calculations, however, especially when using a LCAO approach, this can be somewhat difficult. Sources of error specific to some property calculations have been covered in the material above e.g. BSSE for binding energies; here general systematic errors will be discussed. The main difficulty in assessing potential error is that in most cases we are interested in small differences between large terms and it is to be expected that many of the systematic errors in the calculations will cancel. The sizes of the errors discussed here are therefore to be considered much larger than will actually be observed.

There are three main sources of error associated with the present calculations

(i) Inadequacies of the method, especially the neglect of correlation energy in the HF approximation.

(ii) Errors associated with the use of a finite the basis set.

(iii) Errors associated with using a finite cluster.

To estimate the correlation energy of the systems examined calculations were carried out on a $Ni_sC_{28}H_{36}$ cluster using a 631G* basis set. One calculation used the HF approximation another was a DFT calculation using the full HF exchange energy and the LYP [20] correlation functional: the exchange correlation energy was found to be 8.2 Hartree for in the DFT calculation and the total energies of the two models differed by 7.8 Hartree. The energy difference, which should approximate the correlation energy, was found to be similar for most density functionals (BLYP[20.21] =8.2 Hartree, B3LYP[22,23]= 9.1 Hartree, PBE96 [28]=7.4 Hartree). The exception was the local density approximation (LDA) where using the SVWN5 exchange-correlation functional [24.25] the total energy was found to be 3.5 Hartree lower than the HF method. In this case the total energy error introduced in the HF approximation is found to be smaller than that in the LDA DFT, however, the LDA treats both exchange and correlation energy approximately, whereas the HF method treats the correlation energy exactly but ignores

the correlation energy: cancellation of errors may be better for one method or the other depending on the environment. The energy differences between the HF and DFT (HF exchange + LYP correlation) for $Ni_s^-$ was 7.8 Hartree and for $Ni_i^0$ 7.7 Hartree, this difference of around 0.1 Hartree (2.5 eV) is the sort of error possible when comparing energy differences between clusters, much smaller than the total correlation energy.

The error associated with a finite basis set is hard to assess as with a linear combination of atomic orbitals (LCAO) method there is no methodical way to improve the basis set, unlike the situation when a plane wave basis is utilised. The BSSE errors discussed in section 6.2.4 probably represent a fairly good estimate of the errors in energy differences introduced by the basis sets used – about 1.5 eV for the MINI basis set and 1eV for the larger TZV basis.

Errors introduced by finite cluster size, apart from the electrostatic contribution discussed above (6.2.4), should be modest compared to the other sources mentioned. It was found that results on similar clusters to those used here (80-90 total atoms) were reliable, with results changing by only 1-2% depending on the cluster chosen [3]. For systems liable to large relaxations bigger clusters maybe necessary, but for the present calculations errors due to finite cluster size should be insignificant compared to the other approximations used.

The total error in a given calculation may be very large, but these errors are largely systematic and will, to a large degree, cancel when energy differences are used. In order to show this a brief comparison of results in this thesis with published results is made. Results are compared to those published by J.Goss [26] and Larico *et al* [27]. Both used DFT methods, the former the local spin density approximation and LCAO basis sets, the latter the PBE [28] exchange-correlation functional with a linear augmented plane wave basis.

| | This thesis | Goss [26] | Larico [27] |
|---|---|---|---|
| $Ni_s^-$-C nearest neighbour distance / $A^0$ | 1.82 | 1.89 | 1.77 |
| $Ni_s^-$-C next nearest neighbour dist. / $A^0$ | 2.67 | 2.58 | - |
| $Ni_s^-$ Single electron excitation energy / eV | 4.2 | 1.7 | 3.7 |
| $Ni_i^0$-C nearest neighbour distance / $A^0$ | 1.73 | - | 1.73 |
| $Ni_i^0$ Crystal field splitting / eV | 1.4 | - | 1.8 |
| Stability of $Ni_s^0$ over $Ni_i^0$ / eV | 10.5 | - | 8.7 |

There is little data to compare to, however, the similarity to these results, and to the calculations of Johnston *et al* [5], are encouraging.

In conclusion the estimated errors for energy differences are of the order 1-2 eV BSSE, 2-3 eV neglect of correlation energy and for charged clusters an additional term discussed above (section 6.2.4). However, in practice the errors may be somewhat smaller due to fortuitous cancellations and a total error of 2-3 eV is probably more realistic when comparing different clusters (to avoid overcrowding these error estimates have not been included in the figures below, but should be kept in mind when viewing the results of calculations). The exception is for the binding energy calculations, where the neglect of correlation energy within the Hartree-Fock approximation causes the TM point defects in diamond to be unbound and a large systematic error is present. Comparisons across the transition series are likely to be far more accurate than is suggested here and energy variations across the series should be quite reliable.

## 6.3 Electronic structure.

### *6.3.1 Interstitial TM defects.*

With no dangling bonds, because qualitatively it does not disrupt the bonding of the diamond crystal, the interstitial can be looked at as a good example of the Ludwig-Woodbury model [29]. All the transition metals were found to produce states in the band gap, mainly formed from the metal's d-orbitals. These are split into $t_2$ and e orbitals by the crystal field.

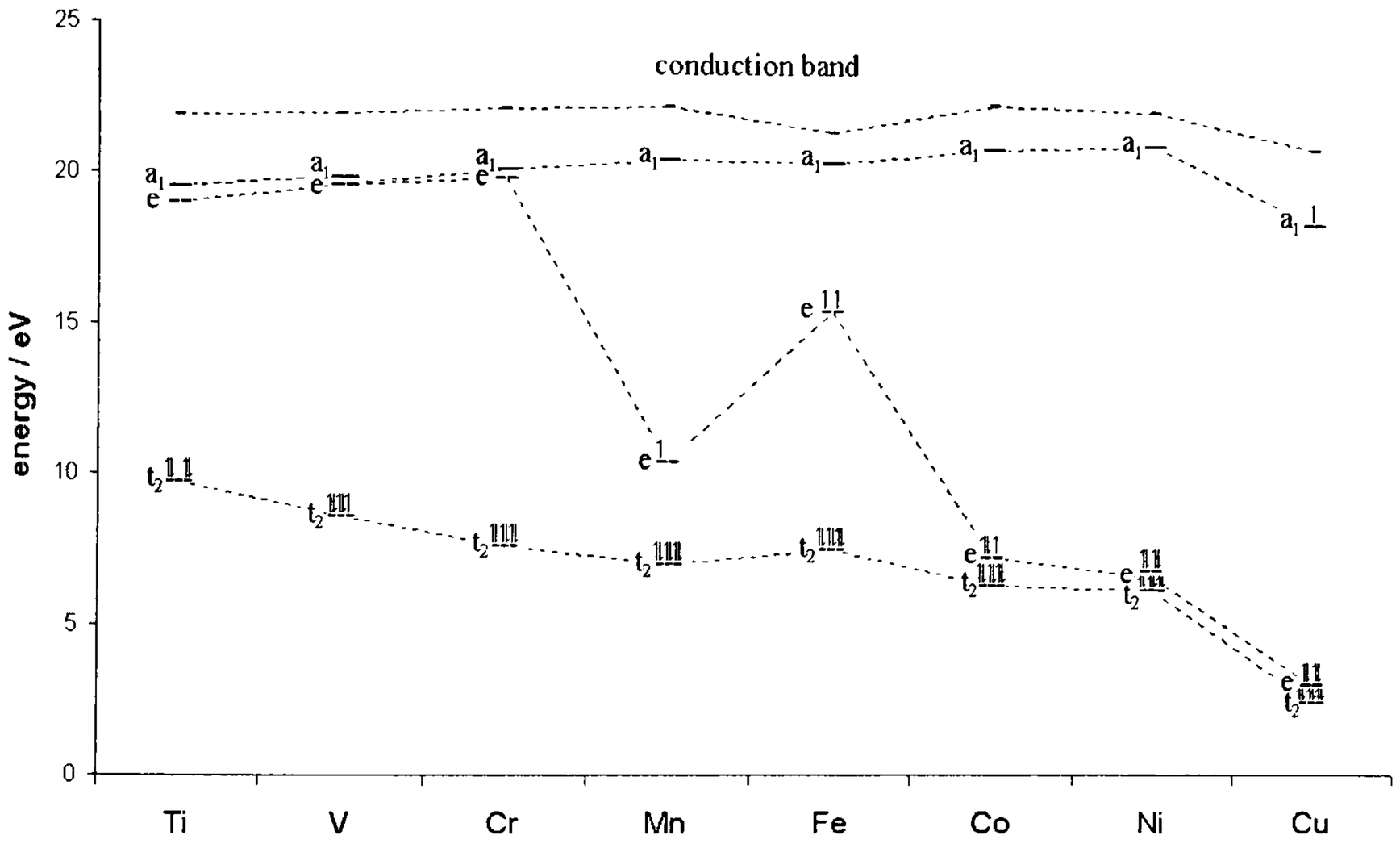


**Figure 6.3.** The energies of the orbitals principally derived from the 3d and 4s orbitals of the atomic TM. Energies are measured relative to the top of the valence band. The conduction band is shown at top of figure. Calculations conducted with a MINI basis set on the $[TM_iC_{26}H_{30}]^0$ clusters.

Figure 6.3 shows the energies of the one-electron orbitals that are considered to derive principally from the atomic metal 3d and 4s orbitals. As observed experimentally for $Ni_i^+$, the ordering of the d-orbital derived states is $t_2$<e. In general, the $t_2$ orbitals drop slightly across the transition series, whilst the energy of the e orbitals rises to a peak somewhere in the middle of the series then decreases towards the $t_2$ orbitals quite rapidly. The

solutions for the negatively charged clusters are highly irregular across the series, indicating that the extra electron is very weakly bound if at all. The negatively charged clusters would not converge at all for the TZV basis set.

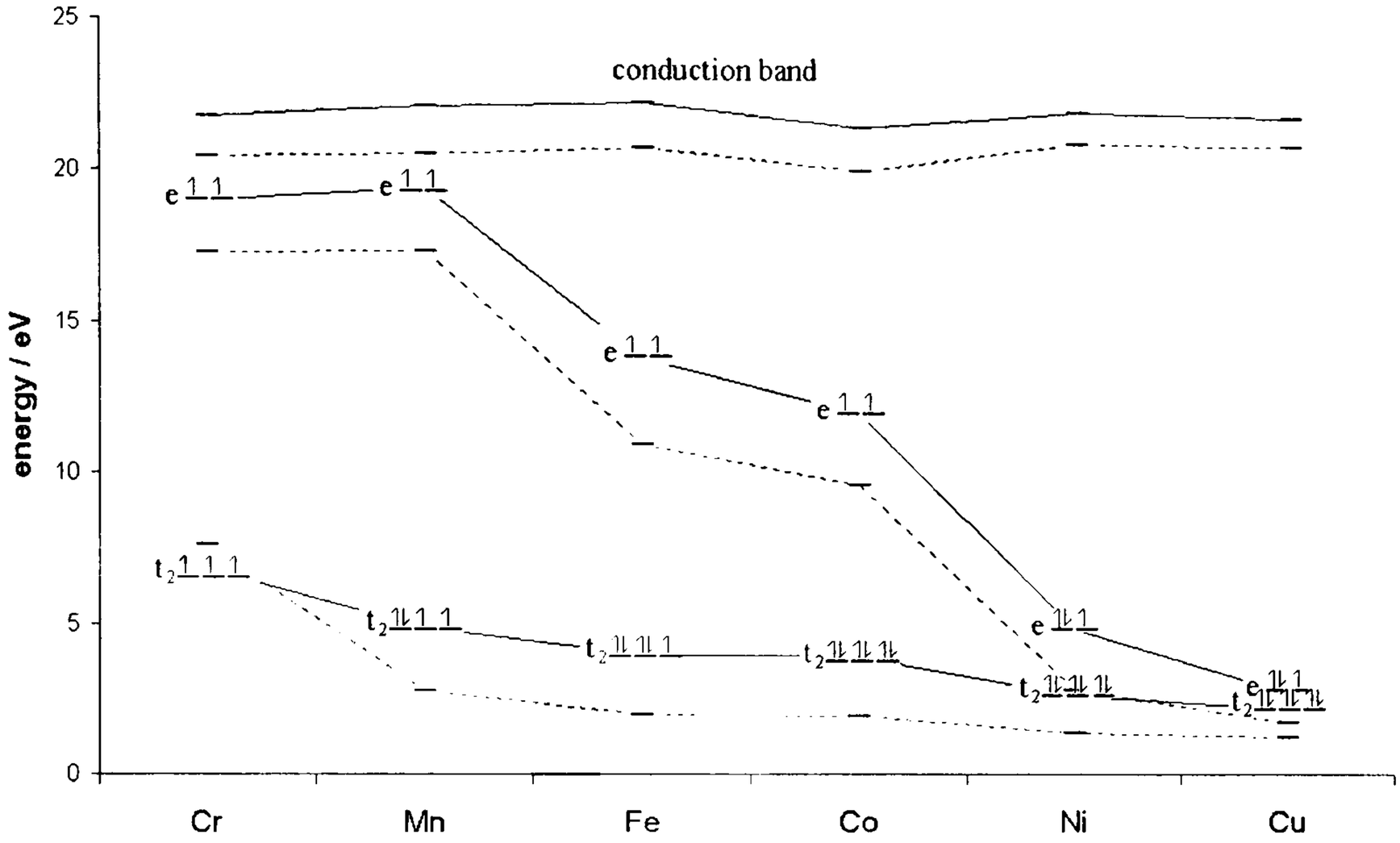


**Figure 6.4.** Orbitals of the $TM_i^+$ defects for the two cluster sizes considered. Orbitals joined by dotted lines are for the larger $TM_iC_{26}H_{30}$ cluster. Energies are measured relative to the valence band.

The orbitals from the two interstitial clusters considered are very similar (Figure 6.4). The effect of the larger cluster is simply to move all the orbitals 2-3 eV closer to the valence band. The similarity of the wavefunctions is again suggested by the analysis of the charge on the TM (see section 6.3.5).

### *6.3.2 Substitutional TM defects.*

The following HF calculations suggest that the two models (see section 2.2.4.2), one due to Ludwig-Woodbury [29] and the other the vacancy model [30], are extremes that are not met in practice. To explain the electronic states obtained form Hartree-Fock calculations on

substitutional transition metal clusters, it is necessary to consider the full set of states, as the vacancy and metal orbitals often appear at comparable energies.

As the transition series is crossed the metal orbitals come down in energy due to the incomplete screening of the additional nuclear charge. This effect suggests that the metal orbital model will be most accurate at the beginning of the transition series, and for the negatively charged substitutional complexes. Figure 6.5 shows this, but even for $Ti_s^-$ it is found that covalent bonding is significant, where the metal $t_2$ orbital has 40% vacancy orbital character. As the series is crossed the e orbitals drop sharply in energy, becoming lower in energy than the vacancy derived orbitals. However, the metal $t_2$ orbitals interact with the vacancy orbitals of the same symmetry; an avoided crossing is approached, where the upper $t_2$ orbitals become increasing vacancy like. This leads to an electronic scheme $(e)^4(a_1)^2(t_2)^6(t_2)^{N-8}$ or $(e)^4(t_2)^6(a_1)^2(t_2)^{N-8}$ for the later transition metals. For example, $Ni_s^-$ (see Figure 6.5) is found to have a ground-state $(e)^4(a_1)^2(t_2)^6(t_2)^3$.

A further effect determines the ordering of the vacancy $a_1$ and $t_2$ orbitals. Previously the metal 4s level has been neglected. This is an old idea from crystal field theory, which mainly deals with positively charged complexes. As exterior and nuclear charge increase, the 3d electrons are stabilised much more strongly than other orbitals (particularly 4s) due to the charge being inefficiently screened. However, in $TM_s^-$ complexes this argument does not hold, and the 4s orbital can be involved in bonding interactions. In $T_d$ symmetry it is of the same totally symmetric representation as the $a_1$ vacancy state, and can interact to form a strongly bonding orbital. This leaves the $a_1$ state lower in energy than the vacancy $t_2$ orbitals for the negatively charged complexes.

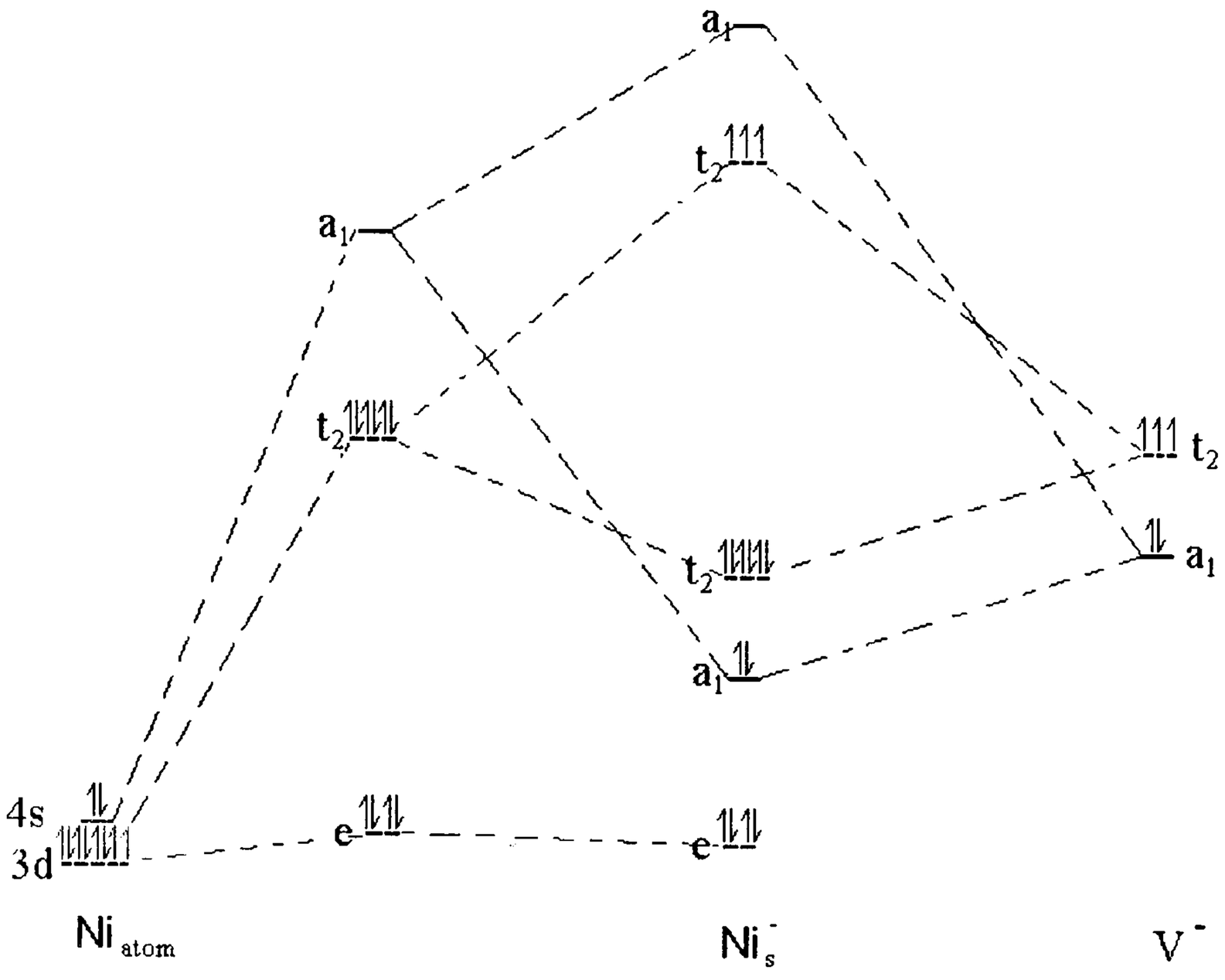


**Figure 6.5.** A schematic molecular orbital diagram for $Ni_s^-$. The energy level structure shown is that obtained from the HF calculations in this thesis. The formation of $Ni_s^-$ is depicted as a negatively charged vacancy interacting with the neutral metal atom.

For the neutral and positively charged complexes this ordering is reversed: the interaction with the metal 4s orbital stabilising the $a_1$ state is reduced, and the interaction between the two $t_2$ states increases. The resulting electronic configuration is $(e)^4(t_2)^6(a_1)^2(t_2)^{N-8}$ which corresponds qualitatively with the vacancy model.

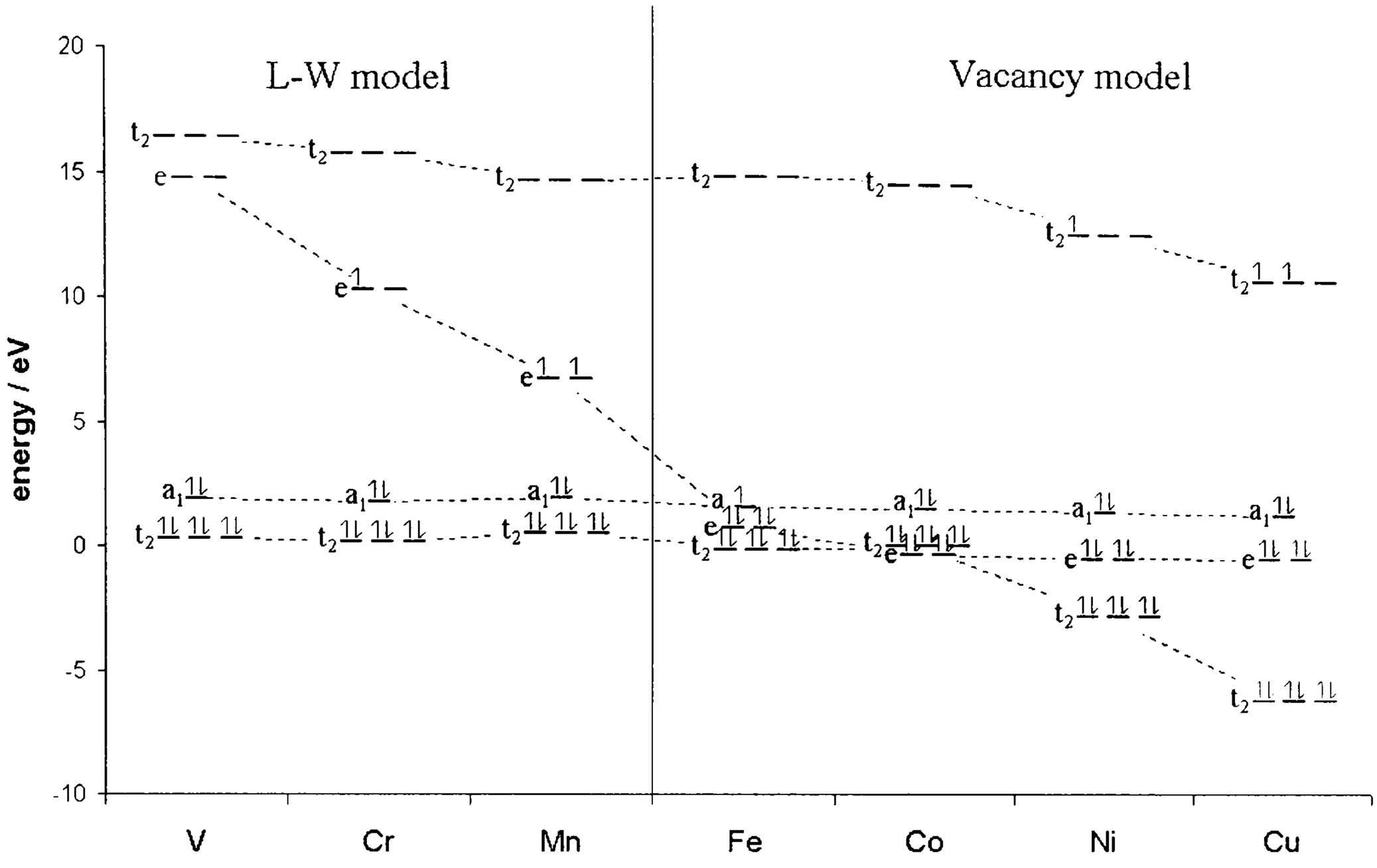


**Figure 6.6.** The one-electron orbitals of $TM_s^+$. The left-hand side clearly shows behaviour typical of the Ludwig-Woodbury model, but from Fe onwards orbitals are qualitatively vacancy like. Energies are in eV relative to the top of the valence band.

The electronic states of the transition metal complexes are, therefore, found to change smoothly between approximating the metal orbital model of Ludwig and Woodbury at the beginning of the transition series in negatively charged clusters, through to approaching the vacancy model for positively charged complexes at the end of the transition series. Furthermore, the character of the higher energy $t_2$ orbitals changes in the same manner, being primarily derived from metal orbitals at the beginning of the series and becoming more vacancy-like as the transition series is crossed.

| | Ti | V | Cr | Mn | Fe | Co | Ni | Cu |
|---|---|---|---|---|---|---|---|---|
| $TM_s^-$ | $(a_1)^2$ $(t_2)^6$ $(e)^1$ | $(a_1)^2$ $(t_2)^6$ $(e)^2$ | $(a_1)^2$ $(t_2)^6$ $(e)^3$ | $(e)^4$ $(a_1)^2$ $(t_2)^6$ | $(e)^4$ $(a_1)^2$ $(t_2)^6(t_2)^1$ | $(e)^4$ $(a_1)^2$ $(t_2)^6(t_2)^2$ | $(e)^4$ $(a_1)^2$ $(t_2)^6(t_2)^3$ | $(t_2)^6$ $(e)^4$ $(a_1)^2$ $(t_2)^4$ |
| $TM_s^0$ | $(a_1)^2$ $(t_2)^6$ | $(t_2)^6$ $(a_1)^2$ $(e)^1$ | $(t_2)^6$ $(a_1)^2$ $(e)^2$ | $(t_2)^6$ $(a_1)^2$ $(e)^3$ | $(e)^4$ $(t_2)^6$ $(a_1)^2$ | $(e)^4$ $(t_2)^6$ $(a_1)^2(t_2)^1$ | $(e)^4$ $(t_2)^6$ $(a_1)^2(t_2)^2$ | $(e)^4$ $(t_2)^6$ $(a_1)^2(t_2)^3$ |
| $TM_s^+$ | | $(a_1)^2$ $(t_2)^6$ | $(t_2)^6$ $(a_1)^2$ $(e)^1$ | $(t_2)^6$ $(a_1)^2$ $(e)^2$ | $(t_2)^6$ $(a_1)^2$ $(e)^3$ | $(e)^4$ $(t_2)^6$ $(a_1)^2$ | $(t_2)^6$ $(e)^4$ $(a_1)^2(t_2)^1$ | $(t_2)^6$ $(e)^4$ $(a_1)^2(t_2)^1$ |

**Table 6.2**. The electronic configurations of low spin substitutional $TM_sC_4H_{12}$ clusters. Lightly shaded complexes have electronic configurations consistent with the metal-orbital model. Darker complexes are consistent with the vacancy model. Unshaded complexes have electronic configurations midway between the two extreme models.

The valence orbitals seemed relatively unaffected by changes in cluster size, or basis set (see Figure 6.7). Comparisons for $Fe_s^0$, $Cr_s^0$ , $Ni_s^-$ and $Cu_s^0$ also showed that the electronic structure of the different clusters and basis sets was similar. This is the justification for carrying out MCSCF calculations on the very small $TM_sC_4H_{12}$ clusters.

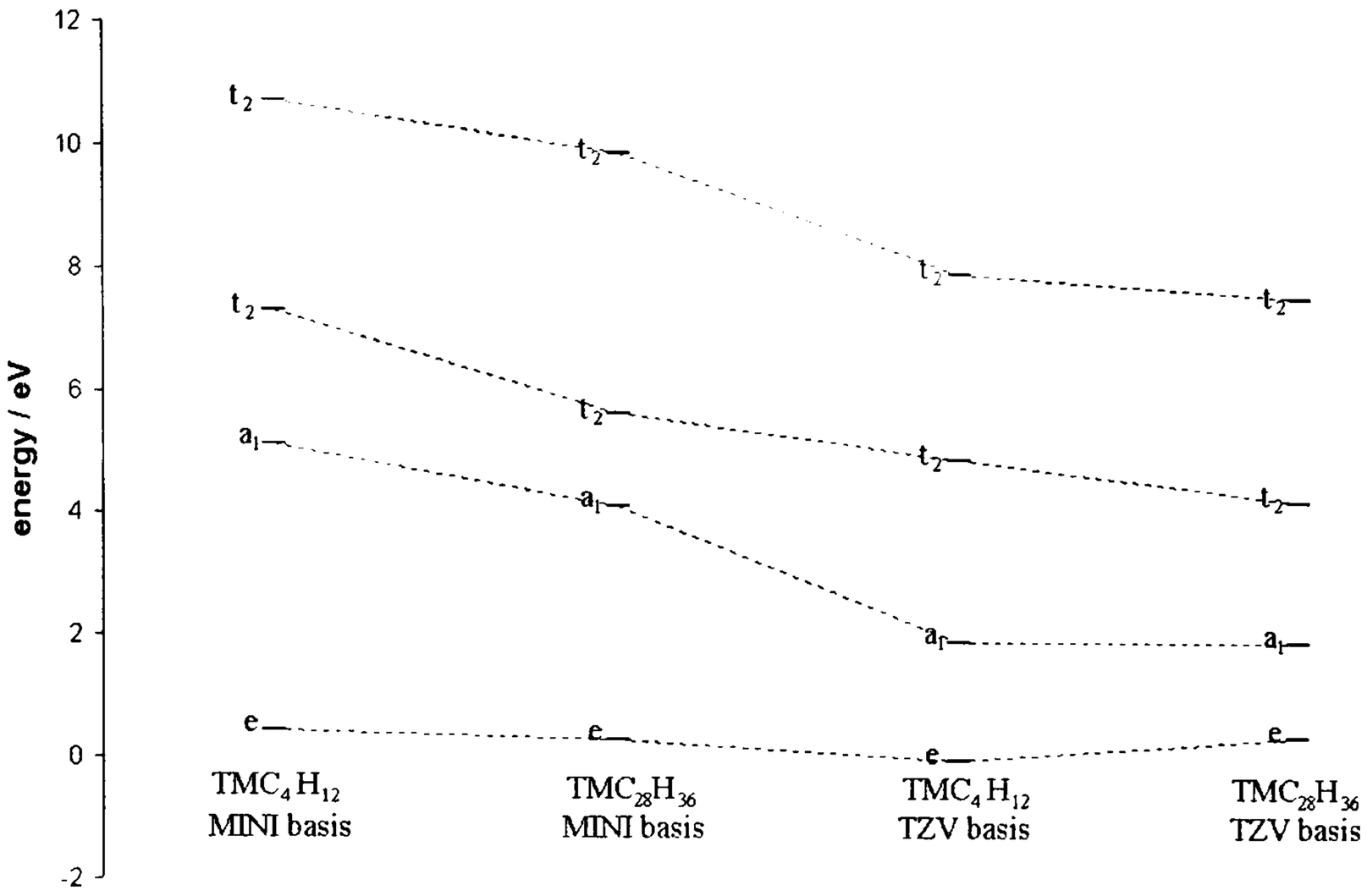


**Figure 6.7.** Orbitals of $Ni_s^-$ in the various clusters and basis sets used. Energies are measured relative to the valence band edge.

### *6.3.3 Semivacancy Complexes.*

A similar situation exists to that of the substitutional TMs. In the divacancy structure the removal of two carbon atoms leads to a defect of $D_{3d}$ symmetry and results in six dangling bonds, of $a_{1g}$, $a_{2u}$, $e_g$ and $e_u$ symmetry. The TM is assumed to occupy the centre of inversion of this structure, and its d-orbitals span $a_{1g}$ and $2e_g$ irreducible representations of the point group. In the divacancy, calculations suggest that the dangling bond orbitals occur in order of increasing energy $a_{1g} < a_{2u} < e_g < e_u$[31]. However, the current calculations suggest that the ability of the metal d-orbitals to mix in and increase the overlap in the *gerade* orbitals reduces their energy, giving an orbital ordering $e_g < a_{1g} < a_{2u} < e_u$. The question that need to be answered, as with the substitutional TM defects, is whether the valence orbitals of the $TM_{sv}$ complexes are divacancy-like or similar to the conventional LW model. The low spin electronic configurations are investigated below.

The one-electron orbitals for the $TM_{sv}^-$ complexes are shown in Figure 5. $V_{sv}^-$ is seen to approximate to the standard crystal-field model, the divacancy orbitals are filled, and the unoccupied metal d-orbitals lie at a higher energy. The metal orbitals are as expected for a slightly distorted octahedral environment – $e_g$ + $a_{1g}$ at lower energy approximately degenerate, and $e_g$ at higher energy. The picture changes, however, as the transition series is crossed. The energy of virtual orbitals in the HF approximation is always too high, and when occupied it is found that the metal orbitals sink below the divacancy orbitals. Consequently it is found that the valence orbitals of all the TM semivacancy complexes are divacancy-like. Physically this indicates that the orbitals involved are at similar energies, and that electron-electron repulsions cause large changes to the one-electron orbitals, depending on the electronic configuration adopted.

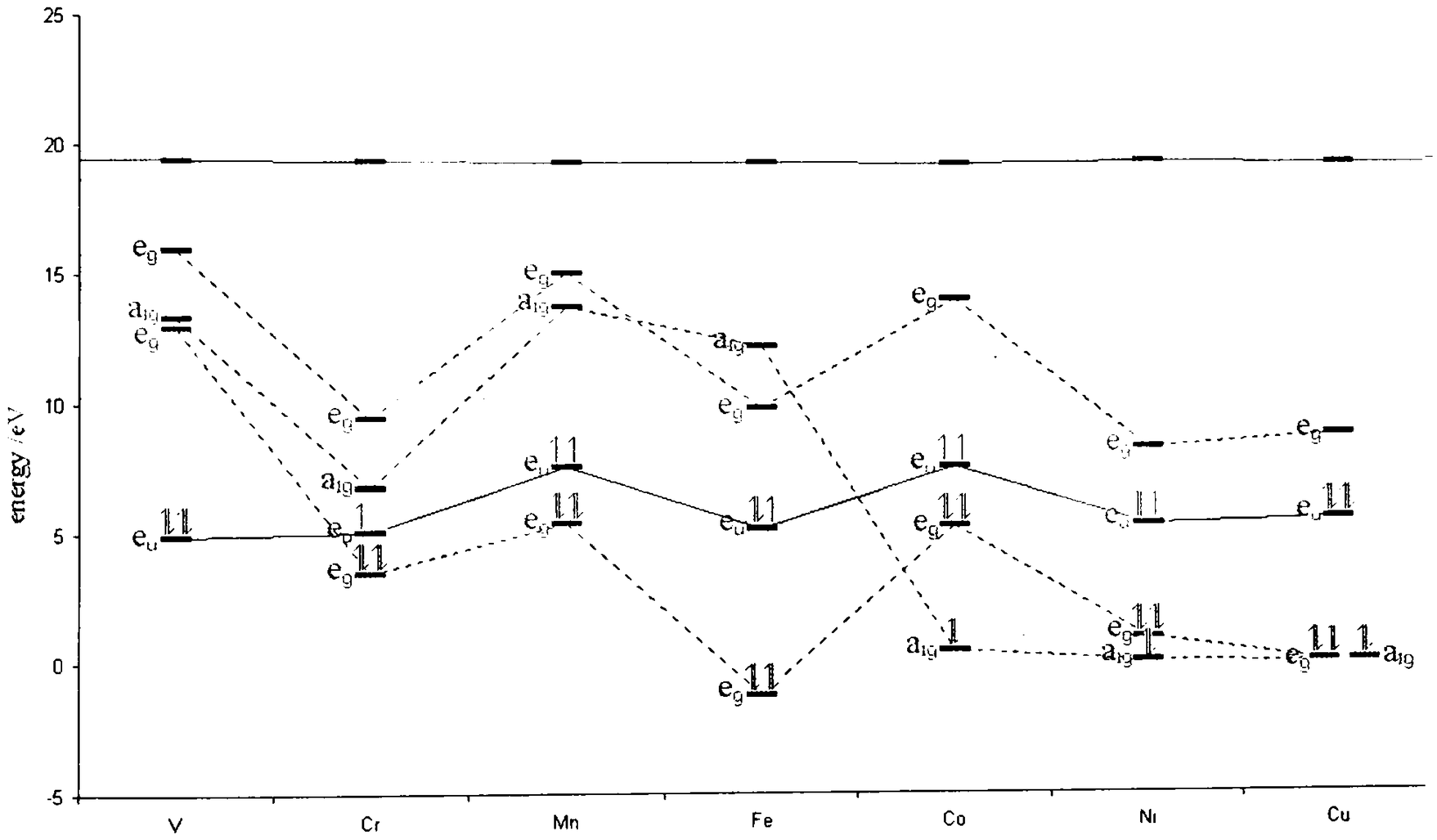


**Figure 6.8.** Orbitals of the $TM_{sv}^-$ complexes. For clarity only the upper divacancy orbital is shown ($e_u$, joined by solid line). Energies are measured relative to the valence band. The conduction band is shown at the top of the diagram.

Moving form $V_{sv}^-$ to $Cr_{sv}^-$ an extra electron must be accommodated. Instead of simply being placed into a metal $e_g$ orbital to give a $(divac)^{12}(metal)^1$ configuration, it is found that the change in electron-electron repulsions strongly favours filling the metal $e_g$ orbital.

at the expense of some of the divacancy orbitals, to give a $(divac)^8(metal)^4(divac)^1$ configuration. The divacancy orbitals then fill until it becomes preferable to occupy another metal orbital, where again, there is a balance between completely filling the metal orbital and leaving holes in the divacancy derived orbitals (favoured) or having partially occupied metal orbitals, which is found to be of higher energy in all cases. It is found that the metal $a_{1g}$ becomes filled at Co onwards for all charge states. The second pair of metal $e_g$ orbitals remain unoccupied.

The electronic configurations for low-spin $TM_{sv}$ are then $(divac)^{12}(metal)^0$ for $V_{sv}^-$, $Cr_{sv}^0$ and $Mn_{sv}^+$, $(divac)^8(metal)^6(divac)^x$ for all charge states of Co, Ni, Cu and $(divac)^8(metal)^4(divac)^y$ for all the other $TM_{sv}$ complexes (Table 6.4). The unpaired electrons always occupy a divacancy like $e_u$ orbital. This would explain the lack of Ni hyperfine structure observed at the NE4 EPR centre (Figure 6.8).

### *6.3.4 Ground States.*

Interstitial defects.

The ground state is in question for $TM_i$ complexes having four to seven d-electrons. Table 6.3 shows the ground state and the energy difference to the alternative spin state ground state (in eV) where appropriate. Low spin states are shown in bold.

| | Ti | V | Cr | Mn | Fe | Co | Ni | Cu |
|---|---|---|---|---|---|---|---|---|
| $TM_i^0$ | $(t_2)^4$ | $(t_2)^5$ | $(t_2)^6$ | $(t_2)^6(e)^1$ | $(t_2)^6(e)^2$ | $(t_2)^6(e)^3$ | $(t_2)^6(e)^4$ | |
| ground state | $^3\mathbf{T_1}$, | $^2\mathbf{T_2}$ | $^1\mathbf{A_1}$ | $^2\mathbf{E}$ | $^3A_2$ | $^2E$ | $^1A_1$ | |
| alternate | (+0.91) | (+1.55) | (+1.42) | (+0.08) | | | | |
| ground-state | $^5E$ | $^6A_1$ | $^5T_2$ | $^4T_2$ | | | | |
| $TM_i^+$ | | $(t_2)^4$ | $(t_2)^3(e)^2$ | $(t_2)^4(e)^2$ | $(t_2)^5(e)^2$ | $(t_2)^6(e)^2$ | $(t_2)^6(e)^3$ | $(t_2)^6(e)^4$ |
| ground state | | $^3\mathbf{T_1}$ | $^6A_1$ | $^5T_2$ | $^4T_1$ | $^3A_2$ | $^2E$ | $^1A_1$ |
| alternate | | (+0.44) | (+0.79) | (+0.05) | (+0.77) | | | |
| ground-state | | $^5E$ | $^2\mathbf{T_2}$ | $^1\mathbf{A_1}$ | $^2\mathbf{E}$ | | | |

**Table 6.3.** Ground state electronic configurations of $TM_i$. Alternative ground states are also indicated, the energy differences between the spin-states (in eV) are shown in brackets. States arising from the strong-field model are in bold-type.

It is found that both high and low spin ground states are predicted here, and the simple assumption that the ligand field is very large in diamond, favouring low spin states, is not supported. It can be seen that the low spin configurations are found at the beginning of the series, for the neutral clusters; this is in agreement with expectation if the splitting between metal orbitals is caused by covalent bonding – the diffuse d-orbitals at the beginning of the series have a good overlap with the ligand orbitals, resulting in large interactions between the orbitals. As the series is crossed, or when positive charge is added to the cluster, the d-orbitals, which shield each other poorly from the charge, become much more localised on the metal and consequently their overlap with the ligand-orbitals is significantly reduced. At the same time as the gap between the one-electron orbitals is reducing, the electron-electron repulsion terms will increase as the orbitals become more localised.

## Substitutional defects.

Low-spin ground-states have been found for the substitutional complexes in MCSCF calculations on small clusters ($TM_sC_4H_{12}$, with a MINI basis set). High spin states are

much less likely to appear for the substitutional complexes than for the interstitial clusters, extremely covalent bonding is found in most cases which reduces electron-electron repulsions, and the energy gap between the levels is found to be much larger than for the interstitial case. In all cases considered the ground state is found to be low spin. For instance, the triplet state of $Co_s^-$ is found to be 3.25 eV more stable than the quintet state, triplet $Cu_s^+$ is found to be 1.1 eV more stable than quintet $Cu_s^+$ and doublet $Ni_s^+$ is found to be 3.15 eV more stable than its quartet state. Unlike the interstitial complexes, or conventional crystal field models, the energy levels between which high spin and low spin configurations are considered are not constant, making a systematic study difficult without being able to use an active space that covers all possible valence orbitals.

## Semivacancy.

Orbital occupations and the many-electron states produced for the low-spin $TM_{sv}$ are shown in Table 6.4. It can be seen that a very consistent set of ground states emerges from the fact that the divacancy like $e_u$ is always found to be the HOMO. Also, all the complexes are expected to be EPR active except $Cu_{sv}^-$.

| | Mn | Fe | Co | Ni | Cu |
|---|---|---|---|---|---|
| $TM_{sv}^+$ | $(e_g)^4(a_{2u})^2$ $(e_u)^2$ **$^3A_{2g}$** | $(e_g)^4(a_{2u})^2$ $(e_u)^3$ **$^2E_u$** | $(e_g)^4(a_{2u})^2$ $(e_u)^2$ **$^3A_{2g}$** | $(e_g)^4(a_{1g})^2$ $(a_{2u})^2(e_u)^1$ **$^2E_u$** | $(e_g)^4(a_{1g})^2$ $(a_{2u})^2(e_u)^2$ **$^3A_{2g}$** |
| $TM_{sv}^0$ | $(e_g)^4(a_{2u})^2$ $(e_u)^1$ **$^2E_u$** | $(e_g)^4(a_{2u})^2$ $(e_u)^2$ **$^3A_{2g}$** | $(e_g)^4(a_{1g})^2$ $(a_{2u})^2(e_u)^1$ **$^2E_u$** | $(e_g)^4(a_{1g})^2$ $(a_{2u})^2(e_u)^2$ **$^3A_{2g}$** | $(e_g)^4(a_{1g})^2$ $(a_{2u})^2(e_u)^3$ **$^2E_u$** |
| $TM_{sv}^-$ | $(e_g)^4(a_{2u})^2$ $(e_u)^2$ **$^3A_{2g}$** | $(e_g)^4(a_{2u})^2$ $(e_u)^3$ **$^2E_u$** | $(e_g)^4(a_{1g})^2$ $(a_{2u})^2(e_u)^2$ **$^3A_{2g}$** | $(e_g)^4(a_{1g})^2$ $(a_{2u})^2(e_u)^3$ **$^2E_u$** | $(e_g)^4(a_{1g})^2$ $(a_{2u})^2(e_u)^4$ **$^1A_{1g}$** |

**Table 6.4**. Electronic configurations of the $TM_{sv}$ complexes. All have a $(e_g)^4(a_{1g})^2$ set of orbitals derived from the divacancy not shown. Orbitals listed of *gerade* symmetry come

principally from the TM, whilst those of *ungerade* symmetry are similar to divacancy orbitals. The many-electron state is shown bold.

An investigation was then made to see whether any of the $TM_{sv}$ adopted high-spin states. High spin states were found to be stable for $Cr_{sv}^{0}$ ($^5A_{1g}$), $Fe_{sv}^{+}$ ($^4A_{1u}$), $Fe_{sv}^{-}$($^4A_{2u}$) and $Co_{sv}^{0}$($^4A_{2u}$), at energies relative to the low-spin state of –8.5, -0.4, -2.2 and –1.9 eV respectively (see Figure 6.9). It can be seen, however, that the basic positioning of the divacancy and metal orbitals does not change and the discussion in the previous section remains valid. The high-spin states were not studied completely systematically as configurations with multiple open degenerate shells were avoided (see Chapter 2). Furthermore, as there are several one-electron orbitals in close proximity, and hence many-electron states, MCSCF calculations would be needed to be certain of the ground-state of these complexes.

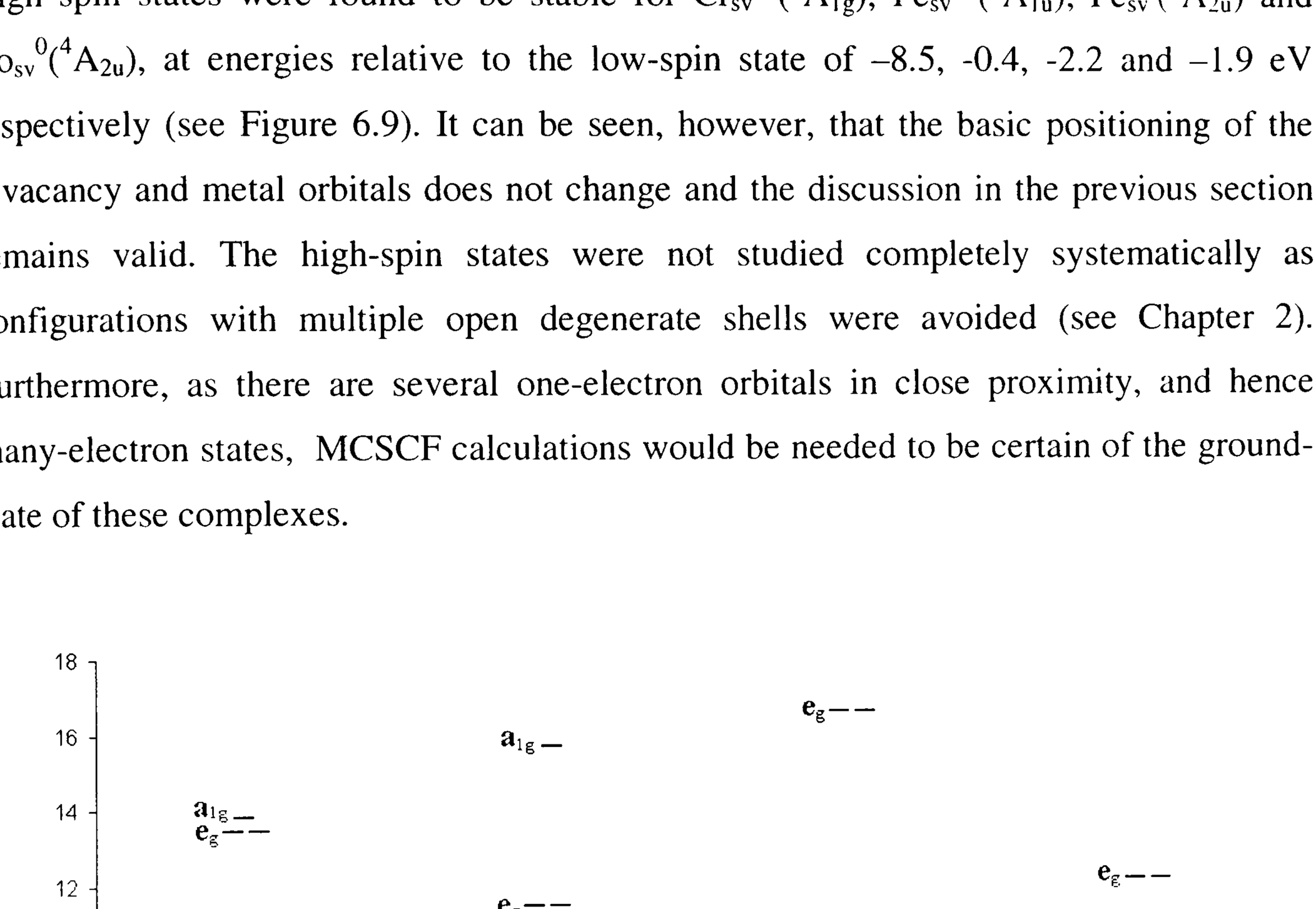


**Figure 6.9.** One-electron orbitals and occupations for the high-spin $TM_{sv}$ defects. All energies are measured from the orbital believed to be the top of the valance band.

### *6.3.5 Charge distributions.*

As discussed in section 6.2.7 charge distributions determined by Mulliken's method need to be treated with care. The dramatic effect of changing basis sets is illustrated in Figure 6.10.

The charge found for the MINI and TZV basis sets is very different. The results for the MINI basis calculations are, however, worth examination. The charge on the TM is very similar for different cluster sizes, as can be seen for $TM_s^0$ in Figure 6.10, and this holds generally for the clusters examined. This supports the similarity in the one-electron orbitals of the different cluster sizes in justifying the use of very small clusters to calculate many-electron states.

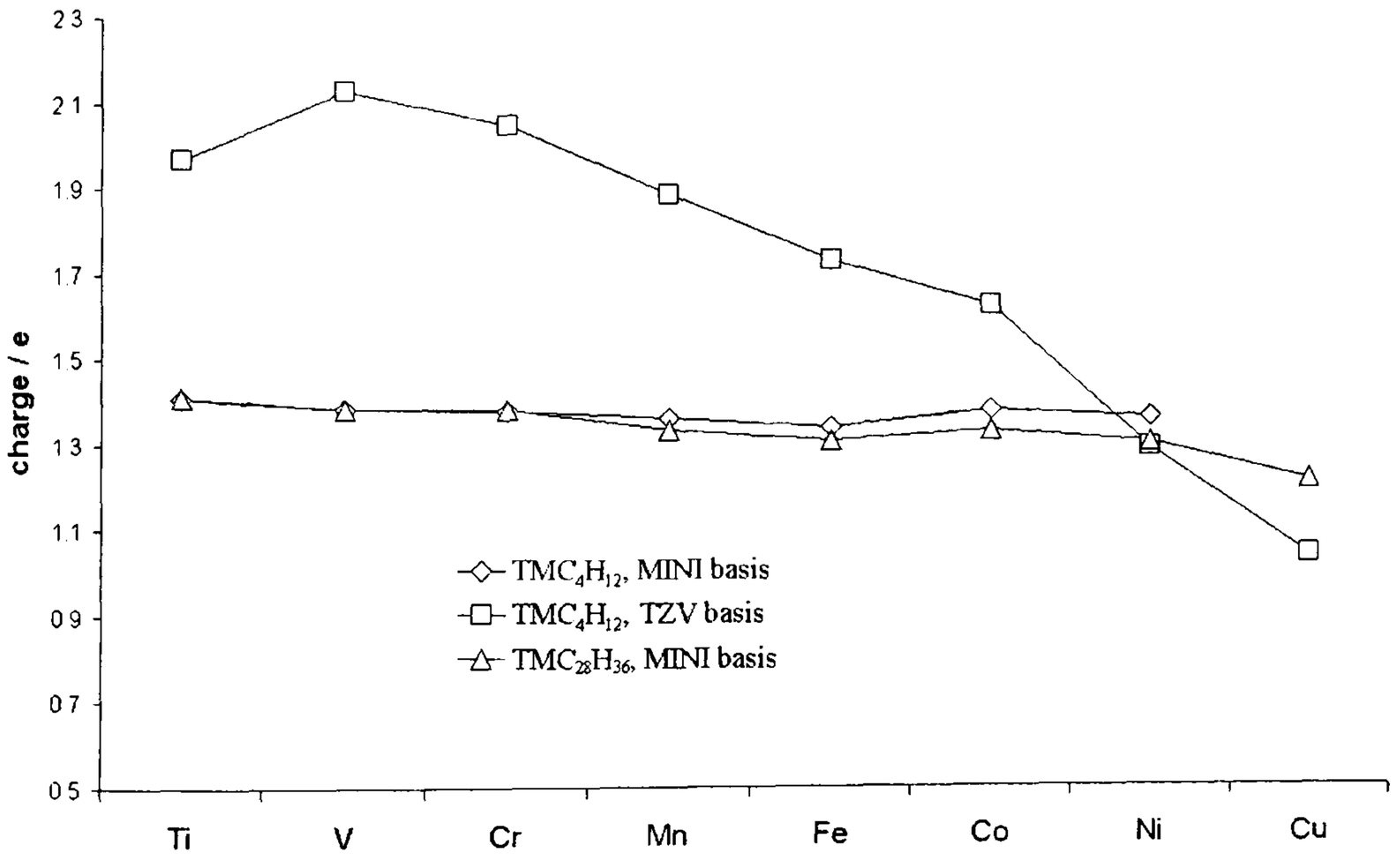


**Figure 6.10.** The Mulliken charge on the TM in $TM_s^0$ clusters.

Another point is that the charge on TM in the clusters behaves very differently for $TM_i$ compared to $TM_s$ or $TM_{sv}$. $TM_i$ show intuitively obvious behaviour, with the charge on the TM increasing as the formal charge on the cluster increases (Figure 6.11).

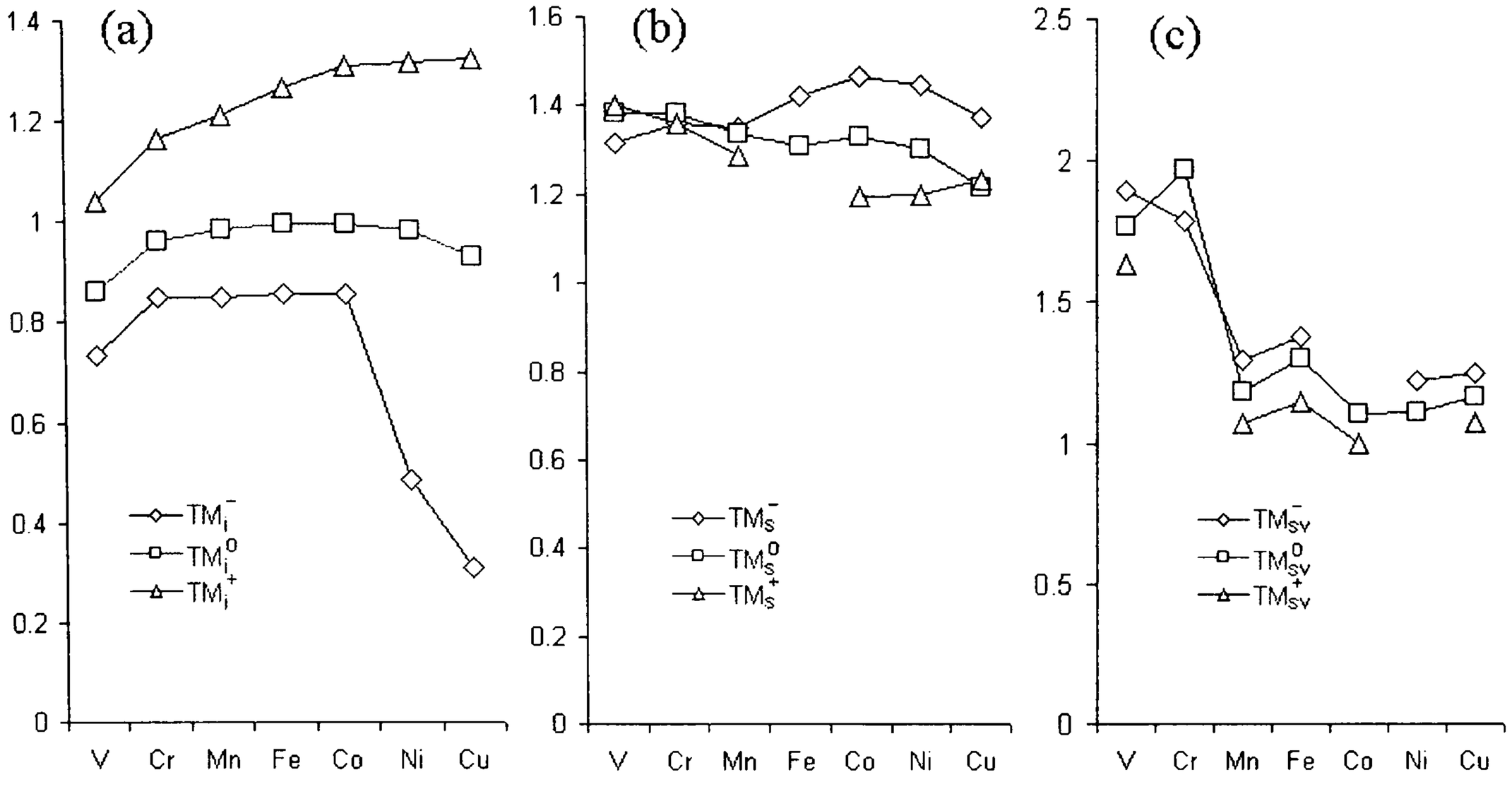


**Figure 6.11.** The Mulliken charges on the TM in TM clusters in diamond. Clusters used are (a) $TM_iC_{26}H_{30}$, (b) $TM_sC_{28}H_{36}$ and (c) $TM_{sv}C_{42}H_{42}$.

For the $TM_s$ and $TM_{sv}$ clusters the reverse is found, the charge on the TM decreases as the formal charge on the cluster increases. This supports the model put forward (section 6.3.3) that the substitutional clusters move towards fitting the vacancy model across the series and as formal charge increases. The charge on the TM in the positive $TM_s$ clusters is lower than in the neutral case because the charge makes the defect more vacancy-like, hence transferring electron density to the TM, the charge is housed in orbitals that are more vacancy-like than the neutral cluster. *Mutatis mutandi* for the negatively charged clusters. The $TM_{sv}$ clusters also show similar behaviour, which supports the notion that they have a similar electronic structure to the $TM_s$ defects.

## 6.4 Binding energies of TM defects.

### *6.4.1 Equilibrium Geometries and Relaxation*

As described in section 2.1.1 the equilibrium geometry of a cluster is found by obtaining the set of nuclear co-ordinates that the minimises its total energy. Geometry calculations

are computationally expensive, as the two-electron integrals must be recalculated at each trial set of nuclear co-ordinates.

It is found that the initial geometries for the clusters specified in section 6.2.3 are good approximations to the equilibrium geometries of the clusters; this means that the geometry of the defect is not very sensitive to the TM present. Including relaxation, whilst gaining a small amount of total energy, makes little difference to the qualitative results obtained from HF calculations. This is especially true for the high symmetry ($T_d$) $TM_s$ and $TM_i$ clusters. The high symmetry means that there are few adjustable parameters in the nuclear co-ordinates, and the clusters stay very close to the standard initial geometries (section 6.2.3). The binding energies for the $TM_sC_{28}H_{36}$ clusters are shown in Figure 6.12, and it can be seen that relaxing a cluster makes a negligible difference to its the binding energy: the energy gains are of the order 0.25 eV.

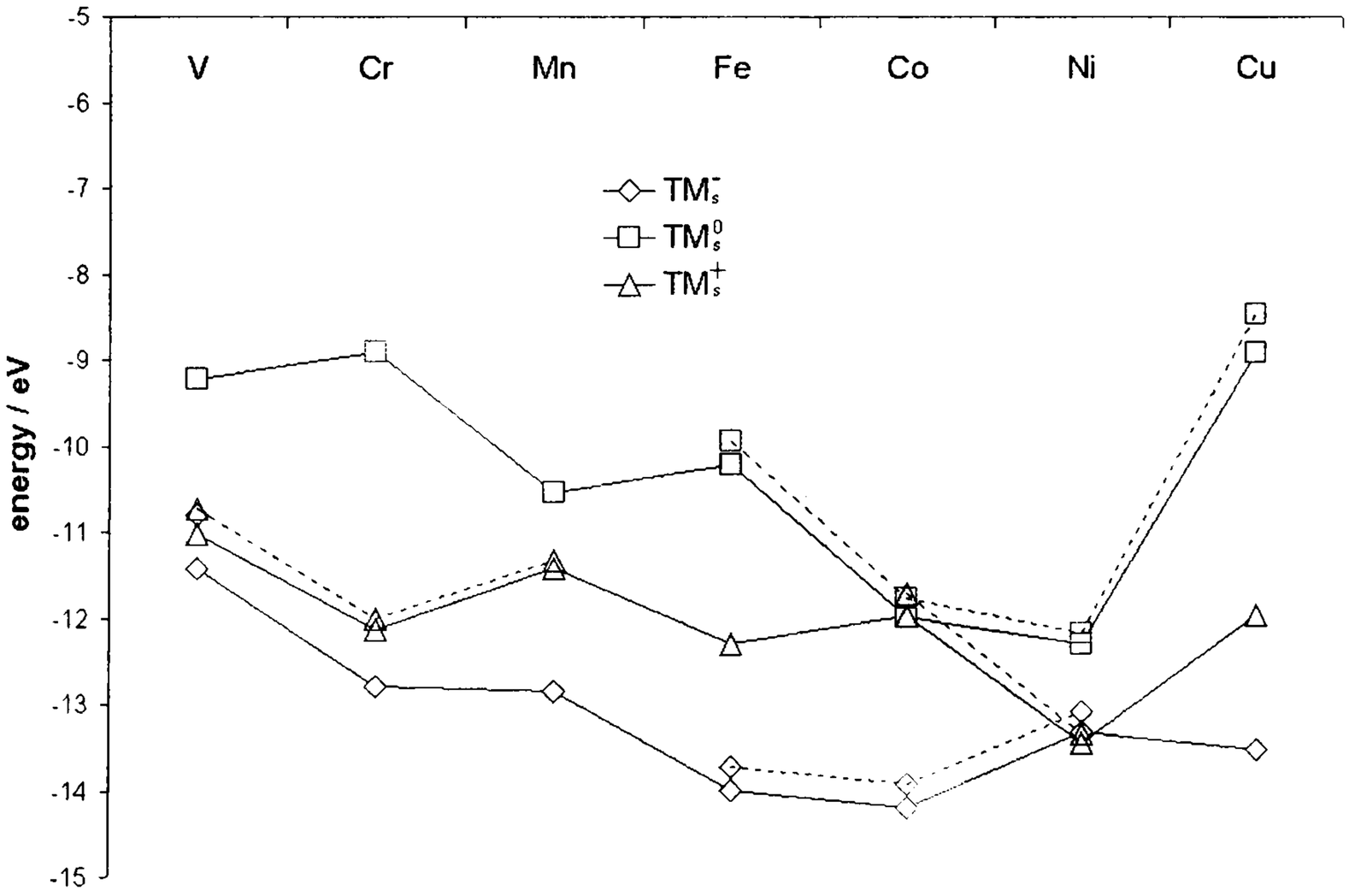


**Figure 6.12.** Binding energies for $TM_s$ clusters, without (solid line) and with (dashed line) allowing the cluster to relax. Unrelaxed clusters use the optimised geometry obtained from a calculation using a TZV basis set on $[Fe_sC_{28}H_{36}]^0$

In lower symmetry relaxation has a greater effect as the equilibrium geometries are further from that of the reference (section 3.5.2). Figure 6.13 below shows the binding energies of the $TM_s(N_s)_2C_{26}H_{36}$ clusters, which are calculated from

$$\Delta H_{BINDING} = E[TM_s(N_s)_2C_{26}H_{36}] + E[C_{29}H_{36}] + E[C_{diamond}] - 2E[N_sC_{28}H_{36}] - E[TM_{solid}] \quad (6.3)$$

The energy gains from relaxation are seen to be in the order of 1-2 eV in this case. The energy gains, however, are found to be fairly consistent across the series, affecting the binding energy but not affecting the general pattern of results. It is also found that the one-electron orbitals are not greatly affected by the change in geometry.

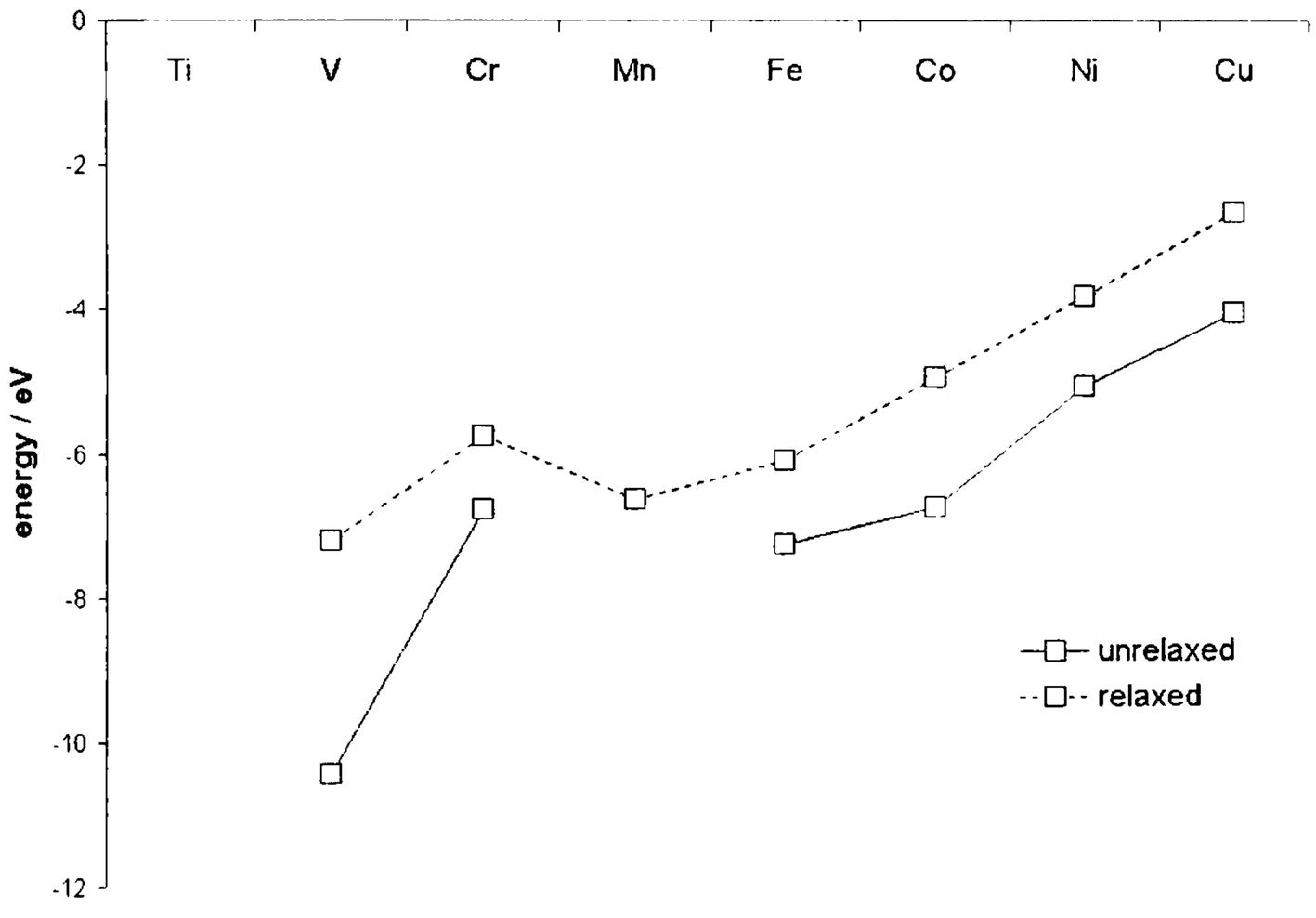


**Figure 6.13.** The binding energies of the neutral $TM_s(N_s)_2C_{26}H_{36}$ complexes.

These results indicate that results from unrelaxed clusters can be used with reasonable confidence, especially when dealing with clusters of high symmetry. The clusters examined in this thesis are quite small, so it is unlikely that accurate equilibrium geometries would be obtained in any case. This is a task that density functional theory is far better suited to, as it can treat much larger clusters efficiently. Many clusters in this

thesis have not been relaxed, but using the geometry of a similar TM defect cluster should still provide a reasonable description of the systems studied.

## Equilibrium geometry of the substitutional TM defects.

The bondlengths of the relaxed $TM_sC_{28}H_{36}$ clusters are shown in Figure 6.14.

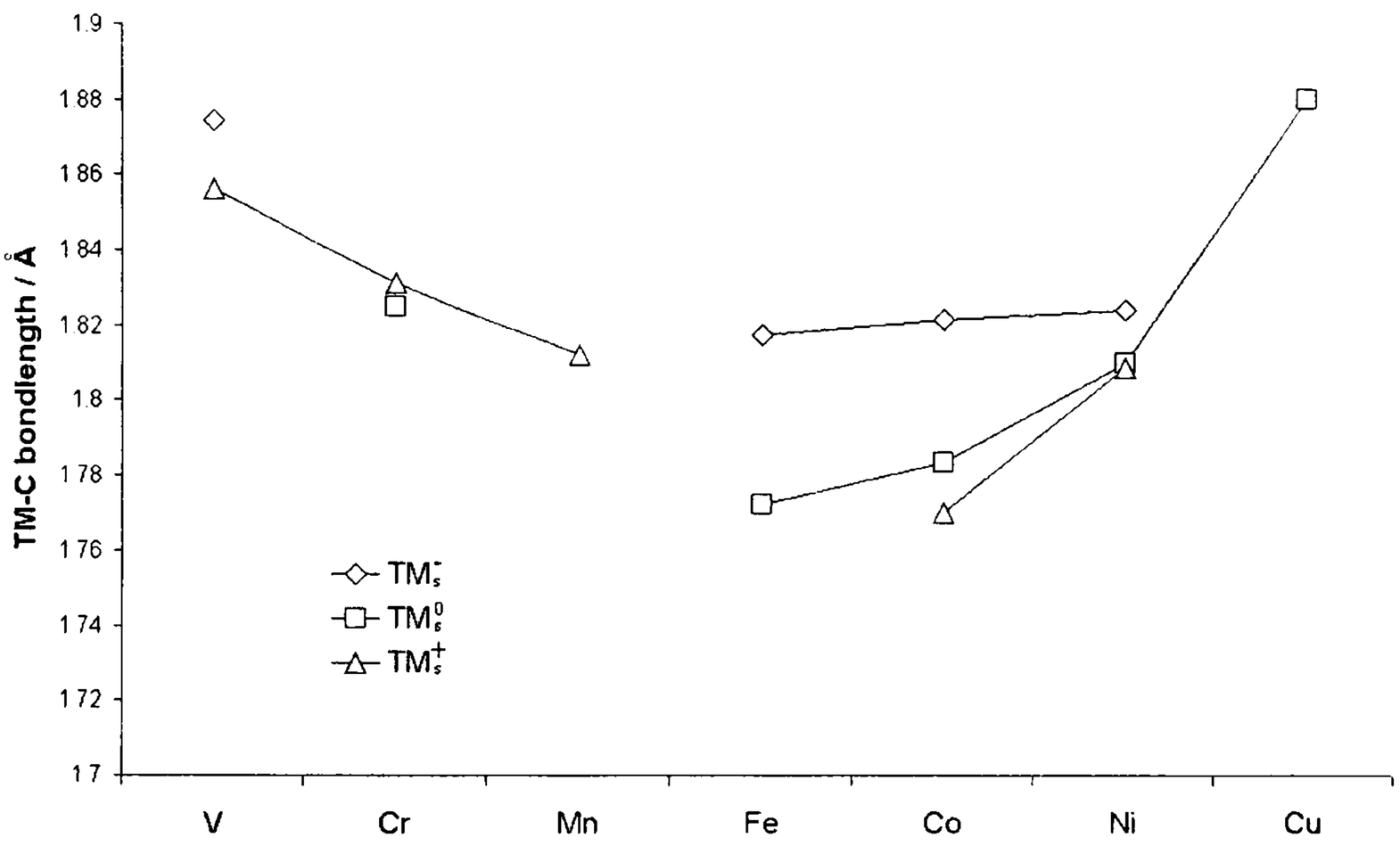


**Figure 6.14.** The bondlengths between the TM and its four nearest neighbour carbon atoms for the $TM_sC_{28}H_{36}$ clusters (MINI basis set).

Early in the series the bondlength diminishes across the series. Here the TM is getting smaller, and extra electrons are being housed in largely non-bonding orbitals (the metal e orbitals in the LW model). This pattern changes when the higher energy $t_2$ orbitals (which as shown in section 6.3.1 are always partially metal-carbon anti-bonding) become occupied. Thus from $Fe_s^0$, $Co_s^+$ (and presumably $Mn_s^-$) the metal-carbon bondlength increases again.

The changes in bond-length are probably exaggerated by the small cluster size, but it can be seen that using the TM-C distance of 0.181 nm (obtained from a calculation using a TZV basis set on $[Fe_sC_{28}H_{36}]^0$) gave good results across the series because it was close to

the average TM-C distance. The ordering of the one-electron orbitals in the clusters was unaffected by relaxation from the reference geometry.

It is expected that the bondlengths will change significantly less for the $TM_i$ and $TM_{sv}$ clusters: the $TM_i$ are not directly bonded into the diamond and $TM_{sv}$ are less stressed, so the size of the TM should be of lower significance. Using clusters with a geometry optimised for one TM should give an adequate description of the other TMs.

### *6.4.2 Interstitial complexes.*

The binding energy of the $TM_i$ defects is defined as

$$\Delta H_{BINDING} = E[TM_iC_xH_y] - E[C_xH_y] - E[TM_{SOLID}] \qquad (6.4)$$

The energy of the TM atom is that of the Hartree-Fock ground-state atom plus the energy of atomisation of the solid metal to account for its environment in the melt (section 6.2.4). The binding energies of $TM_i^0$ are shown in Figure 6.15.

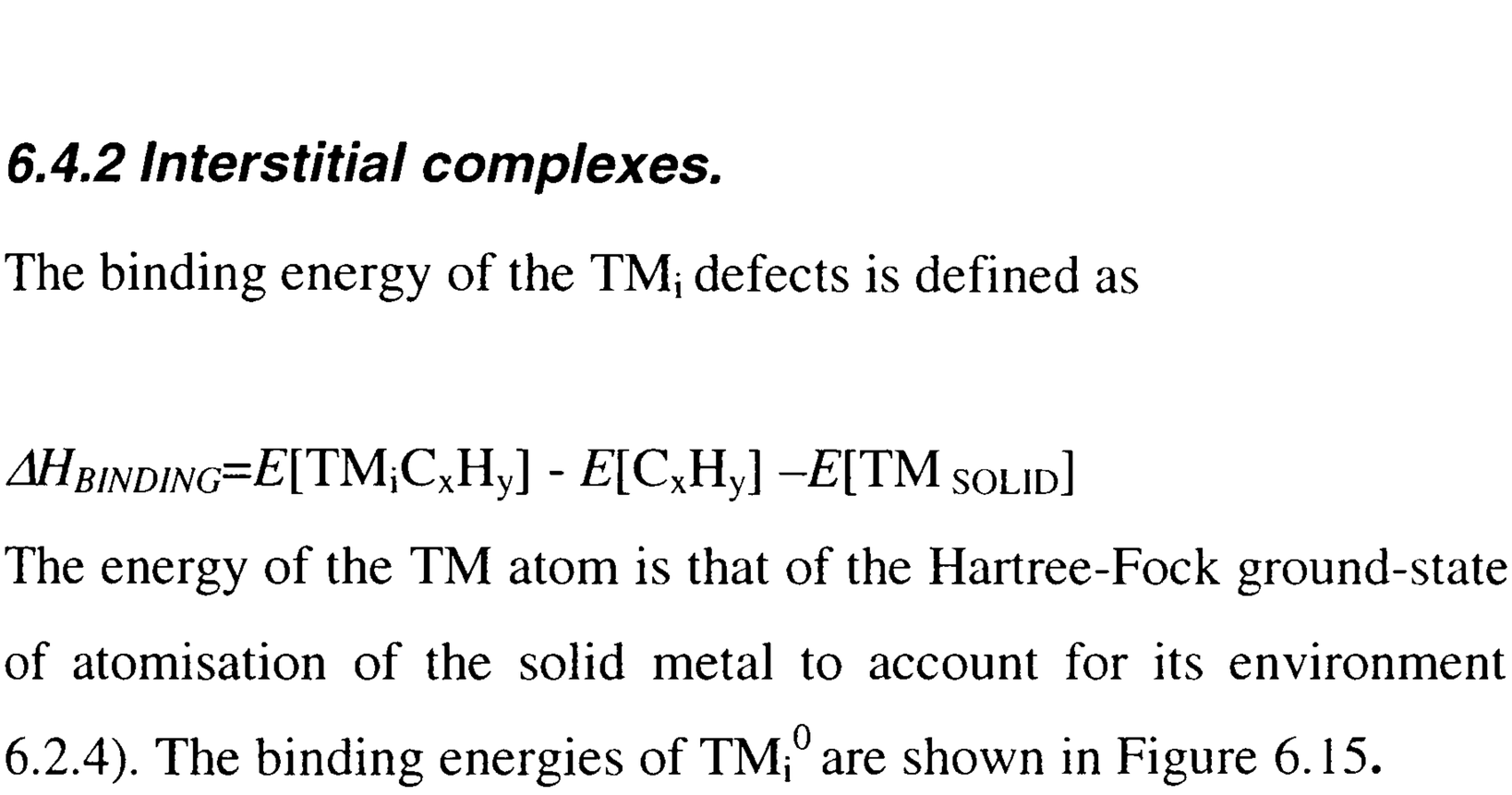


**Figure 6.15**. The binding energy of the neutral interstitial transition metal clusters.

The interstitial centres are observed to become more stable as the transition series is crossed. The binding energies are very similar between the two basis sets used, the TZV basis set being more stable by about 1 eV. The binding energies also show the same discontinuities between metals for the two basis sets (the exception being that Co is relatively more stable in the TZV basis: however, the geometry for these clusters is based on the optimised $Co_i^+$ cluster in a TZV basis, so it is expected that Co will be nearer its equilibrium geometry than the other transition metals). The pattern (excepting Co, TZV) of energy changes is explainable from the electronic configurations of the clusters. There is a relatively constant increase in binding energy across the series. Deviations from this general pattern between two adjacent metals occur when the metal later in the series has a less favourable electronic configuration than the first. For example, from Cr $[(t_2)^6]$ to Mn $[(t_2)^6(e)^1]$ an electron must be accommodated in a high-energy e orbital, consequently Mn shows less extra stability due to its smaller size than might be expected. These changes in energy are small, but when considering the stability of the charged clusters they are reinforced and quite noticeable.

The energy changes across the series are almost identical between the two cluster sizes. However, the larger cluster is significantly less stable. This is due to the larger pure diamond cluster ($C_{26}H_{30}$) being much more stable than the smaller $C_{10}H_{16}$.

As discussed in the introduction (section 6.2.4) the total binding energy includes a term for the promotion of the metal to $3d^N$ from is ground state (normally $4s^2 3d^{N-2}$). Subtracting this energy from the binding energy should give an idea of the strength of the bonding to the crystal.

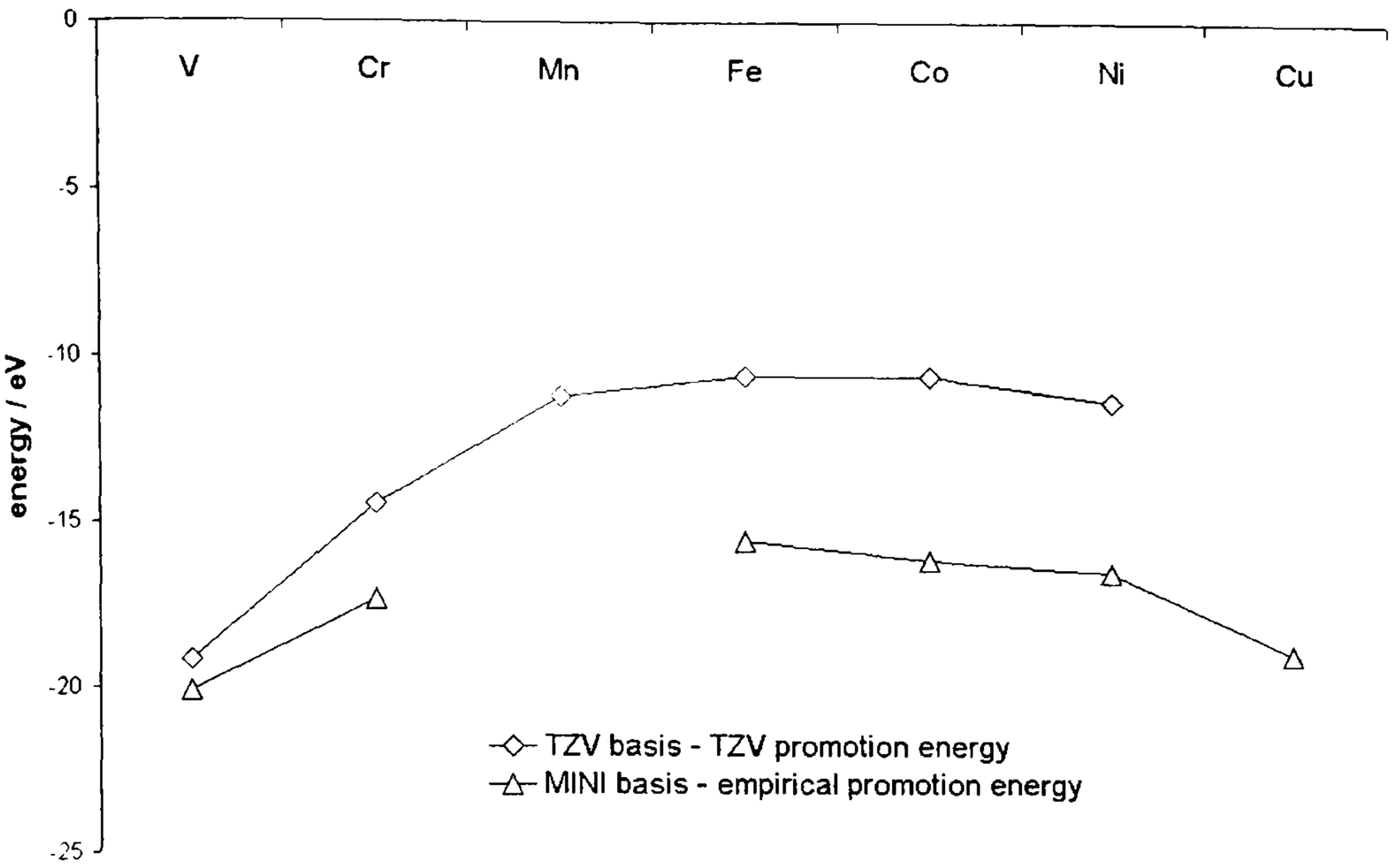


**Figure 6.16.** Binding energy of the $TM_i^0$ clusters relative to the excited transition metal atom - binding energy (Equation 6.4) with the promotion energy of the solvated metal reference atom removed.

The smooth curves in Figure 6.16 are reminiscent of, for instance, the solvation enthalpies of transition metal complexes. The data obtained are explained in terms of a steady increase in stability across the series due to the reduction in atomic radii, with the crystal field stabilisation energy superimposed on top creating the large dome shape [32].

Overall, the stability of the interstitial clusters increases as the series is traversed.

### *6.4.3 Substitutional TM defects.*

The binding energy of a neutral TM into the substitutional cluster is defined as

$$\Delta H_{BINDING} = E[TMC_{x-1}H_y] + E[C_{diamond}] - E[C_xH_y] - E[TM_{solid}] \quad (6.5)$$

where the energy of the carbon atom has been introduced because a carbon atom must be displaced to incorporate the TM into the diamond lattice. This energy is the energy of the ground state Hartree-Fock atom, plus the cohesive energy of a carbon atom in diamond (7.37 eV).

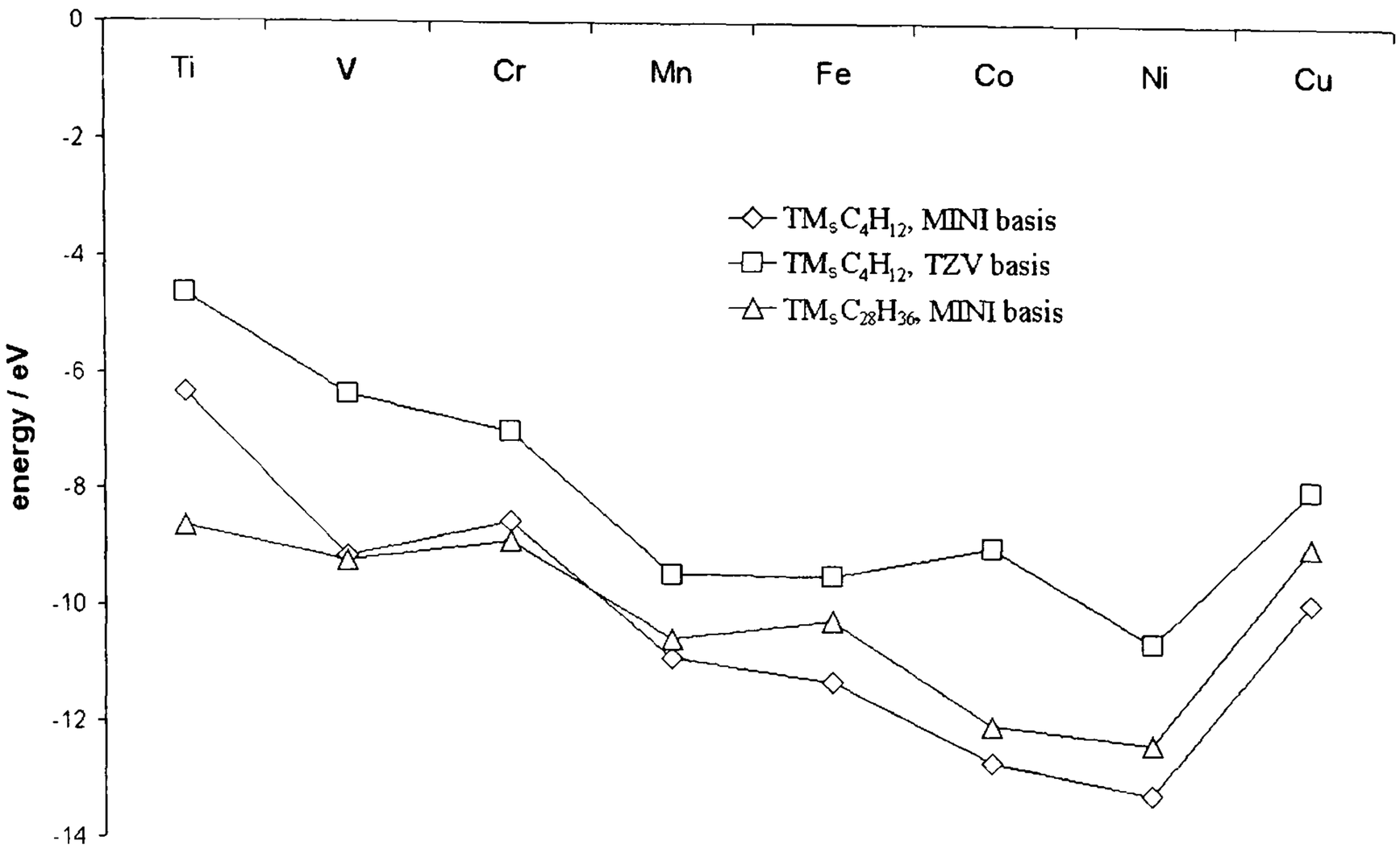


**Figure 6.17.** Binding energies of the neutral substitutional clusters.

No clear trend in relative stability was observed, unlike the results of the DFT calculations of Johnston [4], which showed an increase in binding energy across the series. If anything, there is a suggestion of a decrease in stability across the series. The discontinuities in the binding energy on crossing the series are can be ascribed to the same causes as described for the interstitial defects: the energy drops more sharply between two metals where the second metal's electronic configuration has lost exchange correlation energy compared to the first metal (e.g. $^3$Cr-$^2$Mn) or when the second metal needs to occupy a new orbital of higher energy (Fe[$(e)^4$]-Co[$(e)^4(t_2)^1$]). These changes are small here, but are exaggerated in the next section when the energy differences between the different charge states of a metal are considered, and will be discussed there.

The size of the cluster seems to make little difference to the binding energy of the MINI basis set calculations, and the change in energy across the series is almost identical. It is noted that the larger cluster improves the binding energy of the later metals in the series that are approximately described by the vacancy model by around 0.5 eV; but the earlier metals, where the valence orbitals are described as being localised on the metal, show no

increase in stability. The larger TZV basis follows a very similar pattern across the series, but the binding energies have increased by around 1-2 eV.

Including correlation energy at MP2 level on the small MINI basis clusters appear to make little difference to the binding energy of the transition metals.

### *6.4.4 Semivacancy TM defects.*

As there is some uncertainty in the ground states of these complexes no detailed discussion of their binding energies will be made here. However, the next section (6.4.5) compares the stability of the $TM_{sv}$ centres with the other TM environments.

### *6.4.5 Comparison of TM environments.*

The stability of the different TM environments was compared, taking into account the differences in the number of carbon atoms in the various clusters. For example, to compare the stability of a $TM_i$ in a $C_{10}H_{16}$ cluster with the same TM at a substitutional site in a $C_{28}H_{36}$ cluster we defined

$$TM_i - TM_s = -[E(TM_iC_{10}H_{16}) + E(C_{29}H_{26}) - E(C_{diamond}) - E(TM_SC_{28}H_{36}) - E(C_{10}H_{16})] \quad (6.6)$$

The negative sign means the result is positive if the first named species is more stable. *Mutatis mutandi* for the other pairs of TM environment. The results are shown in figure 6.The most immediate point is that the interstitial complexes are distinctly unstable relative to the other two environments (by around 10 eV for the Ni complexes). This is in agreement with the findings of Goss *et al.* [33]. This suggests that interstitial complexes are only metastable in diamond, certainly the transition to a substitutional site by pushing out a carbon atom along a <1 1 1> direction will be blocked by another carbon.

Substitutional complexes are found to be the most stable environment. This is in contradiction to the observations of Nadolinny *et al.*[34] that the NE4 defect, attributed to

the $Ni_{sv}^-$ centre, appears as $Ni_s^-$ anneals out. However, the effects of long range stress induced by the presence of the TM impurity and entropic terms have been ignored in the present calculation: Johnston and Mainwood have suggested that strain in the crystal is reduced by around 1-2 eV by rearrangement to a semivacancy environment. The generation of a mobile carbon interstitial is likely to be entropically favoured. The magnitude of this effect is hard to estimate, but at the high temperatures at which the transition to the semi-vacancy structure occurs it could be substantial. Whilst inconclusive, this shows that the results are not inconsistent with the experimental observation of the production of $Ni_{sv}$.

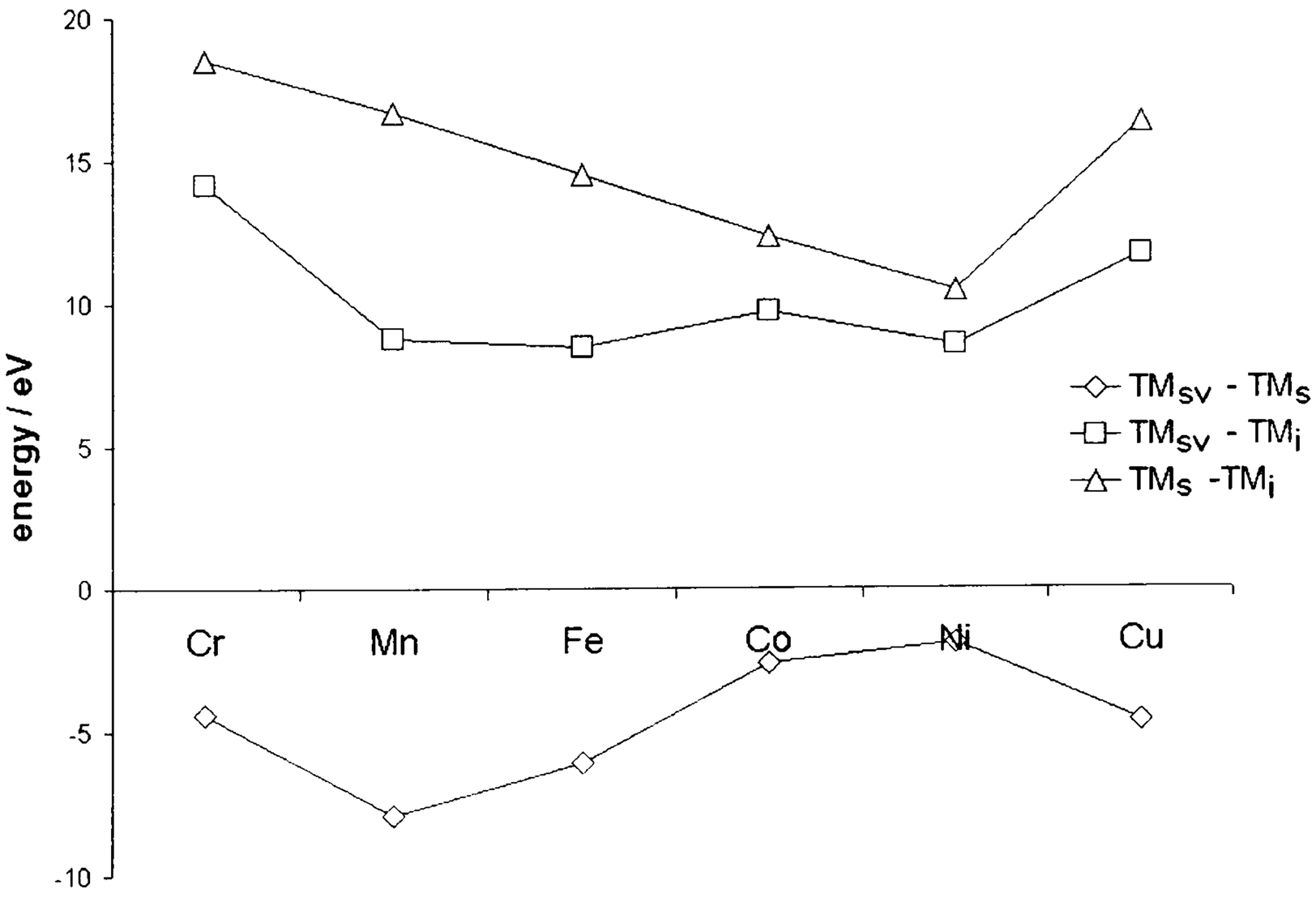


**Figure 6.18.** The relative stability of the different TM environments in diamond. A positive value indicates that the first named species is most stable.

The relative stability of the semivacancy species increases across the transition series, except for Cu and (high-spin)Cr which is unexpectedly stable. $Ni_{sv}$ is about 2.5 eV more stable relative to $Ni_s$ than the Co or Cu systems with Fe another 1.5 eV less favourable.

## 6.5 Charge states of TM defects.

A unique property of transition metals is their ability to exist in multiple charge states. This property would be of great interest if it led to useful *photochromic* centres, or if the magnetic properties of the defects could easily be controlled. The two well-characterised nickel defects are both charged, one negatively and one positively. In this section, the stability of the TM defects in singly charged states relative to the neutral species is examined. The formation of the charged state of the transition metal defect from the neutral complex can be viewed as a kind of redox reaction i.e. in forming a negatively charged TM complex an electron is donated from a $N_s$ centre in the vicinity, oxidising the nitrogen and reducing the metal. This is the measure used to decide on the stability of TM defect charge states, if the redox reaction is energetically favourable the charge state is expected to be stable.

### *6.5.1 Interstitial clusters.*

The stability of the charged $TM_i$ defects were calculated from

$$\Delta H^{+}_{CHARGE} = E[TM_i^{+}] + E[B_s^{-}] - E[TM_i^{0}] - E[B_s^{0}]$$

$$\Delta H^{-}_{CHARGE} = E[TM_i^{-}] + E[N_s^{-}] - E[TM_i^{0}] - E[N_s^{0}] \qquad (6.7)$$

The behaviour of the interstitial clusters is fairly clear cut. Even including the overestimated correction for finite cluster size (section 6.2.4), the negative charge states of the interstitial were found to be unstable relative to the neutral species by 5-7 eV. The charge is expected to be largely confined to the transition metal d-orbitals, so it is not anticipated that this result will be very dependent upon cluster-size. Negative interstitial clusters are unlikely to be found in diamond.

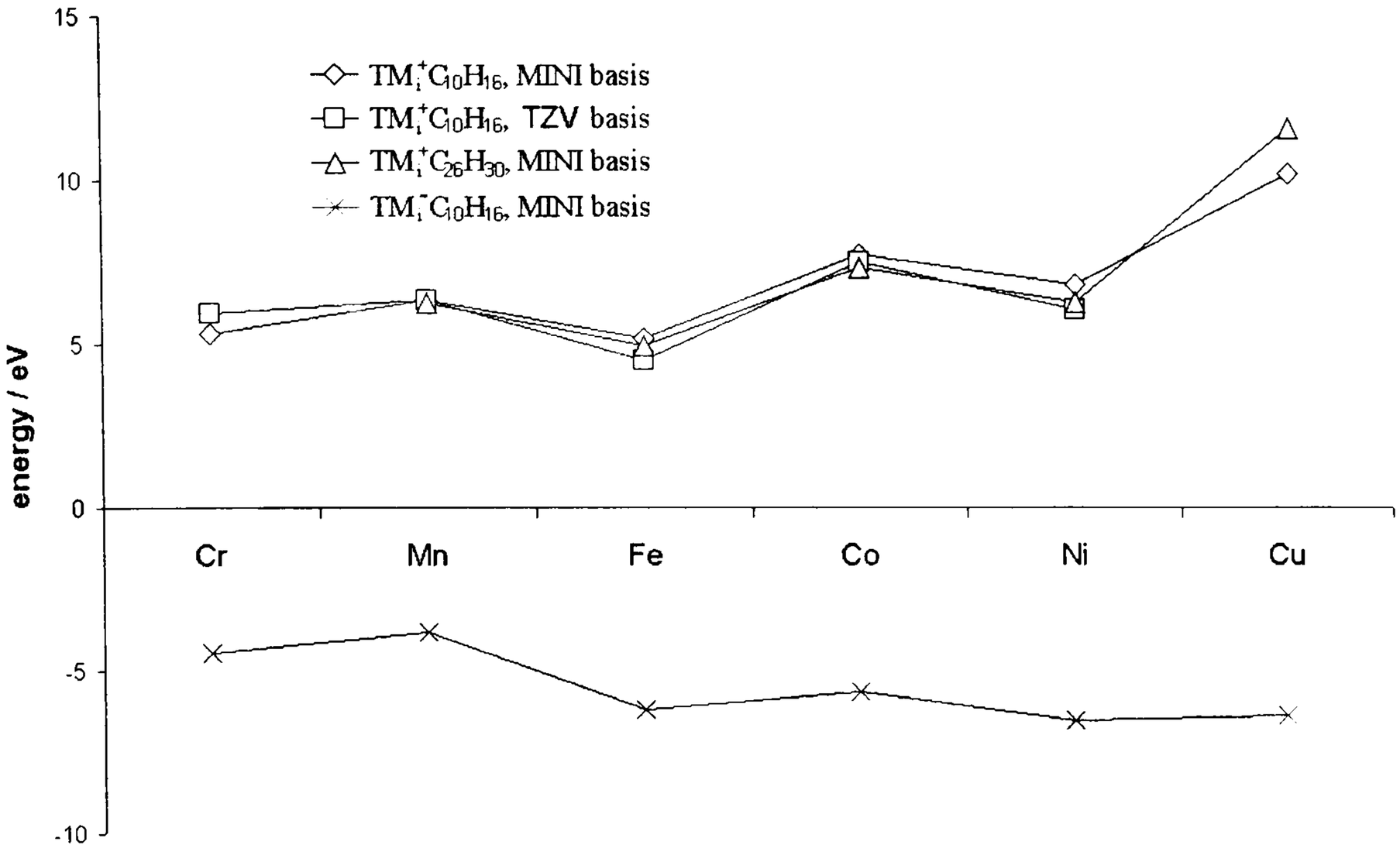


**Figure 6.19.** Energy released on forming charged $TM_i$ clusters and their charge compensating partners. The energetic effect of dielectric screening is included.

Conversely, the positive charge states of $TM_i$ were uniformly found to be stable, even without the dielectric screening correction for the large cluster with a MINI basis set and the small cluster with a TZV basis set. Including the dielectric effect of the crystal, the formation of $TM_i^+ B_s^-$ pairs is found to be highly favourable (Figure 6.19).

Interstitial TMs are expected to be found in a positive charge state when a good acceptor species is present, but neutral in diamonds with significant nitrogen content.

### *6.5.2 Substitutional clusters.*

Negatively charged clusters.

The energies for the formation of $TM_s^-$ are in Figure 6.20. The energies are found from,

$$\Delta H_{CHARGE} = E[TM_s^-] + E[N_s^+] - E[TM_s^0] - E[N_s^0] \quad (6.8)$$

The general trend across the series is to favour the addition of an electron, as the metal orbitals come down in energy, eventually accommodating the electron in a vacancy derived orbital. The breaks in the series can be understood in terms of the relative electronic configurations of the neutral and charged metal clusters. There is a break after V, here the third electron in the e orbitals reduces the exchange stabilisation of the $Cr_S^-$ cluster compared to $Cr_s^0$: no such situation occurs for $V_s^-$ so a dip in energy is observed. Similarly after Mn, $Fe_s^-$ must place the electron in a higher energy $t_2$ orbital as $Fe_s^0$ has a full set of e orbitals and $Cu_s^-$ loses exchange energy compared to $Cu_s^0$ with its half filled $t_2$ shell. Both the basis sets show the same pattern across the series.

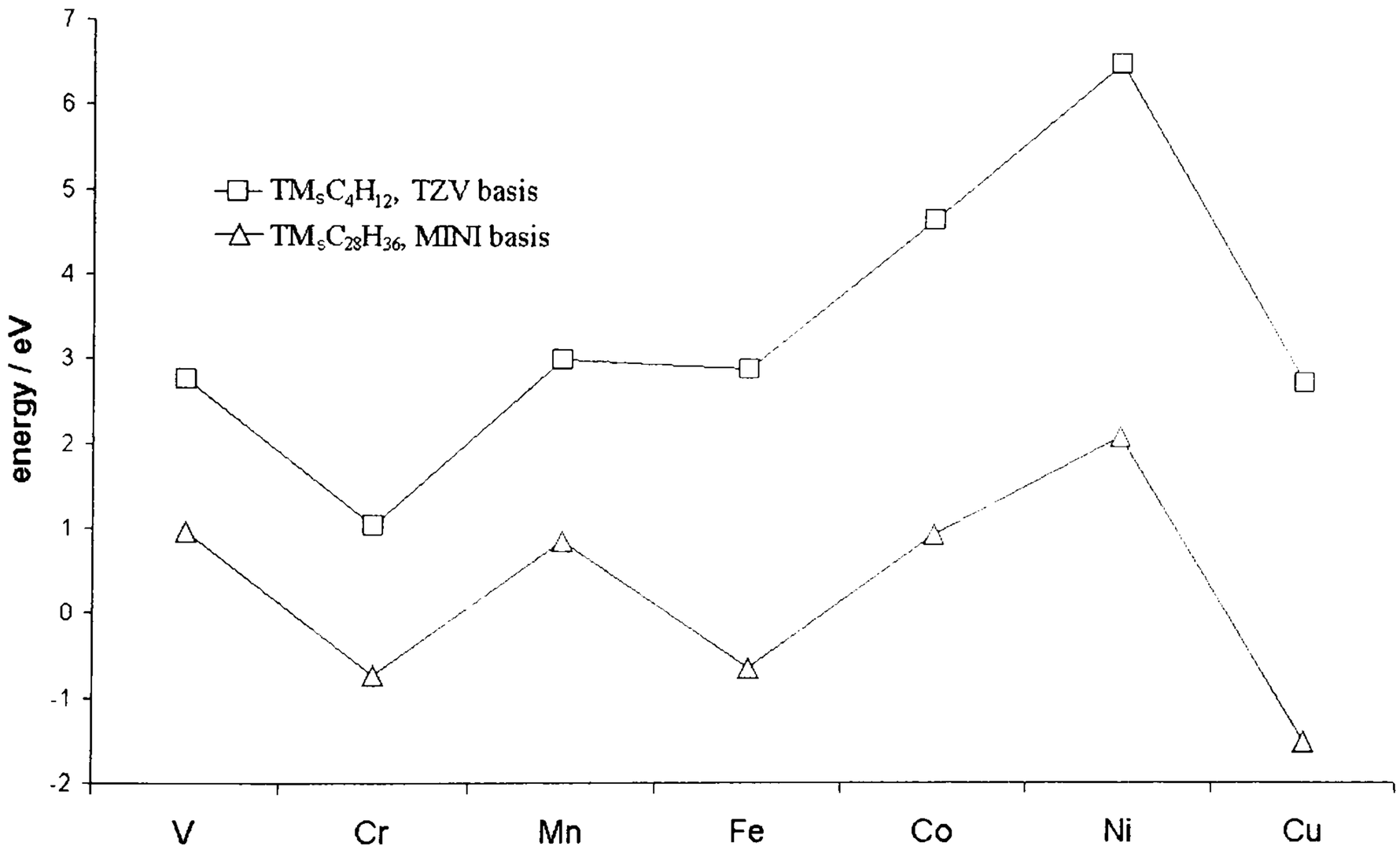


**Figure 6.20.** Energy released upon forming $TM_s^-$ and $N_s^+$ relative to the neutral species. Approximate dielectric screening is included.

The binding energy of the electron is significantly greater for the TZV basis set, by up to about 3 eV for Ni. The TZV basis set describes the more diffuse anionic species much better than the minimal basis set. The binding energy of the electron is seen to peak for the nickel cluster, in agreement with the experimental observation of this species.

Furthermore, the formation energy is seen to be positive for the nickel cluster with the TZV basis set, even without including the effect of dielectric screening.

## Positively charged clusters

The energies of the positively charged clusters relative to the neutral complexes are found from,

$$\Delta H^{+}_{CHARGE} = E[TM_s^{+}] + E[B_s^{-}] - E[TM_s^{0}] - E[B_s^{0}] \qquad (6.9)$$

Here (see Figure 6.21) there is no real general trend across the series; the energy of charging the cluster remains merely oscillates around a mean value. The pattern of energy changes across the series can be interpreted in terms of the relative stability of the $TM_s^{0}$ and $TM_s^{+}$ complexes: the charging energies are lowest for V, Mn, and Co. The $TM_s^{+}$ complexes of these ions are stabilised relative to the $TM_s^{0}$ complex by the $TM_s^{0}$ either having to occupy an orbital of higher energy (V and Co), or losing exchange correlation energy because the positively charged cluster has a half filled shell of maximum multiplicity (Mn). The higher charging energies occur, conversely, when the $TM_s^{0}$ complex is stabilised compared to the $TM_s^{+}$ complex.

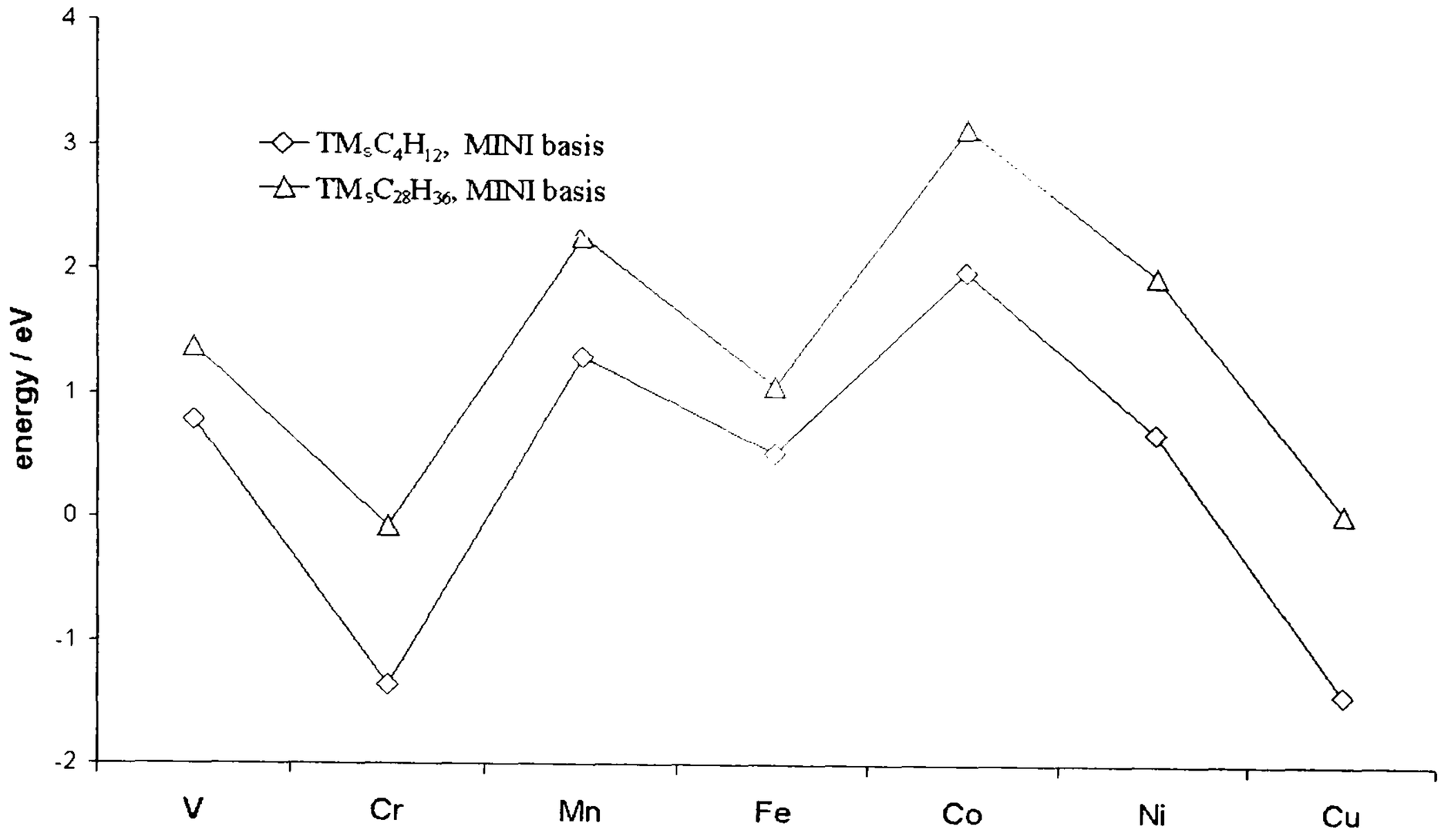


**Figure 6.21.** Energy released on formation of the charge pair $TM_s^+$ - $B_s^-$ from the neutral species. The approximate dielectric screening is included.

The positive charge state is significantly stabilised by increasing the cluster size. This is probably due to the positive charge being placed into vacancy-like orbitals in $TM_s^+$; the larger cluster allows this charge to be delocalised effectively. This effect was less significant for the negatively charged clusters where the charge was placed in orbitals to a large degree localised on the transition metal.

## Comparison of the charge states.

The neutral substitutional clusters have been found to be energetically unstable compared to their constituents by around 5-10 eV. There are several reasons possible for this, but the difficulty in defining the references, especially the solvation energy of the metal in the melt, is likely to make the largest contribution. Possibly, there is also a systematic error with the HF method as reference 15 found the $TM_i$ clusters in silicon to be unstable.

The negative charge states, although generally unstable, show a sharp increase in stability across the series, and also with the superior basis set. $Ni_s^-$ is found to be stable in the TZV basis set.

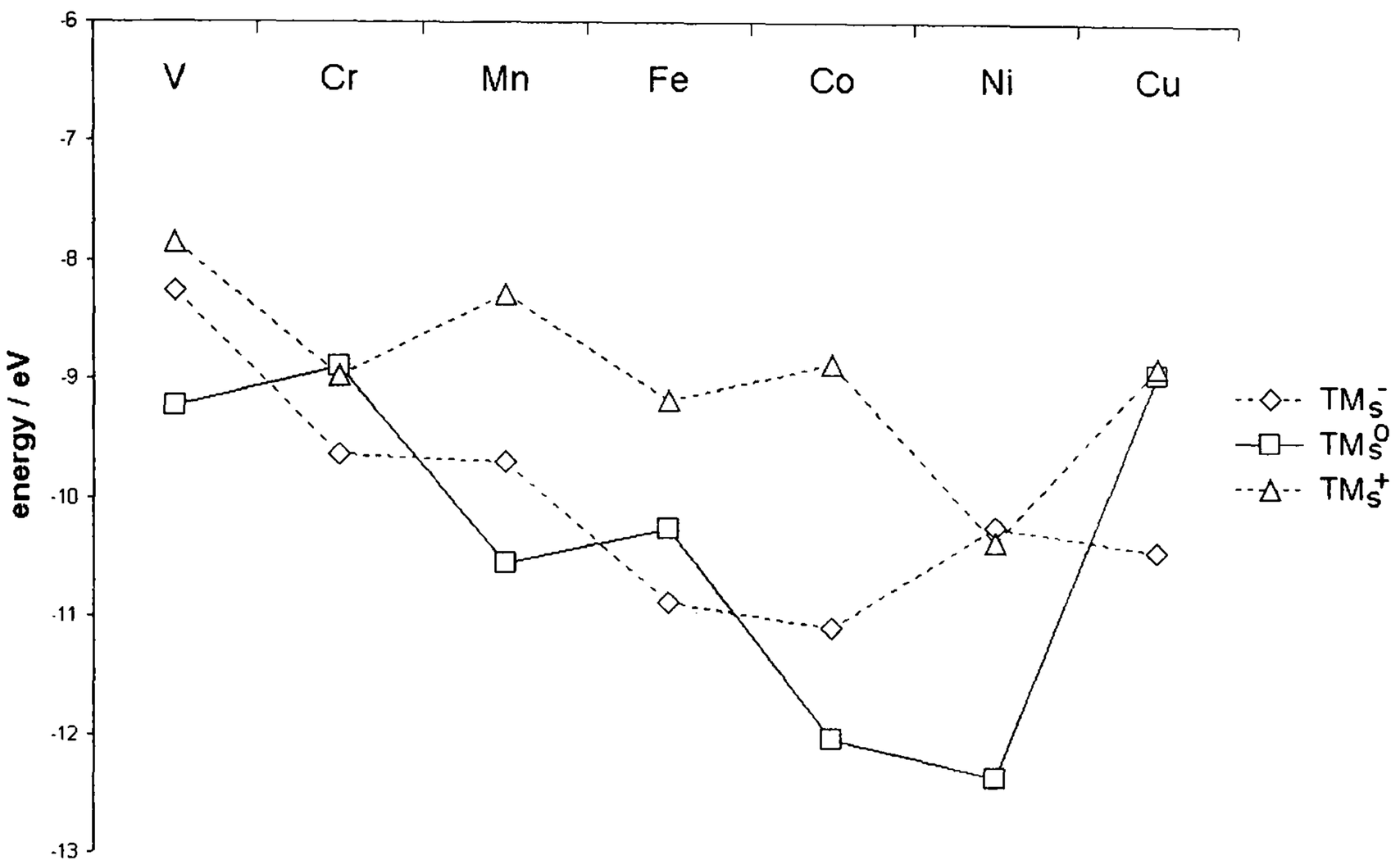


**Figure 6.22.** Energy of forming a charged $TM_s$ complex and its appropriate charge compensating pair relative to the neutral species. The crude compensation for the dielectric effect of the diamond crystal is included. $TM_sC_{28}H_{36}$ clusters were used with a MINI basis set.

If the energy of confining the charge to a finite area is added (section 6.2.4) it is found that all the positively charged clusters are stable (when boron is present as a charge compensator), as are all the negatively charged clusters bar Cr, Fe and Cu (Figure 6.22). It is interesting to note that the two charge states of Ni are similarly stable - $Ni_s^-$ is well known and it has been suggested that $Ni_s^+$ is possibly NIRIM-1 [35].

### *6.5.3 Semivacancy defects.*

The enthalpy of forming the charged semivacancy defects is shown in Figure 6.23.

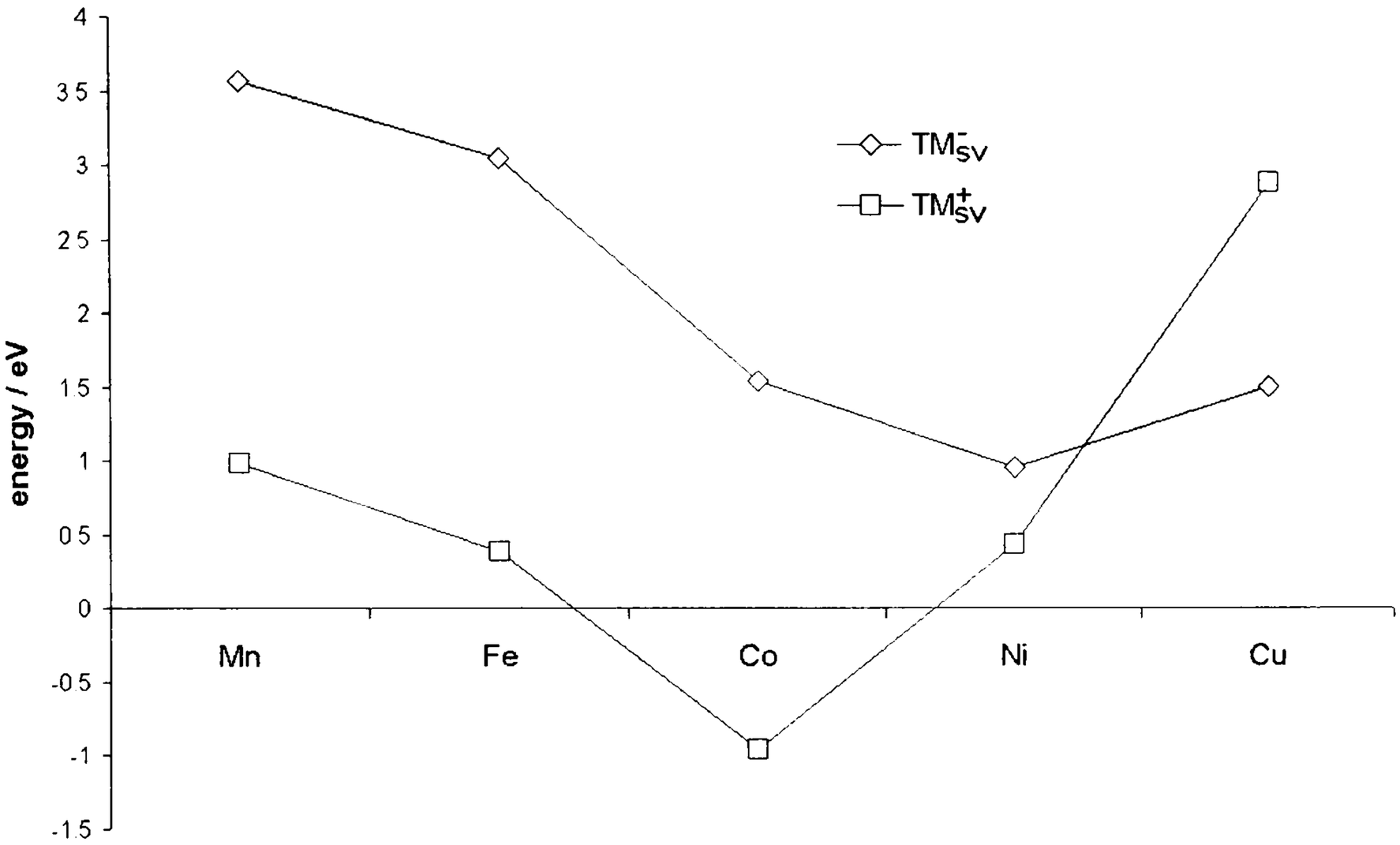


**Figure 6.23.** The enthalpy released on forming the charged $TM_{sv}$ defects, including the effect of dielectric shielding.

The semivacancy defects show similar behaviour to the substitutional defects with the charged defects appearing to be marginally stable relative to the neutral $TM_{sv}$ species if appropriate charge compensators are present. With the approximate dielectric shielding included, only $Co_{sv}^{+}$ is found to be unstable. As with the substitutional defects, all the nickel charge states are found to be close in energy.

## 6.6. Crystal field splitting, and transition energies.

### *6.6.1 Interstitial TMs*

MCSCF calculations were carried out on the smaller interstitial TM clusters. The active space chosen was the five orbitals derived principally from the metal d-orbitals and the MINI basis set was used throughout. The transition energies are shown in Figure 6.24. No transition energy is shown for $Cr_i^+$ as its ground $^6A_1$ state is the only sextuplet state that can be constructed within the d-orbitals and hence there are no spin allowed transitions.

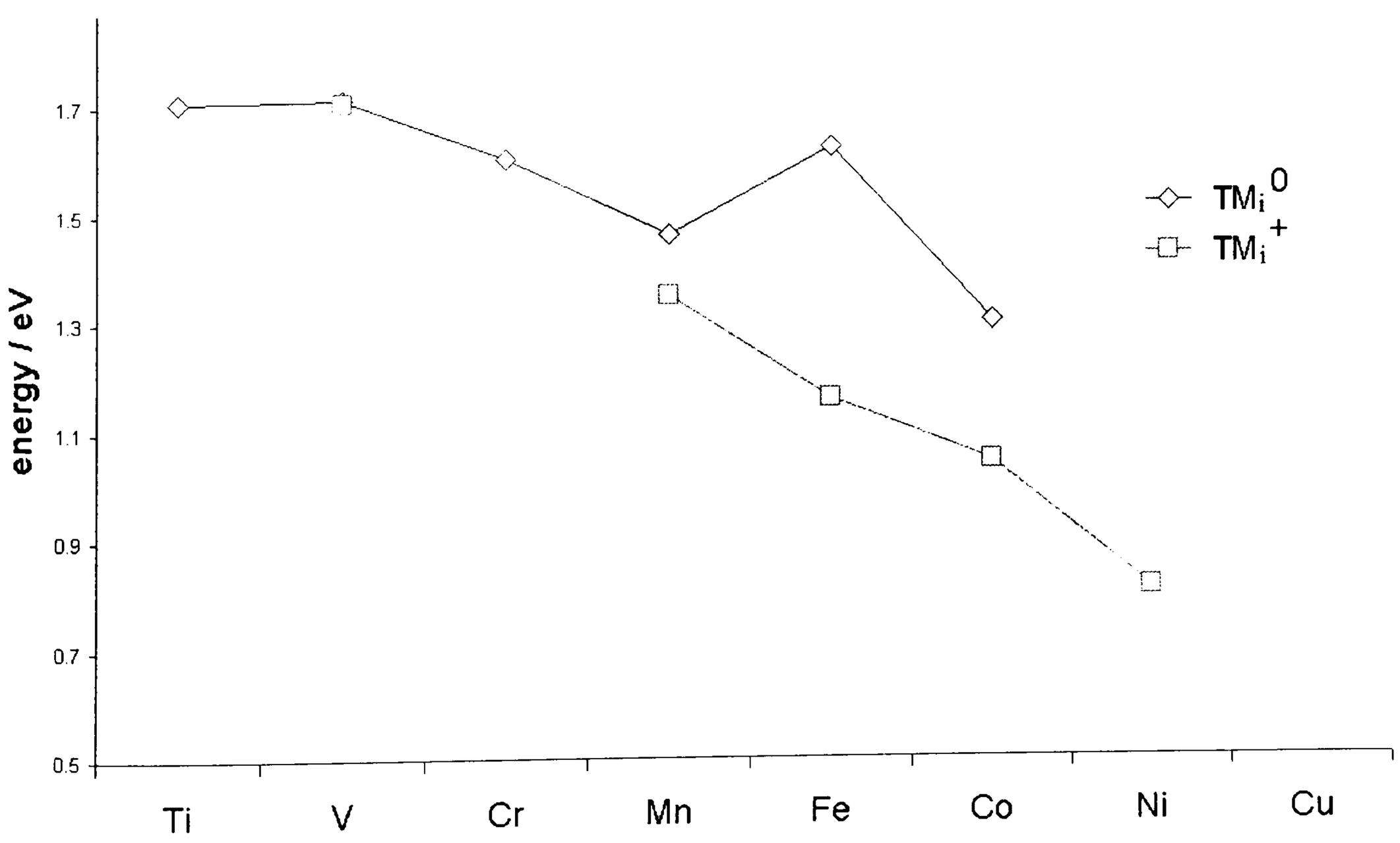


**Figure 6.24.** The energy of the predicted first optical transition of the $M_iC_{10}H_{16}$ clusters. MCSCF calculations with a MINI basis set.

Converging the excited states presented problems in some instances, specifically $Ni_i^0$ and the copper complexes where the active space must be expanded to include the metal 4s orbital. As mentioned before there are objections to comparing the value of the transition energy directly to crystal field parameters, but they should be at least loosely related. The transitions energies reduce across the series, and with increasing positive charge on the cluster. This is in agreement with the observed pattern of complexes with low spin ground-states (section 6.3.4). The absolute values of the transition energies are of the order measured by optical spectroscopy on centres believed to be transition metal related. The experimentally measured value for the $Ni_i^+$ interstitial site is 1.4 eV, whereas the calculated value is in the right area at 0.87 eV.

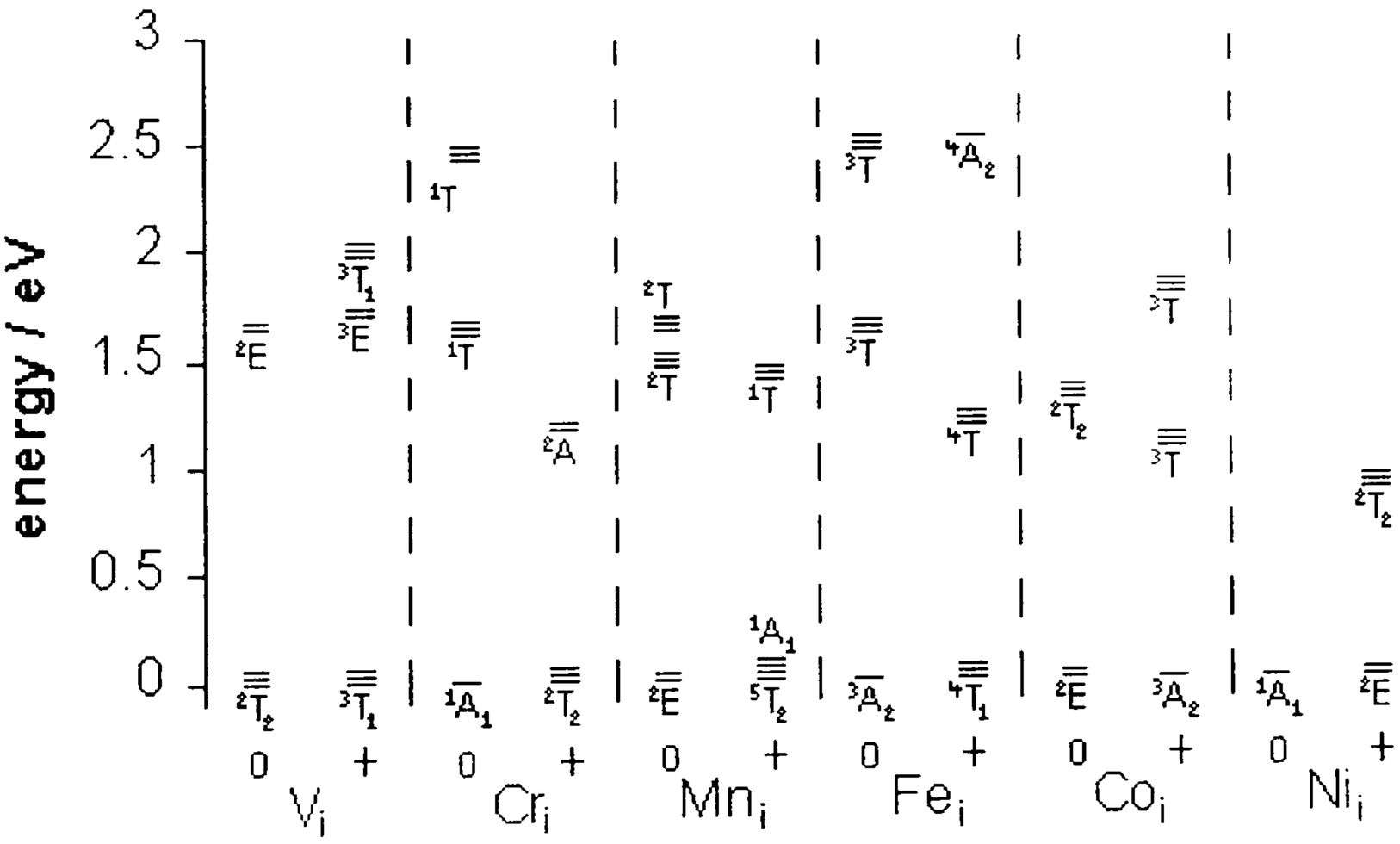


**Figure 6.25.** The electronic states of the smaller $TM_i^{0/+}$ clusters. Energies are measured relative to the ground state of the complex.

### *6.6.2 Substitutional TMs*

One electron picture.

Figure 6.26 shows the energy gap between the one-electron orbitals that are expected to give rise to the lowest energy transition.

The transition energies are many-electron effects and the one electron energy differences are not expected to represent real transition energies, however they are shown as they elucidate the pattern of transition energies found from MCSCF calculations below. The transitions at the beginning of the series are between the filled vacancy-like orbitals and the metal e orbitals. It is expected that this energy gap will tend to reduce as the atomic number of the metal increases – the e orbitals will be reduced in energy due to their poor shielding of the increased charge, but the vacancy orbitals are not expected to shift much. The large jump at the closed shell complexes ($Mn_s^-$, $Fe_s^0$, $Co_s^+$) occurs because an electron must then be promoted to the metal's $t_2$ orbitals, which lie at higher energy. Again the energies are then expected to diminish as the metal $t_2$ orbital drops in energy across the series, but the vacancy like orbital the electron is promoted from stays at a relatively constant energy. Thus a sort of double hump, as seen in Figure 6.26, might be expected.

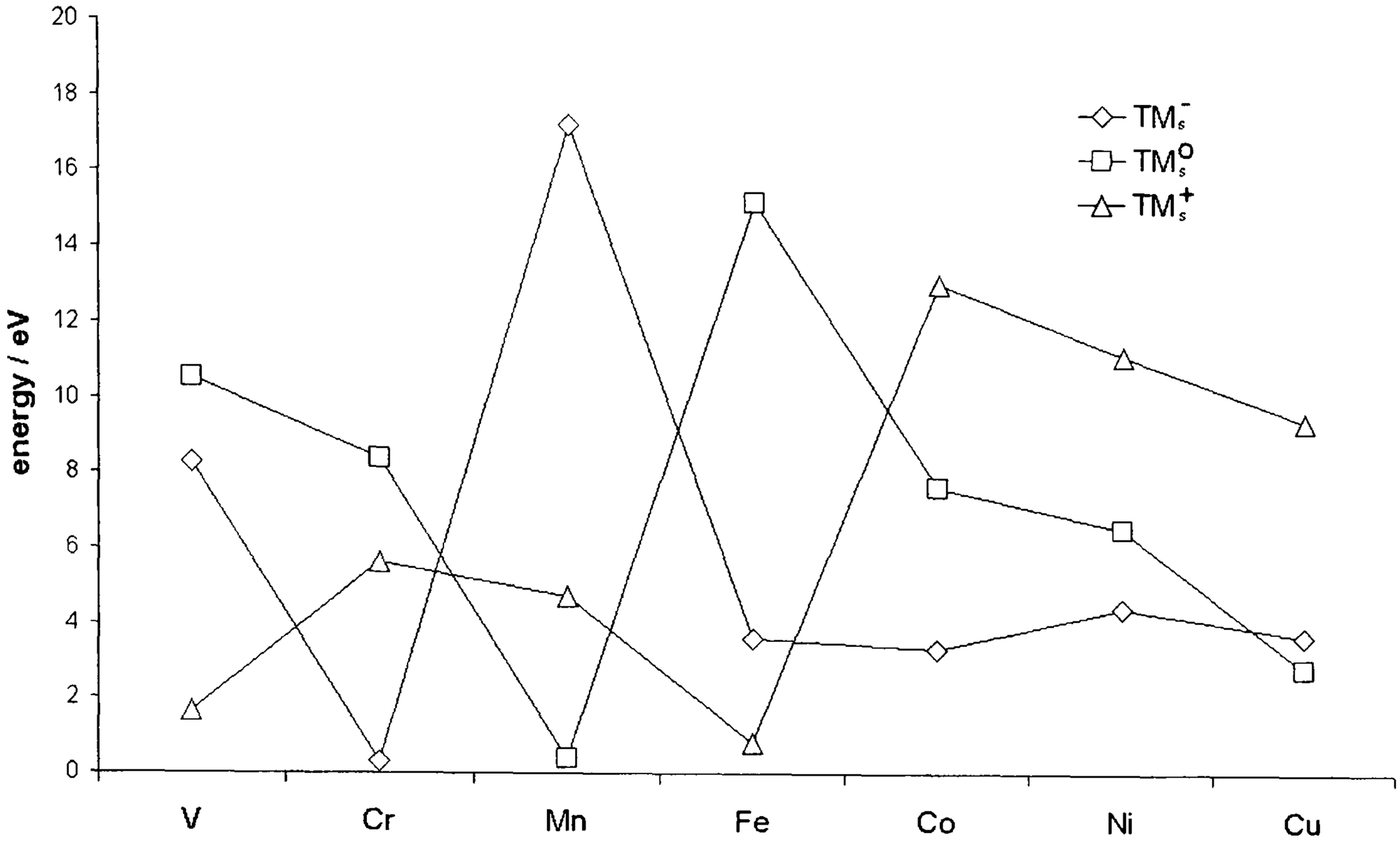


**Figure 6.26.** The energy differences between the highest energy fully occupied orbital and the lowest energy partially unoccupied orbital, between which the lowest energy optical transition is expected to occur - if allowed.

## MCSCF calculations.

Ideally the active space for all of the complexes would have been the same – the metal's 4s and 3d orbitals, and the four dangling bond orbitals from the vacancy. In practice to aid convergence the orbitals used were the highest fully occupied orbitals in the SCF reference and the next empty or partially filled orbitals. The MCSCF transition energies (Figure 6.27) broadly follow the trends observed for the energy gap between the HOMO and LUMO orbitals (Figure 6.26). The transition energy is found to peak at the closed shell species ($Mn_s^-$ and $Fe_s^0$) and then drop. That the energies behave like this indicates that the one-electron orbital picture for the transitions here is fairly respectable.

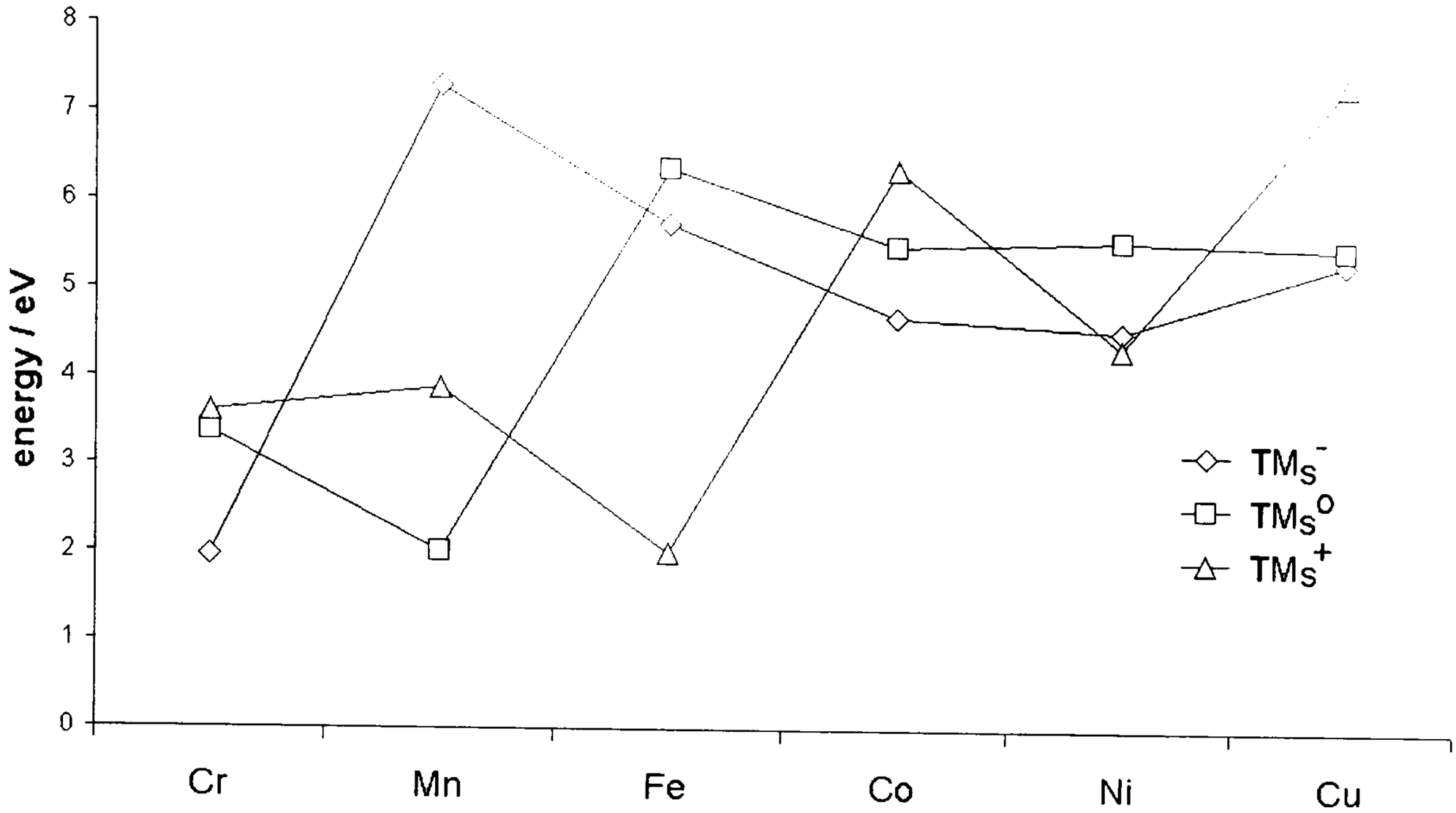


**Figure 6.27.** Transition energies for small substitutional clusters. MCSCF calculations using a MINI basis set.

The transition energies are still found to be rather too high compared to the limited experimental evidence, $Ni_S^-$ at 2.51 eV experimentally but at 4.59 eV from these calculations. However, no attempt here has been made to produce results of chemical accuracy. The active spaces considered are rather small, and as discussed above increasing their size is likely to favour reducing the transition energy. That the energies are qualitatively reasonable (especially given the size of the HF band gap) and can be readily interpreted, lends confidence that they give a reasonable representation of the real system. The calculations suggest that $Co_s^-$ would be observed at a very similar energy to $Ni_s^-$, and that $Fe_s^-$ and $Cu_s^-$ would occur at marginally higher energies. The transition energies of the neutral clusters appear at energies about 1 eV higher than the negatively charged species. $Ni_s^+$ is expected to have a transition at a very similar energy to $Ni_s^-$.

## Characterisation of excited states and transitions.

The MCSCF calculations also provide the symmetry of the excited states of the cluster. The symmetry of the orbitals between which the transitions occur is the most important information obtained from many experimental techniques, e.g. uniaxial stress ( chapter 4), and hence of great interest.

| | $Cr_S^-$ | $Mn_S^-$ | $Fe_S^-$ | $Co_S^-$ | $Ni_S^-$ | $Cu_S^-$ |
|---|---|---|---|---|---|---|
| Ground | $^2E$ | $^1A_1$ | $^2T_2$ | $^3T_1$ | $^4A_2$ | $^3T_1$ |
| 1st Excited | $^2T$, +2.0 eV | ? +7.2 eV | $^2T$, +5.8 eV | $^3T$, +4.7 eV | $^4T$, +4.6 eV | $^3T_2$,+5.4 eV |
| 2nd Excited | $^2T$, +2.9 eV | | $^2T$, +6.5 eV | $^3E$, +5.2 eV | | |

| | $Cr_S^0$ | $Mn_S^0$ | $Fe_S^0$ | $Co_S^0$ | $Ni_S^0$ | $Cu_S^0$ |
|---|---|---|---|---|---|---|
| Ground | $^3A_2$ | $^2E$ | $^1A_1$ | $^2T_2$ | $^3T_1$ | $^4A_2$ |
| 1st Excited | $^3T$, +3.4 eV | $^2T$, +2.0 eV | $T_2$, +6.4eV | $^2E$, +5.5 eV | $^3T$, +5.6 eV | $^4T_1$, +5.6eV |
| 2nd Excited | $^3T$, +4.2 eV | $^2T$, +2.9 eV | | $^2T$, +8.2 eV | $^3E$, +6.9 eV | |

| | $Cr_S^+$ | $Mn_S^+$ | $Fe_S^+$ | $Co_S^+$ | $Ni_S^+$ | $Cu_S^+$ |
|---|---|---|---|---|---|---|
| Ground | $^2E_2$ | $^3A_2$ | $^2E$ | $^1A_1$ | $^2T_2$ | $^3T_1$ |
| 1st Excited | $^2T_2$,+3.6 eV | $^3T$, +3.9 eV | $^2T$, +2.0 eV | $^1T_2$,+6.4 eV | $^2E$, +4.4 eV | $^3T$, +7.4 eV |

**Table 6.5.** The symmetry of the ground and excited states of the neutral and charged substitutional clusters. Transition energies are also indicated.

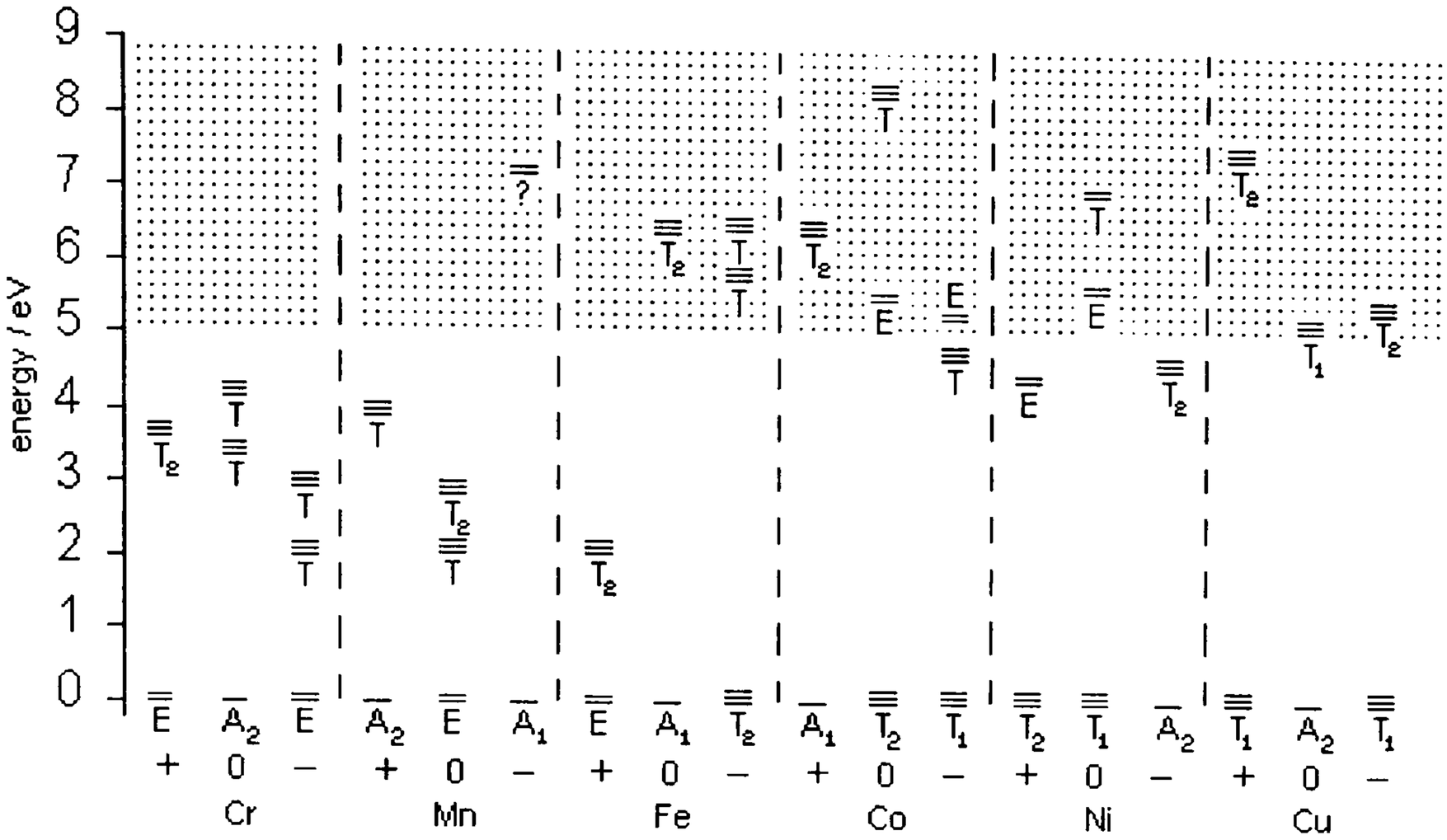


**Figure 6.28.** Schematic representation of the many-electron states of the $TM_s$ complexes.

As the MCSCF calculations were run without any symmetry is not possible to differentiate between T representations when both a $T_1$ and $T_2$ state arise from the same one electron orbital configuration, in some cases the complete symmetry can be identified as the excited state is unambiguously identified by the one-electron orbitals it is formed from. Where this is significant is for $Cu_s^0$ and $Ni_s^-$. $Cu_s^0$ is vacancy-like and the excited state is from an $(a_1)^1(t_2)^4$ configuration. The only quartet state this gives rise to is the $T_1$ state indicated. If the $Ni_s^-$ cluster was also well described by the vacancy model, this would also be its excited state. Because the calculations show its excited state to arise from a $(t_2)^2(t_2)^4$ configuration both $T_1$ and $T_2$ quartet states are formed and the excited state can be $T_2$ in accordance with the model of Ref 36. It has been argued that the spin-orbital coupling parameters used to fit the $Ni_s^-$ centre are not consistent with the Ludwig-Woodbury model and are far more in keeping with the vacancy model [37]. The proposed model intermediate between the two extremes does not cause any discrepancy with the experimental data - it gives the correct excited state, and also as both sets of $t_2$ orbitals contain much vacancy character (for the small MINI basis cluster the lower $t_2$ orbitals are

36% metal d-orbital and the upper 55%), will lead to a value for the spin orbit coupling parameter much reduced from that of the isolated transition metal.

The excited states for other clusters are consistent with crystal field theory predictions (see Figure 6.28 and Table 6.5). Many of the clusters give rise to a wealth of excited states at around the energy quoted for the second excited states. In reality these higher excited states should be lower in energy, as the MCSCF calculation is optimised for the first excited state, but all the transitions listed are well within the HF band gap.

## 6.7 Transition Metal nitrogen centres.

### *6.7.1 Introduction.*

Nitrogen is the dominant impurity in most diamonds; to (nominally) exclude it from HPHT diamonds, special efforts must made during the growth process with "nitrogen getters" such as Ti, Al or Zr added to the growth cell. Defects have been identified in diamond containing both nitrogen and transition metals (see chapter 3): the fairly well characterised NEx EPR centres, the AB5 EPR centre, which is believed to be $[Ni_sN_s]^-$ (Ref 38), and the 2.367 eV photoluminescence centre, tentatively identified with $[Co_sN_s]^0$.

Two species of centres are examined systematically, both based on substitutional transition metal clusters: one or two of the nearest neighbour carbons are replaced by nitrogen atoms, forming clusters of $C_{3v}$ and $C_{2v}$ symmetry respectively. The reduction in symmetry will lift some, or all, of the electronic degeneracy found in the high symmetry substitutional complexes: in $C_{3v}$ symmetry orbitals of e symmetry remain degenerate, but $t_2$ orbitals split into e and $a_1$, whilst in $C_{2v}$ all degeneracy is removed. Complexes with three and four nitrogen atoms around a substitutional transition metal are briefly studied. The clusters examined are $TM_s(N_s)_xC_{28-x}H_{36}$. $x$=1,4 ($x$=1,2 are studied systematically, including the effects of relaxation).

### *6.7.2 Will substitutional TMs trap nitrogen atoms?*

An important question is whether on annealing at high temperature, nitrogen might be expected to substitute for carbon atoms at the TM defects. This was investigated for $TM_S$ defects by comparing the enthalpy of the clusters with $x$ nitrogen atoms around the $TM_S$ to those with $x$-1. Substitutional nitrogen, C centres, were used to balance the number of nitrogen atoms present. We define the enthalpy for the substitution of the $x$th carbon nearest neighbour atom, $\Delta H_{Nx}$, as

$$\Delta H_{N_X} = E[TM_S(N_S)_X C_{28-X} H_{36}] + E[C_{29} H_{36}] - E[TM_S(N_S)_{X-1} C_{28-X} H_{36}] - E[N_S C_{28} H_{36}] \quad (6.10)$$

It is energetically beneficial to add a nitrogen atom to all of the substitutional metal complexes, and this energy gain increases across the transition series. Furthermore, it is observed that the addition of a second nitrogen atom to the $TM_SN_S$ complexes formed is also favoured, except for V (see Figure 6.29).

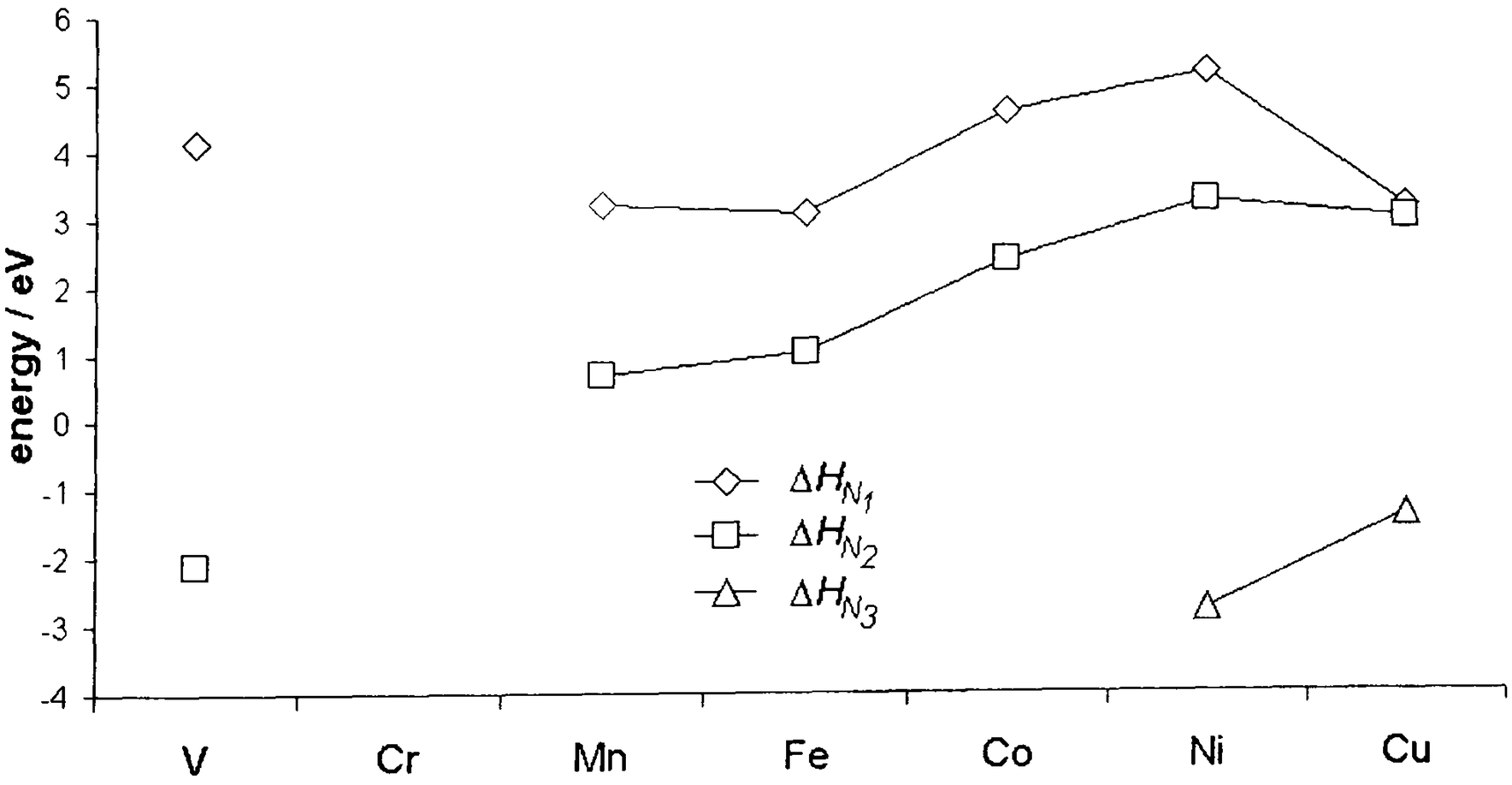


**Figure 6.29.** The enthalpy change on substituting carbon with nitrogen atoms at TM substitutional centres ($\Delta H_{Nx}$ are defined in Equation 6.10).

However, the addition of a third nitrogen to the doubly nitrogen substituted Ni and Cu clusters is found to be energetically unfavourable by 2.76 and 1.38 eV respectively. $Ni_s(N_s)_4C_{24}H_{36}$ is found to be even less likely to form, being 7.6 eV less stable than $Ni_s(N_s)_3C_{25}H_{36}$ and a substitutional nitrogen atom. These highly substituted clusters have not been relaxed, but even adding the anticipated 1-2 eV relaxation energy, there will be little driving force for the addition of the third and fourth nitrogen atoms. Given that the energy of forming $Ni_s(N_s)_2C_{26}H_{36}$ complexes was found to be energetically favourable by 2-3 eV for the later transition metals, these results suggest that the nitrogen substitution will stop after the addition of two nitrogen atoms.

These are thermodynamic arguments, the activation energies for these processes may be large (The 2.367 eV centre that is possibly attributable to $Co_sN_s$ only forms in high nitrogen samples at an annealing temperature of 2100 K [39 40 41 42]), which would explain the persistence of $Ni_s^-$ at high annealing temperatures.

### *6.7.3 Properties of the $TM_s$-$(N_s)_x$ complexes.*

A MINI basis set was used throughout these calculations. Calculations were initially carried out at the equilibrium geometry of the $Fe_sC_{28}H_{36}$ cluster (section 6.1), but the $TM_s(N_s)_xC_{28-x}H_{36}$ clusters were then relaxed for $x$=1,2. A fairly detailed discussion of the $TM_sN_sC_{27}H_{36}$ clusters is given followed by brief comments on the other defects.

#### *$TM_sN_sC_{27}H_{36}$ clusters.*

This cluster has $C_{3v}$ symmetry. Much of the picture developed earlier for the substitutional complexes can be carried over to the lower symmetry, but it becomes more complex and some of the distinctions made earlier become rather blurred.

Considering the set of valence orbitals found for the substitutional cluster - metal $t_2$ and e, and vacancy $a_1$ and $t_2$ – it was found that early in the series the metal orbitals were higher in energy. As the series was crossed the metal orbitals descended in energy,

crossing the vacancy orbitals. In the middle of the series where all the orbitals were of similar energy mixtures of the models based on metal orbitals or vacancy orbitals were found.

In the lower $C_{3v}$ symmetry the valence orbitals are e, $a_1$, and e from the metal and $a_1$, e and $a_1$ from the vacancy. Figure 6.30 shows a schematic MO diagram for these valence orbitals, the electron population is appropriate for $[Ni_sN_s]^0$. The six occupied orbitals of lowest energy derive from the vacancy-like orbitals and a pair of metal orbitals transforming as e. This leaves three higher energy orbitals, of $a_1$ and e symmetry, which will become occupied by one, two and three electrons for Fe, Co and Ni respectively. In the case of $[Ni_sN_s]^0$ the $a_1$ orbital is made up of 91% metal $d_{z^2}$, whilst the e orbital has only 36% metal character; clearly, both the transition metal and vacancy orbitals are close in energy, and interact appreciably.

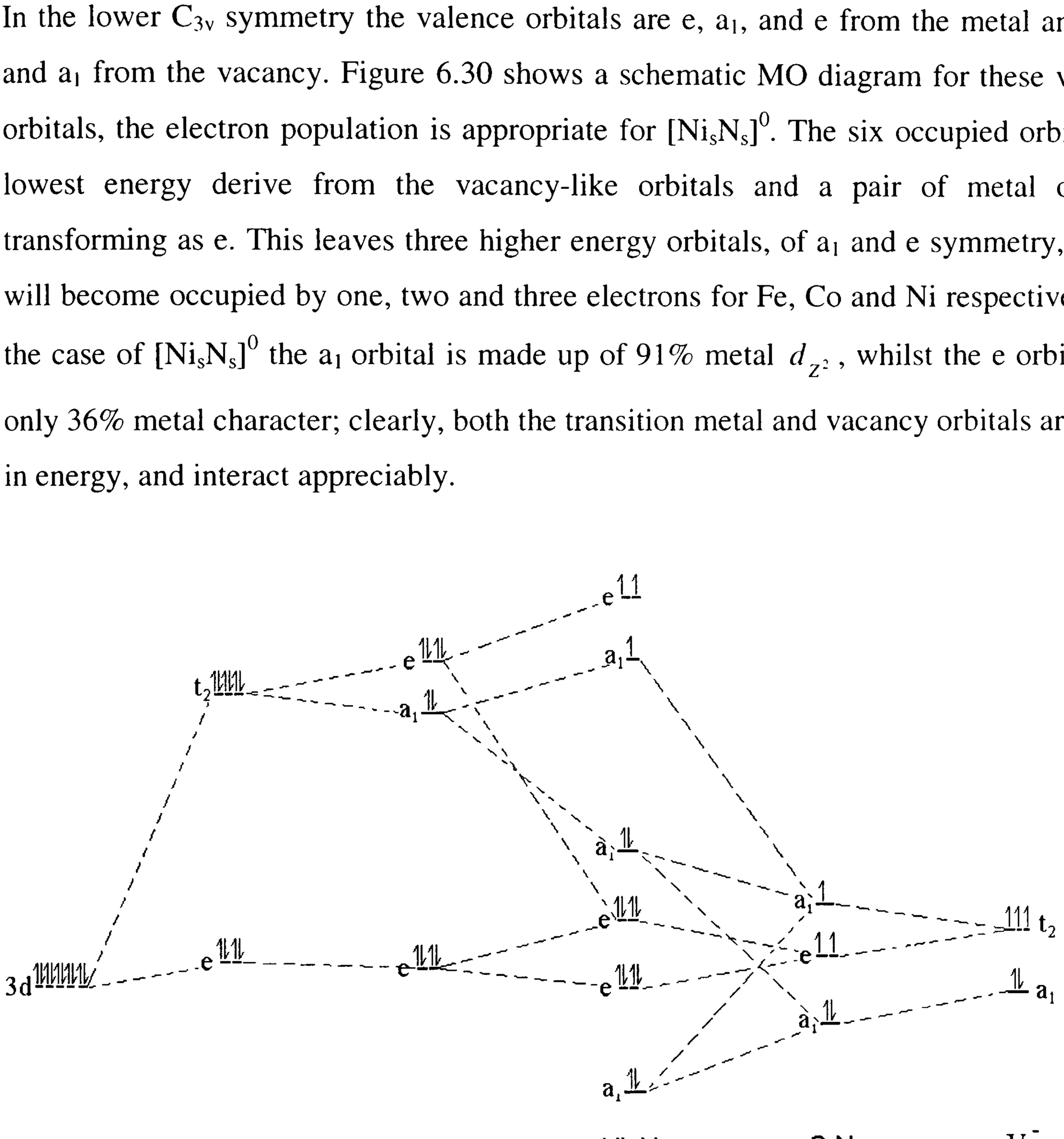


**Figure 6.30.** Schematic MO diagram of the $[Ni_sN_sC_{27}H_{36}]^0$ cluster.

The exact ordering of the lower four energy levels is unpredictable in general, an $a_1$ or e state being highest in energy, depending on the TM involved. As Figure 6.30 shows this ordering depends on the relative position of the metal and vacancy orbitals. Calculations have been carried out on the states of the lowest possible spin except $[Ni_sN_s]^0$, where a quartet state similar to that observed for $Ni_s^-$ defect was used (see Figure 6.31).

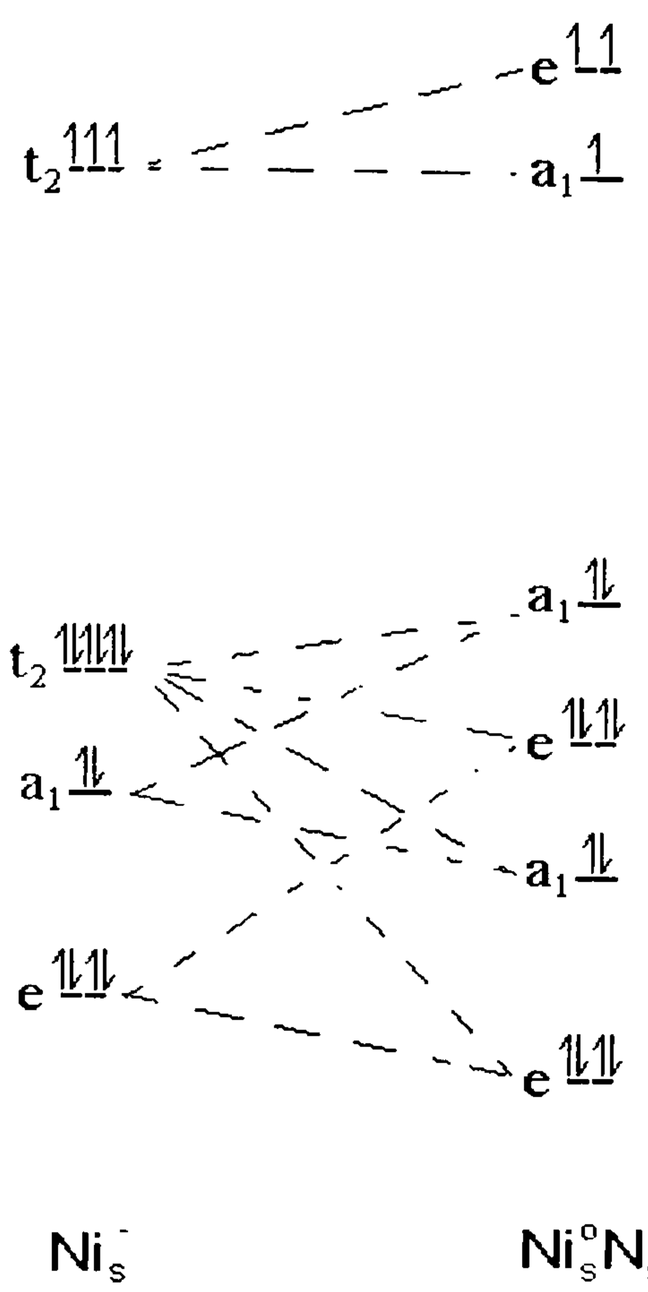


**Figure 6.31.** MO diagram showing the correlation between the molecular orbitals of $Ni_s^-$ and $Ni_sN_s$.

The orbitals that appear in the band gap are related to those found for the substitutional transition metal clusters (Figure 6.31). The orbitals do not appear to resemble either the Ludwig-Woodbury or the vacancy model, but instead are a highly covalent mixture of the vacancy and metal orbitals, indicating that the vacancy and metal orbitals are of similar energy for the later TMs. The orbitals are ordered with six ($2e + 2a_1$) at lower energy, and then three ($a_1 + e$) higher in energy; the two sets are separated by an amount that roughly corresponds to the cubic crystal field splitting $\Delta$. Starting at $Fe_sN_s$ the higher energy orbitals begin to be filled, with the $a_1$ orbital found to be lower in energy than the e. For $[Ni_sN_s]^0$ the gap between the $a_1$ and e orbitals is found to be 0.9 eV, so it is expected that these orbitals will be filled to give maximum spin multiplicity in

accordance with Hund's rules. From this it is expected that the ground states of $Fe_sN_s$, $Co_sN_s$, $Ni_sN_s$ and $Cu_sN_s$ will be $^2A_1$, $^3E$, $^4A_2$ and $^3A_2$ respectively; they would all be expected to be EPR active, and as the trigonal crystal field is around 1eV, at least 10x the spin-orbit coupling strength, to have g values close to 2, and nearly isotropic[43]. This fits with the assignment of AB5 to $[Ni_sN_s]^-$ with spin 1, as this cluster is isoelectronic with $[Cu_sN_s]^o$, and a $^3A_2$ ground-state is predicted. However, the AB5 centre is not isotropic, previous results have shown that the HF one-electron energy differences are too large, so the $a_1$-e splitting of around 1 eV should be treated with caution.

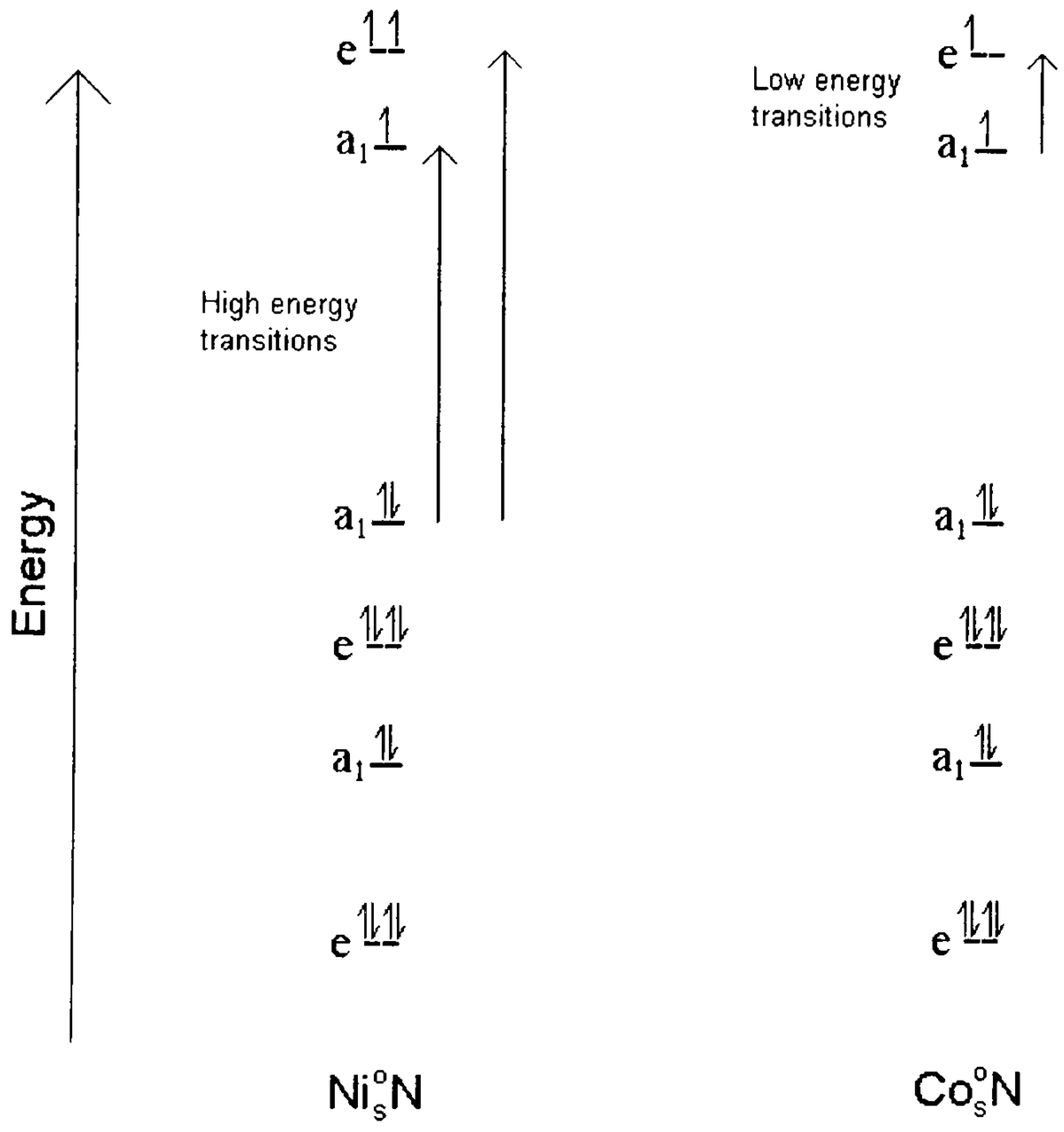


**Figure 6.32.** The expected optical transitions at late TM-N centres. The low energy transitions are forbidden (by the Pauli exclusion principle) at the $[Ni_sN_s]^0$ defect.

Optically two possibilities exist within the one-electron picture – transitions from the six lower energy orbitals to the higher energy $a_1$ and e orbitals, or, transitions between the high energy $a_1$ and e orbitals. The former would be expected to occur at energies similar to $Ni_s^-$. The transitions within the high-energy orbitals would be expected to be at low energy, not more than 1 eV, which corresponds to the trigonal crystal field splitting (see Figure 6.32). Generally, several transitions would be expected form each centre (all the possible many electron states from the $a_1$ and e valence orbitals have symmetry allowed transitions between them).

Equilibrium geometries.

After relaxation the nitrogen is found to move away from the transition metal, and the three nearest neighbour carbons move closer compared to the starting geometry of 1.81 A for all four atoms. This situation is similar to the deformation of the diamond lattice seen around a C centre. The C centre is used as the energy reference in calculating the binding energies for this system, and its relaxed bond-lengths are also indicated.

| | C | V | Cr | Mn | Fe | Co | Ni | Cu |
|---|---|---|---|---|---|---|---|---|
| $TM_s$-$N_s$ / nm | 0.226 | 0.192 | | 0.185 | 0.194 | 0.200 | 0.191 | 0.197 |
| $TM_s$-$C_s$ / nm | 0.153 | 0.189 | | 0.180 | 0.178 | 0.175 | 0.185 | 0.186 |

**Table 6.** Equilibrium bondlengths of the $TM_sN_sC_{27}H_{36}$ clsuters.

The bond distances of the transition metal clusters are fairly constant with TM-N about 1.95 A and M-C around 1.8 A. The variation of the calculated bond-lengths follows the occupation numbers of the anti-bonding orbitals that correspond to the metal $t_2$ orbitals in the $TM_s$ clusters of $T_d$ symmetry. In the lower symmetry point group, the $t_2$ orbitals are split into $a_1$ and e orbitals; the $a_1$ orbital is anti-bonding with respect to the TM-N bond and non-bonding to the TM-C bonds and *vice versa* for the e orbitals. Hence the TM-N bond-length is greatest for $[Co_sN_s]^o$ and $[Cu_sN_s]^o$, which have the $a_1$ orbital doubly occupied.

The trigonal distortion is seen to be moderate, the TM-N bonds 0.005-0.025 nm larger than the TM-C bonds.

***$TM_s(N_s)_2C_{26}H_{36}$***

The introduction of a further nitrogen lowers the symmetry to $C_{2v}$, and allows even more energy levels to interact. The orbitals in the band gap are still found to be covalent

mixtures of metal d-orbitals and the orbitals of the metal's nearest neighbour carbon and nitrogen atoms.

### $TM_s(N_s)_3C_{25}H_{36}$

These complexes are very similar to the $TM_s(N_s)C_{27}H_{36}$ clusters, both have $C_{3v}$ symmetry. Here, however, the level ordering of the three high energy orbitals is reversed, as the carbon and nitrogen atoms are interchanged. See discussion in section 6.6.2.

### $Ni_s(N_s)_4C_{24}H_{36}$

Examination of the orbitals shows there is little mixing between the vacancy-like and metal orbitals. This leaves the metal e and $t_2$ orbitals in a state very similar to the free ion, giving probably the best approximation to the crystal field model found in the diamond transition metal clusters studied. For $Ni_s(N_s)_4C_{24}H_{36}$, the orbitals principally derived from the 3d orbitals are filled by the metal's 10 electrons. The closed shell allows us to equate the splitting of the e and $t_2$ orbitals with the crystal field parameter delta (see section 2.2), which was found to be 2.78 eV. The e-orbitals were 94% metal d-orbital and the $t_2$ were 67%. Calculations suggest that $Ni_s(N_s)_4C_{24}H_{36}$ is highly unstable and will probably not form. However it is also noted that its $^1A_1$ ground state will not be observable in EPR, and that its optical transitions will probably be of very high energy, so it is unlikely to be observed in any case.

## 6.7.4 Conclusions.

The replacement of a carbon nearest neighbour by a nitrogen at a $TM_s$ centre is found to be energetically favourable for the later TMs, by 2-3 eV for Co to Cu (Figure 6.29). The addition of a second nitrogen atom is also favoured. Calculations on $Cu_s(N_s)_3$ and $Ni_s(N_s)_4$ suggest, however, that aggregation of nitrogen around the transition metal would stop at this point after the addition of the second nitrogen atom.

The calculations suggest that the ground states of $Fe_sN_s$, $Co_sN_s$, $Ni_sN_s$ and $Cu_sN_s$ will be $^2A_1$, $^3E$, $^4A_2$ and $^3A_2$ respectively; and will show several optical transitions. All these centres are expected to be EPR active, but calculations suggest that the trigonal splitting could be larger enough to quench any spin-orbit coupling and leave an isotropic *g* value.

The lower symmetry of these centres allows more freedom when they are allowed to relax. The results of these calculations show that relaxation gains about 1-2 eV in total energy, see section 6.2.5. This is probably an overestimate as the small clusters can expand further than is realistic due to the lack of outer shells of carbon atoms.

## 6.8 Transition metal boron centres.

In heavily boron doped diamonds TM-B complexes might form during growth. One indication of this is that the NIRIM-1 EPR centre which is tentatively identified with $Ni_i^+$ interstitial is observed to disappear in heavily boron doped samples [44]. $Ni_i^{2+}$ is expected to be extremely unstable, so it has instead been suggested that Ni-B centres are formed instead [45] - the NOL1 EPR centre has been attributed to a positively charged $Ni_i$-B defect[46].

Here the $TM_sB_sC_{27}H_{36}$ clusters are examined to see if they are stable relative to the $TM_s$ species, and then to examine their properties.

### *6.8.1 Stability of neutral TM-Boron complexes.*

To explain the decrease in the NIRIM 1 EPR centre signal in highly boron doped samples, it has been suggested that TM-B complexes might be formed during growth. The stability of boron substituted $TM_s$ complexes, $[TM_sB_s]^0$, relative to the $TM_s^0$ clusters is investigated. The enthalpy of substituting a boron for a carbon atom at a $TM_s$ centre is defined as,

$$\Delta H_{Bsub} = E[TM_s B_s C_{27} H_{36}] + E[C_{29} H_{36}] - E[TM_s C_{28} H_{36}] - E[B_s C_{28} H_{36}] \qquad (6.11)$$

The energies are seen to increase sharply across the series, until Co. After Co an electron must be accommodated in a high-energy orbital, the analogue of one of the $t_2$ orbitals in tetrahedral symmetry, and a dip in the energy gained on boron substitution is observed. From Fe onwards, however, the process of boron substitution is observed to be energetically favourable.

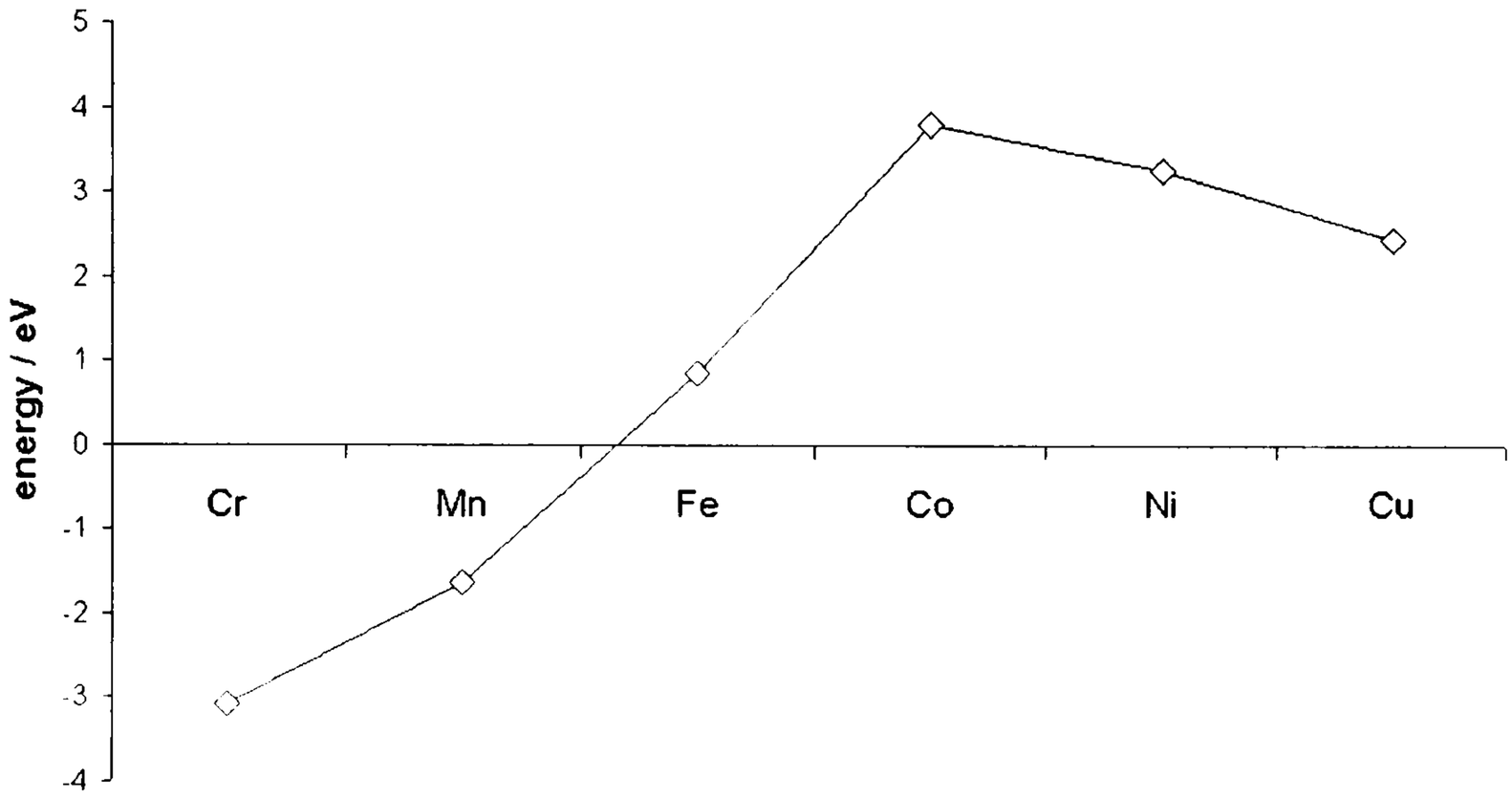


**Figure 6.33.** The enthalpy change on boron substitution at a TM substitutional defect (defined in Equation 6.11).

## Other charge states

Figure 6.34 below shows the energy gain for charging the $TM_s{}^0B_s$ complexes,

$$\Delta H^{+}_{CHARGE} = E[TM_s{}^{+} B_s C_{27} H_{36}] + E[B^{-} C_{28} H_{36}] - E[TM_s{}^{0} C_{28} H_{36}] - E[B^{0} C_{28} H_{36}]$$

$$\Delta H^{-}_{CHARGE} = E[TM_s{}^{-} B_s C_{27} H_{36}] + E[N^{+} C_{28} H_{36}] - E[TM_s{}^{0} C_{28} H_{36}] - E[N^{0} C_{28} H_{36}] \qquad (6.12)$$

The $TM_s{}^{-}B_s$ complexes stabilise the negative charge similarly to the $TM_s$ defects (compare with equivalent calculations on $TM_s$); the formation of $Ni_s{}^{-}B_s$ being unstable by 1.3 eV (without the inclusion of dielectric screening), compared with 1.0 eV for the formation of $Ni_s{}^{-}$. This value assumes that there is nitrogen present to compensate the negative charge on the transition metal. The question of the homogeneity of the Fermi level in diamond has been discussed [47], where it is suggested that charge compensation

depends more on the proximity of the complex to the compensating defect than to overall concentrations. So there is no reason *a priori* to reject the possible existence of these centres which require the simultaneous presence of boron and nitrogen.

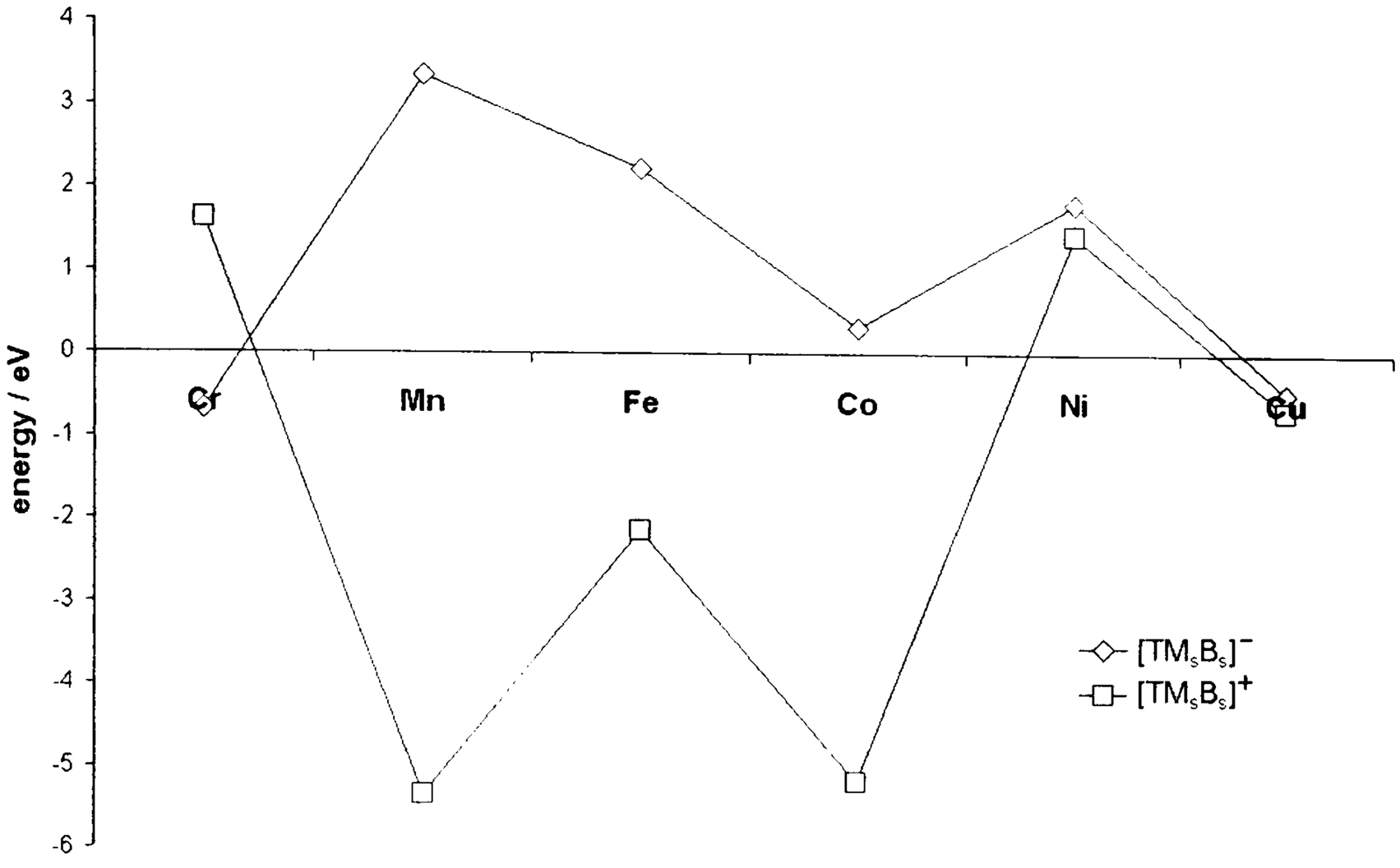


**Figure 6.34.** The energy gained on forming a charged $TM_sB_s$ cluster, and its charge compensating pair (including correction for finite cluster size). The enthalpy changes are defined in Equation 6.12.

The positively charged centres, $[TM_sB_s]^+$, are less stable in general, however, $[Ni_sB_s]^+$ is stable within the error of the calculation. $[Ni_sB_s]^+$ can be attributed to the fact that the extra electron of $[Ni_sB_s]^0$ must be accommodated in a high energy orbital, which is not occupied in $[Ni_sB_s]^+$.

### *6.8.2 Properties of the $TM_s$-$B_s$ complexes.*

The electronic structure of the $TM_sB_s$ defects is very similar to that of the $TM_sN_s$ complexes described above (section 6.6.2). Both resemble the $TM_s$ complexes, but with the symmetry lowered to $C_{3v}$ due to the presence of the odd nitrogen, or boron atom. The

main difference is that the order of the high-energy orbitals is reversed for the TM-boron complexes compared with the TM-nitrogen defects.

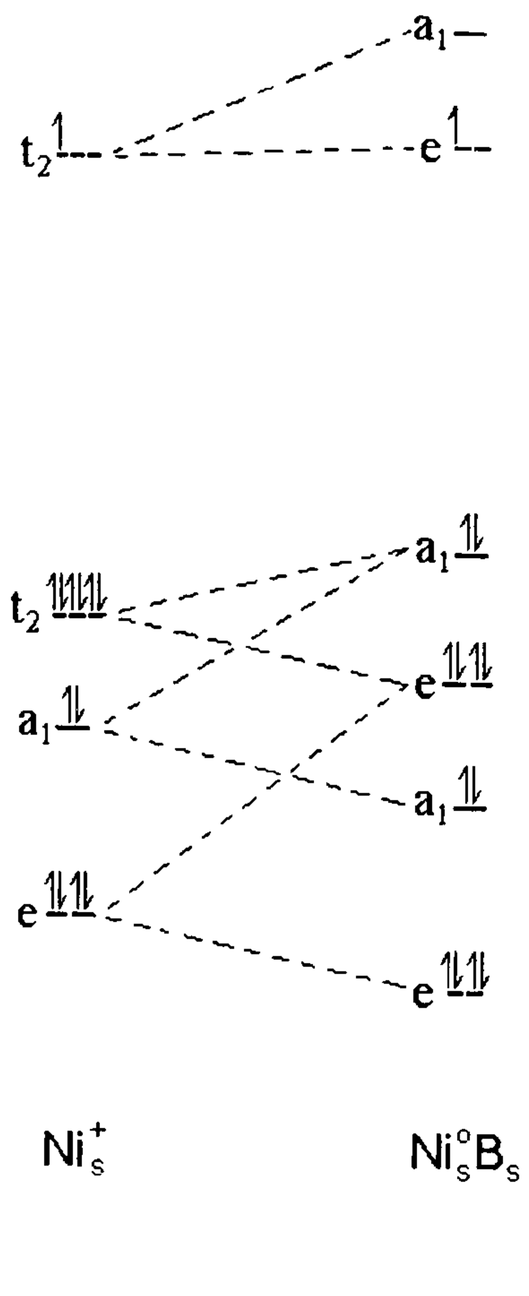


**Figure 6.35.** Schematic MO diagram, showing the correlation between the valence MOs of $Ni_s^+$ and $[Ni_sB_s]^0$.

It is found that the highest energy orbital has high boron character, 54%, whilst the other high energy orbital is only 42% metal d-orbital. This implies that the complex is quite vacancy like. Written as $TM_s^+B_s^-$ the charge on the metal will cause the d-orbitals to drop in energy (section 6.3.2) below the vacancy like orbitals. The ordering of the orbitals can be interpreted from the crystal field point of view. As the boron carries a large partial negative charge the $a_1$ orbital that points directly at it will be of higher energy than the e orbitals pointing toward the carbon atoms. The ordering of these orbitals for the TM-nitrogen complexes is then explained as they can be schematically represented as $(TM_s^-)$-$(N_s^+)_x$ . When $x$=1, the $a_1$ orbital is lowest in energy, as it points toward the positively charged nitrogen. The situation is reversed when $x$=3, as the $a_1$ orbital is now principally directed towards the lone carbon atom.

Assuming that the six low energy orbitals are filled first, then the upper three are filled to give maximum spin multiplicity, the ground states for the TMs of greatest interest are: $Co_sB_s$ ($^1A_1$), $Ni_sB_s$ ($^2A_1$) and $Cu_sB_s$ ($^3E$).

## 6.9 Summary of results.

Substitutional complexes are more stable than interstitial, contrary to Ref 45 but in agreement with Ref 48. Indeed, these calculations suggest that $TM_i$ are only metastable in diamond. The $TM_{sv}$ appear to be similarly stable to the substitutional defects, especially later in the transition series.

The negatively charged states of the interstitial complexes are strongly disfavoured. All other singly charged states of the defects examined appear, in general, to be viable.

The electronic structure of the interstitial complexes is in accord with the Ludwig-Woodbury model. Transition energies decrease across the transition series and with increasing positive charge on the defect: this is reflected with high spin states being predicted for positively charged $TM_i$ at the beginning of the series. Both the $TM_s$ and $TM_{sv}$ defects show behaviour fitting the (di)vacancy model at the beginning of the series, crossing over to fit the Ludwig-Woodbury model for the later transition metals.

Addition of up to two N atoms to $TM_s$ is found to be energetically viable and increasingly favourable as the transition series is crossed. Addition of boron to $TM_s$ is also found to be energetically favoured for the later TM. The electronic structure of these modified defects is consistent with that of distorted $TM_s$.

## 6.10 Conclusions from *ab initio* calculations.

Calculations based on the HF method are not as suitable as DFT for quantitative calculations on large clusters; the number of two electron integrals to be calculated prohibits this. The advantage of HF calculations is that they accord far more closely with

the qualitative ways of describing electronic structure that are commonly used by chemists/physicists. Specifically the one-electron functions can be found from RHF/ROHF/UHF calculations. These orbitals can then be occupied within the MCSCF framework to give genuine multiplets and excited states. This greater accord with our mental picture of the processes occurring, and the greater interpretability it brings, seems to me a valid reason to carry out calculations of these types as a follow up to DFT calculations, as long as they are relatively inexpensive.

It has been shown that even relatively unsophisticated calculations give a good account of the known properties of transition metals in diamond. The present calculations are not accurate enough to give data directly comparable with experimental results, but with much greater computational power becoming readily available, the possibility of calculations with chemical accuracy is feasible. Calculations on clusters of the size presented here, and a little larger, could easily be handled routinely, with greatly improved basis sets.

Much of the trouble with carrying out MCSCF calculations is providing a good enough initial guess to ensure convergence. The PC GAMESS package is soon going to allow wavefunctions from calculations using the MINI basis set utilised in this chapter to be projected onto an improved basis set and used as the initial guess wavefunction. This would greatly aid convergence, and provide an attractive way of calculating excited states.

[1] L Paslovsky and J E Lowther, J. Phys. Condens. Matter, **4,** 775 (1992)

[2] J Goss, A Resende, R Jones and S Oberg, Materials Science Forum, **196-201** , 67 (2001)

[3] K Johnston and A Mainwood, Diam. Relat. Mater., **11**, 631 (2002)

[4] K Johnston and A Mainwood, Physica B, **308-310**, 565 (2001)

[5] K Johnston and A Mainwood, Diam. Relat. Mater., **12**, 516 (2003)

[6] S.Huzinaga, J.Andzelm, M.Klobukowski, E.Radzio-Andzelm, Y.Sakai, H.Tatewaki, *Gaussian Basis Sets for Molecular Calculations*, (Elsevier,Amsterdam,1984)

[7] W J Hehre, R Ditchfield, J A Pople, J. Chem. Phys., **56**, 2257 (1972 )

[8] A J H Wachters, J. Chem. Phys., **52,** 1033 (1970 )

[9] A K Rappe, T A Smedley and W A Goddard III, J. Phys. Chem., **85**, 2607 (1981)

[10] W J Hehre, R F Stewart, J A Pople, J. Chem. Phys., **51**, 2657 (1969 )

[11] W J Hehre, R Ditchfield, R F Stewart, J A Pople, J. Chem. Phys., **52**, 2769 (1970)

[12] C Kittel, *Introduction to Solid State Physics* (Wiley, New York, 1997), 7th ed.

[13] Y Zhang, J Li, L Zhou and S Xiang, Solid State Com., **121**, 411 (2002)

[14] C M Sung and M F Tai, Int. J. Refract. Met. Hard Mat., **15**, 237 (1997)

[15] G Van De Rector, PhD Thesis, University of Groningen, 1988

[16] S.M.Sze, *Physics of Semiconductor devices*, (John Wiley and Sons, New York, 1981)

[17] N F Mott and M J Littleton, Trans. Faraday Soc., **34**, 2182 (1970)

[18] N F Mott and R W Gurney, *Electronic processes in ionic crystals*, (J Wiley and Sons, Oxford University Press: New York, 1940)

[19] R Mulliken, J. Chem. Phys., **23**, 1833 (1955); *ibid* 2343 (1959)

[20] C. Lee, W. Yang and R. G. Parr, Phys. Rev. B, **37**, 785 (1988)

[21] A D Becke, Phys. Rev. A, ***38***, 3098 (1988)

[22] A D Becke. J. Chem. Phys., **98**, 5648 (1993)

[23] P J Stevens, F J Devlin , C F Chabalowski, M J Frisch, J. Phys. Chem., ***98***, 11623 (1994)

[24] J C Slater, *Quantum Theory of Molecular and Solids Vol. 4: The Self-Consistent Field for Molecular and Solids;* McGraw-Hill: New York, 1947

[25] S H Vosko, L Wilk, M Nusair, Can. J. Phys., **58**, 1200 (1980)

[26] J P Goss, Ph.D thesis, University of Exeter, unpublished 1997.

[27] R Larico, J F Justo, W V M Machado, L V C Assali, Physica B, **84-88,** 340 (2003)

[28] J.P. Perdew, S. Burke, M. Ernzerhof, Phys. Rev. Lett. **77,** 3865 (1996)

[29] G W Ludwig and H H Woodbury, Solid State Phys., **13**, 223 (1962)

[30] G D Watkins, Physica B + C, **117B-118B,** 9 (1983)

[31] Coomer *et al*, proceedings of ICDS-20 , (1999)

[32] C J Ballhausen, *Introduction to Ligand Field Theory*, (McGraw-Hill, 1962)

[33] J P Goss, R Jones, P R Briddon, Proceedings of Diamond Conference, 2003

[34] V A Nadolinny et al, J. Phys. Condens. Matter, **11,** 7357 (1999)

[35] M Baker, private communication, 2003.

[36] M H Nazare, J C Lopes, A J Neves, Physica B, **308-310,** 616 (2001)

[37] M Baker, proceedings of Diamond conference, 2002

[38] A J Neves *et al*., Diam. relat. Mater., **9**, 1057 (2000)

[39] I N Kupriyanov *et al*,., Diam. Relat. Mater., **10**, 59 (2001)

[40] A Zaitzev, Phys. Rev. B, **61**, 12909 (2000)

[41] A T Collins, Diam. Relat. Mater., **9**, 417 (2000)

[42] S C Lawson *et al*., J. Appl. Phys., **79**, 4348, (1996)

[43] B Bleaney, Proc. Phys. Soc. (London), **A63**, 407 (1950)

[44] J Isoya, H Kanda, Y Uchida, Phys. Rev. B, **42** 9843 (1990)

[45] U Guestmann *et al*, Physica B **273-274**, 632 (1999)

[46] V A Nadolinny *et al*, private communication, 2001

[47] A Collins, J. Phys. Condens. Matter., **14**, 3743 (2002)

[48] J Goss *et al*, proceedings of Diamond conference, 2002.

# Chapter 7.

# The effect of transition metals on nitrogen aggregation in diamond

## 7.1 Introduction

Synthetic diamonds grown using one of the high pressure, high temperature (HPHT) processes frequently contain some traces of the solvent-catalyst that was used to grow them [1-5]. Where nickel or cobalt are included in the solvent mixture, these metals form point defects in the diamond, usually concentrated in {111} growth sectors, which can be detected by optical [1-3] or electron paramagnetic resonance (EPR) [4,5] spectroscopy. In addition, most of these synthetic diamonds contain appreciable concentrations of nitrogen, unless nitrogen is explicitly excluded by using nitrogen getters. HPHT diamonds grown at relatively low temperatures (1400-1500° C, for example) contain nitrogen in the form of single substitutional atoms, $N_s$ or C centres. Natural diamonds usually contain aggregated nitrogen, either as pairs of neighbouring substitutional atoms, A centres, or four substitutional atoms around a vacancy, B centres.

It is supposed that when natural diamond initially grows, it contains single nitrogen substitutional atoms, and that their aggregation is caused by their long term (billions of years) subjection to high temperatures and pressures under the earth's crust [6]. Thus the state of aggregation can tell us something of the geological history of a natural diamond. By investigating the aggregation of nitrogen in synthetic diamond under known conditions a much better idea of the thermodynamics of these processes can be obtained. Conversely this knowledge allows us to estimate the conditions a synthetic diamond has been subjected to by comparison with natural diamonds of known history. For example, Evans and Harris [7] estimated the activation energy for the formation of B centres to be 6.5-7.1 eV.

## The effect of transition metals on nitrogen aggregation in diamond

Chrenko *et al* [8] were the first to aggregate single nitrogen atoms to form A centres under laboratory conditions They found that the reaction obeyed 2nd order kinetics, which are to be expected if no other factors are involved in the process. However, the activation energy that they obtained, 2.6 eV, was much lower than that which has been derived since by other workers (see the review by Evans [6]). The accepted value for this 2nd order kinetic reaction is about 5 eV [6]. Collins et al [9] showed that the nitrogen aggregation proceeded significantly faster in irradiated diamond, a process then attributed to vacancy-assisted migration of nitrogen. Mainwood [10], using a computational model of the processes, derived an activation energy for migration of the nitrogen by a direct interchange between the atom and its neighbour of 6.3 eV, and a vacancy-assisted mechanism with an activation energy of 4.5 eV. She suggested that both these processes contributed to the migration in unirradiated diamond, but the vacancy-related one dominated in irradiated samples. All these mechanisms would lead to 2nd order kinetics in the aggregation. However, recent studies in nickel [10] and nickel/cobalt [11] containing diamonds show significant deviations from these 2nd order kinetics.

The rate of aggregation is found to be much higher in {111} growth sectors. The nickel and cobalt defects are concentrated in the {111} growth sectors [12,13] and it was suggested that the presence of these metals affects the aggregation rate [14]. Kiflawi *et al* [10] showed that this was the case for nickel and suggested that it could be releasing either a vacancy or an interstitial atom which accelerated the migration of the nitrogen and hence the aggregation.

On the other hand, in HPHT synthetic diamonds grown at higher temperature (>1550° C) aggregation of the nitrogen can occur during growth [15]. The concentration of aggregated nitrogen is greatest at the centre of the crystal, where the diamond has been kept at high temperatures for longest. At the edge of the diamond, very little of the nitrogen has aggregated [15].

In this chapter, it will be shown that in both nickel and cobalt-containing diamond, the aggregation of nitrogen is facilitated by the release of interstitials by the transition metal. The kinetics are modelled numerically, giving rise to a few parameters to

determine the reaction rates. Using these same parameters, in section 4, the aggregation of nitrogen during crystal growth is modelled.

## 7.2 The mechanisms of nitrogen migration

The standard diffusion pathway, for which Evans [6.16] derived an activation energy of 5.0 ± 0.3 eV would lead to 2nd order kinetics if the limiting step in the process is the site to site migration of the nitrogen atom. We can suggest two mechanisms for the enhanced migration:

1) Vacancy assisted - the vacancy (V) is released from the transition metal and it is trapped by a nitrogen ($N_s$) forming a nitrogen vacancy complex, NV. At a temperature of 1400° C, the vacancy would be expected to make about 750 jumps per millisecond, using the annealing data and assumptions of Davies *et al* [17], so we can assume that this process happens effectively instantaneously. The nitrogen moves into the vacancy, and the complex may then dissociate, leaving the vacancy to assist another nitrogen in a step of its migration. Mainwood [18] calculated that the limiting step in this process was the dissociation of the NV centre, with an activation energy of 4.5 eV. When the nitrogen (with or without a vacancy) moves close to another substitutional nitrogen, an A centre (NN) will form, with the release of the accompanying vacancy. To summarise:

$$\text{TM-V} \rightarrow \text{TM} + \text{V}, \quad \text{V} + \text{N}_s \rightarrow \text{NV}, \quad \text{NV} + \text{N}_s \rightarrow \text{NN} + \text{V} \qquad (7.1)$$

In this process, we would expect some nitrogen-vacancy centres (NV and H3 (NVN)) to be present as a by-product of the migration. These have not been observed.

2) Interstitial: The carbon interstitial $C_i$ is released by the transition metal, it displaces a nitrogen, releasing a nitrogen interstitial, $N_i$, which migrates rapidly until it is trapped by an nitrogen substitutional atom forming an A centre and releasing a carbon interstitial.

$$\text{TM-C} \rightarrow \text{TM} + \text{C}_i, \quad \text{C}_i + \text{N}_s \rightarrow \text{N}_i, \quad \text{N}_i + \text{N}_s \rightarrow \text{N-N} + \text{C}_i \qquad (7.2)$$

In this process, the carbon and nitrogen interstitials are expected to have a very low migration energy [18,19] and similarly the displacement of the nitrogen into an interstitial position [18,19] would have a relatively low energy barrier. Therefore, the rate-determining process, once the interstitials have been released, will be the conversion of the nitrogen interstitial-substitutional complex into an A aggregate.

We would expect there to be some nitrogen interstitials present as a by-product of this process, and indeed the H1a infra-red absorption line, which has been identified with the nitrogen interstitial [19], has been seen under conditions of nitrogen aggregation.

It is known that nickel is present in as-grown diamond as interstitials - the positively charged defect is observed by EPR and optical spectroscopy, and as single substitutional atoms - the negatively charged defect has been identified by both techniques. However, on annealing to temperatures at which the nitrogen becomes mobile, these defects disappear and nickel-nitrogen complexes with structures based on nickel in a divacancy, are seen instead. Similar processes probably occur in cobalt-containing diamond, although fewer defects have been detected or studied in these samples, as yet. This implies that carbon interstitials are released as the nickel (or cobalt) converts from an interstitial or substitutional position to a divacancy structure.

For all the above reasons, we favour the interstitial mechanism for the enhanced migration of nitrogen in transition metal-containing (or, indeed, in irradiated) diamond. However, the kinetics do not allow us to distinguish between the two processes [10].

## 7.3 Kinetics

These mechanisms mean that the rate of loss of single nitrogen atoms has three terms[10]. In the vacancy case these are: a term proportional to the rate of release of vacancies, a second term proportional to the concentration of vacancies and the concentration of substitutional nitrogen trapping them, and a third due to the normal second order kinetics of aggregation. In the interstitial case, the terms are mathematically the same: respectively the first term proportional to the rate of release

of interstitials, the second to the concentration of nitrogen interstitial and substitutional nitrogen and the third due to normal aggregation.

Here the rate equations are derived for the interstitial assisted process. The same rate equations can be derived for the vacancy-assisted process, by replacing $[C_i]$ by $[V]$, and $[N_i]$ with $[NV]$.

These coupled differential equations can be solved numerically, with the initial metal complex concentration, $K$, and the initial nitrogen concentration varying from system to system.

At annealing temperatures of 1400-1500°C the reaction $C_i + N_s \rightarrow N_i$ occurs rapidly [18] and it can be approximated that $[N_i] = [C_i]$. The $C_i$ is formed by a first order reaction from the metal complex

$$\frac{d[TM]}{dt} = -\frac{d[C_i]}{dt} = -\frac{d[N_i]}{dt} = -\alpha[TM] \tag{7.3}$$

where $\alpha$ is the rate constant for release of $C_i$ from a metal complex, TM and the concentration of defect X at time t is denoted $[X]$. The separable first order differential equation in $[TM]$ can be solved to give $[TM]=Ke^{-\alpha t}$. Leading to

$$\frac{d[N_i]}{dt} = \alpha K e^{-\alpha t} \text{ and } [N_i] = K(1 - e^{-\alpha t}) \tag{7.4}$$

Then with the additional parameters, $\delta$, the conventional rate constant , $\varepsilon$, the rate constant for the $N_i + N_s \rightarrow NN + C_i$ step, the rate that the $N_s$ centres are annealed out, and that A centres form are given by

$$-\frac{d[N_s]}{dt} = \frac{d[N_i]}{dt} + \varepsilon[N_s][N_i] + \delta[N_s]^2 \tag{7.5}$$

$$\frac{d[N_A]}{dt} = \varepsilon[N_s][N_i] + \delta[N_s]^2 \tag{7.6}$$

An alternative to simply assuming that $[N_i] = [C_i]$ can be obtained by applying the steady state approximation to $[C_i]$. That is assuming that the active carbon interstitial is present in the system at constant small quantities. Then

$$\frac{d[C_i]}{dt} = \alpha[TM] - \beta[C_i][N_S] + \varepsilon[N_i][N_S] = 0.$$

The second two terms in the middle equality can be recognised as the negative of the rate of change of the nitrogen interstitial concentration. This immediately gives $\frac{d[N_i]}{dt} = \alpha[TM]$ and the other kinetic terms follow as before.

All these expressions assume that none of the species involved are trapped at other sites in the diamond (such as the metal complexes themselves for instance). It is hard to estimate how large an error may be perpetrated by this assumption, but in many diamonds substitutional nitrogen will be by far and away the dominant impurity (by 1-2 orders of magnitude) and other traps will be found in much lower concentrations.

## 7.4 Experimental method

The synthetic diamonds were grown with either pure nickel catalyst; 95% cobalt, 5% iron; 65% nickel 35% iron; or 55% nickel, 45% iron. Each was cut into three sections with only {111} growth sectors, and in some cases further samples with {100} growth sectors were cut from the same diamonds. The samples were polished to leave parallel faces. To ensure that the same area of the sample (in case of inhomogeneity) was used for each measurement, the location was marked on the face. Infrared absorption spectra were deconvolved to produce the concentration of nitrogen in the A aggregates (from the 1282 $cm^{-1}$ line), as single substitutional atoms, and as positively charged substitutionals. At the same time the strength of the absorption at 1450 $cm^{-1}$ (which originates at the nitrogen interstitial) was monitored. The three samples from each batch were annealed isothermally at 1400, 1450 and 1500° C, for times up to 68 hours. These experiments were carried out by D Fisher at the DTC (Diamond Trading Center).

## 7.5 Results

The aggregation in the {100} growth sectors of the cobalt grown samples was not measurable, even under conditions where nearly 90% of nitrogen in the equivalent {111} growth sectors had aggregated. In the nickel-grown samples, the aggregation in a {100} growth sector reached just under 5% while the equivalent {111} growth sector showed 82% aggregation.

The data from {111} growth sectors of four solvent systems each annealed at 1400, 1450, 1500° C were used to fit the parameters of Equation 7.3-6 (see Figure 7.1 and Figure 7.2).

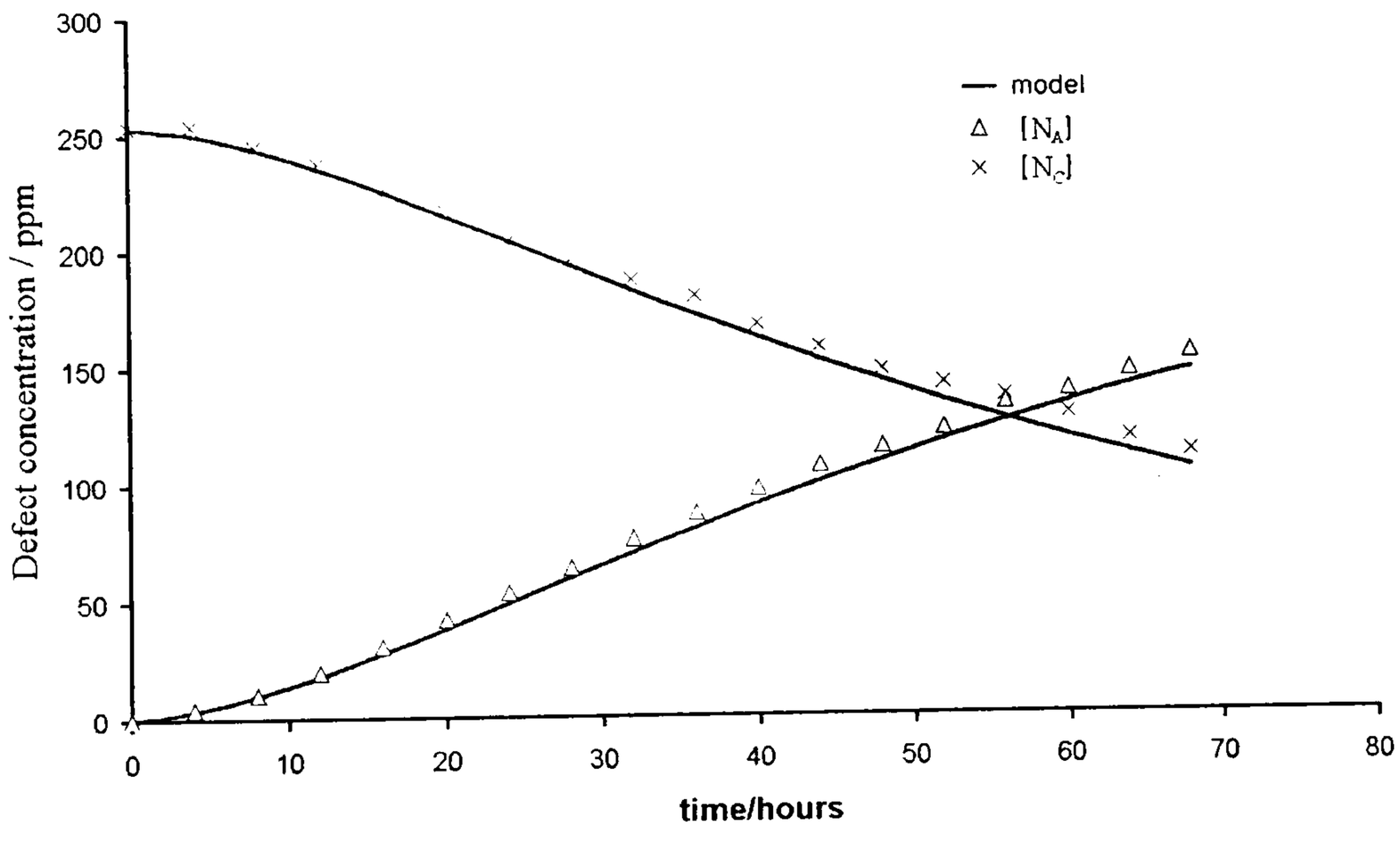


**Figure 7.1.** Showing fit for $[N_C]$ and $[N_A]$ in a diamond grown at $1400^0$C with a cobalt catalyst.

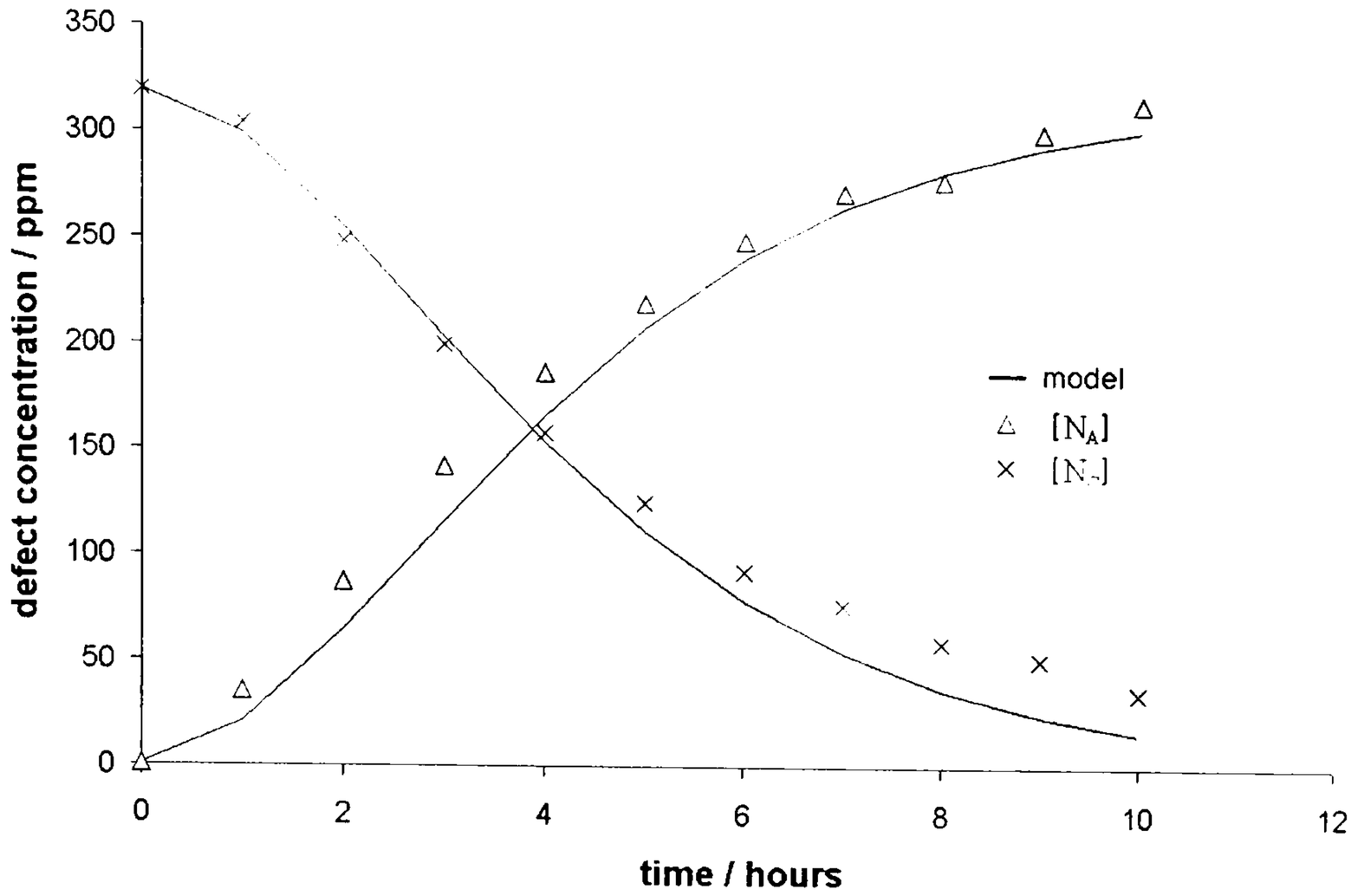


**Figure 7.2.** Showing fit for $[N_C]$ and $[N_A]$ in a diamond grown at $1500^0$C with a cobalt catalyst.

Assuming that the rates vary with temperature ($T$) as

$$\alpha(T) = \nu_\alpha \exp(-E_a^\alpha / kT) \qquad (7.7)$$

with some pre-exponential factor $\nu_\alpha$, (and similar expressions for the other rates), we could determine the activation energies for the processes shown in Table 7.1.

| | Activation energy for | Co | Ni |
|---|---|---|---|
| $E_a^\alpha$ | Release of $C_i$ /V | 3.7 ± 0.2 eV | 3.4 ± 0.2 eV |
| $E_a^\delta$ | Nitrogen diffusion | 5.1 ± 0.2 eV | 4.9 ± 0.2 eV |
| $E_a^\varepsilon$ | $N_i$/V – assisted aggregation | 3.9 ± 0.2 eV | 4.2 ± 0.2 eV |

**Table 7.1:** The activation energies for the migration of nitrogen by the mechanisms described in the text. The activation energies for the processes in the nickel/iron alloy samples were the same as for the pure nickel-grown sample.

## The effect of transition metals on nitrogen aggregation in diamond

The activation energies for the unassisted aggregation mechanism agree within experimental error for all the solvent systems examined, and with the previous accepted value. The activation energies for the assisted processes show activation energies of the order of chemical bond-breaking processes – the cohesive energy of carbon is diamond is 7.1 eV – which is consistent with the proposed mechanism of these processes. The energies derived are again in agreement with each other within experimental error.

The pre-exponential factors can reveal a little more about the processes that may be involved. The release of interstitials (or vacancies) from the transition metal and the conversion from $N_i + N_s$ (or $N_s$ + NV) to A centres are one-step processes, and their pre-exponential factors would be expected to be of the approximate magnitude of the phonon frequencies in diamond. The migration processes, on the other hand, involve many steps and would be expected to have pre-exponential factors quite considerably lower. This simple-minded interpretation is fraught with problems (see, for example Refs 17 and 20), and errors of several orders of magnitude are common.

Table 7.2 gives the pre-exponential factors in the kinetics. Because of the exponential part of , the ±0.2 eV error margin in the activation energies corresponds to factors of $5^{\pm 1}$ in the uncertainty in the pre-exponential. In general the pre-factors are of the order of the Raman frequency in diamond ($\approx 4 \times 10^{13}$ $s^{-1}$), with ε considerably larger than the other processes. This provides some evidence of the interstitial mechanism; since the vacancy assisted mechanism requires the rate limiting step ( the dissociation of the NV complex) at each step of the migration, its pre-factor would be expected to be considerably less.

| | Pre-exponential factor for | pure Ni | Pure Co | Fe/Ni (55:45) | Fe/Ni (65:35) |
|---|---|---|---|---|---|
| $\nu_a^{\alpha}$ | Release of $C_i$ /V | $5.4 \times 10^{13}$ | $3.2 \times 10^{13}$ | $6.6 \times 10^{11}$ | $1.0 \times 10^{12}$ |
| $\nu_a^{\delta}$ | Nitrogen diffusion | $1.4 \times 10^{14}$ | $5.7 \times 10^{13}$ | $1.1 \times 10^{10}$ | $1.5 \times 10^{12}$ |
| $\nu_a^{\varepsilon}$ | $N_i$/V-assisted aggregation | $2.6 \times 10^{15}$ | $9.0 \times 10^{14}$ | $1.9 \times 10^{15}$ | $2.7 \times 10^{15}$ |

**Table 7.2.** Pre-exponential factors (in $s^{-1}$) in equation 7.6 for the processes of migration. The error ranges on these values are factor of five (or a fifth).

The presence of iron in the melt appears to have a pronounced effect upon α and δ, reducing both by two or more orders of magnitude, though the interstitial migration process is unaffected.

If, as is seeming increasingly likely, it is the interstitial process which accounts for the enhanced migration of nitrogen, we would expect to see the nitrogen interstitial absorption at 1450 $cm^{-1}$ to follow . While the initial rise in $[N_i]$ is reproduced well, in some samples there is a fall in the concentration as the aggregation proceeds, presumably due to the $N_i$ becoming trapped by other defects (the transition metal itself, for example).

## 7.6 Crystal Growth

If HPHT diamonds are grown at temperatures above about 1500° C, some aggregation of the nitrogen actually occurs during the growth [15]. One would expect that the regions of the crystal nearest the seed, which grew first and therefore have been effectively annealed at the growth temperature for longest, to show the highest degree of aggregation. This has, indeed, been observed. Babich et al [15] measured the concentration of A and $N_s$ centres as a function of the distance from the seed, along the growth directions. However, in their sample, there were four distinct growth sectors, all with {111} growth direction. Two of these, they termed "fast" growth sectors, with rates of growth of about 30 μm/h. The two "slow" sectors had a much smaller growth rate of nearer 10 μm/h. It is not clear why there is such a discrepancy in growth rates and the conditions in the growth cell are not well known. There is a temperature gradient across the cell, which would keep the growth faces of the slow sectors at a lower temperature than those of the faster sectors, and there is likely to be a concentration gradient of carbon in the nickel solvent-catalyst.

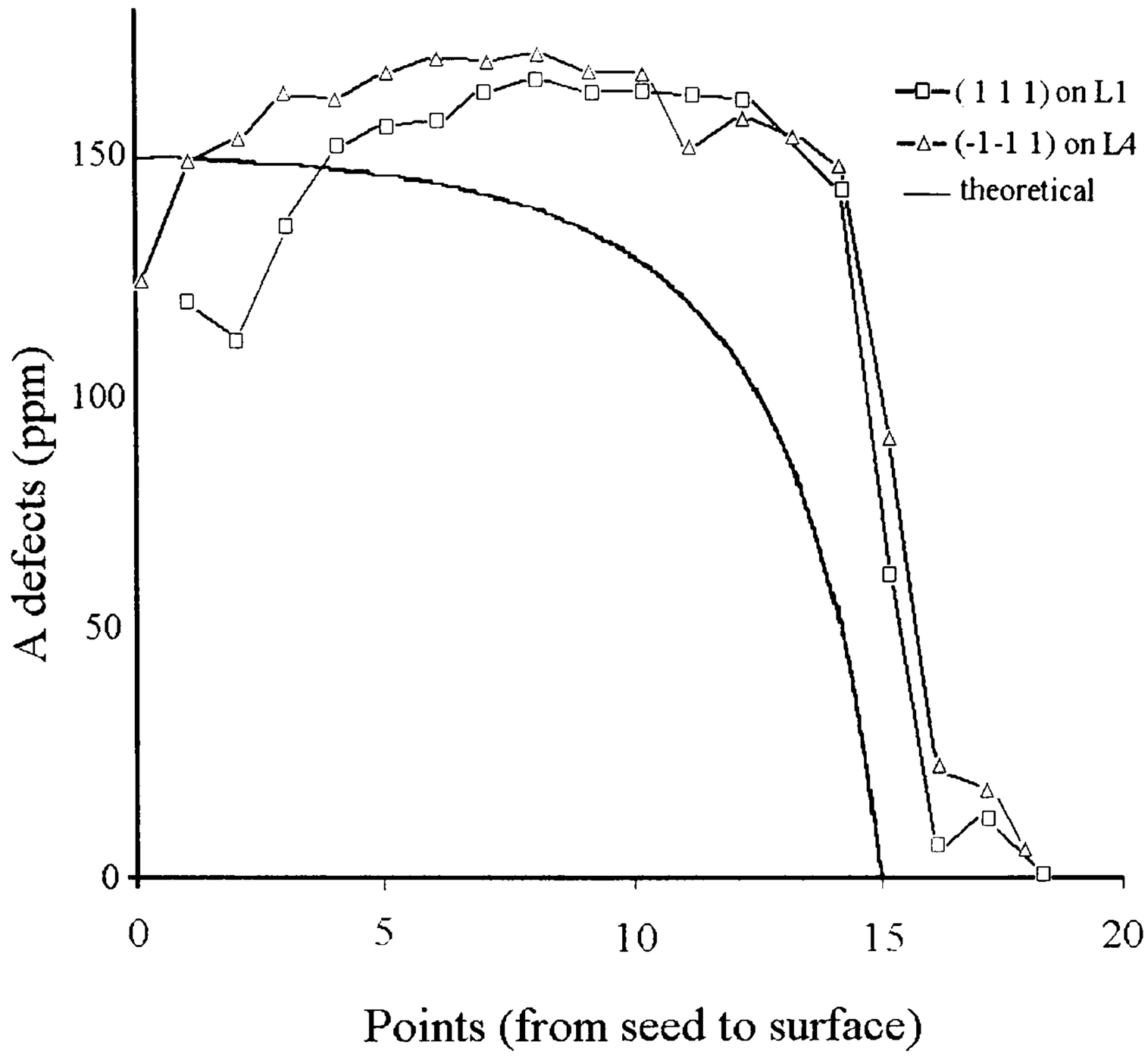


**Figure 7.3.** Distribution of A centres along <1 1 1> directions in fast growth sectors.

Fast growth sectors show the expected distribution (Figure 7.3) - almost complete aggregation to A centres except near the surface. Slow growth sectors however show a quite different behaviour (Figure 7.4). As Babich *et al* have plotted their data, it would be anticipated that the same pattern of aggregation would be observed as in the fast growth sectors, aggregation only depending on length of time the nitrogen atom spent in the crystal.

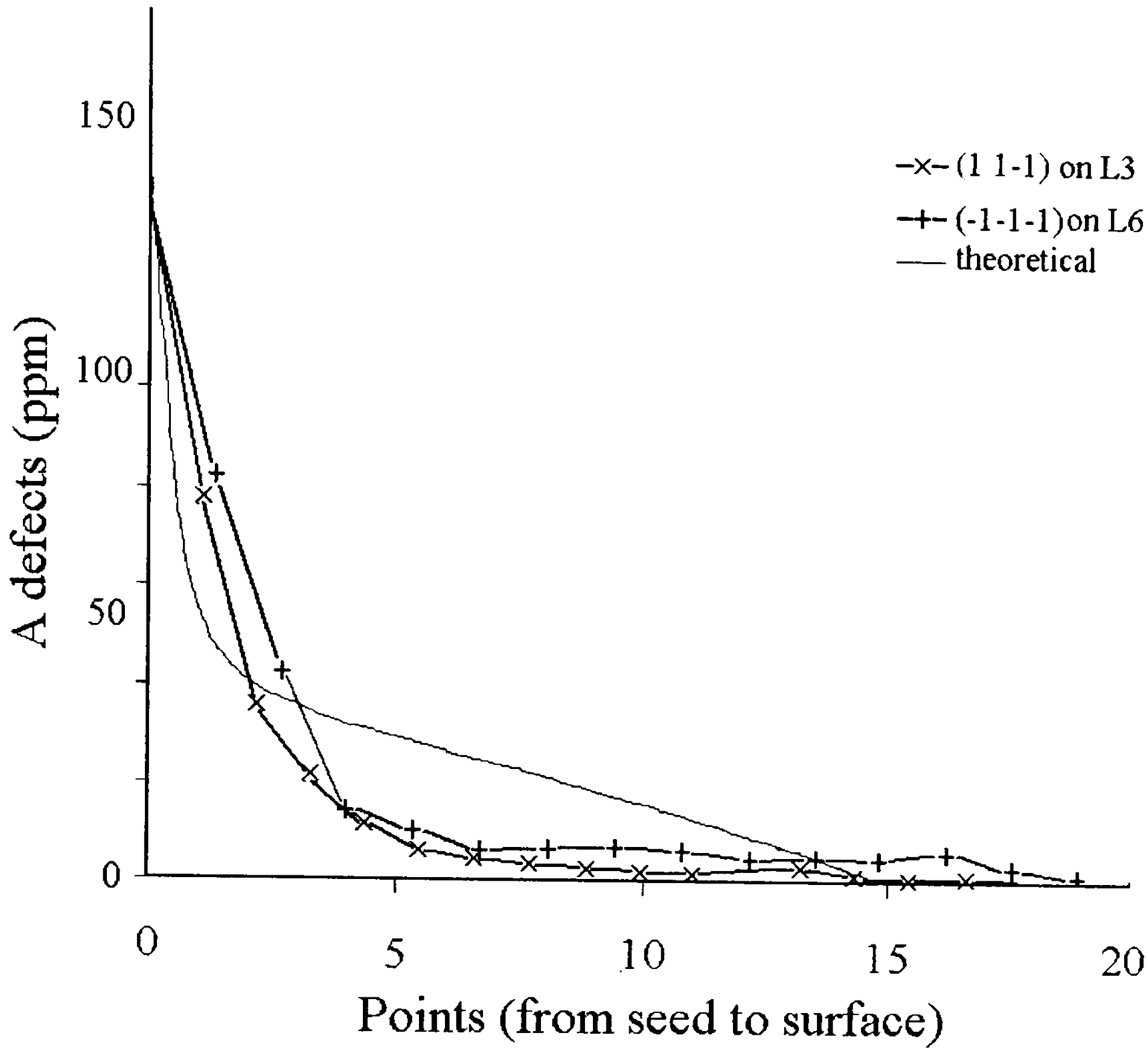


**Figure 7.4.** Distribution of A centres along <1 1 1> directions in slow growth sectors.

The distribution of A and $N_s$ centres in a {1 1 1} growth sector is modelled by assuming the aggregation, by the same processes as before, occurs whilst the crystal is growing. It is assumed that nitrogen impurities enter the crystal as single substitutional atoms, at a constant concentration of 150 ppm. The nickel concentration is taken from the annealing data above and is assumed uniform throughout the sector. The same parameters and activation energies obtained from the fits to experimental data given in the previous section are used in this model. The results are shown as distribution of A and $N_s$ centres from the centre of the crystal along the growth direction. For the fast growth sectors, agreement with the experimental data is good (Figure 7.3)

To reproduce the experimental results for the slow growth sectors, it is necessary to assume the nickel distribution is not homogeneous in these regions. Babich *et al* [15] noted that infrared absorption at 1332 $cm^{-1}$ due to $N^+$, which is known to correlate with the nickel concentration [3], was only observed near the crystal seed. Taking this

into account by assuming the same nickel concentration as before only very close to the seed, falling off as the inverse of the distance beyond that, the experimental results are qualitatively reproduced (Figure 7.4). There is no suggestion that this is the functional form of the variation of the nickel concentration with distance from the seed, merely that the concentration of nickel drops off quickly and Figure 7.4 shows that this is mirrored by the degree of nitrogen aggregation.

## 7.7 Conclusions

The fits to the annealing data are satisfactory for all of the systems and the activation energies derived are physically reasonable, with the activation energy for the direct process agreeing closely with previous estimates. This suggests that the interstitial mechanism provides a plausible explanation for enhanced nitrogen aggregation in nickel or cobalt containing diamond.

The results of modelling the distribution of unaggregated and aggregated nitrogen through a crystal suggest that nickel is distributed quite unevenly in the slow growth sectors, which is supported by the observation of $N^+$ absorption only occurring near the seed [15].

## References

[1] A T Collins and P M Spear, J. Phys D., **15,** L183 (1982)

[2] S C Lawson, H Kanda, K Watanabe, I Kiflawi, Y Sato and A T Collins, J. Appl. Phys, **79,** 4348 (1996)

[3] S C Lawson and H Kanda, J. Appl. Phys, **73,** 6 (1993)

[4] J Isoya , H Kanda and Y Uchida, 1990 Phys. Rev. B, **42,** 9843 (1990)

[5] D C Hunt, D J Twitchen, M E Newton, J M Baker, JK Kirui, JA van Wyk, TR Anthony, WF Banholzer, Phys. Rev. B, **62,** 6587 (2000)

[6] T.Evans, in "*The Properties of Natural and Synthetic Diamond*", edited by J.E.Field (Academic, London, 1992), p.259

[7] Evans & Harris, Proceedings of the 4th International Kimberlite Conference, Perth 1986

[8] R M Chrenko, R E Tuft, and H M Strong, Nature (London), **270,** 141 (1977)

[9] A T Collins, J.Phys. C, **13,** 2641 (1980)

[10] I Kiflawi, H Kanda, A Mainwood, Diam. Relat. Mater., **7,** 327 (1998)

[11] D Fisher and S C Lawson, Diam. Relat. Mater., **7,** 299 (1998)

[12] A T Collins, H Kanda, R C.Burns, Phil. Mag. B, **61,** 797 (1990)

[13] H Kanda, H Watanabe, Diam. Relat. Mater., **6,** 708 (1997)

[14] S.Satoh, H. Sumiya, K. Tsuji, S.Yazu, in "*Science and Technology of New Diamonds*", S Saitom, O Fukunga, Y Yoshokawa (Eds.), KTK Science Publications, Tokyo 1990

[15] Y V Babich ,B N Feigelson, D Fisher, A P Yelisseyev, V A Nadolinny and J M Baker, Diam. Relat. Mater., **9,** 893 (2000)

[16] T Evans and Z Qi, Proc. R. Soc. (London) Ser. A, **381,** 159 (1982)

[17] G Davies, SC Lawson, AT Collins, A Mainwood, S J Sharp, Phys. Rev. B, **46,** 13157 (1992)

[18] A.Mainwood, Phys. Rev. B, **49,** 7934 (1994)

[19] I Kiflawi A Mainwood, H Kanda, D Fisher, Phys. Rev. B, **54,** 16719 (1996)

[20] J F Prins, Nucl. Instr. Meth. B, **166,** 364 (2000)

# Chapter 8.

# Summary and suggestions for further work.

Chapters 4, 6 and 7 have set out the original work conducted for this thesis. At the end of each chapter conclusions have been drawn, but in this chapter the main points of interest will be reviewed. Also in this chapter, suggestions for further work and ideas for constructive extensions of the work presented earlier will be given.

Chapter 4 was directed at the technique of uniaxial stress. It was pointed out that experimentally there are some optical lines associated with TM centres that have not been amenable to uniaxial stress analysis. Also, the effects of spin orbit coupling on uniaxial stress data had not been systematically investigated to our knowledge. We aimed to see whether spin-orbit coupling would have an appreciable effect on uniaxial stress data and whether this effect could be responsible for the odd behaviour of the TM related optical lines. By ignoring configuration interaction, a fairly simple perturbation scheme was set up to deal systematically with spin-orbit coupling for any tetrahedral system; the complete set of matrix elements is given in section 4.4. The results, however, suggest that spin-orbit coupling is not the cause of the odd behaviour observed. This conclusion comes about because, whenever the spin-orbit coupling is strong enough to cause a significant change to the uniaxial stress spectra, its effects are also visible in the non-stressed transition. The results of the chapter could easily be expanded to take small trigonal or tetragonal distortions into account, which would partially quench the spin-orbit coupling.

A systematic study is made of the basic TM environments si made in Chapter 6 and some of the defects with nitrogen or boron aggregated around the TM are investigated. The use

of Hartree-Fock-Roothaan methods and their extensions with multiple electronic configurations provide a contrast with the prevalent DFT studies. We point out that, despite some shortcomings, the HF based methods provide a much greater degree of interpretability. As a result of the calculations we are able to put forward consistent models of the behaviour of the TMs across the transition series in different environments.

Particularly noteworthy points are:

the instability of the TM interstitial defects, as has also been noted in recent DFT studies. This raises a key point about the TM and their role as catalysts in the diamond growth process – if thermodynamically unstable defects are being incorporated the explanation of the absence of TM other than nickel or cobalt cannot be explained simply by thermodynamic arguments. We will return to this point later.

the similarity in stability of the semivacancy and substitutional defects. This is in broad agreement with the observation of semivacancy related defects appearing at elevated annealing temperatures. We point out that the whilst our calculations show the semivacancy defects to be slightly less stable than the substitutional, the transition to a semivacancy environment will be driven by a release of strain energy and be entropically favoured. Neither of these effects is included in our modelling.

the change in electronic structure of the TM substitutional defects as the transition series is crossed. We show that at the beginning of the series the $TM_s$ defects qualitatively fit the Ludwig-Woodbury model, the valence orbitals possessing high metal content. As the transition series is traversed the metal orbitals are reduced in energy, because of the additional nuclear charge, and the valence orbits take on the character of a vacancy defect.

the parallels in electronic structure of the semivacancy and substitutional defects. The semivacancy electronic structure is similar to the substitutional TM defects, but with states derived from a divacancy mixing into the metal orbitals rather than a vacancy.

The benefits of the method used show clearly in the observation and systematisation of the patterns of change in electronic structure as the series is crossed. The similarity of the output for GAMESS to the qualitative molecular orbital approach generally adopted for thinking about defects made these trends much easier to see. This needs to be considered when suggesting further work in this area. With the rapid increase in processing power the obvious suggestion is to use bigger clusters and larger basis sets; this is undoubtedly necessary, but there is a danger of the benefits in interpretation being swamped by huge basis sets and large numbers of orbitals. Another trouble is that the MCSCF methods used to obtain excited states cannot use symmetry and, as such, will use the increased processing power much more quickly than the HF calculations and they will also be harder to converge with enhanced basis sets. TM are notoriously difficult to model using the HF approach, but I feel calculations such as these in support of more accurate DFT calculations are of value for the reasons expressed above. In this light it would make sense to take an intermediate approach, take fairly large basis sets and use moderate clusters to keep the calculations relatively inexpensive whilst still providing reasonable reliability. The GAMESS code seems particularly good for this task.

Given the success of the calculations on TM defects, it seems logical to conduct work on other defects in diamond that HF calculations should be able to tackle more easily, preferably defects that have already been tackled with DFT – the NV centre for instance. Calculations of this sort, gaining genuine excited states, should advance the understanding of the defect's electronic structure substantially. This ability of HF based calculations to obtain genuine excited states is another feature that should be exploited. Initial targets should be fairly well understood defects so that there is god experimental data to compare computational results to.

## Summary and suggestions for further work.

The final section of my work is in chapter 7 of this thesis. It has previously been shown that the aggregation of nitrogen in diamond is influenced by the presence of TM defects. Additional experimental data has been fitted using a interstitial (or possibly vacancy) mediated mechanism. The results fit the experimental data well and the parameters derived are all consistent and of sensible magnitude. The results of modelling the growth of a diamond crystal again throw up the result that the incorporation of TMs into diamond is often not thermodynamically controlled. In fast growing sectors the TMs are found to be fairly homogeneously distributed, however, in slow growing sectors the TMs are only found near the nucleus of the crystal. This suggests to me that the TMs do play a role in keeping the nucleation site reactive initially, but once the diamond has reached a critical size they are no longer needed. In the fast growing sectors some TMs still get trapped, but in the slow growth sectors the thermodynamic instability of the TM defects excludes them from the crystal. If the growth process does occur in anything like this manner it means the TM to be an effective catalyst must be able to dissolve carbon efficiently and bind to the nucleation site in a transient fashion i.e. with a moderate bond strength. If the TM were to bind permanently the nucleation site would become closed off and the crystal would not grow. This is all speculation, but I believe that some mechanism like this will be needed to explain the widespread observation of nickel and cobalt, but not iron and copper. The mechanism sketched out is roughly analogous to the that of TMs in the growth of carbon nanotubes. *Ab initio* calculations simply do not support the idea that defects of nickel and cobalt are much more stable than the other transition metals. Further experimental work, especially on the spatial distribution of the TMs, is needed before a full understanding of the TM's role as a catalyst can be fully understood.

HPHT synthesis of diamond has not evolved as quickly as anticipated. Specifically the synthesis process has not become economically viable for large scale gem or high quality usage. When this changes, understanding the synthesis process is detail will be of huge

interest to both the gem trade and other markets needing diamonds with specific characteristics.